Pulsed Mid-Infrared Upconversion Imaging in Rotating Detonation Combustors

by

Logan White

A dissertation submitted in partial fulfillment
of the requirements for the degree of
Doctor of Philosophy
(Aerospace Engineering)
in the University of Michigan
2020

Doctoral Committee:

Associate Professor Mirko Gamba, Chair
Professor James F. Driscoll
Professor Volker Sick
Professor Herbert G. Winful

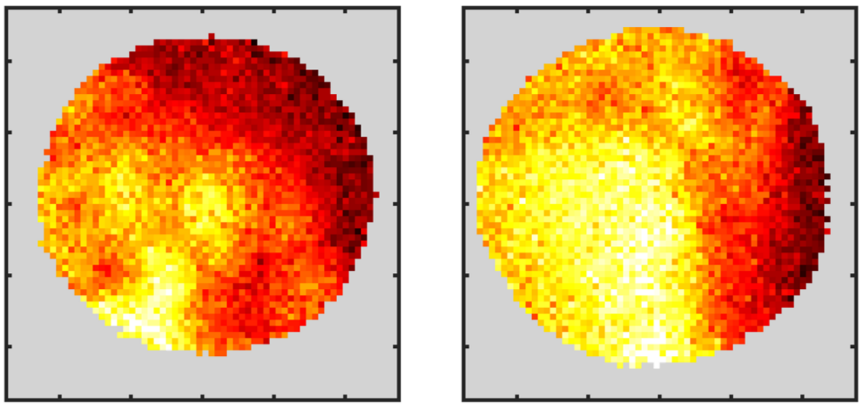

Logan White

Lwwhite@umich.edu

ORCID iD: 0000-0002-2316-0598

For my parents, Mark and Deanna.

ACKNOWLEDGMENTS

I would first like to thank my PhD advisor, Professor Mirko Gamba, for his guidance and tireless support. He introduced me to the field of optical diagnostics, a concept that was completely new to me when I arrived on campus. His willingness to let me take risks and encouragement for me to pursue new ideas made this work possible.

Thank you to my committee members, Professor James Driscoll, Professor Volker Sick, and Professor Herbert Winful, for serving on my dissertation committee. Their comments and feedback were very helpful, especially in establishing the proper scope for this work. I also thank them for helping me schedule both my pre-defense and dissertation defense meetings during a period of time that was a very busy and trying for everyone in the world due to outside circumstances.

I would like to acknowledge the help of several members of the Aerospace Engineering Department's technical staff, without whom this work would not have been possible. Thank you to Sam Reed, Aaron Borgman, Dave McLean, Chris Chartier, and Tom Griffin for help with a number of technical and infrastructure issues. Thank you to Terry Larrow for machining so many custom components that allowed this work to happen. Thank you to Denise Phelps for doing so much to make my path through graduate school as smooth as possible.

I would like to thank Steve Katnik, the College's high-energy laser expert, for his help with laser system maintanence and repair. Steve deserves credit for initially suggesting that Q-switch delay tuning should be investigated to control the laser pulse-shape, which turned out to be a far superior alternative to other pulse-shaping schemes that were being considered.

I want to acknowledge my friends throughout the department, college, and university and how thankful I am to know them. I am grateful for the help and comradery I have received from the members of my laboratory group including Rohan Morajkar, Yasin Abul-Huda, Robin Hunt, Jacob France, Chad Harvey, James Duvall, Louis Edelman, Daniel Pacheo, and Rahul Ramesh. I also acknowledge the memory of my late friend Abhinav Dasari, whom I miss dearly.

I want to especially thank Fabian Chacon, Alex Feleo, and Josh Shepard for providing their help and expertise with the RDC facility. They spent many hours laboring to properly configure the facility for the measurements in this work and many more running the combustor during the data acquisition campaign.

I thank my friends and family for their constant love and support. Even Carter, Chloe, and Sophie.

This work was partially supported by the Department of Defense (DoD) through the National Defense Science & Engineering Graduate (NDSEG) Fellowship Program from 2015 through 2018.

TABLE OF CONTENTS

LIST OF FIGURES

FIGURE

LIST OF TABLES

TABLE

LIST OF APPENDICES

APPENDIX

ABSTRACT

This work examines the application of pulsed mid-IR UpConversion Imaging (UCI) to study processes in unsteady combustion environments. UCI is a method for mid-IR light detection that leverages a nonlinear optical process known as Sum-Frequency Generation (SFG) to shift the wavelength of IR light carrying a target image to shorter, more easily detected wavelengths. This can be used to detect images in the mid-IR wavelength band (2 to 5 micrometers) that is populated with spectral signatures from many important combustion species with a silicon-based CCD camera that only responds to wavelengths below 1100 nanometers. Not only does this extend the operational range of silicon-based cameras, but UCI also exhibits unique detection properties that make it useful for unsteady combustion applications. These include a narrowband spectral response that can be tuned in real-time to isolate spectral signals from selected target species. Pulsed pump implementations of UCI also allow for precise time-gating of mid-IR imaging measurements, providing the temporal resolution that is critical for highly transient unsteady combustion environments. Despite these potential advantages of pulsed UCI compared to direct detection mid-IR cameras, there have been no prior reported examples of UCI used in practical combustion systems.

As part of this work, a pulsed mid-IR UCI system was designed and developed that was suitable for species-specific imaging measurements in unsteady combustion systems. This system was applied to perform spatiotemporally resolved mid-IR imaging measurements in a laboratory-scale Rotating Detonation Combustor (RDC) to demonstrate and test the capabilities of pulsed UCI. RDCs are an emerging combustion technology where chemical energy release is achieved primarily by a detonation wave that continuously rotates in an annular combustion channel; a configuration that may enable system-level gains in both fuel and size efficiency over conventional alternatives. Many research questions remain open related to RDC operation including the conditions under which stable detonation wave propagation can be maintained and how to maximize pressure-gain benefits to efficiency. Examples of imaging diagnostics within these systems have been limited due to the challenges associated with implementing optical diagnostics in them including vibrations, high background luminosities, and the requirements for high spatial and temporal

resolution to observe features near the detonation wave front. Addressing these issues by leveraging the unique properties of pulsed mid-IR UCI is a goal of this work.

The pulsed mid-IR UCI system developed in this work was used to detect thermal radiation from CO_2 within the combustion channel of an RDC. These measurements were sensitive to the local pressure and temperature in the high-temperature regions of the RDC flow field. The results demonstrate species-specific imaging at the leading edge of detonation waves with sub-millimeter spatial resolution (an object plane Gaussian point-spread width of 400 micrometers) and sub-microsecond temporal resolution (an effective exposure time of 240 nanoseconds). These measurements are novel in that they are the first application of mid-IR UCI to a practical combustion system and they are the first examples of fully spatiotemporally resolved mid-IR imaging in RDCs. The UCI system was also used to design a mid-IR absorption diagnostic that enables tracer-free detection of hydrocarbon fuel species distributions within RDCs. The results of this work demonstrate that pulsed mid-IR UCI is a valuable tool for studying unsteady combustion processes.

CHAPTER I

Introduction and Background

This work presents an examination and demonstration of the application of parametric mid-Infrared (mid-IR) UpConversion Imaging (UCI) to study combustion processes. Specifically, the mid-IR UCI measurements in this work were designed to study combustion physics in an experimental Rotating Detonation Combustor (RDC) that serves as an example of the extreme environments encountered in unsteady combustion science. Techniques to achieve practical mid-IR UCI have been developed in the photonics community over the previous decade. These new approaches to UCI exhibit several properties that make them attractive as diagnostics for unsteady combustion. Despite this, there are no documented examples of mid-IR UCI being used to study unsteady combustion in practical systems.

The overall purpose of this work is to develop and evaluate mid-IR UCI as a diagnostic tool for use by the unsteady combustion community. This dissertation has been written with a target audience of combustion researchers who may benefit from incorporating mid-IR imaging into their experiments. It has been assumed that the reader has little to no experience with or knowledge of nonlinear optics, the foundational field of UCI. This work explains the essential nonlinear optical theory for UCI and presents discussions with an emphasis on diagnostic applications, rather than a focus on optical science. It is therefore intended that an experimental combustion researcher could design and implement a UCI system that is suitable for their application by using this dissertation as a primary reference.

1.1 Description of mid-IR parametric upconversion imaging

Parametric mid-IR UCI is a technique for detecting images carried by light in the mid-IR wavelength range by using a nonlinear optical process known as Sum-Frequency Generation (SFG) to shift the carrier light to shorter wavelengths within the spectral response envelope of a chosen visible/near-IR camera sensor. The meaning of the word *parametric*

to describe this technique and differentiate it from other imaging approaches will be discussed below, but for the rest of this document the word will be omitted for the sake of brevity. The word *upconversion* in the name describes the increase in the frequency of a light wave associated with shifting from longer to shorter wavelengths. Figure 1.1 illustrates the concept of UCI in spectral space with a target signal that has a spectral signature that initially falls entirely outside of the response of the intended detector. Through the SFG process, the spectral content of the signal of interest is shifted to wavelengths near the peak response of the chosen detector. The motivation for the use of this approach to mid-IR light detection in combustion applications comes from the unique properties that result from the SFG process, which are described below.

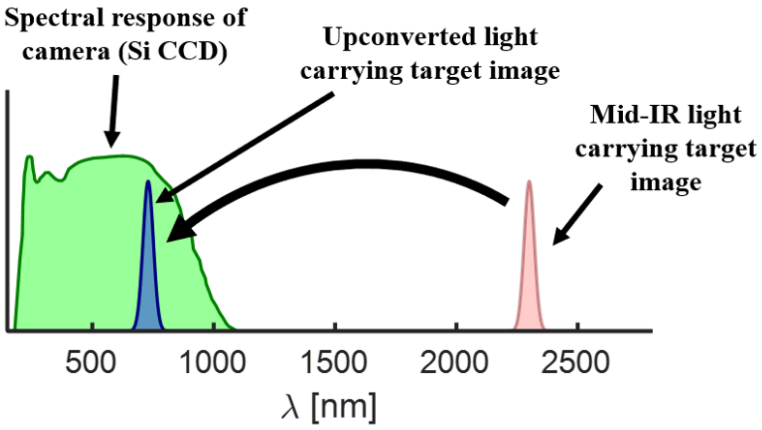

Figure 1.1: A notional schematic of UCI in the wavelength dimension.

This SFG process is typically accomplished by mixing the target light within a second-order nonlinear optical crystal medium with a *pump* beam generated by a laser system. The notional schematic in Figure 1.2 shows a typical configuration for combining mid-IR light and a pump beam within a nonlinear crystal and then separating the upconverted signal for detection. Through their influence on the SFG process, the properties of the nonlinear medium and the pump beam will determine the detection properties of the UCI system. The nonlinear optical response of the crystalline medium produces a coupling of the incident mid-IR and pump waves to a shorter wavelength output wave that gains energy along the direction of light propagation within the crystal. On a quantum level SFG can be thought of as a "photon fusion" interaction where pairs of mid-IR and pump photons annihilate each other to generate an *upconverted* photon. Conservation of energy is satisfied by the requirement that the energies of the created photon match the sum of the energies of the mid-IR and pump photons (equivalently that the frequencies of the upconverted wave match the sum of the frequencies of the input waves). This condition is captured in its description

as a *parametric* process, meaning that the photon energies are conserved. This distinguishes UCI from similarly named *upconversion fluorescence* and *photon upconversion* diagnostic techniques that are common in biomedical science and rely on energy gained from a system of matter to increase the light frequency [9].

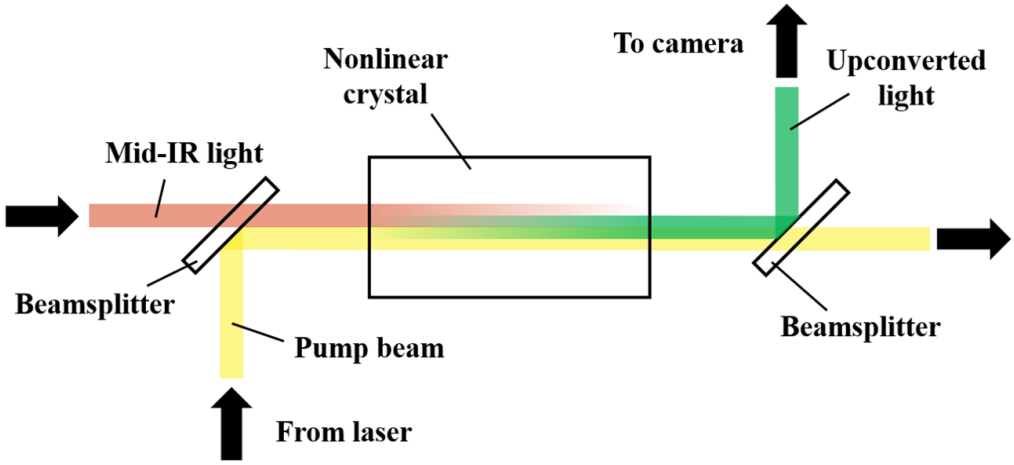

Figure 1.2: A notional schematic of a configuration using sum-frequency generation to perform frequency upconversion for mid-IR light detection.

Another crucial requirement in the SFG process is known as the *phase-matching criterion* or the *phase-matching condition*. An analysis of nonlinear wave dynamics shows that for efficient mixing of the light field to occur, the nonlinear response induced within the medium by the input waves must maintain a constant phase relationship with the output wave that is generated as they move through the medium. This can be conveniently stated as the requirement that the wavevector, the number of cycles completed by a wave along its direction of propagation, of the upconverted wave be equal to the sum of the mid-IR and pump wavevectors within the medium. On a quantum level, this represents the condition of conservation of momentum enforced between the upconverted and input photons. The phase-matching condition is critically important to the UCI technique because it determines the components of the input light field that are efficiently upconverted, and therefore detected, and those that are not. In this way, phase-matching endows UCI with the spectral selectivity that is central to its application to combustion science and determines how many relevant design parameters affect UCI system performance.

Because of its importance to UCI, phase-matching and its implications will be discussed throughout this work, especially in the theory and modeling treatment presented in Chapter II. Knowledge of the properties of the nonlinear medium, the pump beam, and the optical configuration of a UCI system can be used to accurately predict its response. It

should be noted that phase-matching is a polarization-dependent process, and so only the appropriately polarized component of a mid-IR light field will be efficiently upconverted. The inherently polarized nature of UCI detection can either be a benefit or a drawback depending on the application.

In addition to the influence of phase-matching, there is a relationship between the upconversion efficiency and pump beam intensity. This pump intensity dependence determines the temporal response characteristics of a UCI system. It can be intuitively understood that in the absence of pump beam radiation there will be no SFG and the system will not respond to any mid-IR signals. It will be shown in Chapter II that at an optimal pump beam intensity the SFG process will theoretically achieve a unity conversion efficiency of the phase-matched mid-IR radiation. It is then clear that by varying the pump beam intensity in time, the temporal response of a UCI system can be controlled. In this way, a short duration pump pulse is analogous to the shutter of a camera that controls its exposure time.

This link between pump pulse shape and temporal resolution is important to the application of UCI to study rapid processes in unsteady combustion. The capability of modern lasers to produce pulse durations at or below nanosecond time scales allows UCI measurements to achieve ultrafast imaging responses *regardless of the properties of the detector*. This is exemplified in this work where a high-sensitivity CCD with minimum exposure times in excess of one millisecond is used to perform sub-microsecond imaging of microscale processes in a supersonic flow. It should be noted that temporal resolution has been used with different meanings in the community when discussing optical measurements. It is sometimes said that a measurement is temporally resolved if its sampling rate is sufficiently high to capture the dynamics of a system in time. This work will use temporal resolution exclusively to refer to localization of a measurement in time, as determined by effective exposure time. Due to limitations of the pump laser repetition rate ($10\,\mathrm{Hz}$), none of the measurements presented in this work of unsteady combustion environments are temporally resolved in the alternative sense of sampling rate.

The benefits conferred and the limitations imposed by the dependence of UCI on the SFG process and pump pulse temporal shapes are focuses of the examination presented in this work. It is important to mention that UCI can be considered a special form of the broader category of UpConversion Detection (UCD) that includes pointwise and spectrometry measurements in addition to imaging. The focus of this work is specifically imaging techniques, and therefore UCI, however other forms of UCD are important in understanding the history of UCI development and its current capabilities. Both are discussed in the following sections with non-imaging measurements identified as UCD while any involve imaging applications, *i.e.* spatial multiplexing in a single exposure, referred to as UCI.

1.1.1 Comparison between UCI and direct detection

Mid-IR UCI is an alternative to imaging with direct mid-IR detection systems. Direct detection uses low band-gap materials that exhibit photoelectric responses at longer wavelengths to construct focal plane array sensors. Examples of these low band-gap materials include mercury callium telluride (HgCdTe) and indium antimonide (InSb) [10]. Under optimal conditions, these sensors can achieve very high quantum efficiencies, above 90% in the case of InSb [11].

Direct detection methods come with some drawbacks. These systems are typically more expensive to purchase than silicon-based visible/near-IR cameras with similar pixel densities. Major limitations of direct detection include high dark noise levels and the need to use low-temperature cooling, often cryogenic cooling, to achieve good detection performance. High dark currents related to spurious thermal light detection and poorer readout noise characteristics compared to silicon-based detectors can compromise low-light performance.

The key differences that distinguish pulsed UCI from direct mid-IR detection can be summarized as:

- Detection and readout are performed with silicon-based sensors rather than low band-gap mid-IR sensors, offering benefits including higher pixel densities, lower readout noise, and lower dark currents.
- The phase-matching condition of UCI generates a narrowband spectral response (between $2\,\mathrm{nm}$ to $350\,\mathrm{nm}$ in this work).
- In UCI the peak spectral response wavelength of the system can be fine-tuned in real-time through temperature control of the nonlinear medium.
- The exposure time, and therefore the temporal resolution of pulsed UCI measurements, are determined by the pump laser pulse characteristics and not the characteristics of the sensor.
- UCI detection is polarized in the sense that a system only responds to one polarization component of mid-IR light.

There have been examples of experimental comparisons between recently developed high-sensitivity mid-IR UCD and direct detection methods. These tests focused on the sensitive low-light detection capabilities of UCD and its advantage in dark current noise compared to direct detection methods. Høgstedt *et al.* [12] used a UCD system and a cryogenic InSb detector to detect IR Degenerate Four-Wave Mixing (DFWM), a technique based in nonlinear optics that is typically used for species-specific gas detection, signals from low concentrations of acetylene. Thanks to its improved noise properties, the UCD approach

exhibit vastly superior low-light performance compared to the InSb detector, achieving a factor of 500 improvement in detectability limits and achieved sensitivity to C_2H_2 concentrations below 1 ppm. Pedersen *et al.* [13] compared the performance of a UCD system to that of an InSb photodiode for IR polarization spectroscopy (another nonlinear four-wave mixing technique related to DFWM) measurements of small concentrations of methane. That study showed a factor of 64 improvement in measurement Signal-to-Noise Ratio (SNR) for the UCD approach over direct detection.

The previously mentioned studies detected coherent, polarized signal beams that allowed them to leverage the superior low-light detection capabilities of UCD. In this work, the mid-IR light carrying the target images is incoherent and unpolarized, and so these low-light advantages are not fully realized. It is still important to recognize the multiple dimensions of differences between UCD and direct detection. In the area of low concentration optically coherent gas sensing techniques, UCD has clearly been demonstrated as a better performing alternative to direct detection.

1.1.2 Motivation for applying UCI in combustion experiments

The justification for exploring the application of pulsed UCI to study combustion processes as an alternative to mid-IR direction detection relies on the unique properties of UCI. These include high spectral selectivity, temporal resolution, and polarized detection.

Due to the phase-matching condition associated with SFG, UCI inherently exhibits a narrowband spectral response. The system designed in this work produced spectral detection bandwidths between $2\,\mathrm{nm}$ to $300\,\mathrm{nm}$ within the $2\,\mu\mathrm{m}$ to $5\,\mu\mathrm{m}$ wavelength band. This provides species-specificity in imaging measurements with techniques based on processes such as thermal radiation emission and laser-induced fluorescence. For monochromatic, polarized signals, such as those from DFWM, UCI can achieve high spectral background rejection with theoretically 100% throughput (something that is not possible with direct detection). This is an improvement on the external spectral filters required by direct detection systems to compensate for their broad spectral responses in terms of both bandwidth and throughput.

Temporal resolution is critical in highly transient combustion environments. Because of the dependence of SFG efficiency on pump beam intensity, pulsed pump operation achieves temporal resolution on the order of the pump laser's temporal pulse width. The system in this work used a nanosecond-scale pulsed laser that achieved effective exposure times between $10\,\mathrm{ns}$ to $240\,\mathrm{ns}$. This temporal resolution capability is an improvement on that of the top-performing direct detection cameras that are currently available (FLIR cameras

provide minimum exposure times of $270\,\mathrm{ns}$ [14]). It is also shown in this work to be sufficient to freeze the advective motion of supersonically propagating detonation waves (see Chapter V).

In addition to using the precision time-gating of pulsed UCI to achieve temporal resolution when detecting spontaneously generated signals, it can also be leveraged to minimize interference from background light when detecting laser-excited processes. The thermal radiation imaging measurements in this work demonstrate that spontaneous mid-IR thermal signals can be significant over nanosecond-scale exposure times and could potentially contaminate target signals. The shortest time-gating that can be achieved in this work ($10\,\mathrm{ns}$) is currently an order of magnitude less than can be achieved with direct detection systems. Prior work has demonstrated pulsed UCI time-gating at exposure intervals as short as $100\,\mathrm{fs}$ [15]. This exceeds the time-gating capabilities that could be expected to be achieved in the foreseeable future by current direct detection technologies (six orders of magnitude below the current state of the art).

Additional background rejection capabilities are provided by the polarized nature of UCI detection. Because phase-matching in SFG is dependent on the polarization vectors of the participating light waves, only one polarization component of mid-IR light will be efficiently detected by a system. Similar to the case of spectral selectivity, UCI can provide polarization selectivity without the need for an external polarizer that is required with a direct detection camera (also not possible with direct detection). This avoids possible reductions in throughput and inferior extinction ratios associated with external polarizers. In this way, UCI can be a superior alternative for the detection of polarized signals. For example, a four-wave mixing diagnostic known as *polarization spectroscopy* relies on the separation of orthogonal polarization components in a coherent beam to isolate the relevant signal [16]. This makes UCI conducive to detecting such signals, and prior work has demonstrated performance in pointwise polarization spectroscopy measurements that exceeds the performance of direct detection methods [13].

Though the measurements described in this work do not leverage all of the previously discussed benefits of pulsed mid-IR UCI, they are a necessary step toward realizing practical application of pulsed UCI in a wide variety of combustion measurements. As will be shown by the historical perspective provided in section 1.3, imaging measurements based on UCI had not been previously performed in highly transient or practical combustion systems. The applications in this work demonstrate that UCI can be effectively applied in such environments to perform meaningful measurements. The system that has been developed in this work can be further applied beyond the diagnostic techniques in this campaign to take advantage of additional unique properties of UCI. The approach to UCI design outlined in

this work along with lessons learned can be used to design other systems specialized for different diagnostic applications that may benefit greatly or even require pulsed UCI.

1.2 Dissertation objectives

The specific objectives of the work presented in this dissertation are the following:

1. **To design, develop, and characterize a pulsed mid-IR UCI system suitable for applications in unsteady combustion environments.**

    - Implement a design analysis that can be used to predict the performance of pulsed mid-IR UCI systems.
    - Generate a design that can use spectral selectivity to isolate signals from important combustion species and achieve sub-millimeter spatial resolution and sub-microsecond temporal resolution.
    - Perform characterization measurements with well-known mid-IR illumination sources to examine system performance and validate models of the system's response in spatial, temporal, and spectral dimensions.

2. **To design optical diagnostic techniques that use the UCI system to study unsteady combustion processes and perform measurements to test the capabilities of the UCI system.**

    - A laboratory-scale RDC is used as a measurement target because it represents a highly-transient unsteady combustion environment that presents multiple challenges to the implementation of optical imaging diagnostics.
    - Design and implement measurement techniques that utilize the unique properties of UCI to make measurements in the RDC that would otherwise be difficult to perform with alternative detection approaches.
    - Conduct those measurements in the RDC to test the capabilities and performance of the UCI system in unsteady combustion experiments.

3. **To evaluate the capabilities and effectiveness of pulsed mid-IR UCI for unsteady combustion science.**

    - Consider how the major attributes of UCI act as either benefits or limitations of when it is applied for unsteady combustion measurements depending on the diagnostic technique and circumstances.

- Base the evaluation on the results of the design analysis and RDC experiments performed in this work.
- Identify applications where UCI could perform well and those where it would likely not be appropriate for use.

The remainder of this chapter describes how these objectives were approached in this work. This includes providing context related to prior work in both mid-IR UCI and imaging diagnostics in RDCs.

1.3 History of mid-IR UCI

The development of UCI as a measurement technique was enabled by two key advancements in the field of photonics: the invention of the laser by Maiman in 1960 [17] and the demonstration of optical harmonic generation by Franken in 1961 [18]. The concept of parametric upconversion in laser-pumped nonlinear media for IR light detection was first proposed shortly after in 1962 in the seminal nonlinear optics paper by Armstrong *et al.* [19] (see section VIII.B.). The first examples of UCI can found by the end of the decade with independent implementations by Midwinter [20] and Warner [21] in 1968. Midwinter used mixing with $694\,\mathrm{nm}$ emission from a ruby laser in a Lithium Niobate (LN: $LiNbO_3$) crystal to detect spatially modulated IR light near $1.6\,\mu\mathrm{m}$ generated by a xenon arc lamp. Warner used a $694\,\mathrm{nm}$ ruby laser pump source and a proustite (Ag_3AsS_3) nonlinear crystal to upconvert a spatially modulated CO_2 laser beam at $10.6\,\mu\mathrm{m}$.

Progress in the area of UCI, and more broadly the category of UCD, was slow in the subsequent three decades. This lack of development of a practical UCI system can be attributed to several factors [6] with the chief causes being low upconversion efficiencies with available nonlinear crystals and pump laser sources and immaturity of silicon-based visible/near-IR detector technology. In one example of the highest efficiencies observed during that period, Boyd *et al.* [22] reported a Quantum efficiency of the upconversion process of just 1.4%. Silicon-based CCDs were more than a factor of two worse in performance in terms of readout noise at the end of the 1980s compared to commercially available cameras today [23].

While practical implementations of UCD were hampered by limits of technology during this time, there was a significant development of the theoretical understanding required to perform effective UCI measurements. A geometric optics treatment of UCI arrangements and implications for the spatial resolution and potential aberration sources was presented by Chiou [24]. A three-part analysis of upconversion imaging theory and system designs

was presented by Firester [25, 26, 27]. Milton performed a systems analysis of UCD and proposed the use of intra-cavity pump configurations where the nonlinear medium is placed within the cavity of the pump source [28]. This intra-cavity pumping configuration was subsequently experimentally tested by Falk and See [29].

Breakthroughs in crystal fabrication capabilities were made beginning in the 1990s through the early 21st century. These directly benefited efforts toward practical UCI systems by enabling the manufacture of high-quality crystals of sizes appropriate for imaging systems. Additionally, new mineral doping techniques in crystal growth chemistry allowed their maximum pump intensity thresholds to be increased. For example, 5% MgO doping of Lithium Niobate (LN: $LiNbO_3$) was shown to mitigate photorefractive damage in such crystals by raising the intensity threshold by over an order of magnitude [30]. Importantly for the approach used in this work, a process known as periodic poling was developed and made commercially available during this time. This enables a particular type of phase-matching known as Quasi-Phase-Matching (QPM) in bulk crystals [31]. What QPM is and its significance to this work will be discussed in detail in Chapter II.

These developments coincided with the proliferation of advanced CCDs that achieved the high pixel densities, high QEs, and low readout noise promised by silicon technology. This set the stage for the realization of practical, high-sensitivity UCI measurements that could potentially be used for unsteady combustion science. The first demonstration of such a system was reported in 2009 by a research group at the Technical University of Denmark (DTU) Fotonik led by Pedersen [32]. These measurements used mixing with $1342\,\mathrm{nm}$ pump radiation in periodically poled $KTiOPO_4$ (ppKTP) crystals to upconvert masked $765\,\mathrm{nm}$ laser radiation to a detection wavelength of $488\,\mathrm{nm}$. The system exhibited conversion efficiencies of up to 25% in terms of mid-IR detection quantum efficiency using a continuous-wave (cw) pump source. This was the highest detection efficiency reported until that time and was achieved through a combination of high-quality periodically poled nonlinear crystals and an intracavity pump configuration.

Progress in UCI blossomed after this demonstration, led by a series of examples from the DTU group across a variety of applications. Kehlet *et al.* [33] explored how the unique properties of UCI can be used to perform hyperspectral imaging through crystal temperature sweeps. Israelson *et al.* [34] used UCI to perform real-time optical coherence tomography scans of nano-scale silicon electronic components. Ashik *et al.* [15] performed femtosecond imaging through UCI with an ultra-fast Optical Parametric Oscillator (OPO) laser pump source.

UCD has been applied to gas sensing experiments that leverage the species-specific capabilities of the technique that make UCI attractive for combustion studies. Høgstedt *et*

al. [12] performed sensitive detection of acetylene using pointwise IR DFWM with UCD, achieving a factor of 500 improvement in minimum detectable concentration compared to the use of direct detection. Høgstedt *et al.* [35] used UCD for remote lidar detection of atmospheric CO_2 concentrations at wavelengths near $1572\,\mathrm{nm}$. Pointwise UCD has been used for standoff detection of gaseous fuel species by Wolf *et al.* [36] and to raster scan methane plume distributions by Imaki and Kobayashi [37]. In an early example of UCI in 1999, a decade before the breakthrough of the DTU group in 2009, Morishita *et al.* [38, 39] performed planar IR DFWM imaging of an expanding cesium vapor plume. These measurements represent the only prior example of UCI in a highly transient flow environment.

UCD methods have been used to study combustion processes in several examples. Hot *et al.* [40] used UCD for pointwise IR DFWM measurements of HCN concentrations near burning biomass pellets. The technique was effective at quantitative detection of HCN in hot combustion environments (temperatures of up to $1630\,\mathrm{K}$) at concentrations between $200\,\mathrm{ppm}$ to $1500\,\mathrm{ppm}$. Barh *et al.* used UCD to perform mid-IR spectroscopy of spontaneous emissions from candle flames [41]. The only currently available example of UCI in combustion environments is the species-specific thermal emission imaging performed by Dam *et al.* in 2012 [42]. They used the spectral selectivity of UCI to isolate thermal emissions from H_2O, CO_2, and hydrocarbons in a candle flame. While these measurements were effective in a relatively steady combustion environment, they used cw intra-cavity pumping that resulted in an exposure time of approximately $300\,\mathrm{ms}$. The temporal resolution of these measurements would be insufficient for a highly-transient combustion environment, like the one encountered in an RDC.

These examples demonstrate the maturation of UCD technology over the past decade. It has reached the point of commercialization as the DTU Fotonik group spun-off a private firm known as NLIR that offers mid-IR detectors and spectrometers based on UCD for sale [43]. Their products include a high-sensitivity, uncooled single element mid-IR detector (D2250) and mid-IR spectrometers covering the spectral range from $2\,\mu\mathrm{m}$ to $12\,\mu\mathrm{m}$ (S2050 and S60120). These products leverage the relatively high sensor operation temperature, low readout noise, and high-speed electronic responses to make them superior alternatives to direct detection in some applications. However, NLIR does not offer any off-the-shelf imaging systems and so UCI must still be implemented through custom-designed systems.

A more detailed summary of the development of UCI can be found in the comprehensive review of UCI applications was published in the previous year by Barh *et al.* [6]. Despite the wide array of applications of UCI, there are no reported examples of UCI measurements in practical unsteady combustion systems. The goal of this work is to address that

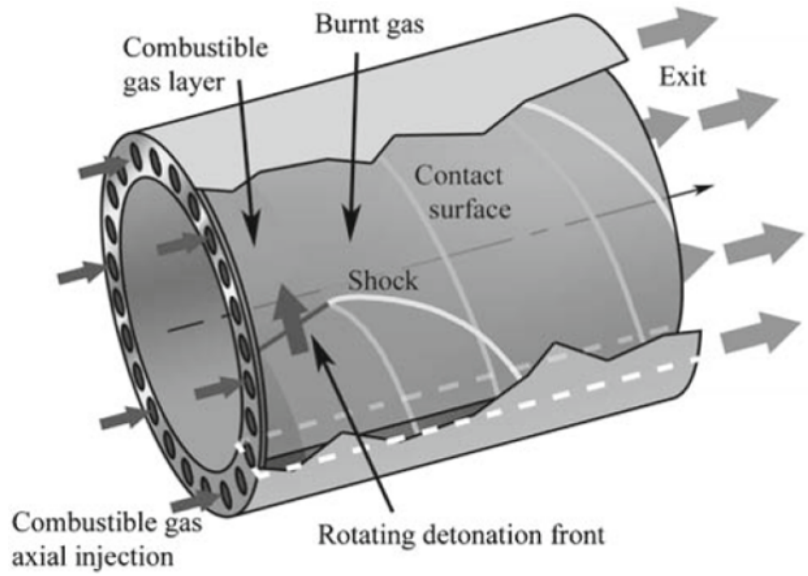

Figure 1.3: A schematic of a typical RDC configuration. Reproduced from Hishida *et al.* [1].

gap by evaluating how UCI can be used effectively in the study of unsteady combustion, demonstrate this application of the technology, and evaluate its diagnostic performance.

1.4 Rotating detonation combustors

An RDC, sometimes referred to as an RDE (Rotating Detonation Engine), comprises a narrow annular channel between a solid cylindrical body inside of a hollow outer cylindrical wall. Combustible reactants flow into the channel through one axial end and are processed by one or more detonation waves traveling circumferentially around the channel. Burnt combustion products are exhausted out of the axial end opposite the incoming reactants. The persistent axial inflow of reactants allows the detonation waves within the channel to continuously propagate around the circumference of the channel. Figure 1.3 shows a schematic of the flow field within an RDC reproduced from Hishida *et al.* [1]. From a thermodynamic perspective, these devices are similar to widely-studied Pulsed Detonation Engine (PDE) technology [44]. RDCs differ from PDEs through the perpetual propagation within the combustion channel that does not require periodic re-ignition. This eliminates the need for actuated refill and ignition mechanisms, as well as reducing intermittency in the properties of the exhaust gas produce at the combustor outlet compared to PDEs.

The sudden pressure rise and subsequent heat release caused by the passage of the detonation waves make RDCs a form of what is known as *pressure gain combustion*. The

potential gains in thermodynamic efficiency associated with this type of cycle have been estimated to be up to 4% to 9% [45] relative to the amount of fuel burned. This potential step-change in fuel efficiency makes the development of RDCs attractive for power generation applications. Additionally, the mechanical simplicity of the system and the ability of the detonation wave to rapidly burn large quantities of reactants allow for combustor designs with relatively small footprints for a given power output [46]. The promise of high-efficiency, compact combustors makes RDC technology an area of interest for vehicle propulsion systems.

The understanding of RDC combustion physics and engineering best practices is still developing. The flow field of RDCs can be spatially complicated, with multiple distinct structures and highly heterogeneous thermochemical properties. Primary detonation waves that provide the desired heat release mode are characterized by strong spatial gradients in pressure, temperature, and chemical species concentrations. The finite extent and heterogeneity of the fresh reactant mix that the detonation waves propagate into leads to multiple entities, as shown in Figure 1.3, that always include the primary detonation wave, an associated oblique shock wave in the burnt products, and contact surfaces separating disparate post-detonation regions [1]. Numerical and experimental studies have found examples of non-ideal behavior in RDCs that could potentially compromise operability and performance. Some of the unresolved technical challenges that result from these phenomena are discussed in the following section.

1.4.1 Unresolved questions and technical challenges in RDCs

RDCs are an active area of research aimed at addressing several major outstanding scientific questions and technical issues related to RDC operation and performance. This section provides a summary of some of these unresolved areas of inquiry and their importance to the development of the technology. This is not an exhaustive list of technical challenges in RDCs (more details can be found in other references [46, 1, 47]), but is instead meant to give some context to the measurements performed in this work and how they can contribute to progress in this area.

All current practical applications of RDCs require them to be operated as non-premixed systems that must inject fuel and oxidizer species independently and mix them adequately before the passage of each detonation wave cycle. This process is critical to the stability of the detonation wave cycle and the achievement of high-efficiency combustor performance. In general, it is a complicated process that experiences influences from several mechanisms in the combustor. The design of the injection system is a primary factor controlling the

injection dynamics and subsequent mixing. Several alternative injector designs have been considered in prior RDC work, including axial air inlets and semi-impinging jets [48]. Designs that produce deficient mixing lead to stratification in reactant mixtures that can reduce detonation wave stability and combustor performance.

Another effect that can influence reactant injection and mixing is the local pressure rise associated with the passage of detonation waves. This pressure rise can introduce an effective blockage in the injection system that can temporarily restrict or eliminate flow through one or both reactant streams. If the two reactant streams (fuel and oxidizer) respond differently, specifically with different time delays before resuming in-flow, then it can lead to regions of the refill region containing only one reactant component. Fuel injectors in most previously tested systems exhibit greater "stiffness" (a measure of the ratio between the injection plenum pressure and that of the combustion channel) than oxidizer streams. This is expected to lead to regions that are pure fuel that will prevent efficient combustion in some parts of the flow field. In addition to the influence of the primary detonation wave, evidence has been observed of secondary pressure waves propagating within the combustion channel that cause similar injection disruptions [49]. Identifying and characterizing these mechanisms and their effects on mixing is important to understanding how to design practical RDCs.

Another major consideration in RDC systems is the location of heat release within the flow field relative to the structure of the detonation wave. Detonation wave fronts, each comprised of a leading shock wave followed by rapid heat release, generally exhibit the highest gas pressures immediately behind shock wave and decaying pressure with increasing distance behind the wave front. In an ideal RDC, the vast majority of heat release will be released in these peak pressure regions associated with the detonation wave front and therefore allow the realization of efficiency benefits of pressure gain combustion. To allow the released energy to reinforce the propagation of the wave, combustion must occur before what is known as the *sonic plane* found in the expansion region behind the detonation wave front. The sonic plane is formed by the locus of points where the gas velocity relative to the wave front equals the local speed of sound, and so disturbances beyond the sonic plane cannot interact with the detonation wave front.

In real systems, some of the heat release can occur in locations other than the high-pressure regions immediately behind the detonation wave. These are known as secondary combustion events [50]. Sometimes secondary combustion occurs aft of the sonic plane and therefore cannot support the detonation wave. This is in effect lost energy that could have otherwise supported a stronger detonation wave, though it does not otherwise have a detrimental effect on the wave. This is known as *commensal combustion*. In other cases,

secondary combustion can occur in the fresh reactant regions ahead of the detonation wave. This is known as *parasitic combustion*.

Parasitic combustion is critically important to RDC performance because it impacts the strength of the primary detonation wave in two ways [50]. First, it consumes fresh reactants that then become unavailable to support the detonation wave through detonative chemical energy release. Second, the heat released by parasitic combustion increases the temperature of the gas regions ahead of the detonation wave front. The increased temperature of the gas that the detonation wave is propagating into causes an increase in the speed of sound of the gas, leading to lower effective Mach numbers for the detonation wave. Because the "strength" of a detonation wave, as defined by the resulting pressure rise, is determined by its Mach number, the temperature increase induced by parasitic combustion results in reduced detonation wave pressure ratios that can affect detonation stability and overall RDC performance. This makes the identification and characterization of parasitic combustion an important aspect of experimental RDC research.

Completeness of combustion is a concern in RDCs. The rapid nature of detonation processes leads to relatively short effective reaction time scales that can affect combustion progress. Detecting unburnt fuel in both the exhaust gases and in the post-wave regions of the flow field is important to evaluate combustion efficiency in experimental studies. Incomplete combustion can also result in significant CO concentrations. Measurements of CO distributions near the detonation wave front could provide insight into the mechanisms that inhibit complete oxidation. Pollutant emissions related to NOx species can be significant in addition to CO and unburnt hydrocarbon fuel species [47]. Pollutant emissions will need to be characterized and addressed before wide-spread adoption of RDCs in propulsion applications.

1.4.2 Prior imaging experiments in RDCs

Imaging experiments in RDCs are often performed in modified variants of combustor designs typically referred to as "optically-accessible" RDEs or RDCs. One prominent example is operated by the AFRL which has the outer metal cylindrical wall replaced with a transparent quartz outer wall [51]. In this way, the entire combustion channel and even parts of the injection system are visible through the outer wall for imaging measurements. The design enables wide Field-of-View (FoV) imaging using both passive and laser-excited techniques that are not otherwise possible with traditional designs and small window ports. The drawbacks of these variants include image distortion due to the curvature of the quartz wall that has a lensing effect on both the image signals and injected laser beams that may

need to be accounted for in post-processing.

This design has been used for several imaging studies. Naples *et al.* [51] reported the development of this RDC variant and initially used it to perform broadband chemiluminescence imaging. Rankin *et al.* subsequently used this facility to perform acetone tracer Planar Laser-Induced Fluorescence (PLIF) measurements to image fuel mixing dynamics [52] and UV OH^* chemiluminescence to identify reaction zones and hot product regions [53, 54]. These studies used a radial "rocket" style injection scheme. In contrast, a similar optically-accessible design was reported by Athmanathan *et al.* [55] with an axial "pintle" type injection system and a turbine inlet incorporated into the exhaust. This system has been used for broadband chemiluminescence imaging at $500\,\mathrm{kHz}$ [55] and subsequently at up to $1\,\mathrm{MHz}$ [56] where the sampling rate was limited by the speed of the intensifier. High-speed broadband chemiluminescence imaging has also been performed in the AFRL facility at $1\,\mathrm{MHz}$ [57].

An alternative type of optically-accessible RDC design is known as the Race Track RDC (RT-RDC) variant. This RDC design changes the combustion channel geometry by adding two straight sections that connect two semi-circular turning sections. The straight sections can accommodate large, flat windows for optical access. Chacon and Gamba [58] developed and demonstrated an example of an RT-RDC. This facility has been used for OH^* chemiluminescence and shadowgraph imaging to identify detonation wave structure secondary combustion phenomena [50]. This facility also incorporated a novel laser window design at the end of one of the curved sections of the combustion channel. This window was shaped to allow a planar laser sheet to be injected into the straight section of the RT-RDC with minimal distortion. This feature was leveraged to perform OH PLIF measurements in the straight section of the RT-RDC by Chacon and Gamba [2]. The RT-RDC configuration and the previously mentioned OH PLIF measurements are illustrated in Figure 1.4.

Mid-IR imaging in RDCs

Mid-IR imaging within the AFRL optically accessible RDC was performed by Rankin *et al.* [59]. These measurements were of thermally excited H_2O emission bands near $2.9\,\mu\mathrm{m}$. These were captured with direct mid-IR detection using an InSb focal plane array at a frame rate of $1.2\,\mathrm{kHz}$ and a $5\,\mu\mathrm{s}$ exposure time with a $66\,\mathrm{nm}$ wide spectral filter. The measurements showed post-combustion regions where high-temperature H_2O was present and revealed the large-scale structure of the RDC flow field because of the large FoV that was achieved. However, the small-scale resolution of the images is compromised by the length of the exposure time. For the $1.2\,\mathrm{km/s}$ to $1.7\,\mathrm{km/s}$ detonation wave speeds observed

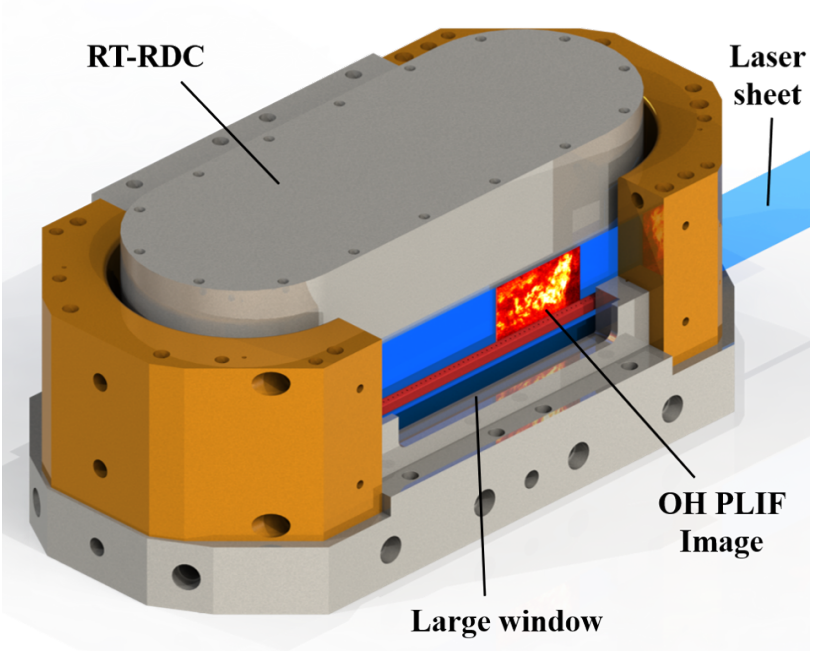

Figure 1.4: A depiction of OH PLIF measurements inside of an RT-RDC. Reproduced from Chacon and Gamba [2].

in the experiment the $5\,\mu\mathrm{m}$ exposure time translated to wave displacements of $6\,\mathrm{mm}$ to $9\,\mathrm{mm}$ and this causes a blurring of the sharp gradients at the wave front and any small-scale structures immediately behind the wave.

These prior mid-IR imaging measurements reveal the important link between spatial and temporal resolution in RDCs and other detonation-based systems. If sufficient temporal resolution cannot be achieved, then spatial resolution will be compromised regardless of the resolving power of the imaging optics that are employed. More sophisticated direct detection IR cameras are available that can achieve the sub-microsecond exposure times required for resolved imaging in RDCs, such as the FLIR X8500sc MWIR (reported minimum integration time of $270\,\mathrm{ns}$ [14]). The approach taken in this work is to leverage the time-gating effect of pulse pump sources in UCI to achieve sub-microsecond temporal resolution.

1.4.3 Key features of RDC flow fields

Examples of the OH PLIF measurements by Chacon and Gamba [2] are shown in Figure 1.5. The top row of images in Figure 1.5 shows three examples of OH PLIF measurements captured with the experimental configuration shown in Figure 1.4 while the bottom row shows those same images with labels of key structures superimposed. The brighter

regions in these images indicate stronger OH PLIF signals, which can be interpreted as approximately proportional to the local concentration of hydroxyl radicals, OH, within the interrogation plane of the laser sheet. OH is an important high-temperature chemical intermediate in combustion reactions that can be used as a marker of reacting zones and post-combustion product regions. In this way, high-signal regions in the images in Figure 1.5 can be seen as indicating on-going or recently concluded combustion events. Chacon and Gamba provide an interpretation of the flow structures observed in these measurements [50, 2] that will be briefly summarized here for context.

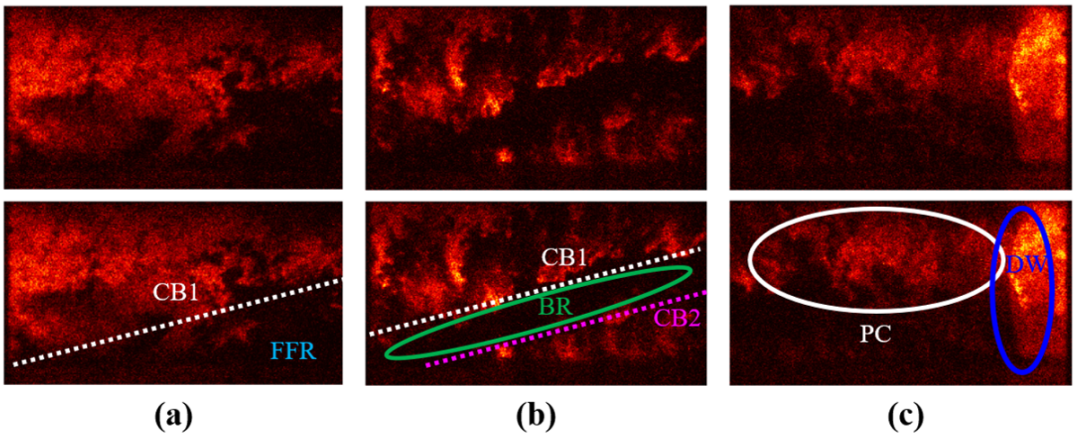

Figure 1.5: Examples of OH PLIF images from the RT-RDC showing various phases of the detonation cycle in each column with labels of key structures superimposed on images in the bottom row. Reproduced from Chacon and Gamba [2].

Figure 1.5(a) shows an example of the flow structure immediately behind the detonation wave front. Some of the signal seen in the top half of the image is the result of deflagrative secondary combustion of residual reactants that survived the passage of the detonation wave. This is defined by Chacon and Gamba as *commensal combustion* that increases the system-level combustion efficiency as defined by fuel oxidation, but does not support the strength of the detonation wave because it occurs on the aft side sonic line, the spatial threshold beyond which disturbances cannot interact with the detonation wave front. The dashed line in Figure 1.5(a) labeled "CB1" indicates the *contact burning 1* region where a diffusion flame consumes the fresh reactant mixture that is being supplied by the injection system at the bottom of the image frame. The blue label name "FFR" indicates the *fresh fill region* where relatively cold, unburnt reactants in the process of mixing have filled the combustion channel as a result of fuel and oxidizer injection. At this point in the cycle, the FFR resembles a triangular shape when viewed from this side-on perspective, which is what is expected based on the canonical model of RDC flow structure [47].

Figure 1.5(b) shows an example of the flow structure at a later point in the RDC cycle

relative to frame (a). Here, ignition events near the injection plane give rise to another deflagrating zone known as *contact burning 2* that is indicated by the dashed magenta line and the label "CB2". The contact burning surfaces both axially upstream (CB1) and downstream (CB2) create a non-ideal banded shape of the unburnt reactant region. This is defined by Chacon and Gamba as the *buffer region*, indicated by the green ellipse and "BR" label in frame (b), that contains cold reactants separating the two hot, reacting zones present at CB1 and CB2. This flow structure differs significantly from the homogeneous, cold reactant mixture zone that was expected to extend from the detonation products region all the way down to the injection plane in the canonical flow model. It has been hypothesized that the buffer region resists burning because it is either almost entirely fuel or entirely oxidizer due to differing responses of the two components of the no-premixed injection system to the passage of the high-pressure detonation wave. This hypothesis can be explored with optical diagnostics capable of sensing fuel concentrations.

Taken together, CB1 and CB2 represent non-idealities in the form of secondary combustion events, specifically parasitic combustion. The importance of parasitic combustion is discussed above in section 1.4.1. Figure 1.5(c) shows an example of parasitic combustion, indicated by the white ellipse and "PC" label, observed immediately ahead of a detonation wave front, indicated by the blue ellipse and "DW" label. An ideal detonation wave front is typically described as a shock wave that causes a rapid rise in the pressure and temperature of the reactant gas followed by a small "induction length" after which chemical energy is released through rapid combustion at high pressures. Detonations in two-dimensional flow environments with uniform, premixed reactants have been well-studied [60, 61] and typically exhibit mostly one-dimensional variation in fluid properties along the direction of wave propagation with a subtle periodic transverse structure. Both experimental [59, 2] and computational studies [62, 63, 64, 65] have revealed that the conditions in non-premixed RDCs vary significantly from the ideal case and result in more complicated, unsteady wave structures. Imaging measurements that are sensitive to the local gas state, as determined by pressure, temperature, and composition, can be used to explore these non-ideal detonation wave morphologies in practical devices.

1.5 How UCI can be used in RDC studies

An important question encountered in this work is how can UCI be utilized to perform meaningful measurements in an RDC. A major factor determining the scope of available diagnostic techniques is the design of the combustor used for the experiments. Unlike most of the previous RDC imaging experiments performed in section 1.4.2, the UCI observa-

tions in this work were performed with a more conventional RDC design that did not have a quartz outer wall, like in the optically-accessible AFRL design, nor did it have long, flat window sections, like in the RT-RDC design. Instead, this laboratory-scale $145\,\mathrm{mm}$ diameter cylindrical combustion channel design [48] provided optical access with a $25\,\mathrm{mm}$ diameter ($19\,\mathrm{mm}$ clear aperture) sapphire window installed in the outer wall and a $12\,\mathrm{mm}$ diameter ($9\,\mathrm{mm}$ clear aperture) sapphire window that could be installed on the inner wall. This more limited optical access precludes the use of some of the laser-based and wide FoV diagnostic techniques described in section 1.4.2. There are several reasons for using this combustor design as opposed to the more optically-accessible alternatives.

The quartz outer wall used in the AFRL design exhibits poor optical transmission in several mid-IR wavelength bands, particularly dropping off for wavelengths above $4\,\mu\mathrm{m}$. This would be unacceptable in this work because CO_2 emissions were targeted in this wavelength range, and so a custom cylindrical wall would have needed to be made of a mid-IR transparent material that could withstand RDC operation. This design and manufacturing process would have been prohibitively expensive. Additionally, the effects of a different heat-transfer boundary condition presented by an optical wall compared to the steel wall in practical designs have yet to be quantified. For these reasons of fabrication challenges and experimental fidelity, a fully optical outer wall design was not used. The RT-RDC used in the experiments by Chacon and Gamba [58] was available for use in this work, however it also used custom quartz windows to provide optical access and would have similarly prevented imaging measurements related to CO_2. Efforts have been undertaken to design and procure sapphire windows for mid-UCI measurements in the RT-RDC, however they were not available at the time that this work was carried out.

With these facility-based limitations in mind, there are several candidate measurement techniques that can be proposed for use in the RDC that will leverage the unique properties of UCI detection. Two examples of those candidate techniques were examined in this work. One technique (mid-IR passive thermal radiation imaging) was implemented to perform measurements in the previously described RDC facility and another (mid-IR absorption imaging) was examined with preliminary benchtop measurements but was not tested in the RDC due to constraints of the RDC configuration during this work. These two techniques are described in more detail in the section below and Chapters V and VI, respectively. Other potential applications of UCI for unsteady combustion science that were not closely examined in this work are proposed in Chapter VIII (see section 8.3.2).

1.5.1 UCI-based RDC diagnostics examined in this work

Mid-IR passive thermal radiation imaging

Passive thermal emissions imaging relies on the fact that all matter at a finite temperature will emit electromagnetic radiation. For a perfect blackbody emitter, its spectral radiance will be a function of its temperature alone, governed by the Planck curve. For a volume of a particular chemical species in its gas phase, the spontaneous thermal radiance that it emits will be governed by Kirchoff's law of thermal radiation [66]. Kirchoff's law states that the emitted thermal radiation intensity will be equal to the spectral product of the Planck curve corresponding to a blackbody at the temperature of the gas and its spectral absorption (fraction of light absorbed at every wavelength). In this way, passive thermal imaging is sensitive to the temperature of a gas (through the Planck curve contribution) and its pressure, emitter concentration, and again temperature (through the spectral absorption contribution). An analysis in Chapter V will show that at room temperature the passive thermal emission from a gas volume is negligible below $5\,\mu\mathrm{m}$ due to the Planck curve effect. At combustion temperatures, the mid-IR emissions become significant and monotonically increase with increasing pressure as a result of the spectral absorption effect. This makes passive thermal imaging a useful tool for studying RDC flow fields where the different combustion modes, detonative and deflagrative, result in similar temperatures but significantly different pressures in their products. The fact that the emission spectrum of a gas is determined by the spectral signature of its composition makes it possible to perform species-specific measurements.

Passive thermal imaging was demonstrated in RDCs in the previously discussed study by Rankin *et al.* [59]. These experiments measured emissions of H_2O near $2.9\,\mu\mathrm{m}$ in wavelength. Species-specific UCI measurements of passive thermal radiation emission in candle flames were demonstrated by Dam *et al.* [42] for H_2O, CO_2, and hydrocarbons. What both examples are missing for effective application in an RDC is temporal resolution. For reasons discussed above, sub-microsecond resolution is required to resolved small, millimeter-scale features near the detonation wave front. Both the direct detection system used by Rankin *et al.* and the cw-pump UCI system used by Dam *et al.* were designed for measuring slower processes and were incapable of fast time-gating. The passive thermal imaging in this work uses a sub-microsecond UCI pump pulse to achieve the necessary time resolution and demonstrate the first spatiotemporally resolved mid-IR imaging in RDCs.

The species that could be targeted with pulsed UCI of thermal emissions in the RDC also differed from those available to Rankin *et al.* and Dam *et al.* . The two main reasons for this are the narrower spectral bandwidth of the UCI system in this work and the shorter

exposure time required for temporal resolution. Rankin *et al.* used a direct detection mid-IR camera that exhibited a broadband spectral response and fitted it with a $66\,\mathrm{nm}$ wide spectral filter to isolate H_2O emission bands. As will be shown in Chapter II, the system in this work exhibits a spectral bandwidth of just $8\,\mathrm{nm}$ for those same wavelength bands. Additionally, if the thermal emission processes are assumed to be steady, then the signal level in thermal imaging will be proportional to the effective exposure time. For these measurements, that effective exposure time was $240\,\mathrm{ns}$ compared to $5\,\mu\mathrm{s}$ for Rankin *et al.* resulting in a reduction of the available signal by a factor of 20. These two factors combined preclude the use of the pulsed UCI system to perform single-shot measurements of H_2O thermal emissions in the RDC, as will be demonstrated in Chapter IV.

Instead, passive thermal imaging was used to target CO_2 emissions near $4.2\,\mu\mathrm{m}$ because of the stronger emission by those bands and the higher spectral bandwidth of the UCI system at those wavelengths. During hydrocarbon operation of the combustor, there would be nascent, high-temperature CO_2 in the flow as a product of combustion processes. However, a wide range of stable hydrocarbon-fueled test conditions have yet to be identified in the RDC used in this work at this time; hydrogen-air operation has been observed to be far more stable. Additionally, the variation in naturally occurring CO_2 concentration in the flow during hydrocarbon-fueled operation would introduce additional ambiguity when interpreting the data. For these reasons, passive thermal imaging was performed in the RDC by seeding both the hydrogen fuel and air streams with the same concentration by volume (either 5% or 10%) to achieve both high thermal emission signal strengths and approximately constant concentrations of CO_2 throughout the flow. This approach allowed high-temperature regions to be distinguished from relatively cold regions (which produce negligible signal) and detected differences in pressure in combustion products, making it an effective tool for studying small-scale detonation wave front morphology. The details and results of this study are presented in Chapter V.

Mid-IR absorption imaging

Absorption-based diagnostic methods detect the attenuation of a known illumination spectrum passing through a volume of gas to infer the presence, and possibly concentration, of a particular absorbing species. The importance of H_2O and hydrocarbon fuel species to RDC combustion combined with their strong mid-IR absorption bands make them good candidate targets for absorption studies. Mid-IR fixed wavelength He–Ne laser absorption at $3.9\,\mu\mathrm{m}$ has been used to detect the temporal variation of ethylene concentrations in the combustion channel of an RDC [67]. Tunable diode laser absorption spectroscopy has been used to measure H_2O concentrations in both the exhaust [68] and in the combus-

tion channel [69] of RDCs. While these experiments used lasers as a spectral source, any well-characterized light source can be used, including incoherent ones.

This work examines the feasibility of performing mid-IR absorption imaging measurements in RDCs by installing small, roughly collimated blackbody emitters in the inner body of the combustor. By aligning the sapphire windows on the inner and outer walls of the combustion channel the attenuation due to species-specific gas absorption can be measured by a UCI detector outside of the combustor. The motivation for these measurements is to test the hypothesis that the buffer region identified in Figure 1.5 is almost entirely either fuel or oxidizer. If the RDC is operated with a hydrocarbon fuel, then the UCI system in this work can be used to detect absorption by the C–H stretch vibrational bands at wavelengths near $3.35\,\mu\mathrm{m}$. In this type of measurement, regions with no fuel would produce no absorption, regions of entirely fuel would produce a predictable maximum absorption value, and regions with the design mixture of fuel and oxidizer would produce an absorption value somewhere in between. Through the spatial multiplexing offered by the imaging configuration, these types of measurements could be used to test the hypothesis about the nature of buffer regions.

As was mentioned above concerning passive thermal emission measurements, the RDC facility did not support operation with fuel comprised of large amounts of hydrocarbons at the time of this work. This prevented direct testing of the absorption imaging technique within the RDC during operation. Instead, preliminary benchtop hydrocarbon absorption experiments were performed with UCI detection to identify suitable fuel species and provide a proof-of-concept for UCI detection of hydrocarbon gases at relevant concentrations. The details and results of this study are presented in Chapter VI.

1.6 Contributions of this work

In brief, the novel contributions of this work are:

1. First application of mid-IR UCI to study unsteady combustion processes in practical combustion systems

2. Comprehensive description of a design analysis to develop a pulsed mid-IR UCI system for unsteady combustion

3. Examination of the influence of pump temporal pulse shape and energy on UCI performance

4. Implemented a novel CO_2 doping approach for passive mid-IR imaging of high temperature, high-pressure regions in RDCs
5. First spatiotemporally resolved mid-IR imaging in RDCs
6. Examination of the feasibility of using mid-IR UCI detection of hydrocarbon fuel absorption to observe RDC mixing processes and fuel-rich regions

A brief description of each of these contributions is provided below.

First application of mid-IR UCI to study unsteady combustion processes in practical combustion systems

Despite recent progress in UCI technology, there have not been any reported examples of the technique being used to perform mid-IR imaging in unsteady combustion studies, nor are there currently any commercially available UCI systems capable of doing so. The properties of pulse mid-IR UCI make it highly suitable for such applications, and so this work aims to fill that gap in UCI development. While the spectral selectivity and superior detector electronic performance associated with UCI have been leveraged in the past for mid-IR imaging in simple combustion environments [42], the application in this work is novel in targeting a practical system of contemporary interest in the combustion community. This enables this work to provide the first evaluation of pulsed mid-IR UCI as a diagnostic tool for unsteady combustion science.

Comprehensive description of a design analysis to develop a pulsed mid-IR UCI system for unsteady combustion

The current lack of commercially available UCI systems means that in the immediate future any researcher who intends to implement mid-IR UCI will need to develop a system from scratch. The types of modeling and design activities will vary depending on the intended application. Previous works on UCI such as the dissertation by Høgstedt [70] guide design modeling for a particular application, in that case atmospheric gas spectroscopy, but do not address all of the aspects relevant to unsteady combustion science, *e.g.* pump pulse shape tailoring. This work develops design tools and guidance specifically for systems capable of species-specific imaging in RDCs. Those were applied to create a system with a spectral response ranging from $1.9\,\mu\mathrm{m}$ to $5\,\mu\mathrm{m}$ that targets spectral transitions of H_2O, CO, CO_2, and hydrocarbon fuel species. Those implementing a similar system can use this design analysis as a starting point or apply the tools to pursue their own desired system parameters.

Examination of the influence of pump temporal pulse shape and energy on UCI performance

Most previously reported examples of UCI used either cw pump sources or measured laser-excited processes that were limited in time duration by the characteristics of the excitation laser. In contrast, this work considers UCI detection with a pulse pump source of spontaneous thermal emission processes that emit signal light continuously at relatively low intensities. This means that for these measurements the UCI pump pulse duration controls both the temporal resolution and signal strength of the measurements. This creates a trade-off where too long of a pump pulse compromises temporal resolution while too short of a pump pulse results in insufficient signal strength and a corresponding low SNR. This work shows how sub-microsecond resolution can be achieved with enough signal strength to produce SNRs of approximately 20 in single-shot measurements of CO_2 radiative emissions. Included in this is a strategy for controlling the pulse duration of a non-pulse shaping Nd:YAG pump laser system.

Implemented a novel CO_2 doping approach for passive mid-IR imaging of high-temperature, high-pressure regions in RDCs

Mid-IR imaging typically is performed to detect thermal emission from either a reactant (*e.g.* CH_4) or product species (*e.g.* H_2O) that is consumed or created by reactions distributed throughout the flow field. This means that in addition to the inherent dependence of thermal emission signal on temperature and pressure, there is a strong relationship between the signal and the variable emitter concentration. This work uses a novel approach of seeding both the fuel and oxidizer streams during hydrogen-air operation of the RDC with the same concentration of inert CO_2. This creates an approximately constant molar concentration of the emitting species throughout the flow field that is independent of local reaction progress. These imaging measurements are well described as a function of only local temperature and pressure. Results demonstrate that these types of measurements are capable of distinguishing particular regions of the flow as cold reactants (no UCI signal), high-pressure products of detonative combustion (highest UCI signal level), and deflagrative combustion products (medium UCI signal level).

First spatiotemporally resolved mid-IR imaging in RDCs

As was previously discussed, prior examples of mid-IR imaging in RDCs were performed with exposure times of $5\,\mu s$ or longer. This, combined with the supersonic propagation of RDC detonation wave fronts at velocities above $1\,km/s$, resulted in a smearing of small-

scale structures and sharp gradients (length scales on the order of $1\,\mathrm{mm}$ or less) immediately behind the wave. The temporal resolution of pulsed mid-IR UCI allows the system in this work to freeze the motion of the detonation wave front and realize the spatial resolution capabilities of the optical configuration. Results presented in this work exhibit an effective temporal resolution of less than $240\,\mathrm{ns}$ which allows length scales of less than $1\,\mathrm{mm}$ to be resolved near the propagating detonation wave front. These represent the first reported examples of sub-microsecond, sub-millimeter resolved mid-IR imaging in RDCs, a capability that is valuable for studying the underlying physics of detonation-based combustion technologies.

Examination of the feasibility of using mid-IR UCI detection of hydrocarbon fuel absorption to observe RDC mixing processes and fuel-rich regions

The importance of fuel mixing and parasitic combustion processes in non-premixed RDCs make the morphology of the fresh fill region a critical aspect in understanding these systems. For this reason, the capability to measure fuel distributions within an RDC is a major objective for optical studies of these systems. This work provides an examination of the use of UCI to detect 2D distributions of fuel concentrations through imaging of mid-IR light absorption near $3.35\,\mu\mathrm{m}$ in wavelength. Absorption cell experiments were used to characterize the UCI response to mid-IR absorption by three hydrocarbon fuel species: methane, ethylene, and ethane. The results of these measurements and subsequent modeling showed that ethane would be the best fuel species for implementing this type of diagnostic in RDCs.

1.7 Dissertation outline

The remaining chapters in this work describe a design analysis and experimental demonstration of a pulsed mid-IR UCI system for imaging in RDCs.

Chapter II provides the essential theory governing SFG processes that underlie the mid-IR UCI technique. These include a detailed explanation of the phase-matching condition and how it is modified by the application of QPM. This theoretical understanding is used to construct a UCI model to predict a system's spectral, spatial, and temporal response that can be used for designing a UCI system and interpreting measurements made with it. It is then shown how the model was applied to design the UCI system used in this work and predict its detection characteristics.

Chapter III describes the experimental setup used for the different types of UCI measurements in this work. This covers the physical configuration of the UCI system and its

optical arrangement. The properties of the silicon-based detector and its effects on measurements, specifically through a phenomenon known as spectral fringing, are discussed. Specifics of the pump laser source are provided, including details of the pump temporal pulse shape control that was implemented to achieve temporal resolution of UCI measurements in the RDC.

Chapter IV presents the results of experiments carried out with well-known mid-IR light sources to characterize the response of the UCI system along spectral, spatial, and temporal dimensions. These experimental measurements serve multiple purposes. The first is to validate the model predictions that are developed in Chapter II and confirm the performance of the system is consistent with the design intentions. The other purpose is to determine in what ways the system can be effectively used to study the RDC. For instance, the presented results explain why imaging of thermal radiative emissions from CO_2-doped operation in the combustion channel is feasible while similar measurements from nascent H_2O are not.

Chapter V presents the results of pulsed UCI measurements of mid-IR thermal emission from CO_2 in an RDC. The results are presented from two perspectives: as cycle phase correlated point measurements and as individual images. The cycle phase correlation perspective provides insight into the large-scale structure of the phase averaged flow field within the combustor. The individual images exhibit high spatiotemporal resolution that allows for the identification of sharp gradients and small structures within the flow.

Chapter VI examines the use of UCI to perform absorption field imaging with mid-IR back-illumination. Benchtop experiments were performed to observe the response of the system to known gas absorption environments. These measurements identified ethane as a superior target fuel species for absorption measurements within the RDC compared to methane and ethylene.

Chapter VIII summarizes the contents of the dissertation and provides an evaluation of pulsed mid-IR UCI for combustion applications based on the presented results. It also provides comments on future work including recommended improvements to the design of the UCI system presented here and further applications of the UCI technique.

CHAPTER II

UCI Theory and Modeling

2.1 Sum-frequency generation efficiency modeling

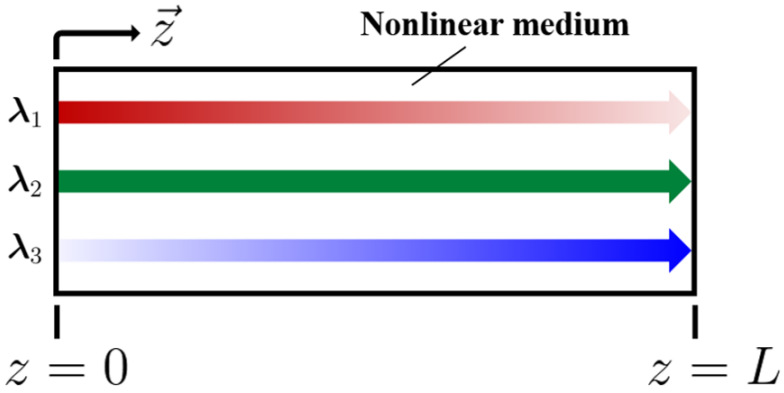

Figure 2.1: A conceptual diagram showing an SFG process that is mixing two input waves, a mid-IR wave at a wavelength λ_1 and a pump wave at a wavelength λ_2, to generate an output wave, the upconverted wave at a wavelength λ_3. The three waves travel through the nonlinear medium in the z direction in a collinear fashion, though they have been separated here for clarity, and exchange energy representing by strengthening or weakening of each arrow.

In this analysis, spatial and spectral properties associated with the three electromagnetic waves participating in the Sum-Frequency Generation (SFG) interaction will be denoted by subscripts 1, 2, and 3 corresponding to the target mid-IR image, pump beam, and upconverted signal image light waves, respectively. All three light waves will be treated in approximation as semi-infinite plane waves within the nonlinear medium. The electric field associated with each of these three waves can be written as:

$$\vec{E}(z,t) = A_j(z)e^{i(k_j z - \omega_j t)}\hat{\epsilon}_j + \text{c.c.} \tag{2.1}$$

Here $i = \sqrt{-1}$, A_j is the complex amplitude of a particular wave, k_j is the angular wavenumber, ω_j is the angular frequency, and $\hat{\epsilon}_j$ is a unit vector pointing in the direction of the wave's polarization. Both k_j and ω_j can be related directly to the vacuum wavelength of the light wave, λ_j:

$$k_j = \frac{2\pi n_j}{\lambda_j} \tag{2.2}$$

$$\omega_j = \frac{2\pi c}{\lambda_j} \tag{2.3}$$

where c is the speed of light in a vacuum and n_j is the *index of refraction* for that wave in the medium. The index of refraction represents the phase speed (how fast peaks and troughs of the value of $\vec{E}$ appear to move along the direction of light propagation) of a light wave in a particular medium relative to the speed of light. The index of refraction depends on the material through which light is propagating and for a given material is typically modeled as a function of wavelength and the temperature of the medium, T: $n_j = F(\lambda_j, T)$. The dependence of n_j on λ_j is known as *dispersion*, and this dispersion effect is a critical part of where UCI's spectral selectivity comes from. The temperature dependence of n_j will also be leveraged to increase the versatility of UCI. The significance of these index of refraction dependencies becomes clear after examining the coupled-wave equations that determine variation in wave amplitude within a second-order nonlinear medium. The complex amplitude of a light wave can be directly related to its intensity by:

$$I_j = 2\varepsilon_0 n_j c A_j A_j^* \tag{2.4}$$

where ε_0 is the vacuum permittivity constant.

At the heart of UCI is the SFG process, and modeling this process is critical to predicting the performance of a UCI system. Figure 2.1 gives a conceptual illustration of SFG involving the three previously defined waves within a nonlinear medium (from now on interchangeably referred to as a nonlinear crystal) of length L. The three waves enter the crystal at $z = 0$ and travel along the z direction in a collinear fashion (this collinear restriction will be relaxed later in section 2.3.1), though they are shown as separated in Figure 2.1 for clarity. Initially, only the mid-IR wave and the pump wave have non-zero intensities, indicated by the relative darkness of each arrow in the diagram. As they propagate along the length of the crystal, the three waves exchange energy such that the mid-IR wave is diminished and the upconverted wave is strengthened. This is the goal of SFG implemented for UCI, to generate a significant upconverted signal by converting energy from the mid-IR beam at the input side of the crystal into the upconverted wave by the output side of the crystal. The pump beam is depicted as unchanged along the length of the crystal to repre-

sent an approximation that will be invoked later which states that the much higher intensity of the pump beam relative to the mid-IR wave will cause it to be effectively constant in intensity along the length of the crystal.

The evolution of the amplitudes of the three waves participating in the SFG process along the length of the nonlinear medium is governed by what are known as the *coupled wave equations*. These equations are derived assuming that the interacting waves are semi-infinite plane waves, propagating in a lossless medium, all traveling collinearly in what will be defined as the z direction. It is also assumed that the strength of the nonlinear interaction in the medium is quantified by the effective nonlinear coefficient d_{eff}, which is equal to half of the second-order nonlinear susceptibility in SI units of $\mathrm{m/V}$. There are several forms of the coupled-wave equations depending on the units and variables used for the expression. This work will use the SI units form given by Sutherland [71]:

$$\frac{\mathrm{d}A_1}{\mathrm{d}z} = i\frac{2d_{\text{eff}}\,\omega_1}{n_1 c}A_3 A_2^* e^{i\Delta k\, z} \tag{2.5}$$

$$\frac{\mathrm{d}A_2}{\mathrm{d}z} = i\frac{2d_{\text{eff}}\,\omega_2}{n_2 c}A_3 A_1^* e^{i\Delta k\, z} \tag{2.6}$$

$$\frac{\mathrm{d}A_3}{\mathrm{d}z} = i\frac{2d_{\text{eff}}\,\omega_3}{n_3 c}A_1 A_2 e^{-i\Delta k\, z} \tag{2.7}$$

where Δk is known as the *wavenumber mismatch*, defined as:

$$\Delta k = k_3 - k_1 - k_2 \tag{2.8}$$

To interpret these equations, we will make a couple of assumptions. First, we will assume that the amplitude of the signal beam is initially zero: $A_3(0) = 0$. Second, we will assume that the initial pump beam amplitude is much greater than that of the mid-IR light: $A_2(0) \gg A_1(0)$. This is sometimes known as the *non-depleting pump approximation* because as a consequence the relative change in A_2 along the crystal due to Eq. (2.6) will be negligible for all conditions, and so A_2 can be treated as approximately constant in z.

The coupled wave equations can now be examined to determine how to achieve the goal of SFG of a large depletion of the mid-IR light amplitude, A_1, and a large growth in the upconverted signal amplitude, A_3, along the length of the crystal. Eq. (2.7) shows that initially at $z = 0$ the value of the exponential factor, $e^{-i\Delta k\, z}$, will be unity and so the magnitude of A_3 will grow along the length of the crystal. After the initial growth with propagation along the crystal, if the value of Δk is non-negligible then the sign of the exponential factor will reverse periodically with increasing z. This means that while A_3 always grows initially, for significant wavenumber number mismatches the upconverted

wave amplitude will sometimes be growing and other times be depleting over same sized propagation intervals. It is clear that in these cases the strength of the upconverted wave will not be significant at the crystal outlet.

If instead the wavenumber mismatch takes a value equal to or close to zero, $\Delta k \approx 0$, then the exponential factor will always remain close to unity and the upconverted wave grows along the entire length of the crystal. Therefore, to achieve efficient upconversion, the system must satisfy this small wavenumber mismatch condition. This is the *phase-matching condition* referred to in Chapter I. It is called phase-matching because it is equivalent to the requirement that a constant phase relationship is maintained between the output (upconverted) wave and the nonlinear polarization induced in the medium by the input waves. It is conveniently quantified with the wavenumber mismatch, which can be expressed in terms of wavelengths and temperature-dependent dispersion as:

$$\Delta k = 2\pi \left(\frac{n_3(\lambda_3, T)}{\lambda_3} - \frac{n_1(\lambda_1, T)}{\lambda_1} - \frac{n_2(\lambda_2, T)}{\lambda_2} \right) \tag{2.9}$$

If the pump beam is approximately monochromatic with a chosen wavelength λ_2, then the three wavelengths can be related by applying the photonic conservation of energy:

$$\frac{1}{\lambda_3} = \frac{1}{\lambda_1} + \frac{1}{\lambda_2} \tag{2.10}$$

Combining Eqs. (2.9) and (2.10) allows knowledge of the dispersive properties of a nonlinear medium to be used to calculate the wavenumber mismatch for any mid-IR wavelength λ_1. In general, some wavelengths may satisfy the phase-matching condition while others do not. This is where the spectral selectivity of UCI originates, as the system can be designed so that desired wavelengths are phase-matched while undesired wavelengths do not satisfy phase-matching and are not detected by the system.

Approaches to phase-matching

There are several approaches to phase-matching that are used to achieve efficient SFG. An exhaustive analysis and discussion of available phase-matching techniques is beyond the scope of this work, but broader discussions of phase-matching can be found in references by Sutherland [71] and Boyd [72]. Instead, this section will describe several common methods of phase-matching and some of their implications in UCI. The choice of phase-matching configuration employed in the design of a UCI can have a significant impact on the properties of the system.

Various phase-matching techniques are categorized by the mechanism that is used to

control the dispersion properties such that Eq. (2.9) is satisfied. Uniaxial crystals exhibit a phenomenon known as birefringence where components of light waves with polarization vectors that are either parallel or perpendicular to the *optical axis*, a particular direction that characterizes the medium's anisotropy, of the crystal experience different indices of refraction. The component of light with a polarization parallel to the optical axis is known as the *extraordinary ray* and experiences an index of refraction, n_e, that is different from the index of refraction, n_o, experienced by the light of the other polarization component, known as the *ordinary wave*.

One strategy for phase-matching rotates the alignment of the nonlinear crystal relative to the propagation of the mixing waves to control the index of refraction experienced by the extraordinary wave. This is known as *angle-tuning* or *critical phase-mathcing* as the extraordinary index of refraction, n_e, is dependent on the angle between the polarization vector of a wave and the optical axis of the crystal. Therefore, different angular orientations of the nonlinear crystal will produce different phase-matching conditions that target particular wavelengths. Critical phase-matching is often used in Second-Harmonic Generation (SHG), a subset of SFG where the two input waves have the same wavelength and produce an output wave with a wavelength equal to half that of the input waves, in high-energy pulsed lasers because of its high efficiency and ease of adjustment. Critical phase-matching has also been used in prior UCI examples, such as imaging performed by Junaid *et al.* [73] of mid-IR light at wavelengths of $6\,\mu\mathrm{m}$ to $8\,\mu\mathrm{m}$ through upconversion in $AgGaS_2$ crystals with critical phase-matching. The advantages of this approach are that a variety of large aperture nonlinear media are available for use. Drawbacks include the need for precise alignment and control of the crystal angle to accurately set the spectral response of the system. Additionally, critical phase-matching exhibits a phenomenon known as walk-off where the overlap of the mixing beams changes due to displacement induced by birefringence. This can potentially compromise both the efficiency of the SFG process and spatial resolution of the image in the walk-off direction.

A more popular approach to phase-matching in UCI is known as *temperature tuning* or *noncritical phase-matching*. In noncritical phase-matching, the mixing waves propagate along a principal axis of the crystal and have a polarization that is either parallel or perpendicular to the optical axis of the crystal. The elimination of angle tuning means that the indices of refraction experienced by each wave become functions of temperature alone (in addition to the spectral dispersion). The temperature of the nonlinear crystal must be varied to achieve the desired phase-matching condition, hence the name temperature tuning. This approach is advantageous in UCI because it eliminates the effects of spatial walk-off and is much less sensitive to the spatial alignment of the crystal [6]. For this reason, this work

will focus exclusively or noncritical phase-matching techniques.

All noncritical phase-matching techniques require a particular polarization orientation of the participating mixing waves. This means that the detection is inherently polarized as **only one polarization direction of mid-IR input light will satisfy the set phase-matching condition and be upconverted efficiently**. This can be beneficial in laser-based diagnostic techniques that produce a coherent, polarized signal as it can be directly distinguished through phase-matching from cross-polarized background light. However, this property of UCI results in an efficiency penalty when attempting to detect light that is incoherent and exhibits a random polarization direction (in other words unpolarized). In those cases, only the appropriately polarized component of that light will participate in upconversion and be detectable. Therefore, 50% of the mid-IR light intensity would be detectable while the other 50% cannot be detected by the system. This can be considered a limitation of UCI in unpolarized imaging applications as the maximum system QE relative to all available unpolarized photons will be 50%. With this in mind, all QE values discussed in the remainder of this work will be calculated relative to light in the appropriate polarization component.

Noncritical phase-matching can be implemented in several different ways depending on the relative polarizations of the waves that are being mixed. The two primary kinds of noncritical phase-matching are *type I phase-matching*, where the two input waves have parallel polarizations that are perpendicular to the output wave (either $e+e \rightarrow o$ or $o+o \rightarrow e$), and *type II phase-matching*, where the two input waves have perpendicular polarizations (either $e+o \rightarrow e$ or $e+o \rightarrow o$). As an example of applications in UCI, Andrews [74] used type I noncritical phase-matching in KDP crystals to upconvert scenes back-illuminated with a pulsed ruby laser into blue wavelengths.

It is often observed that nonlinear media will exhibit the strongest nonlinear coupling coefficients, d_{eff}, for phase-matching configurations where all three waves have the same polarization direction (either $e+e \rightarrow e$ or $o+o \rightarrow o$), sometimes referred to as *type 0 phase-matching*. This type of phase-matching is advantageous because of the increased coupling strength (which lowers the crystal length and pump intensity required for high-efficiency upconversion), but generally cannot be achieved in nonlinear materials that exhibit *normal dispersion*, *i.e.* an index of refraction that decreases with increasing wavelength. One way to circumvent the inability to perform this type of phase-matching is QPM, described in the following section. The system developed in this work makes use of co-polarized ($e+e \rightarrow e$) QPM in ppLN, which provides an uplift in d_{eff} of more than three times what is achievable in LN without QPM [75]. The strong nonlinear coupling makes this a popular approach in UCI with many examples in existing literature [32, 42, 76, 41].

2.2 Quasi-phase-matching

Quasi-phase-matching (QPM) is a strategy for augmenting the phase-matching condition to accommodate wavelengths that cannot be perfectly phase-matched in a system. The concept was first proposed by Armstrong *et al.* [19] and was subsequently elaborated by Rustagi *et al.* [77]. It works by addressing the mechanism of efficiency loss due to phase mismatches described in section 2.1 where non-negligible values of Δk cause the direction of energy flow between the input and output waves to periodically reverse. The upconverted wave initially grows, but after propagating one *coherence length*, defined as $l_c = \pi/\Delta k$, energy begins to flow back into the input waves because the upconverted wave and the nonlinear polarization have drifted to be $180°$ out of phase. QPM works by changing the sign of the effective nonlinear coefficient, d_{eff}, after an integer number of coherence lengths to cancel the changing sign of the exponential factor [78]. In this way, wavelengths that are not perfectly phase-matched can still be efficiently upconverted by fabricating a crystal with an appropriate periodic reversal of the sign of the nonlinear coefficient.

The effect of QPM can be modeled mathematically by the addition of an extra term to Eq. (2.8). If the sign of d_{eff} is reversed and changed back with a spatial period along the z direction of Λ_{P}, a distance known as the *poling period* in modern implementations, then the QPM condition can be expressed as:

$$\Delta k_{\text{QPM}} = k_3 - k_1 - k_2 \pm \frac{2\pi}{\Lambda_{\text{P}}} \tag{2.11}$$

Through the crystal fabrication process Λ_{P} can be chosen by the crystal designer to satisfy the QPM condition for a certain wavelength by setting $\Lambda_{\text{P}} = |\Delta k|/2\pi$ to cancel out the wavevector mismatch preventing perfect phase-matching. This comes with an efficiency penalty compared to perfect phase-matching. For the upconversion efficiency relationships provided in section 2.3.2, one must use a scaled down value of effective nonlinearity, d_{eff}:

$$d_{\text{eff,QPM}} = \frac{2d_{\text{eff}}}{\pi} \tag{2.12}$$

This penalty in nonlinear coupling strength is often more than compensated for by the efficiency gains of satisfying the QPM condition, as will be shown in the following section.

Figure 2.2 provides a conceptual illustration of how the QPM process works to build up output wave energy along the length of the crystal. The top half of the figure shows an SFG process that fails to satisfy the phase-matching condition. As a result, energy oscillates back and forth between the input and output waves without consistently amplifying the upconverted field. The bottom of the figure shows a QPM process in a crystal with a poling

period, Λ_P, that was chosen to cancel out the residual wavenumber mismatch and satisfy the QPM condition. This allows energy to consistently flow into the output wave without any reverse conversion. Although the upconverted wave does not grow as quickly it would in a perfectly phase-matched case, this QPM condition still accomplishes the intended goal of generating a strong output upconverted wave.

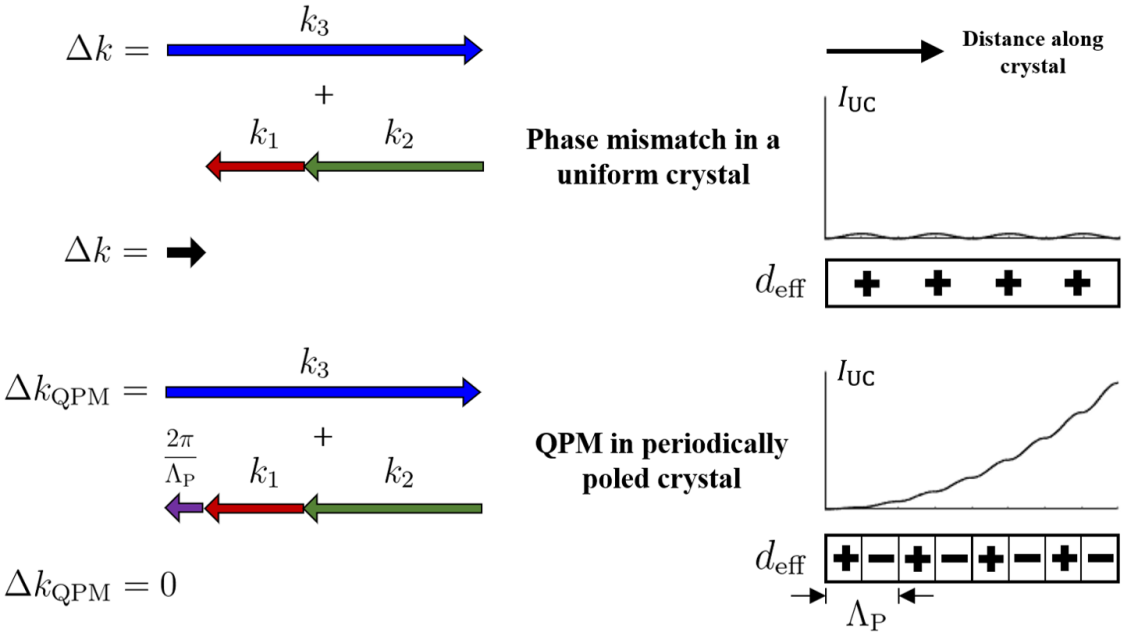

Figure 2.2: A conceptual diagram comparing an SFG process that fails to satisfy the phase-matching condition to a similar process where the QPM condition is satisfied. In the non-phase-matched case, energy oscillates between the output wave, I_{UC}, and the input waves and fails to generate a strong upconverted signal. The QPM case for the same wavelengths generates a strong output through appropriate selection of the poling period, Λ_P.

Initial attempts at performing QPM used optically bonded alternating slabs of nonlinear media to achieve the required periodic variation in the mixing phase relationship. As an example, Thompson *et al.* [79] used a stack of 19 GaAs crystal slabs interfaced at the Brewster angle to enhance the non-phase-matched second harmonic generation of an IR CO_2 laser beam. These early approaches were difficult and expensive to perform because coherence lengths are typically on the order of $10\,\mu\mathrm{m}$, and they suffered from efficiency losses due to reflections at the slab interfaces, despite attempts to use optical bonding and Brewster angle mating. Advancements in the 1970s and 1980s in crystal fabrication techniques led to the commercial availability of large, high-quality nonlinear crystals treated with a technique known as *periodic poling* (the origin of the term poling period). In these treatments, high-strength electric fields (typically on the order of $10\,\mathrm{kV/mm}$) are applied to crystal media that are masked with a dielectric stencil [31]. This electric field induces a re-

versal of the directional optical properties of the material with a precise spacing to achieve the desired Λ_P while being free of any internal interfaces. This technology can be used to achieve high-quality QPM in crystals with thicknesses of $1\,\mathrm{mm}$ or greater and lengths of $100\,\mathrm{mm}$ or greater. Importantly, these manufacturing techniques can be used to fabricate multiple poling periods in distinct *gratings* within the same crystal chip, so that one crystal can be used for multiple QPM conditions.

Figure 2.3 gives an example of the wavenumber mismatch (solid black line) for mid-IR wavelengths mixed with co-polarized $1064\,\mathrm{nm}$ pump radiation in LN (this describes the SFG process used in the design described in section 2.5). Here it is clear that the perfect phase-matching condition, $\Delta k = 0$ (dashed black line), is not satisfied for any of the mid-IR wavelengths. However, if a periodically poled LN crystal is used with poling periods of $\Lambda_P = 17.85\,\mu\mathrm{m}$ or $\Lambda_P = 22.45\,\mu\mathrm{m}$, these correspond to contributions of $0.352\,\mathrm{rad}/\mu\mathrm{m}$ and $0.280\,\mathrm{rad}/\mu\mathrm{m}$ as the final term of Eq. (2.11), respectively. The QPM condition is satisfied in each of these cases where the Δk curve (black line) intersects the red dashed lines, corresponding to QPM wavelengths of $2.3\,\mu\mathrm{m}$ and $3.4\,\mu\mathrm{m}$, respectively. These examples are two of the poling periods of the system design described in section 2.5.

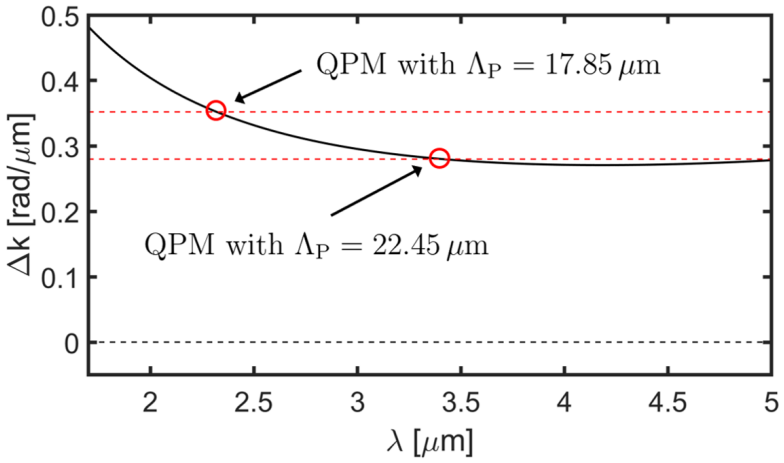

Figure 2.3: Wavenumber mismatch for mid-IR wavelengths mixing with $1064\,\mathrm{nm}$ pump radiation in LN at $100\,^{\circ}\mathrm{C}$. The two red dashed lines indicate the effective wavenumber contributions of poling periods of $17.85\,\mu\mathrm{m}$ (upper line) and $22.45\,\mu\mathrm{m}$ (lower line).

The concept of QPM is of great importance to UCI in combustion applications for two reasons. First, it allows strongly nonlinear materials to be used for upconversion that reduce the length of the nonlinear crystal and intensity of the pump beam required for adequate signal strengths. Second, it allows a designer to precisely select the wavelength bands that they want to target. Versatile systems can be built because individual crystal chips can house multiple poling periods. Adjustments of the crystal position in the imaging system

of a few millimeters can shift the operation of the system to completely different parts of the mid-IR spectrum when desired.

2.3 Predicting upconversion efficiency

The coupled-wave equations in Eqs. (2.5), (2.6), and (2.7) can be solved under the relevant conditions to determine the amplitude of the upconverted wave at the outlet of the crystal. To solve these equations it is assumed that the waves can be reasonably treated with the *quasi-cw* approximation (that the amplitudes of the waves in pulsed situations vary much more slowly than ω_j for each wave) and the *slowly-varying envelope* approximation (that spatial variation in the wave amplitudes in the z direction is small over the distance of one wavelength, λ_j, for each wave). When these assumptions are applied along with those previously mentioned in section 2.1 (particularly the infinitely strong pump approximation), then the solution yields the upconverted field amplitude at the crystal outlet, $z = L$. Because light detectors typically fall into the category known as *square law detectors* that respond to the *intensity* of a light field instead of the wave amplitude, it is more practical to express the result in terms of intensity [71]:

$$I_3(L) = \frac{\lambda_1 I_1(0)}{\lambda_3} \sin^2\left(4\pi d_{\text{eff}} L \sqrt{\frac{I_2(0)}{2\varepsilon_0 n_1 n_2 n_3 c \lambda_1 \lambda_3}}\right) \text{sinc}^2\left(\frac{\Delta k L}{2}\right) \tag{2.13}$$

where the sinc function is defined as $\text{sinc}(x) = \sin(x)/x$. This form can then be converted to a quantum efficiency, η, of upconverted photons generated per incident mid-IR photon:

$$\eta = \frac{\lambda_1 I_3(L)}{\lambda_3 I_1(0)} = \sin^2\left(4\pi d_{\text{eff}} L \sqrt{\frac{I_2(0)}{2\varepsilon_0 n_1 n_2 n_3 c \lambda_1 \lambda_3}}\right) \text{sinc}^2\left(\frac{\Delta k L}{2}\right) \tag{2.14}$$

It can be helpful from a design perspective to decompose the SFG efficiency into two components: a phase-matching efficiency, η_{PM}, and a temporal efficiency, η_t. The total efficiency of the SFG process then can be expressed as the product of the phase-matching and temporal efficiencies:

$$\eta = \eta_t \eta_{\text{PM}} \tag{2.15}$$

where:

$$\eta_t = \sin^2\left(4\pi d_{\text{eff}} L \sqrt{\frac{I_2(0)}{2\varepsilon_0 n_1 n_2 n_3 c \lambda_1 \lambda_3}}\right) \tag{2.16}$$

$$\eta_{\text{PM}} = \text{sinc}^2\left(\frac{\Delta k L}{2}\right) \tag{2.17}$$

Note that both the temporal and phase-matching efficiencies retain a dependence on λ_1, and so the decomposition is not a perfect separation between spectral and temporal dependencies. However, the spectral dependence of η_t will be shown to be slowly varying as a function of IR wavelength while the spectral dependence of η_{PM} will cause some wavelengths to be strongly upconverted while others will produce zero or negligible signals. In this way, η_{PM} is primarily responsible for determining the mid-IR spectral bandwidth detected by the system and η_t will control the absolute magnitude of the UCI signal by determining how many phase-matched IR photons are upconverted over the duration of a pump pulse. The functional dependencies of these efficiencies for modeling UCI response will be examined in the next two sections.

2.3.1 Noncollinear phase-matching

Up to this point, it has been assumed that all three waves participating in the SFG process are collinearly propagating exclusively in the z direction. It is intuitively clear that image formation cannot occur without multiple propagation directions associated with both the mid-IR and upconverted fields. This means that the collinear propagation restriction must be relaxed in the analysis to consider noncollinear propagation, and therefore noncollinear phase-matching, within the nonlinear medium.

The nature of the noncollinear propagation in a system is going to be determined by the type of optical arrangement employed. Two primary configurations have been investigated in prior literature. The first will be referred to as the *4f configuration* (which is adopted in this work) where the nonlinear crystal is placed at the Fourier plane of a 4f imaging arrangement. The alternative is an optical configuration where the nonlinear crystal is placed at the image plane of an optical system such that a de-magnified mid-IR image is reconstituted within the aperture of the crystal. Barh *et al.* [6] provide a detailed comparison of the two configurations. That comparison showed that the 4f configuration exhibits superior performance in terms of FoV and spatial resolution, and for these reasons it is the focus of this discussion.

The geometric configuration of a 4f UCI system must be described to effectively analyze the system. Figure 2.4 gives a conceptual schematic of the 4f geometry. The arrangement consists of a canonical 4f configuration with an objective lens focal length of f_1 and a detector lens focal length of f_3. Important definitions include the in-plane distances from the centerline axis of the system: r_1, r_2, and r_3 corresponding to positions in the object,

Fourier, and image planes of the system, respectively. The angles θ_1 and θ_3 are the propagation direction angles of the IR and upconverted waves relative to the centerline axis of the system *within the nonlinear crystal*. These are distinct from the propagation angles *outside of the crystal*, θ_1' and θ_3', though they can be directly related through Snell's law.

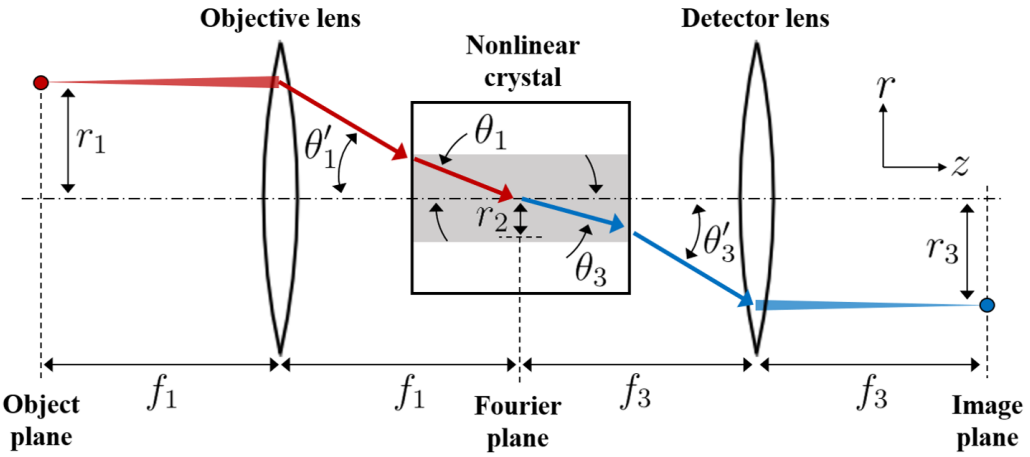

Figure 2.4: A schematic illustrating the 4f UCI configuration and defining important geometric parameters that are used in UCI modeling.

In this noncollinear case, the phase-matching condition must be applied vectorially, such that for QPM the condition can be expressed as:

$$\Delta\vec{k}_{\text{QPM}} = \vec{k}_3 - \vec{k}_1 - \vec{k}_2 \pm \frac{2\pi}{\Lambda_{\text{P}}}\hat{z} \tag{2.18}$$

where the direction of each $\vec{k}_j$ is determined by the propagation direction of each corresponding j^{th} wave. The *wavevector mismatch*, $\Delta\vec{k}$, can be decomposed into a longitudinal component, Δk_z, that lies along the z axis and a transverse component, Δk_{T}, that lies in a plane perpendicular to z axis.

A more detailed analysis of the noncollinear phase-matching process [80, 6] shows that in the semi-infinite plane wave approximation, the transverse wavenumber mismatch must vanish for significant upconversion field growth. This vanishing Δk_{T} restriction means that the phase-matching efficiency will be determined by the longitudinal phase-matching condition: $\Delta k_z = 0$. Figure 2.5 shows a representation of a set of noncollinear waves satisfying the QPM condition and their orientation relative to the z axis. The pump beam, represented by $\vec{k}_2$, is assumed to be injected so that it always travels along the z axis. The mid-IR and upconverted waves travel through the crystal at angles θ_1 and θ_3 relative to the z axis. Examination of this geometry leads to an expression for the longitudinal wavenumber

mismatch:

$$\Delta k_z = k_3 \cos(\theta_3) - k_1 \cos(\theta_1) - k_2 \pm \frac{2\pi}{\Lambda_P} \tag{2.19}$$

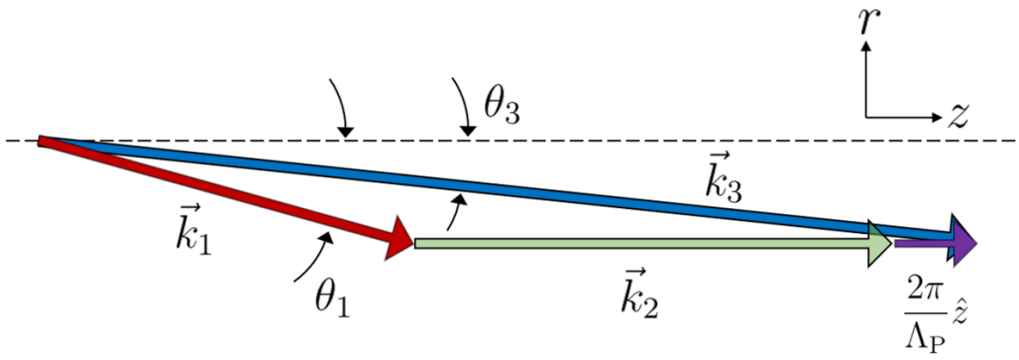

Figure 2.5: A diagram showing the noncollinear QPM condition with negligible transverse wavenumber mismatch.

Spatial-spectral coupling in 4f UCI

The longitudinal wavenumber mismatch can be further reduced so that it can be represented as a function of only θ_1, λ_1, and T (the crystal temperature). The vanishing transverse wavenumber mismatch condition can be invoked to require that the transverse components of the mid-IR and upconverted wavevectors be equal: $k_1 \sin(\theta_1) = k_3 \sin(\theta_3)$. This yields:

$$\theta_3 = \sin^{-1}\left(\frac{k_1}{k_3}\sin(\theta_1)\right) \tag{2.20}$$

and because λ_3 is uniquely determined by λ_1 (through Eq. (2.10) assuming a set λ_2), this makes k_3 and θ_3 functions exclusively of θ_1, λ_1, and T. Eq. (2.20) can be substituted into Eq. (2.19) to express Δk_z as:

$$\Delta k_z = k_3 \cos\left\{\sin^{-1}\left[\frac{k_1}{k_3}\sin(\theta_1)\right]\right\} - k_1\cos(\theta_1) - k_2 \pm \frac{2\pi}{\Lambda_P} \tag{2.21}$$

The phase-matching efficiency relationship in Eq. (2.17) can be applied to Δk_z to predict the spectral response of the corresponding system. This result shows that for every mid-IR propagation angle the system will exhibit a different spectral response. The implications of this can be further tied to the dimensions of the object being imagined by considering the geometry of the optical configuration.

For mid-IR point sources in focus in the object plane of the 4f arrangement, there is a direct mapping between r_1 and θ_1': $r_1 = f_1 \tan(\theta_1')$. Through Snell's law and the approx-

imation that $n_1 = 1$ in air, the propagation angles inside and outside of the crystal can be related: $\sin(\theta_1) = n_1 \sin(\theta_1')$. Combining these two relationships leads to the expression:

$$\theta_1 = \sin^{-1}\left(\frac{1}{n_1}\sin\left(\tan^{-1}\left(\frac{r_1}{f_1}\right)\right)\right) \approx \frac{r_1}{n_1 f_1} \tag{2.22}$$

where the approximate result comes when invoking the small angle approximation for both θ_1 and θ_1'. This same approach can be applied for a point on the detector by working backward through the detector lens to yield:

$$\theta_3 = \sin^{-1}\left(\frac{1}{n_3}\sin\left(\tan^{-1}\left(\frac{r_3}{f_3}\right)\right)\right) \approx \frac{r_3}{n_3 f_3} \tag{2.23}$$

Through Eqs. (2.21) and (2.22) it can be seen that the spectral response of a UCI system depends on location in the object plane, r_1 (or equivalently r_3 in the image plane). In this work **the fact that different regions of the FoV will exhibit different spectral responses is referred to as spatial-spectral coupling**. This has critical implications for design as the effect must be accounted for if a particular wavelength band is intended to be detected across a wide FoV. Some intrinsic properties of the nonlinear material can even limit the effective aperture of a measurement, as shown in the example mid-IR tuning curves described below. This also makes the implementation of temperature tuning valuable as it can be used to modify the spatial-spectral coupling relationship in a system. Kehlet *et al.* [33] leveraged this to perform hyperspectral imaging by sweeping through a range of crystal temperatures to detected a range of distinct wavelength bands at each point in the image without the need to move any parts in the UCI system.

The spatial-spectral coupling for a system design is typically visualized using IR tuning curves that display variation in SFG efficiency with mid-IR wavelength and propagation angle within the crystal. These curves depend on the nonlinear crystal material, its poling period, its length, and the pump wavelength, but are otherwise independent of the optical arrangement of the system. Figure 2.6 shows examples of IR tuning curves calculated with the previously described model for two poling periods in ppLN at room temperature, conditions that represent the state of the UCI system to perform measurements later described in Chapter IV.

Examination of the tuning curves in Figure 2.6 reveals some important properties of the UCI system. In both cases, the UCI response occurs at the shortest wavelengths near the center of the FoV with peak response wavelength increasing at points farther from the image center. The $\eta_{\text{PM}} = 1$ contour for the $19.4\,\mu\text{m}$ poling period extends out to and beyond 5° from the center of the image in a "smile" shaped contour. This indicates that the QPM

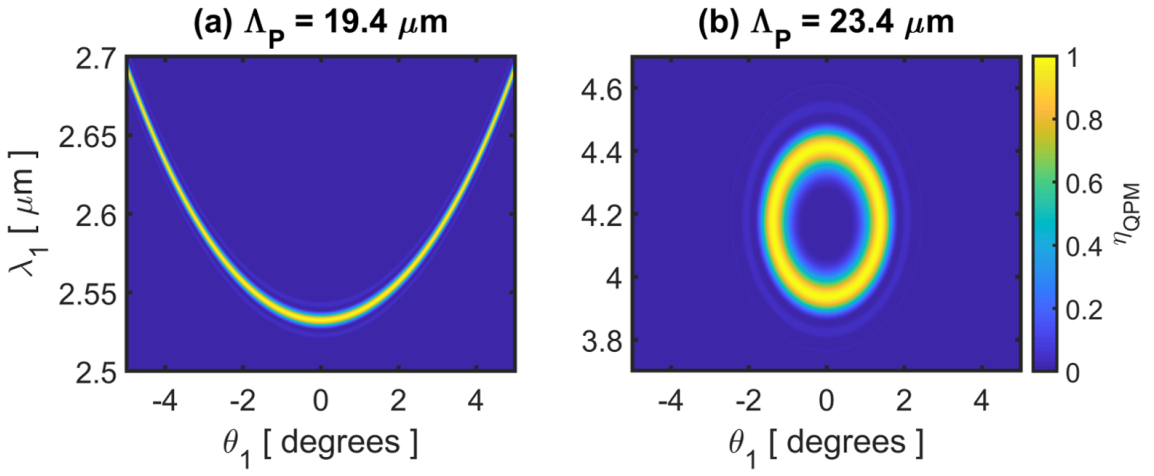

Figure 2.6: Mid-IR tuning curves for the UCI system with a $1064\,\mathrm{nm}$ pump beam and a crystal temperature of $21\,^{\circ}\mathrm{C}$ for two poling periods: (a) $\Lambda_P = 19.4\,\mu\mathrm{m}$ used to target H_2O transitions and (b) $\Lambda_P = 23.4\,\mu\mathrm{m}$ used to target CO_2 transitions.

condition does not limit the field of view, assuming broadband illumination, for this poling period and it will instead be limited by the effective clear aperture of the imaging optics.

In contrast, the high-response contour for the $23.4\,\mu\mathrm{m}$ poling period forms a closed ring that could be called a "donut" shape in θ_1–λ_1 space. This shows that non-negligible UCI response with this poling period is confined to within $<2°$ of angular separation from the centerline of the optical arrangement. In this case, as will be seen in the measurements presented in section 2.6, the FoV is limited by the QPM condition despite optics that could accommodate a wider acceptance angle. This effect is a result of non-monotonic variation of Δk with λ_1 in unpoled LN and is unavoidable at these wavelengths.

UCI de-magnification is another effect that is related to spatial-spectral coupling. In a conventional 4f imaging system, the image magnification is equal to the ratio of the focal length of the detector lens to that of the objective lens, f_3/f_1. In a UCI system there is an additional geometric influence on the effective magnification due to the transverse phase-matching constraint that is described by Eq. (2.20). When the small angle approximation is applied to Eq. (2.20) and the result is combined with Eqs. (2.22) and (2.23), it leads to:

$$r_3 = \frac{f_3\lambda_3}{f_1\lambda_1} r_1 \tag{2.24}$$

This shows that the effective magnification of the system is augmented by a factor of the ratio of the wavelengths, λ_3/λ_1, which will always be less than unity for UCI. In this way, UCI measurements exhibit an effective de-magnification compared to 4f systems employing the same focal lengths.

2.3.2 Pulsed UCI temporal efficiency

As shown by Eq. (2.16), the instantaneous efficiency of the upconversion process at a particular mid-IR wavelength depends on the pump beam intensity and several other parameters related to the configuration of the system. The decomposition in Eq. (2.15) aims primarily to separate the spectral response of the UCI process into η_{PM} and the factors governing signal strength into η_t. As was mentioned, the form of η_t retains a dependence on the mid-IR wavelength, λ_1, and the directly related upconverted wavelength, λ_3. However, the spectral bandwidth of the upconversion process is limited primarily by the phase-matching efficiency such that differences in the mid-IR wavelengths being imaged are small relative to the value of λ_1 that satisfies QPM. For this reason, the spectral dependence of η_t will be small over the range of wavelengths that are detected.

The expression for η_t in Eq. (2.16) is valid for large pump intensities, and captures the nonlinear dependence of upconversion efficiency on pump intensity. Many prior examples of UCI measurements in the available literature used relatively low-power cw pump sources that produced lower instantaneous efficiencies on the order of 20% to 30% [32, 42, 81]. In these relatively low pump intensity cases it is reasonable to linearize the efficiency dependence on pump intensity so that η_t can be expressed as:

$$\eta_t = \frac{8\pi^2 d_{\text{eff}}^2 L^2 I_2}{\varepsilon_0 n_1 n_2 n_3 c \lambda_1 \lambda_3} \tag{2.25}$$

This is the form generally reported in cw applications. However, for high pump intensities, the nonlinear effects become important and the form for η_t given in Eq. (2.16) must be used to capture them.

Figure 2.7 shows an example of the value of η_t calculated as a function of $1064\,\text{nm}$ pump beam intensity. Here it was assumed that a ppLN crystal $1\,\text{cm}$ in length was used to upconvert mid-IR light at wavelengths near $4.2\,\mu\text{m}$ with an effective nonlinear coupling coefficient assumed to be $d_{\text{eff}} = 14\,\text{pm/V}$ (representative of QPM in ppLN). The solid line shows the full nonlinear model of Eq. (2.16) while the dashed line shows the linear approximation of Eq. (2.25). For pump intensities above $5\,\text{MW}\,\text{cm}^{-2}$, the nonlinear effects become clear in Figure 2.7 as increasing pump intensities provide diminishing returns in marginal efficiency gain. The efficiency peaks at unity for a pump intensity of approximately $15\,\text{MW}\,\text{cm}^{-2}$. Above this intensity the efficiency begins to decrease again, exhibiting the periodic fluctuation characteristic of the $\sin^2$ dependence. This shows that for operation in the nonlinear regime, which can be accessed with high-energy pulsed pump lasers like the one used in this work, there is an optimal intensity that should be targeted. Operating above that optimal intensity would increase the risk of damage to the crystal and

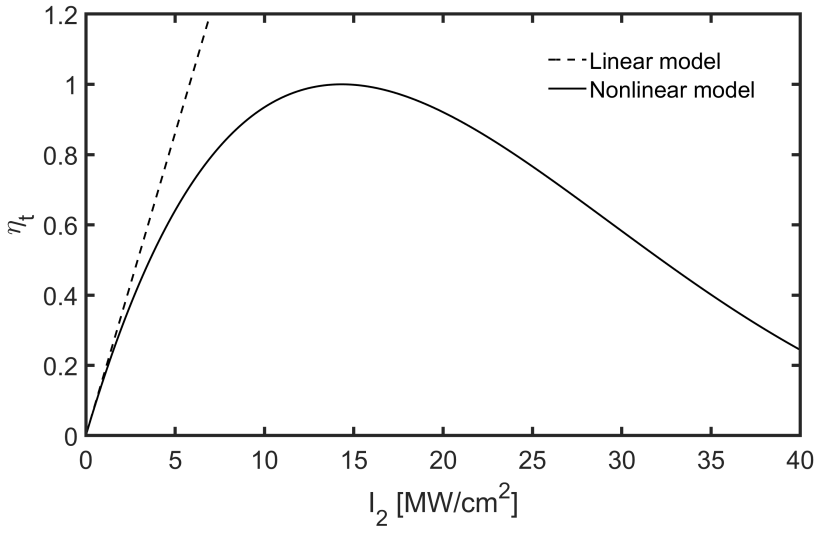

Figure 2.7: A comparison of the linear and nonlinear models of η_t as a function pump intensity.

other optical components with no associated efficiency gains.

The temporal efficiency is a function of pump intensity and in a practical pulsed pump system, the pump intensity will vary as a function of both time and location within the cross-section of the crystal. This means that the temporal efficiency will vary in both of those dimensions. The variation of system efficiency with time can be modeled if the spatial and temporal profiles of the pump pulse are known. The total signal strength produced by UCI of a steady mid-IR source, S_{UCI} (measured in upconverted photons), will then be proportional to an integration of η_t over both space and time:

$$S_{\text{UCI}} \propto 2\pi \int_0^\infty \int_{-\infty}^\infty \eta_t(t, r_2) r_2 \, \mathrm{d}t \, \mathrm{d}r_2 \tag{2.26}$$

This assumes that the mid-IR source is a spatial point source so that it creates an approximately uniform illumination of the Fourier plane.

The spatial and temporal profile of high-energy pulsed Nd:YAG lasers can typically be reasonably approximated with Gaussian functions. If $G(x; x_0, \Delta x)$ is a Gaussian function with a unity integrated value centered at x_0 with an FWHM of Δx, then the intensity variation of a Gaussian pump pulse could be written as:

$$I_2(r_2, t) = E_p \, G^2(r_2; 0, \sqrt{2}\Delta r) \, G(t; t_0, \Delta t) \tag{2.27}$$

where E_p is the pulse energy, Δr is the spatial FWHM of the beam profile, t_0 is the time

of peak power, and Δt is the temporal FWHM of the pulse-shape. However, the infinite spatial extent of the pump cross-section will not be compatible with Eq. (2.26) because of the finite aperture of the nonlinear crystal. Upconversion will only be excited by the pump beam within the cross-section of a crystal, and so an additional factor is needed to negate pump energy falling outside of the crystal. $F(r_2)$ is defined to account for the finite extent of a square poling period aperture, and it takes the form:

$$F(r_2) = \begin{cases} 1 & , \quad r_2 < a/2 \\ 1 - (4/\pi)\cos^{-1}(a/2r_2) & , \quad a/2 \leq r_2 < a/\sqrt{2} \\ 0 & , \quad r_2 \geq a/\sqrt{2} \end{cases} \tag{2.28}$$

where a is the width of the periodically-poled domain aperture ($1\,\mathrm{mm}$ in this work).

Incorporating $F(r_2)$ into the signal strength integral of Eq. (2.26) gives:

$$S_{\mathrm{UCI}} \propto 2\pi \int_0^\infty \int_{-\infty}^\infty F(r_2)\, \eta_t(t, r_2) r_2 \mathrm{d}t \mathrm{d}r_2 \tag{2.29}$$

For the example of the Gaussian pump pulse, this integral becomes:

$$S_{\mathrm{UCI}} \propto 2\pi \int_0^\infty \int_{-\infty}^\infty F(r_2)\, \sin^2\left(4\pi d_{\mathrm{eff}} L \sqrt{\frac{E_p\, G^2(r_2; 0, \sqrt{2}\Delta r)\, G(t; t_0, \Delta t)}{2\varepsilon_0 n_1 n_2 n_3 c \lambda_1 \lambda_3}}\right) r_2\, \mathrm{d}t\, \mathrm{d}r_2 \tag{2.30}$$

This integral can also be evaluated in the low-intensity limit for η_t given in Eq. (2.25). For the low-intensity limit:

$$S_{\mathrm{UCI}} \propto \frac{8\pi^2 d_{\mathrm{eff}}^2 L^2 E_p}{\varepsilon_0 n_1 n_2 n_3 c \lambda_1 \lambda_3} \int_0^\infty \int_{-\infty}^\infty F(r_2)\, G^2(r_2; 0, \sqrt{2}\Delta r)\, G(t; t_0, \Delta t) 2\pi r_2\, \mathrm{d}t\, \mathrm{d}r_2 \tag{2.31}$$

This result shows that in the low-intensity limit the UCI signal strength is directly proportional to the pump pulse energy, E_p (note that the integral is unity if $a \gg \Delta r$, otherwise it is less than 1). This is not true in general for short pulses or relatively high pulse energies where nonlinear effects result in lower signal strengths than would be predicted by Eq. (2.31).

Figure 2.8 shows an example of the predicted variation in UCI signal with pump pulse energy. This plot used the same crystal and wavelength parameters that were used to generate Figure 2.7. The pump pulse was assumed to have a temporal FWHM of $10\,\mathrm{ns}$ and a spatial beam FWHM of $800\,\mu\mathrm{m}$. Figure 2.8 shows the signal variation using both the

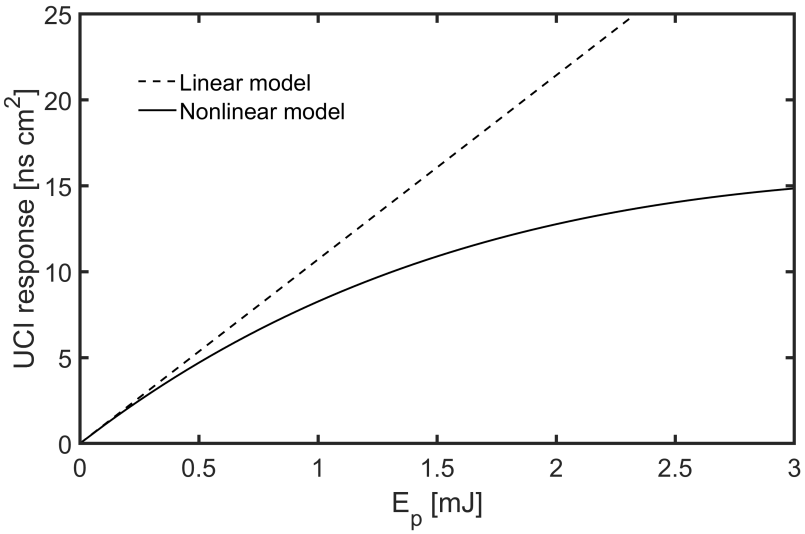

Figure 2.8: A comparison of the linear and nonlinear models of pulsed UCI response as a function pump pulse energy.

nonlinear model (solid black) and the linear approximation (dashed black line). The results show that for nanosecond pulses, the nonlinear effects become significant at relatively low pulse energies near $0.5\,\mathrm{mJ}$. As the energy is increased beyond this threshold some parts of the crystal exceed the optimal pump intensity during the peak intensity of the pulse. The signal response continues to rise monotonically with E_p in the nonlinear region because efficiency is increased in the spatial and temporal wings of the beam to offset the diminished efficiencies at peak power. The linear approximation is poor for pulse energies above $0.5\,\mathrm{mJ}$. However, if the pump pulse is shaped so that it provides a low intensity over a longer time interval, then the linear approximation can be accurate for higher pulse energies. One example of this type of scenario is the long-pulse mode operation of the pump laser that is discussed in section 3.3.1.

2.4 UCI image quality

Publications by Pedersen *et al.* [80] and Dam *et al.* [81] presented an analysis of the image formation process in UCI. They integrate the Fourier optics equations governing the propagation of mid-IR and upconverted light within the crystal with the addition of a source term in the upconverted field equations to account for SFG. The result is a relationship between the upconverted light intensity in the image plane at a particular, $I_3(\vec{r}_3, \lambda_3)$, and the mid-IR

illumination field in the object plane, $I_1(\vec{r}_1, \lambda_1)$ [80]:

$$I_3(\vec{r}_3,\lambda_3) = \frac{8\pi^2 d_{\text{eff}}^2 L^2 P_2}{\varepsilon_0 n_1 n_2 n_3 c \lambda_3^2} \times \int_{\mathcal{A}} I_1(\vec{r}_1, \lambda_1) \left\{ \frac{w_0^2 k_3^2}{2\pi n_3^2 f_3^2} \exp\left(-\frac{w_0^2 k_3^2 \left| \vec{r}_3 + \frac{\lambda_3 f_3}{\lambda_1 f_1} \vec{r}_1 \right|^2}{2\pi n_3^2 f_3^2} \right) \times \text{sinc}^2 \left[\frac{L}{2} \left(\Delta k(\vec{r}_1, \vec{r}_3) - \frac{k_3^2 \left| \vec{r}_3 + \frac{\lambda_3 f_3}{\lambda_1 f_1} \vec{r}_1 \right|^2}{2 k_2 n_3^2 f_3^2} \right) \right] \right\} \frac{\lambda_3 f_3}{\lambda_1 f_1} \mathrm{d}\vec{r}_1 \tag{2.32}$$

assuming a Gaussian pump beam profile with a $1/e$ width of w_0 and a total beam power of P_2. This long equation incorporates both the effects of phase-matching efficiency and temporal efficiency (in the low-intensity limit) that were decomposed in the previous sections, as well as some important imaging effects.

An important feature of this result is the exponential factor in the integrand of Eq. (2.32). This integral acts as a convolution of that Gaussian exponential with the spatial mid-IR illumination field, $I_1(\vec{r}_1, \lambda_1)$. In this way, the exponential can be viewed as a Gaussian Point-Spread Function (PSF) for the UCI system. The FWHM of that PSF in the image plane can be expressed as [81, 6]:

$$\Delta_{\text{PSF}} = \frac{\sqrt{2\ln(2)}\lambda_3 f_3}{\pi w_0} \tag{2.33}$$

Note that the variables $\lambda_3 f_3$ can be replaced with $\lambda_1 f_1$ to project this result back into the object plane by accounting for UCI de-magnification under the small-angle approximation. This blurring represents the effects of spatial filtering due to the finite aperture of the SFG process in the crystal. Because the nonlinear crystal chip is located at the Fourier plane of the 4f imaging arrangement, the cross-section of the pump beam exciting the SFG process acts as an aperture that can limit the spatial frequencies resolved by a UCI system.

With this influence on spatial resolution in mind, the size of the crystal, which limits the maximum pump beam size, and the collection lens focal length should be chosen to accommodate the desired spatial resolution for the system. If the aperture of the nonlinear crystal or the beam waist of the pump beam is too small, then spatial resolution of the UCI measurements can be compromised. This is typically limited by the maximum crystal thickness that can be periodically poled (usually in the range of $0.5\,\text{mm}$ to $2\,\text{mm}$). This also motivates the use of pump beam cross-sections that fill the entire crystal aperture.

2.5 UCI system design

2.5.1 Choosing a nonlinear medium

A primary consideration in choosing a nonlinear crystal is spectral transparency. The coupled wave equations in section 2.1 assume propagation in a lossless medium; any even modest internal absorption can significantly limit the efficiency of the SFG process. A medium must be chosen that accommodates all three mixing wavelengths with high spectral transmission.

It is also beneficial to choose a nonlinear medium with a large nonlinear coefficient, d_{eff}, as this reduces the pump intensity required to achieve high-efficiency upconversion. The nonlinear coefficient of a material depends on the type of phase-matching being employed. Nonlinear coefficients are reported as elements of a d-matrix and are indicated as d_{ij} where i and j take values of 1 to 6 depending on the polarization and propagation vectors of mixing waves within the nonlinear medium (as an example, $e+e \rightarrow e$ QPM in LN accesses the d_{33} coefficient). Multiple coefficients may need to be combined to compute the relevant value of d_{eff} for a particular phase-matching approach (see Sutherland Chapter 2 [71]).

Barh *et al.* [6] conducted an exhaustive review of nonlinear media used in previously reported UCD experiments. They also identified media that had not been tested but may be good candidates for future use in UCD. A reduced version of the list provided in Barh *et al.* [6] is reproduced in Table 2.1 for convenience. This table includes the parameter $\frac{\mathrm{d}n}{\mathrm{d}T}$ that quantifies the temperature tunability that a material can exhibit and may be an important factor in a system design.

LN is a popular medium for nonlinear optics applications in the mid-IR regime, including UCD techniques. This is due to several favorable properties. LN is highly transparent for wavelengths from the visible spectrum through mid-IR wavelengths up to $4.5\,\mu\mathrm{m}$ where the transmission begins to fall slightly and heavy losses occur at wavelengths above $5\,\mu\mathrm{m}$. This opens the $1.5\,\mu\mathrm{m}$ to $5\,\mu\mathrm{m}$ spectral range for upconversion where several important combustion species exhibit isolated transitions. Additionally, LN exhibits a high effective nonlinear coupling coefficient that can be accessed through QPM. Multiple wavelength bands can be targeted with a single-chip system by fabricating multiple poling periods within the chip. For these reasons, ppLN was chosen for the nonlinear medium in this work. Specifically, the chemical makeup of the crystal was Congruent Lithium Niobate (CLN) with 5% MgO doping to increase the photorefractive damage threshold.

Nonlinear material	Transmission window [μm]	Nonlinear coefficient [pm/V]	$\frac{dn}{dT}\times10^5$ [K^{-1}]
Proustite (Ag_3AsS_3)	0.6–13	18(d_{22}); 11.3(d_{31})	N/A
KDP (KH_2PO_4)	0.18–1.5	0.43(d_{36})	-3.94(o); -2.54(e)
LBO (LiB_3O_5)	0.16–2.6	1.05(d_{31}); -1.0(d_{32}); 0.05(d_{33})	-0.93(x); -1.36(y); -0.63(z)
BBO (β-BaB_2O_4)	0.2–3.5	2.3(d_{22}); 0.16(d_{31})	-1.66(o); -0.93(e)
$KNbO_3$	0.4–4.5	20.4(d_{32})	2.2($\|\|c$); 6.5($\|\|a$)
KTP ($KTiOPO_4$)	0.35–4.5	6.5(d_{31}); 13.7(d_{33})	1.1(x); 1.3(y); 1.6(z)
LN ($LiNbO_3$)	0.4–5.5	-4.52(d_{31}); 31.5(d_{33})	-0.09(o); -3.91(e)
$ZnGeP_2$	1–12	79(d_{36})	21.18(o); 23.01(e)
$AgGaS_2$	0.47–13	12.6(d_{36})	16.7(o); 17.6(e)

Table 2.1: A partial list of nonlinear materials used in previous UCD experiments modified from the full list found in Barh *et al.* [6].

2.5.1.1 Modeling relevant properties of LN

The QPM-based SFG process can be tuned by controlling the temperature of the nonlinear medium. This is especially important for control of the spectral response of UCI. For example, in ppLN temperature variation between room temperature and $200\,^{\circ}\mathrm{C}$ can cause a shift in the wavelength of peak efficiency that is several times the spectral bandwidth of the upconversion process. For this reason, it is critical in both experimental design and interpretation of UCI measurements that the temperature dependence of these material properties be accurately modeled. Changes in the temperature of the nonlinear crystal can affect the SFG process in two ways: through thermally induced changes in the index of refraction and thermal expansion of the crystal.

Changes in the length of both the crystal and the poling period of the grating within the crystal are caused by thermal expansion and contraction of the material as its temperature changes. These changes have a relatively small impact on the temporal efficiency of SFG in the material, however the precise QPM relationships that control the spectral response of UCI are typically sensitive to these changes, and they must be accounted for. The length of the crystal and the poling periods in its gratings can be modeled as proportional to a thermal expansion factor $\delta_T(T)$ that captures relative expansion and contraction due to changes in

temperature so that:

$$L(T) = L_0 \delta_T(T) \tag{2.34}$$

$$G(T) = G_0 \delta_T(T) \tag{2.35}$$

where L_0 and G_0 are the lengths at a particular reference temperature of the crystal and poling period, respectively. For a second order model, $\delta_T(T)$ takes the form:

$$\delta_T(T) = 1 + \alpha \left(T - 25^{\text{o}}\text{C}\right) + \beta \left(T - 25^{\text{o}}\text{C}\right)^2 \tag{2.36}$$

where α and β are the empirically determined coefficients. Kim and Smith [82] report values of $\alpha = 1.54 \times 10^{-5}\,\text{K}^{-1}$ and $\beta = 5.3 \times 10^{-9}\,\text{K}^{-2}$ for LN along the crystallographic direction of light propagation in this application for a reference temperature of $25\,^{\circ}\text{C}$ (therefore $L_0 = L(25^{\text{o}}\text{C})$ and $G_0 = G(25^{\text{o}}\text{C})$). These values are used in this work to model the effects of thermal expansion of the ppLN chip.

The precise dispersion properties of a nonlinear medium are critical to calculating the phase-matching condition for UCI measurements, and therefore its spectral response. The index of refraction can be modeled as a function of wavelength and the temperature of the medium, $n_j(T, \lambda_j)$. These dependencies are typically modeled using the temperature-dependent Sellmeier equation, which can take different forms depending on how it is constructed from data. The Sellmeier equation and necessary coefficients for MgO-doped LN were taken from Gayer *et al.* [7]. The specific form and values are given in Appendix A.

2.5.2 Choosing QPM poling periods and crystal size

A major decision in the design of a UCI system is the choice of poling periods when employing QPM. QPM provides the freedom to target specific mid-IR wavelength ranges without needing to satisfy the strict phase-matching condition of the nonlinear medium. Because contemporary manufacturing techniques allow multiple poling periods to be generated in the same crystal chip, versatile systems can be designed that target multiple mid-IR wavelengths. For combustion applications, this in turn means that multiple species of interest can be accessed using the same crystal chip.

Figure 2.9 gives a plot of the mid-IR spectral signatures of a collection of important product and intermediate species in combustion. This plot does not give an accurate representation of the absorption or emission spectrum that might be observed in a flame but instead scales the absorption spectra of the species to balance clarity and representations of their relative strengths. The major product species of H_2O and CO_2 exhibit strong mid-IR absorption bands near $2.7\,\mu\text{m}$ and $4.2\,\mu\text{m}$, respectively. These strong, relatively broad spec-

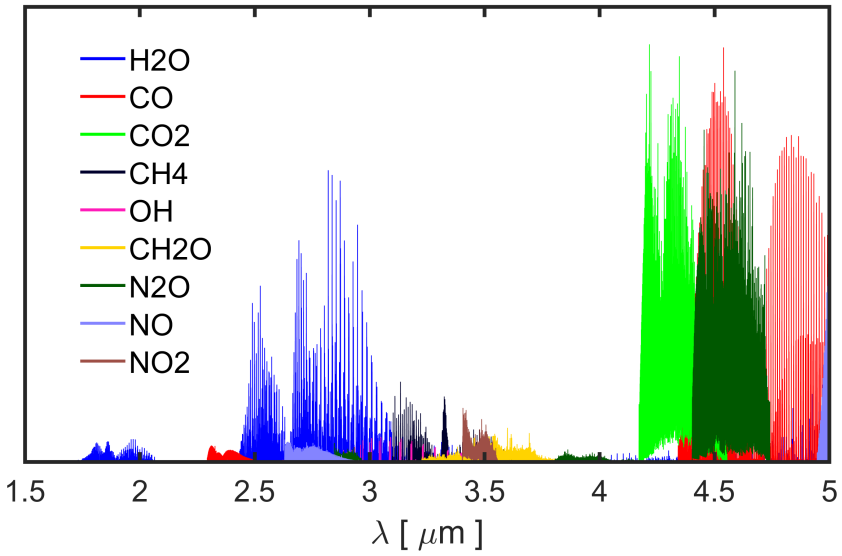

Figure 2.9: Mid-IR spectral signatures of a collection of species found in combustion environments.

tral bands combined with the high concentrations expected in combustion flows make them good targets for a range of measurements including emission and absorption imaging. O_2 and H_2 are not particularly active in the mid-IR regime, however hydrocarbon fuel species exhibit strong lines related to C–H stretch bands between $3.3\,\mu\mathrm{m}$ to $3.4\,\mu\mathrm{m}$ that could be targeted to measure the distribution of reactant species. CO is an important species in combustion that, depending on the circumstances, can act as either a reactant, an intermediate, or a pollutant emissions species in the combustion products. CO exhibits very strong bands at wavelengths between $4.4\,\mu\mathrm{m}$ to $5\,\mu\mathrm{m}$, however detection at these wavelengths would be susceptible to cross-talk from CO_2 due to the broader response of UCI at longer wavelengths that is demonstrated below in Figure 2.11(b). For this reason, the weaker, but more spectrally isolated bands of CO near $2.3\,\mu\mathrm{m}$ were targeted in this work. Spectral signatures of other minor and pollutant species are found throughout the mid-IR spectrum, however they were not pursued in this work because the sensitive laser-based measurements required to detect them were not conducive to imaging, which is the focus of the scope of this study.

For the design of the system used in this work, the poling periods in the ppLN crystal were chosen to respond to vibrational bands of H_2O, CO, CO_2, and hydrocarbon fuel species between $1.9\,\mu\mathrm{m}$ to $4.5\,\mu\mathrm{m}$. Table 2.2 provides a list of the chosen poling periods, the phase-matched IR and upconverted wavelengths at a particular crystal temperature, and the corresponding target species. To leverage the temperature tuning capabilities of a system, it is advisable to set the poling period to satisfy QPM for a wavelength in the middle

of the targeted band at a temperature in the middle of the oven's temperature range (in this work $21\,^{\circ}\mathrm{C}$ to $200\,^{\circ}\mathrm{C}$) so that temperature tuning can be used to span the range of desired mid-IR wavelengths. This was done for all but one of the poling periods in Table 2.2 and is reflected by the $100\,^{\circ}\mathrm{C}$ design temperature. This was not done for the $23.4\,\mu\mathrm{m}$ poling period for two reasons. First, the finite FoV caused by the spatial-spectral coupling effect shown in Figure 2.6 limited the temperature tuning capabilities of this poling period. Second, this poling period was designed to operate at room temperature for passive CO_2 thermal imaging in the RDC to reduce the complexity of integration and operation of the UCI system for those measurements.

Poling period, Λ_P [μm]	T_{crystal} [$^{\circ}$C]	λ_1 [μm]	λ_3 [nm]	Target species
14.5	100	1.87	680	H_2O
17.85	100	2.32	730	CO
19.4	100	2.6	750	H_2O
22.45	100	3.4	820	hydrocarbon fuels
23.4	21	4.2	860	CO_2

Table 2.2: Parameters of ppLN crystal used for UCI experiments in this project assuming $1064\,\mathrm{nm}$ pump excitation. The dimensions of the crystal are $10\,\mathrm{mm} \times 10\,\mathrm{mm} \times 1\,\mathrm{mm}$ with five side-by-side poled gratings that are each $1\,\mathrm{mm}$ in width.

The choice of nonlinear crystal length used in a UCI system is an important one because the parameter L plays a key role in both the phase-matching efficiency and the temporal efficiency of upconversion. Examination of Eqs. (2.16) and (2.17) shows how these effects can be interpreted. For phase-matching, if small dispersion effects are neglected then the spectral bandwidth of UCI will be proportional to L^{-1}. For temporal efficiency, the pump intensity or pulse energy required to achieve a desired upconversion efficiency will be proportional to L^{-2}. In design, these two considerations may need to be balanced or they might push in the same direction. For mid-IR spectroscopy applications, a narrow spectral response is likely desired and such designs will be better served by long crystal lengths which also provide lower pump source power requirements. The system in this work was intended to explore a range of applications, but passive thermal imaging was a major area of focus. In this case, a somewhat broad spectral response was needed to provide adequate signal but exceeding the capabilities of available pump lasers was to be avoided. The chosen design used $L = 10\,\mathrm{mm}$ to strike a balance between the need for sufficient spectral acceptance, particularly in the CO_2 bands near $4.2\,\mu\mathrm{m}$, and the goal to keep required pump

pulse energies below $10\,\mathrm{mJ}$.

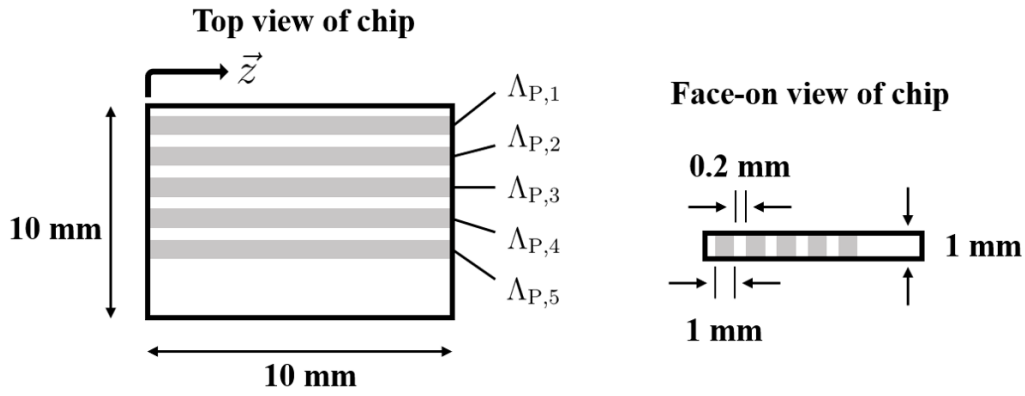

Figure 2.10: A schematic of the size and layout of the ppLN crystal chip used in this work. Dark gray regions indicate periodically poled regions (gratings) in the nonlinear material.

The custom ppLN crystal chip (Covesion Ltd.) had a length along the direction of light propagation of $10\,\mathrm{mm}$, a width of $10\,\mathrm{mm}$, and a chip thickness of $1\,\mathrm{mm}$. Figure 2.10 depicts the size and layout of the ppLN crystal used in this work. Because the pump beam profile is assumed to be symmetrical, the $1\,\mathrm{mm}$ thickness of the crystal chip sets the width of each poling period domain at $1\,\mathrm{mm}$, and so all five different poling periods could be located adjacent to each other along the $10\,\mathrm{mm}$ width of the crystal chip. The adjacent poling periods are separated by $200\,\mu\mathrm{m}$ wide unpoled regions within the chip.

The spectral response of the system design presented in table 2.2 can be modeled by considering the QPM criterion. As was previously described and illustrated in Figure 2.6, the QPM wavelengths vary as a function of position within the image field, and so we will restrict our analysis to the response of the system at the center of the field of view ($\theta_1 = 0°$) for clarity. Figure 2.11(a) gives the QPM wavelength (the wavelength of peak response) as a function of crystal temperature for each of the five poling periods of the ppLN chip in this work. The changes in QPM wavelength demonstrate the temperature tunability of the system, with significant increases in nominal tunability observed for longer poling periods compared to shorter ones. The effective UCI spectral bandwidth also varies depending on poling period and crystal temperature.

The bandwidth was computed by integrating $\eta_{\mathrm{PM}}(\theta_1 = 0°)$ over all IR wavelengths. This variation is plotted in Figure 2.11(b) as a function of QPM wavelength where the primary trend is increasing bandwidth with increasing QPM wavelength. UCI spectral bandwidth at a particular mid-IR wavelength can be critically important to determining what types of measurements may be performed with a system. If the target signal being measured is spectrally narrowband, then the narrow spectral response exhibited by the sys-

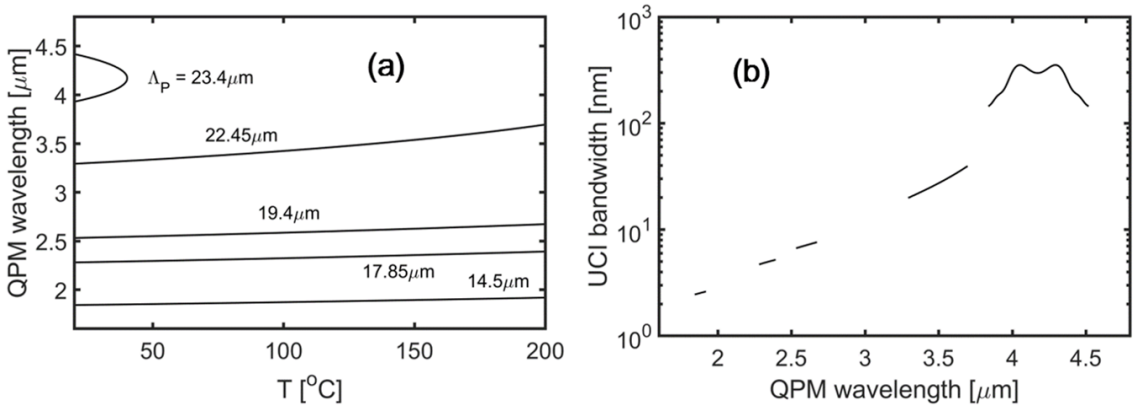

Figure 2.11: (a) The quasi-phase-matched wavelength as a function of crystal temperature for the five poling periods in the system described in table 2.2. (b) The effective spectral bandwidth of the UCI system as a function of QPM wavelength.

tem in Figure 2.11(b) at lower QPM wavelengths can be beneficial by rejecting background light and cross-talk from other signals. However, if the target signal is spectrally broadband compared to the spectral response of the UCI, then low spectral bandwidth will limit the strength of the signal that is collected. An example of this is shown in the comparison between passive thermal imaging of H_2O and CO_2 in section 4.3 that ultimately determined the species that could be accessed in the measurements in Chapter V. In that case, the low spectral bandwidth of the UCI system for QPM wavelengths near $2.55\,\mu\mathrm{m}$ precluded the use of UCI for single-shot measurements of H_2O emissions, instead measurements were focused on CO_2 emissions that can be detected with the broader UCI spectral response near $4.2\,\mu\mathrm{m}$.

2.5.3 Choosing optics and pump source

The focal lengths of the objective and detector lenses were chosen to balance concerns related to angular collection efficiency, field of view, and resolution. The selected focal lengths were $100\,\mathrm{mm}$ for the objective lens and $150\,\mathrm{mm}$ for the detector lens. According to Eq. (2.33) this produces a point source Gaussian spot size of $120\,\mu\mathrm{m}$ in the image plane and $400\,\mu\mathrm{m}$ projected into the object plane at an IR wavelength of $4.2\,\mu\mathrm{m}$. This satisfies the design objectives for this work to resolve millimeter-scale structures within combustion flow fields.

As discussed above in section 2.3.2, the temporal characteristics of the pump pulse determine the temporal characteristics of upconversion efficiency. Upconversion, and therefore exposure in a UCI measurement, does not occur while the pump beam is "turned off". In this way, the pump pulse acts like a time-gate for UCI measurements. This makes it

important to either choose a pump source with the desired pulse shape characteristics or one that can be tuned to achieve the desired temporal performance. This makes specially-designed pulse-shaping lasers, such as the Amplitude Agilite Nd:YAG laser [83], promising options for this application. Those systems can generate approximately top-hat temporal pulse profiles with widths of $50\,\mathrm{ns}$ to $50\,\mu\mathrm{s}$, and therefore would perform like a binary camera shutter for UCI measurement with a fast time response. The approach taken in this work was to use standard pulsed laser systems and de-tune the Q-switch delay to generate Gaussian temporal pulses of the desired width. A description of this approach is provided in section 3.3.2.

2.6 Simulating UCI of a spatially-uniform spectral source

The SFG efficiency models described in the previous sections of this chapter can be used to predict the response of the UCI system to different mid-IR illumination fields in the object plane. In general, this can be applied to predict the UCI signal that results from an arbitrary illumination field that varies in both spatial and spectral dimensions. How these variations manifest in the resulting image depends on the properties of the system that determine its characteristic spatial-spectral coupling (as visualized by the mid-IR tuning curves of the type shown in Figure 2.6). Though it is possible to perform these types of simulations, they are computationally expensive because unique spectral responses must be computed at each point in the two-dimensional object plane for an appropriate spectral bandwidth.

A specific case that is both more computationally tractable and relevant to several aspects of this work is that of a spatially-uniform spectral emitter. This is a mid-IR illumination field that exhibits the same spectral intensity distribution at every location in the object plane. This will produce variation in the signal intensity detected by the UCI system in the image plane due to spatial-spectral coupling effects that cause different spectral responses depending on the location within the FoV. This type of signal is relevant because it is a reasonable representation of several illumination sources experimentally examined in this work including uniform blackbody sources, thermal emissions from flat flame combustors, and mid-IR transmission through absorption cells. It is also useful for designing and interpreting measurements as it can predict the response of the system at each point in the FoV for spectral illuminations that might be representative of an experiment. Simulating these types of responses is computationally efficient because the only a single illumination spectrum needs to be generated and the spatial variation in the response only needs to be considered in a single direction (radial distance from the center of the FoV).

Two effects have been found to substantially change the spectral signal detected by the

UCI system compared to the initial emitted mid-IR spectrum. These are mid-IR spectral absorption due to atmospheric gases between the source and the nonlinear crystal in the UCI system and the wavelength-dependent detection efficiency of the visible/near-IR camera sensor. The absorption effects can be quantified by a spectral absorption coefficient computed for the relevant atmospheric conditions, $\alpha_{\text{atm}}(\lambda_1)$. This was typically computed in this work using spectral models based on the HITRAN database [4]. The wavelength dependence of a camera's response is typically provided by the camera manufacturer in terms of QE as a function of detected (in this case upconverted) wavelength, $\eta_{\text{Cam}}(\lambda_3)$. Because the spectral response of the UCI system is independent of the intensity of the mid-IR light, this wavelength dependence can be treated as an equivalent QE in at the mid-IR wavelengths by using the photonic conservation of energy condition ($\lambda_1^{-1} = \lambda_3^{-1} - \lambda_2^{-1}$) to map detected wavelengths to mid-IR wavelengths: $\lambda_3 \mapsto \lambda_1$ such that $\eta_{\text{Cam}}(\lambda_3) \mapsto \eta'_{\text{Cam}}(\lambda_1)$.

To account for these effects and implement the model, one must first generate a target mid-IR spectral signal, $L_{q,1}(\lambda_1)$, that is representative of the process being observed. This is treated in this analysis in terms of spectral photon flux, but can be related to light intensity as $I_1(\lambda_1) = (hc/\lambda_1)L_{q,1}(\lambda_1)$. In the case of a blackbody emitter this would be determined the Planck curve, and for a hot, thermally emitting gas volume it would be governed by Kirchoff's law of thermal radiation. Once $S_1(\lambda_1)$ is determined, it can be used to compute an equivalent IR spectrum available for UCI detection, $L_{q,\text{IR}}(\lambda_1)$, that accounts for the effects of atmospheric absorption and wavelength-dependent camera response by the relationship:

$$L_{q,\text{IR}}(\lambda_1) = \eta'_{\text{Cam}}(\lambda_1)e^{-\alpha_{\text{atm}}(\lambda_1)l}L_{q,1}(\lambda_1) \tag{2.37}$$

While there is no actual variation of the illumination field within the object plane in this case, there could significant variation in the image plane due to the spatial-spectral coupling effect. For this reason, it is more relevant to consider the system response in image plane coordinates, as measured by r_3, rather than object plane coordinates, as measured by r_1. Additionally, this makes comparisons between experimental observations and model predictions more straightforward without the need to transform the coordinates of the sensor array into the object plane. The noncollinear phase-matching relationship that governs a UCI system's spatial-spectral response, η_{PM}, is given by Eq. (2.21) as a function of λ_1 and θ_1. By combining Eqs. (2.20) and (2.23), the mid-IR propagation angle, θ_1, can be expressed as a function of r_3 and λ_1:

$$\theta_1(r_3, \lambda_1) = \sin^{-1}\left\{\frac{\lambda_1}{n_1\lambda_3}\sin\left[\tan^{-1}\left(\frac{r_3}{f_3}\right)\right]\right\} \tag{2.38}$$

This relationship allows the UCI spectral response at each point in the image plane to be

directly computed as $\eta_{\text{PM}}(r_3, \lambda_1)$. The measured signal intensity at that point, $S_3(r_3)$, can then be found directly by integrating the product of the available IR spectrum, $L_{q,\text{IR}}(\lambda_1)$, with the phase-matching efficiency, $\eta_{\text{PM}}(r_3, \lambda_1)$, over all IR wavelength (or at least the relevant IR band):

$$S_3(r_3) = \int_0^\infty \eta_{\text{PM}}(r_3, \lambda_1) L_{q,\text{IR}}(\lambda_1) \mathrm{d}\lambda_1 \tag{2.39}$$

A simple algorithm that can be implemented to perform this type of simulation is described by the pseudo-code below:

1. Generate an array of mid-IR wavelength values, $\{\lambda_{1,g}\}$, that defines the spectral bandwidth and resolution of the simulation

2. Generate an appropriate illumination spectrum, $L_{q,1}(\lambda_{1,g})$, depending on the characteristics of the emitter (*e.g.* blackbody, thermal radiation from gas species, etc.)

3. Compute the mid-IR spectral absorbance, $\alpha_{\text{atm}}(\lambda_{1,g})$, based on the atmospheric conditions between the source and the nonlinear crystal and the transformed spectral response of the camera, $\eta'_{\text{Cam}}(\lambda_{1,g})$

4. Compute the effective IR spectrum available for UCI detection, $S_{\text{IR}}(\lambda_{1,g})$

5. Generate an array of image plane radial locations, $\{r_{3,m}\}$, at which to compute the UCI system response

6. Loop through for each $r_{3,m}$ value and:

   (a) Compute the set of mid-IR propagation angles corresponding to the particular image plane location at each wavelength, $\theta_{1,m,g}(r_{3,m}, \lambda_{1,g})$

   (b) Compute the integral over all mid-IR wavelengths of the product of the UCI spectral efficiency and the available IR spectrum, $\eta_{\text{PM}}(r_3, \lambda_{1,g}) L_{q,\text{IR}}(\lambda_{1,g})$, to find the value of $S_3(r_{3,m})$

Figure 2.12 shows two examples of modeled UCI responses computed using the previously described model for uniform spectral emitters and the system design parameters described in section 2.5. Figure 2.12(a) shows the image plane distribution of UCI signal strength in response to hot ($2080\,\text{K}$) H_2O vapor in the combustion products of a methane-air flat flame detected at wavelengths near $2.55\,\mu\text{m}$ with a $19.36\,\mu\text{m}$ poling period and a crystal temperature of $21\,^\circ\text{C}$. Figure 2.12(b) shows the same type of simulation for a uniform blackbody illumination field (at a blackbody temperature of $950\,^\circ\text{C}$) detected at wavelengths near $4.2\,\mu\text{m}$ with a $23.415\,\mu\text{m}$ poling period and a crystal temperature of $21\,^\circ\text{C}$.

Both of these examples were chosen because of their relevance to experiments performed as part of the system characterization in Chapter IV (the measurement results in that chapter are also the reason for the subtle difference between the assumed poling periods and those specified in the system design in section 2.5).

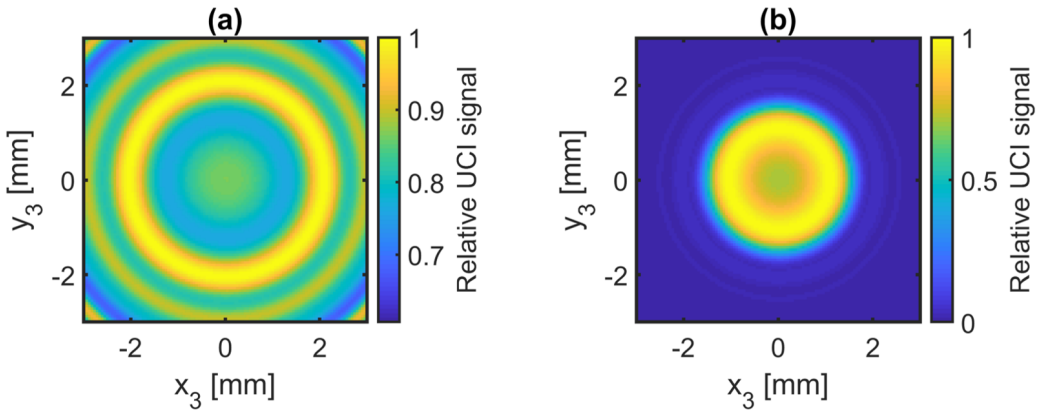

Figure 2.12: Examples of UCI image plane signal distributions calculated for the design parameters given in section 2.5. UCI responses are calculated for (a) hot (2080 K) H_2O vapor in the combustion products of a methane-air flat flame detected at wavelengths near 2.55 µm with a 19.36 µm poling period and a crystal temperature of 21 °C and (b) a uniform 950 °C blackbody emitter detected at wavelengths near 4.2 µm with a 23.415 µm poling period and a crystal temperature of 21 °C.

Note that even though the illumination field is assumed to be uniform across the entire object plane, the examples in Figure 2.12 show significant spatial structure in the detected signal strength distribution in the image plane. This demonstrates the influence of spatial-spectral coupling on UCI. The bright and dark circular bands seen in Figure 2.12(a) are a result of strong H_2O spectral lines at different mid-IR wavelengths. The limited illumination of the FoV in Figure 2.12(b) is a result of the "donut" type UCI response curve for this poling period shown in the tuning curve example in Figure 2.6)(b).

CHAPTER III

UCI System Experimental Setup

This chapter describes the practical implementation of the UCI system used for measurements in this work. This includes the optical arrangement used to realize the design described in the previous chapter. Several components of the UCI system are addressed in detail. This includes the silicon-based CCD camera that was used to record UCI images, with particular attention to observed spectral fringing phenomena. The temporal resolution that was critical for measurements of fast unsteady combustion processes was achieved through the pulsed laser Q-switch tuning described in this chapter. A discussion is provided of the integration of the UCI system with the RDC for measurements described in Chapter V. This includes both physical integration of the UCI optical arrangement with the optical access in the RDC and coordination of the UCI data acquisition with other sensor systems on the combustor that provide the context required for meaningful interpretation of the results.

3.1 General configuration of the UCI system

The optical arrangement used for the measurements in this work is illustrated in the conceptual schematic in Fig. 3.1. Most of the components are used for spectral filtering to control what bands of wavelengths can propagate into various parts of the system. To eliminate spurious signal contributions from visible and near-IR light, a germanium window that is AR-coated for $2\,\mu\mathrm{m}$ to $5\,\mu\mathrm{m}$ wavelengths was placed in front of the objective lens. A critical component in the system was the IR beamcombiner (see item D in Figure 3.1) that routed the pump beam into the optical arrangement. This part was a custom-fabricated optic (manufactured by Lambda Research Optics from a $6\,\mathrm{mm}$ thick CaF_2 substrate) designed to meet the requirements that it be highly transparent to mid-IR wavelengths, highly reflective to the near-IR pump wavelength, and have a high Laser-Induced Damage Threshold (LIDT) to tolerate the narrow waist pulsed laser pump beams.

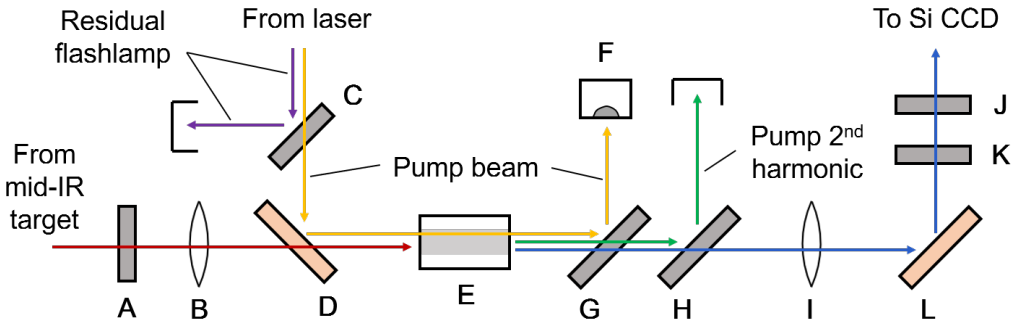

Figure 3.1: Conceptual schematic of the UCI optical arrangement. Labeled items include: (A) germanium window, (B) CaF_2 100 mm focal length lens, (C) 950 nm long-pass filter, (D) custom near-IR/mid-IR beamcombiner, (E) ppLN crystal chip, (F) laser power meter, (G) 950 nm short-pass filter, (H) 650 nm long-pass filter, (I) N-BK7 150 mm focal length lens, (J) 945 nm short-pass filter, (K) 593 nm long-pass filter, and (L) reflective filter (reflect $\lambda < 900$ nm).

Because the Si CCD was sensitive to the fundamental wavelength of the pump beam and highly sensitive to its second harmonic, it was important to incorporate spectral filters into the optical arrangement to suppress these wavelengths. These were implemented as two reflective filters before the detector lens to isolate the beams for energy measurements using a laser power meter (see G and H in Fig. 3.1) and two more filters immediately in front of the detector to eliminate any residual laser light (see items J and K in Fig. 3.1). Despite a lack of phase-matching for the process, second harmonic generation of the pump beam within the ppLN chip was observed. The energy in the second harmonic beam was not significant enough to be measurable ($<60\,\mu$J), however the second harmonic strength was greater from the periodically poled domains in the crystal than in the un-poled regions and could be used to roughly align the system at low pump energies.

It was observed that for some orientations of the pump routing laser mirrors the residual flash lamp light could propagate into the UCI optical system. The light from the xenon flash lamp near 820 nm would be readily transmitted by the spectral filters in the UCI optical arrangement and is within the region of strong spectral response for the Si-based camera sensor. This has also been observed in some previously reported UCD experiments [41]. A 950 nm long-pass filter was placed in the pump beam path upstream of the custom beamcombiner to block the spurious flash lamp light (see item C). This eliminated all background signals when the pump laser was on with no mid-IR illumination of the field of view. Previous work by other research groups had identified a background signal due to Upconverted Spontaneous Parametric DownConversion (USPDC) that contributed noise to their high-sensitivity measurements [35, 6]. USPDC signals were not observed in any of

the measurements in this work regardless of pump energy level and pulse duration.

Due to the high sensitivity of the camera used for UCI measurements, stray light was a major concern and could cause large spurious background signals. To mitigate the amount of ambient light that could make it to the camera sensor, an optical enclosure was used to house the detector lens and all downstream components (items I, L, J, and K in Figure 3.1), including the CCD sensor. This enclosed portion of the system is shown in the close-up photograph in Figure 3.2. The enclosure included a 1" diameter lens tube that held the detector lens in alignment with the pump beam and the upconverted image light. A 1/2" aperture adjustable iris was installed at the front of the lens tube that could be close to block all light from entering the enclosure while testing the dark response of the camera but did not block any upconverted image light from entering the enclosure when fully opened. The enclosure cube (Thorlabs C4W) housed the $50\,\mathrm{mm}$ diameter long-pass filter (see item L) that reflected the upconverted signal at a $90°$ angle toward the CCD sensor while transmitting most of the residual $1064\,\mathrm{nm}$ pump energy.

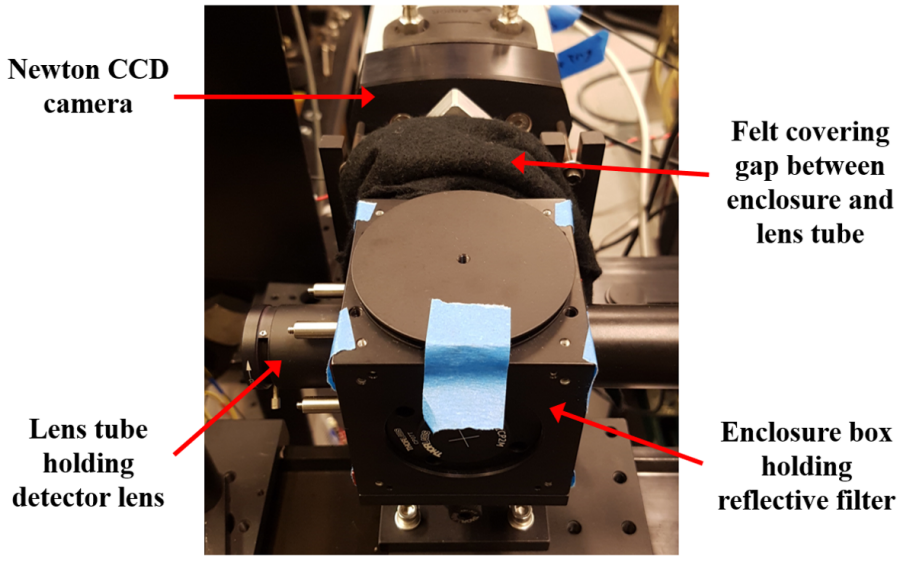

Figure 3.2: A close-up of the enclosed part of the UCI system.

Despite the double layer of pump beam rejection filters (items G and L) there remained a detectable level pump beam energy that could contaminate the UCI measurements. To eliminate this, a second pair of spectral filters was installed in a lens tube that was secured to the face of the CCD camera. These included a $593\,\mathrm{nm}$ long-pass filter to suppress residual pump second harmonic beams (see item K) and a $945\,\mathrm{nm}$ short-pass filter (see item J) to suppress residual $1064\,\mathrm{nm}$ radiation. This filter combination succeeded in eliminating any image contamination related to the pump beam. The length of the lens tube attached to the

camera face was chosen to come within $1\,\mathrm{cm}$ of the enclosure cube outlet port when the CCD sensor was placed at the focal plane of the $150\,\mathrm{mm}$ focal length objective lens. A quadruple layer of black felt was wrapped around the gap between the lens tube and the enclosure cube to block ambient light from entering the enclosed space through the gap.

When the system was operated with the fluorescent lighting in the labs turned on, there was a very strong background signal that overwhelmed any pulsed UCI signals. For this reason, the room lighting was turned off in the labs when running experiments to mitigate the contamination. This was effective in reducing the ambient light detected to very low levels (some remained due to the screen of the camera control PC and other dim instrumentation lights in the room), on the order of a few counts, that could be eliminated in post-processing with minimal dark noise contributions. An ideal system design would enclose the entire optical arrangement with only two inlet ports: one inlet for the mid-IR image and another inlet for the pump laser beam. With this configuration, the germanium window at the mid-IR inlet would admit only long wavelengths that are associated with the signal and any stray mid-IR light from outside of the FoV will not be upconverted and therefore will not be detected by the CCD. The pump beam inlet could be covered with a long-pass filter to admit the near-IR pump beam which, along with other near-IR wavelengths, would be blocked from contaminating the image by the short-pass filter in the camera's lens tube (item J).

An enclosed system with this design could be operated with the room lights on without experiencing any stray light contamination. Dam *et al.* [42] demonstrated a fully enclosed UCI configuration for their measurements of thermal radiation from candle flames. Because of the intra-cavity pump design of that system, it effectively had only one inlet port to collect the mid-IR image light (the enclosure contained two additional ports to input the laser diode used for laser pumping and to attach a modular CCD camera, both attached with light-tight seals). A fully enclosed configuration was not used in this work for several reasons. First, a lack of a priori knowledge about the performance of temporally-resolved UCI systems led to uncertainties during the design of the system. These led to adjustments during testing, such as the inclusion of additional spectral filters and changes to the dimensions of some mounting components, that might not have been possible to accommodate in a fully integrated, enclosed design. Second, the system needed to be able to interface with the optical access of the RDC facility that was subject to change as that experimental facility evolved. Narrow clearances and additional structural components that were added to the RDC were negotiated with changes to the open configuration of this system that could not have been done with a fully enclosed system. Finally, the open configuration aided in aligning the system before measurements and quickly adjusting its alignment during

testing. An enclosed system must have a sophisticated design for checking and adjusting optical alignments to ensure operability in all conditions.

The description given above in this section covers aspects of the UCI system configuration that are common to all of the measurements discussed in this work. To help ensure alignment of the optics train and allow for quick adjustments along the optical axis, the components were mounted on sliding platforms attached to a $1\,\mathrm{m}$ long optical rail. The camera and oven controller could either be mounted directly to the optical table or onto an adjacent optical rail. Characterization measurements used the UCI system in a "benchtop" configuration where the optical rails were mounted to vertical translation platforms to adjust the height of the imaging FoV. Installation of the system for RDC measurements provided additional challenges due to the location of the combustor relative to available mounting locations and potential clearance issues related to the RDC infrastructure. The unique aspects of the integration of the UCI system with the RDC are described in section 3.4.2.

3.2 UCI system components

Silicon-based visible/near-IR CCD camera

The camera used in this study was a back-illuminated silicon CCD (Andor Newton 940-BU2). The back-illuminated design provided high QE across a wide range of wavelengths. However, back-illuminated silicon sensors have been observed to exhibit a phenomenon known as spectral fringing where alternating bright and dark bands of response are superimposed on recorded images when detecting narrowband light at wavelengths above about $600\,\mathrm{nm}$ [84]. This is due to etalon-like behavior within the depletion layer of the sensor that becomes non-negligible for longer wavelengths. Because UCI with a $1064\,\mathrm{nm}$ pump beam detects light in the $2\,\mu\mathrm{m}$ to $5\,\mu\mathrm{m}$ range at wavelengths between $700\,\mathrm{nm}$ to $880\,\mathrm{nm}$, this system and similar designs will experience this spectral fringing effect.

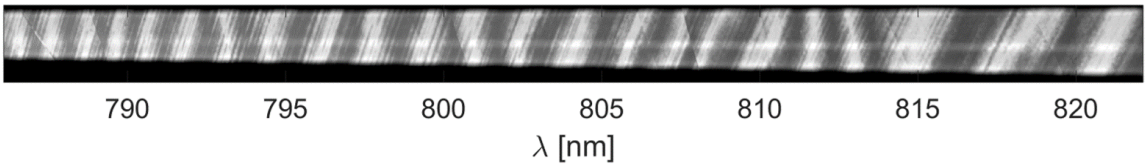

Figure 3.3: Image of spectrometer measurement of a $900\,^{\circ}\mathrm{C}$ blackbody with the silicon CCD camera.

To test that spectral fringing is an artifact caused by the properties of the camera and not

a direct result of the UCI technique, the camera was installed in a Czerny-Turner imaging spectrometer to observe narrowband near-IR radiation. The spectrometer was a McPherson 216.5 $0.5\,\mathrm{m}$ focal length monochromator that was retrofitted to accommodate imaging detectors. The retrofit closely followed the procedure described by Airey [85] and its response was characterized in previous UV spectroscopy experiments [86]. A fiber optic bundle was coupled to the entrance slit of the spectrometer with the collection end of the bundle placed at the exit plane of a blackbody source operated at $900\,^{\circ}\mathrm{C}$. The spectrometer used a $1200\,\mathrm{lines/mm}$ grating and was tuned to detect light near $800\,\mathrm{nm}$. Figure 3.3 shows an image from that setup, showing the distinct, high-contrast fringing pattern in response to the narrowband near-IR illumination. This fringing pattern would not appear in broadband imaging of a blackbody source because patterns generated by significantly different wavelengths would add together and effectively cancel each other out. It is the narrowband illumination of the spectrometer that caused the high visibility of the pattern.

A similar pattern can be seen in the example UCI image shown in Figure 3.4. Here a uniform blackbody emitter at $800\,^{\circ}\mathrm{C}$ was detected by UCI at mid-IR wavelengths near $2.55\,\mu\mathrm{m}$ using the $19.4\,\mu\mathrm{m}$ poling period at a $21\,^{\circ}\mathrm{C}$ crystal temperature to upconvert the signal to wavelengths near $750\,\mathrm{nm}$. The fringing pattern that resulted from the narrowband ($0.6\,\mathrm{nm}$ bandwidth) near-IR light detection can be seen with significant contrast and a non-uniform fringe spacing and orientation. These fringing patterns were observed for all five poling periods, however they were much less pronounced when using the $23.4\,\mu\mathrm{m}$ poling period to detect mid-IR light near $4.2\,\mu\mathrm{m}$ because of the significantly larger near-IR spectral bandwidth ($8.3\,\mathrm{nm}$ at wavelengths near $850\,\mathrm{nm}$).

Because of its dependence on the nanoscale structure of the CCD sensor, the spectral fringing pattern cannot be predicted a priori. However, if the temperature of the sensor is precisely maintained, something that is achievable with the camera system's integrated TEC, then the fringe pattern will be consistent throughout the data collection. If a flat field signal can be taken for the same system configuration and same signal spectral content, then the spectral fringing pattern can be corrected in post-processing. The process used for correcting these and other artifacts in passive thermal imaging is described in Chapter V.

The Newton camera sensor has a pixel array format of 512×2048 with an individual pixel pitch of $13.5\,\mu\mathrm{m}$. For the UCI measurements described in this work, the camera was operated with 4×4 pixel binning. This binning was chosen for multiple reasons. First, the readout speed of the camera was unable to produce a frame rate to match the $10\,\mathrm{Hz}$ repetition rate of the pump laser when operated with a full vertical FoV and individual pixel detection. A minimum of 4 pixel binning was required to achieve a $10\,\mathrm{fps}$ frame rate with the Newton camera. Another motivation for using pixel binning was decreased

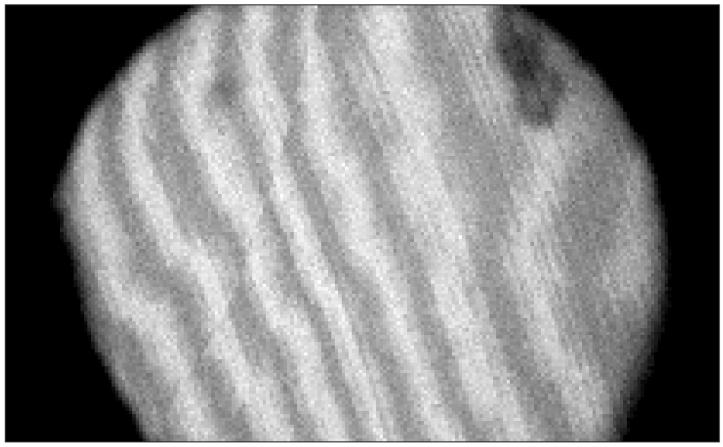

Figure 3.4: UCI measurement of a $800\,^{\circ}\mathrm{C}$ blackbody source with the silicon CCD camera.

noise in low-light measurements using the binned super-pixel mode. This was particularly advantageous in the passive imaging measurements of thermal radiation from inside the RDC that are presented in Chapter V. The 4×4 binned super-pixels had an effective pitch of $54\,\mu\mathrm{m}$ on the sensor, which was sufficient to sample the $120\,\mu\mathrm{m}$ wide PSF in the image plane of the UCI system that was predicted in section 2.5.3 through the application of Eq. (2.33). In this way, the binning did not compromise the spatial resolution achieved with the system.

Corrections were required to account for dark current signals in images captured with the camera and set its dark field signal strength to zero. For 4×4 binned operation of the camera with typical settings ($10\,\mathrm{ms}$ exposure time, $3\,\mathrm{MHz}$ readout rate, $\times4$ pre-amplifier gain) the dark signal ranged from between 2360 to 2420 counts. Additionally, faintly visible wavelength light pollution from within the room due to control computer screens, indicator lights, and combustion events can leak into the enclosure and create a small background signal that was usually observed to be uniform in the horizontal direction but sometimes have slight variations in the vertical direction. Both spurious signals were corrected for using the pixels on the left and right side of the wide-format sensor that fell outside of the UCI FoV. First, an area of interest was identified that contained the entire UCI FoV. Next, reference regions of the same vertical extent were identified to the left and right sides outside of the area of interest, each between 50 to 100 pixels wide. The average value of

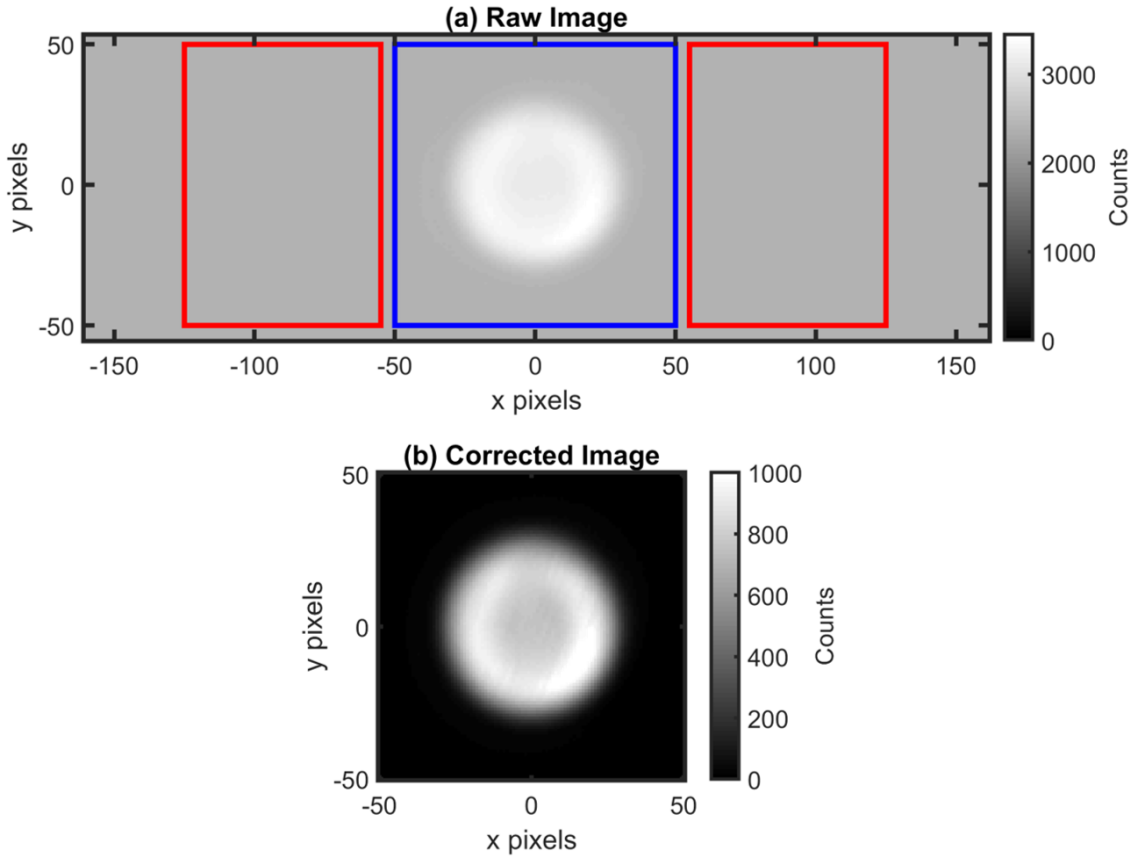

Figure 3.5: An example of the dark signal and background correction performed on UCI measurements showing (a) a raw image and (b) the corresponding corrected image. The blue rectangle in (a) represented the area of interest and the red rectangles represent the regions used for row-by-row dark signal subtraction.

pixels in each row across both reference regions was computed and subtracted from the corresponding rows in the area of interest.

An example of this correction process is shown in Figure 3.5 for a UCI image of a uniform blackbody source at mid-IR wavelengths near $4.2\,\mu\mathrm{m}$. The background signal primarily due to dark current was approximately 2400 counts and obscured the true contrast in the UCI signal that had an amplitude of approximately 1000 counts. The blue region in Figure 3.5(a) indicates the area of interest and the two red rectangles indicate the selected reference regions that are far outside of the UCI FoV. The previously described row-by-row subtraction correction was applied to generate the processed image shown in Figure 3.5(b).

Crystal oven

The ppLN crystals come packaged in small copper holders with a $1\,\mathrm{mm}$ thick layer of ITO glass covering the top of each chip. Two thin retaining straps press down on the top of the ITO glass to hold it and the ppLN chip in place. A mounting component is then needed to secure the location of the chip holder in the optical arrangement. For most UCI systems, including this one, the mounting component is a crystal "oven" capable of monitoring and controlling the temperature of the crystal. A controlled oven enables temperature tuning of the system response through the effects of crystal temperature on the phase-matching condition, as described in Chapter II.

The oven used in this work was machined from a 2" long piece of 3/4" $\times$ 3/4" C110 copper bar stock. A recess was machined in the top surface where the chip was seated. A small copper retaining bar held in place by two screws was placed on top of the installed crystal chip to hold it in place. The oven has a second retaining bar on its back surface to hold a thermocouple (K type) onto the surface of the oven to track the temperature of the system. A 1/4" hole was drilled through the long axis of the oven directly beneath the crystal recess. This hole accommodated a $40\,\mathrm{W}$ cartridge-style resistance heater that could be inserted to elevate the temperature of the system and the crystal. When performing tests at elevated crystal temperatures, a PID controller (Omega model CN7633) monitored the thermocouple signal and modulated the heater output to achieve the desired temperature. Once thermal steady-state was reached, the temperature read by the thermocouple was assumed to be the crystal temperature. Tests of the oven found that it was capable of reaching temperatures above $250\,^{\circ}\mathrm{C}$.

Pump beam configuration

In all of the experiments in this work, the pump beams were generated by Spectra-Physics Quanta-Ray Lab series lasers (a Lab 150 and a Lab 250). These generated high-energy, polarized $1064\,\mathrm{nm}$ wavelength pulses at a $10\,\mathrm{Hz}$ repetition rate. The lasers were operated at their maximum flash lamp power settings to ensure the stability of the output properties. The energy in each beam was controlled by a combination of a Half-Wave Plate (HWP) and a Polarizing BeamSplitter (PBS). The HWP allowed for an arbitrary assignment of the direction of the pump beam polarization and then the PBS was used to extract the vertically polarized component. The vertically polarized component must be used in the UCI system because the crystal is manufactured so that QPM occurs with vertically polarized light (the extraordinary polarization in the LN crystal). The energy of the pump beam pulses was precisely controlled By rotating the HWP.

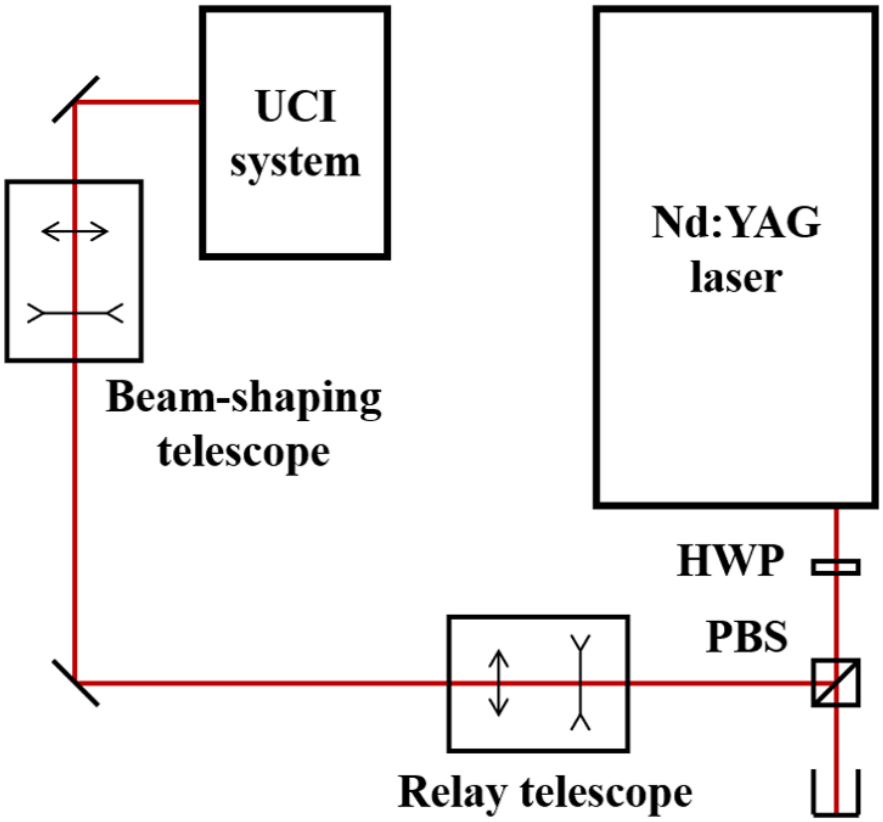

Figure 3.6: Notional schematic of the pump beam routing for UCI measurements.

The vertically polarized pump beam that was extracted by the PBS was then routed to the location of the UCI system. For longer routing paths, such as the one between the laser and the RDC, the divergence of the laser caused a significant spatial broadening of the beam cross-section that exceed the reflective aperture of some of the downstream mirrors. To prevent loss of energy and beam distortion, a relay telescope (+100 mm focal length lens followed by a -30 mm focal length lens to produce a factor of 3.3 reduction in beam size) was placed after the PBS. After the beam propagated to near the UCI, it was necessary to use another telescope (+200 mm focal length lens with a -30 mm lens) to properly fill the 1 mm aperture of the periodically poled gratings. Beam shape optimization was done by removing the crystal oven from the optical arrangement and taking photosensitive paper burns at the plane where the crystal had been located. The separation between the two lenses in the beam shaping telescope was adjusted until the desired beam shape was achieved. The goal of this optimization was to create a beam cross-section that appeared slightly larger than 1 mm in diameter on paper burns to try to energize the entire aperture of the crystal to maximize both signal strength and spatial resolution.

After an acceptable beam shape was attained and aligned with the optical components,

the crystal oven was placed back into the optical arrangement. The lateral and vertical positions of the crystal oven were adjusted until the laser beam passed through the center of the desired periodically poled grating. A notional schematic of the pump beam routing is provided in Figure 3.6. UCI experiments were performed in different labs and on different experimental targets that required slight variations of the actual beam routing. However, all of the arrangements incorporated the key features indicated in Figure 3.6 to control the pump beam pulse energy and the beam shape.

3.3 Pump laser operation modes

As Chapter II shows, the temporal resolution of a pulsed UCI measurement is controlled by the duration of the pump pulses. The Quanta-Ray lasers used in this work could produce pulses in two different operating modes: long-pulse mode and Q-switched mode. These two modes corresponded to different behaviors of the Q-switch that is installed in the laser cavity. The Q-switch in these lasers is a combination of Pockels cell and a linear polarizer that can be used to prevent power circulation in the laser cavity when *closed* and allow it when *open*. Cavity resonance and subsequent radiation emission from the laser can only occur when the Q-switch is open. The Q-switch is timed to open at a particular time relative to the firing of the flash-lamps that pump excited states in the laser gain medium. The two different operating modes handle this timing differently. Long-pulse mode opens the Q-switch the instant that the flash-lamps are fired so that cavity resonance and radiation emission can occur at any time after a population inversion has been established. This results in the emission of a pulse train over a relatively long duration, as described below in section 3.3.1. Q-switched mode delays the opening of the Q-switch until some delay, typically on the order of hundreds of microseconds, after the flash-lamps have fired. Optimal choice of the Q-switch delay can produce very short, high-energy pulses with pulse widths on the order of 10 ns. Variation of the Q-switch delay causes changes in the emitted pulse durations and energies, which are discussed in section 3.3.2.

3.3.1 Long-pulse mode operation of pump laser source

For almost all of the benchtop characterization experiments described in Chapter IV the target source was steady and temporal resolution was not required. For these measurements, the pump laser could be operated in long-pulse mode. The lower laser intensity of long-pulse mode compared to Q-switched mode allowed higher pulse energies to be used with a much lower risk of damage and diminishing efficiency returns, leading to higher

signal strengths. Long-pulse mode operation causes the laser to emit a series of sub-pulses at unpredictable times with unpredictable energies.

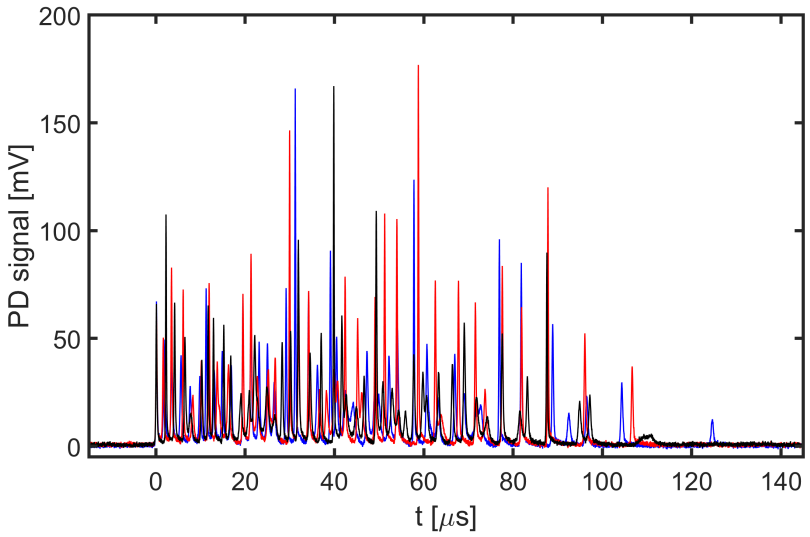

Figure 3.7: Three examples of photodiode measurements of the temporal output of the pump laser operated in long-pulse mode.

Figure 3.7 shows three examples of temporal emission profiles of the Quanta-Ray Lab 250 laser operated in long-pulse mode at $41\,\mathrm{mJ}$ per pulse train measured with a silicon photodiode (Thorlabs DET10A, $1\,\mathrm{ns}$ rise time). The measurements show that each "firing" of the laser emits dozens of sub-pulses over a duration of approximately $120\,\mu\mathrm{s}$. Each sub-pulse is relatively broad with FWHMs of approximately $200\,\mathrm{ns}$. The measurements show that each pulse train is unique, and so the properties of each sub-pulse cannot be predicted. Because any UCI signal produced with a long-pulse mode pump beam will be an aggregate of upconversion occurring during the entire pulse train, long-pulse mode cannot be used for measurements requiring a temporal resolution of better than $120\,\mu\mathrm{s}$. This means that long-pulse mode is not suitable for measurements in the RDC where sub-microsecond resolutions are required.

3.3.2 Q-switch tuning of pump laser source

Q-switched operation of the Quanta-Ray lasers produced pulse durations as short as $10\,\mathrm{ns}$, sufficiently short to freeze detonation wave motion. However, pump pulse durations near $10\,\mathrm{ns}$ produced low signal strengths and unacceptable SNRs because of the shorter effective exposure times, assuming that the pulse energy is limited to avoid damage to the crystal. This necessitated tuning of the pump laser system to achieve optimal pump pulse temporal

shapes that satisfy both the temporal resolution required to freeze detonation wave dynamics and provided sufficiently high signals for single-shot measurements.

The Q-switch delay can be changed to tune the duration of the pump pulse produced by the laser. As the Q-switch delay is moved above or below the optimum delay, the temporal width of the laser pulse increases while the pulse energy decreases. The Q-switch delay was varied by externally triggering both the flash-lamps and Q-switch of the laser using signals generated from a function generator box (SRS DG535). Both trigger signals were generated at $10\,\mathrm{Hz}$ with a variable delay between the flash-lamp trigger and the subsequent Q-switch trigger. Changes in laser output characteristics were tested by reducing the Q-switch delay and monitoring the output temporal pulse-shape with a photodiode and the pulse energy with a laser power meter. The laser continued to operate above the lasing threshold as the Q-switch delay was decreased down to $90\,\mu\mathrm{s}$, but failed to produce consistent output for shorter delays. Figure 3.8 shows examples of the measured pulse shapes for the three shortest Q-switch delay times. All pulse-shapes were well fit by Gaussian functions and so the FWHM of an average of ten pulse shapes at each Q-switch delay was used to quantify pulse duration. Measured trends in the laser output with decreasing Q-switch delay are shown in Figure 3.9(a).

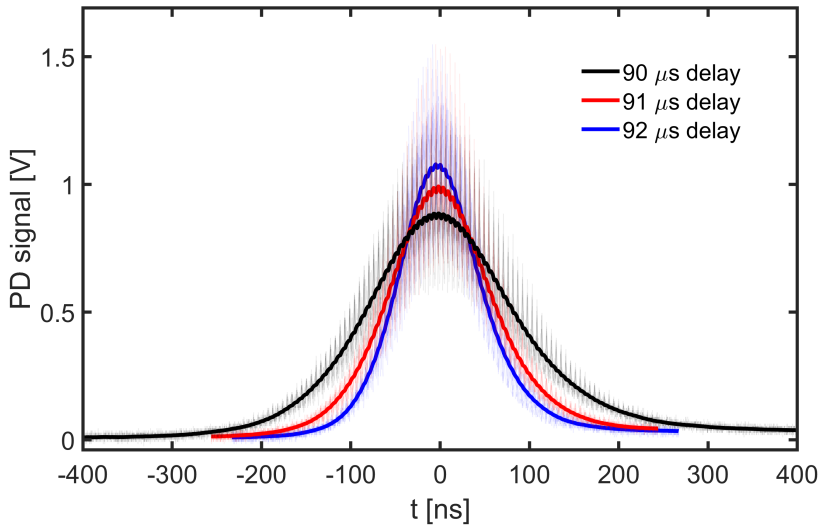

Figure 3.8: Average recorded pulse shapes for the three shortest Q-switch delays superimposed over ten photodiode measurements of each pulse shape.

The solid lines in Figure 3.9(a) show the nonlinear best fit models that were used to predict UCI efficiency at each Q-switch delay. For the sake of computational efficiency, the centerline SFG effective exposure time, found by integrating Eq. (2.16) for the time history of pump intensity at $r_2 = 0$, was used to estimate the UCI response. Figure 3.9(b) shows

the maximum effective exposure time computed for the laser pulse widths and energies at each Q-switch delay. The maximum effective exposure time produced by the system is $240\,\mathrm{ns}$ which was achieved at the minimum feasible Q-switch delay of $90\,\mu\mathrm{s}$. This Q-switch delay was used for most RDC measurements to achieve both high temporal resolution and sufficiently high signal strength. When testing during a period of hot outside ambient conditions during one RDC test set (case D in Chapter V) the lab air conditioning was incapable of keeping the room temperature below $25\,^{\circ}\mathrm{C}$. This appeared to compromise the cooling capabilities of the laser system and it was no longer stable for a Q-switch delay of $90\,\mu\mathrm{s}$. For this case only, the laser was operated at a Q-switch delay of $91\,\mu\mathrm{s}$ so that laser output stability could be maintained despite the elevated ambient temperature conditions.

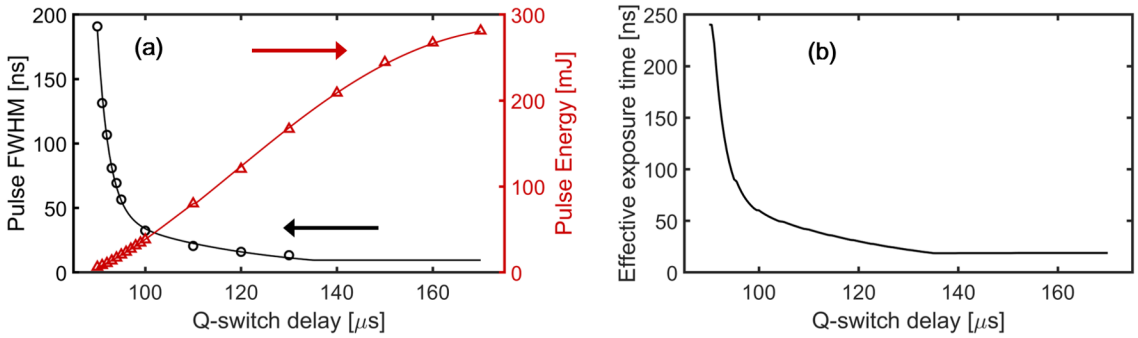

Figure 3.9: (a) Variation in pump laser operating characteristics, pulse width and pulse energy, with changing Q-switch delay. (b) Modeled effective UCI exposure times at the center axis of the system based on the laser pulse parameters at each Q-switch delay.

3.4 Experimental RDC

The experiments in this study were performed in a laboratory-scale RDC that has previously been characterized [48]. The combustor's annular channel has a mean diameter of $146\,\mathrm{mm}$. The modular design of the combustor allowed the axial height of the combustion channel to be varied. All measurements in this work were performed with an axial channel height of $105\,\mathrm{mm}$. The RDC was tested with a non-premixed injection system that had an axial chocked air injection stream along the outer wall. Fuel was injected through discrete circular injection ports in a surface on the inner body that was inclined at $30°$ relative to the air stream [87]. The system has been observed to exhibit both stable and unstable operations under different reactant flow rates and global equivalence ratios. This work focused on stable operating conditions so that cycle averaging could be used to investigate large scale structures in the flow field.

3.4.1 RDC optical access

Optical access into the combustion channel of the RDC for mid-IR was available through two window ports. The first was a $25\,\mathrm{mm}$ diameter sapphire window installed in the outer wall of the combustion channel. The flat window did not match the curvature of the cylindrical outer wall but was mounted so that the center of the window was tangent to the curvature of the channel. The mounting frame used to secure the window reduced the clear aperture of the port to $19\,\mathrm{mm}$. The second port was a smaller $12\,\mathrm{mm}$ diameter installed in the inner wall of the RDC. The center-body of the combustor inside the inner wall had a hollow cavity where optical components or other instruments could be placed with optical access through this window. Mounting components reduced its clear aperture to $9\,\mathrm{mm}$. Sapphire was chosen for both of these windows because of its high spectral transmission from UV wavelengths up to $5\,\mu\mathrm{m}$ in the mid-IR regime with few dips in transmission.

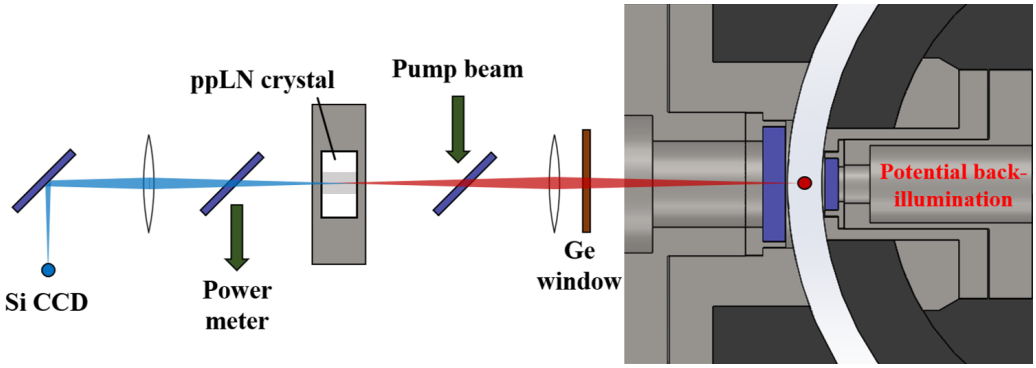

Figure 3.10: A cut-away through the RDC showing available optical access for mid-IR measurements both to the exterior of the combustor and into its center-body.

Figure 3.10 shows a cut-away through the combustor in the plane of the UCI imaging system that shows the location of both sapphire window ports. This configuration shows the inner and outer wall windows co-aligned with each other. Through the modular design of the combustor, the relative location of the windows could be changed so that they were not necessarily co-aligned during RDC tests. To perform absorption imaging, the windows would need to be aligned so that a spectral source installed in the center-body of the RDC could back-illuminate the channel, as is indicated in Figure 3.10. For measurements of thermal radiation described in Chapter V, the inner wall window was used to measure OH^* chemiluminescence and was not axially aligned with the outer wall window (see section 3.4.3).

3.4.2 UCI optical arrangement for RDC measurements

To capture measurements within the combustion channel of the RDC, the UCI optical arrangement beginning with the objective lens must be aligned with the outer wall window at a distance equal to the focal length of the objective lens ($100\,\mathrm{mm}$) away from the combustion channel (determined by the mid-plane the inner wall and outer wall windows). To ensure proper placement of the objective lens, a 1" lens tube containing the germanium window and the objective lens was attached directly onto the window mount installed in the RDC. These were held in place by optical cage system posts secured into tapped holes in the window frame. A telescoping lens tube could be deployed to enclose the gap between the window and the lens tube holding the optics, although tests showed no difference in the results with and without it deployed. A close-up photograph of these components installed on the combustor is shown in Figure 3.11.

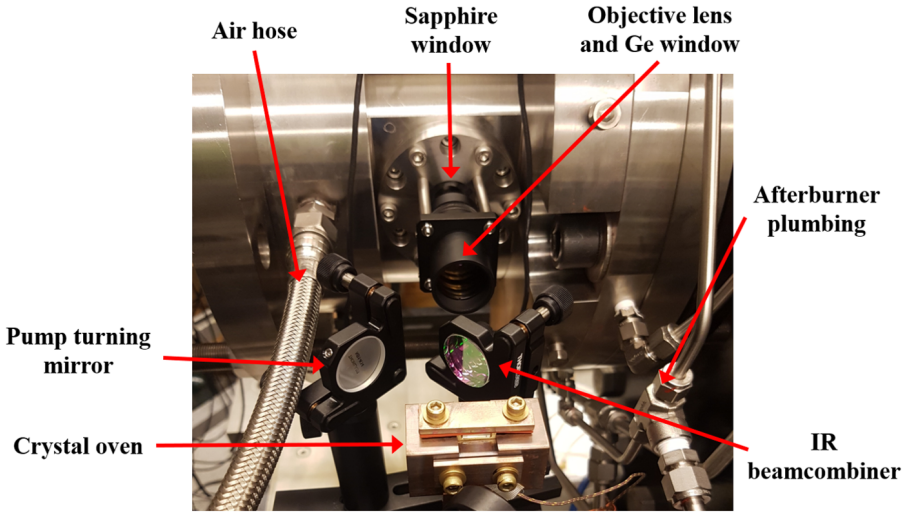

Figure 3.11: Close up photograph of the objective lens installed on the RDC window and pump beam injection optics.

The remaining UCI system components were mounted onto a common optical rail like the benchtop configuration. This rail was supported by a vertical translation platform attached to a table located approximately $31\,\mathrm{cm}$ below and $66\,\mathrm{cm}$ laterally away from the window frame. The optical rail supports the optical components positioned in alignment with the objective lens at an appropriate distance in a cantilever manner, which led to concerns about the effect of structural vibrations excited during RDC runs on the alignment of the optics. However, an examination of the results presented in Chapter V showed no evidence of spurious response fluctuations during the tests that might indicate significant effects due to vibrations.

The configuration of the UCI optical arrangement is shown in Figure 3.12. In the following discussion, left and right will be defined from the perspective of standing in the room outside of the combustor and looking straight into the sapphire window port. Potential clearance issues were identified due to flexible hoses delivering air to the left of the window port and afterburner reactant feed lines made of stainless-steel tubing to the right of the window port. These are indicated in Figure 3.11. The maximum clearance distances from the center axis of the sapphire window were $6.3\,\mathrm{cm}$ to the air hose on the left and $8.6\,\mathrm{cm}$ to the afterburner plumbing on the right. Because the air hose extended more than $38\,\mathrm{cm}$ from the combustor, the camera had to be mounted on the right side of the enclosure box, where the afterburner plumbing extended only $23\,\mathrm{cm}$ from the combustor. With the enclosure box aligned with the window (offset by approximately $1\,\mathrm{mm}$ to account for the refraction by the IR beamcombiner, item D) there is enough room for the pump beam to be routed parallel to the left side of the enclosure box (with $6\,\mathrm{mm}$ of clearance) and the final turning mirror to be mounted near to the IR beamcombiner for pump beam injection with $7\,\mathrm{mm}$ of clearance to the air hose. The CCD camera was mounted on a parallel optical rail to align with the outlet port on the right side of the enclosure box.

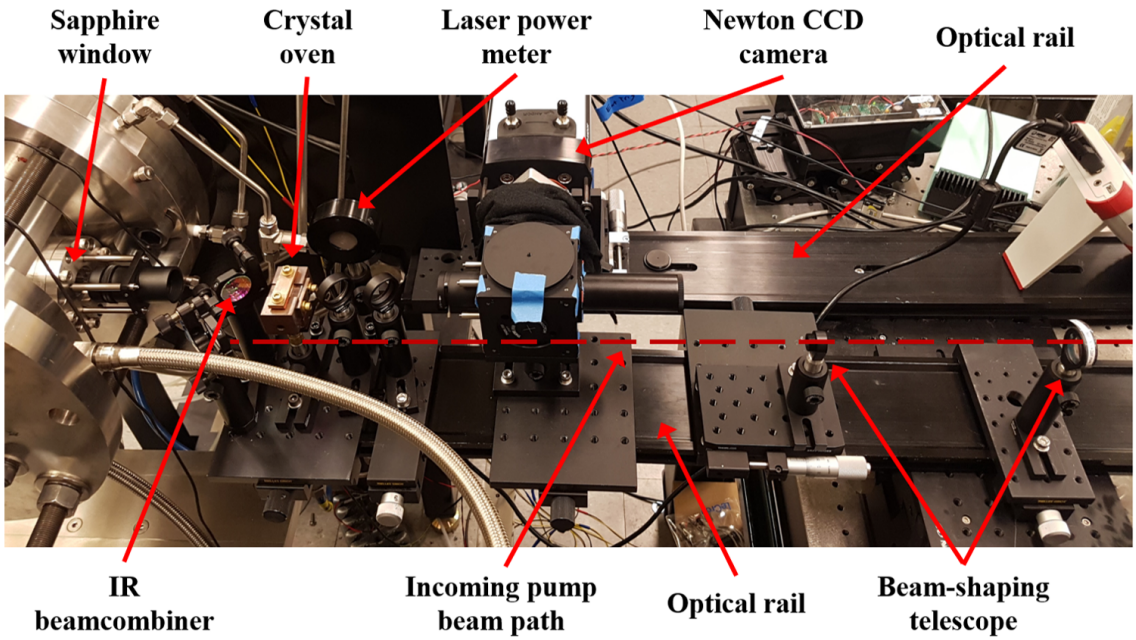

Figure 3.12: Photograph of the entire UCI optical arrangement installed for thermal imaging measurements in the RDC.

3.4.3 Additional RDC instrumentation

A high-speed camera (Phantom V711 at 55 000 fps) was placed behind a window in the exhaust plenum to conduct broadband luminescence imaging axially down through the combustion channel. This was used to track the approximate position of the wave during combustion tests so that wave speeds could be estimated and as an independent measurement for timing the UCI exposures. An image analysis program was used to analyze the position of the wave in the combustor during the run which could be used to estimate the relative part of the detonation wave cycle that was viewed through the sapphire window during each UCI exposure.

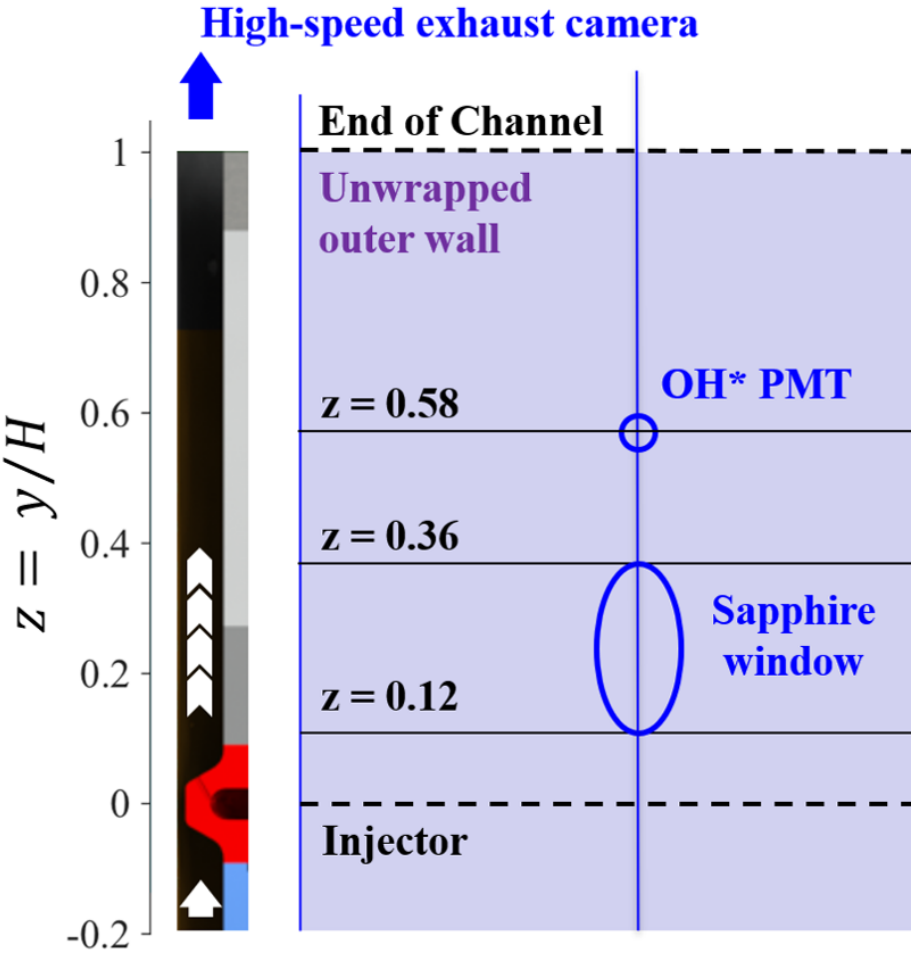

Figure 3.13: Relative locations of the UCI optical access window and other instruments in an unwrapped view of the RDC.

During passive thermal imaging tests, a PhotoMultiplier Tube (PMT) with filters to isolate OH^* chemiluminescence near 310 nm was fiber-coupled to collection optics installed on the inner wall window of the combustion channel at the same circumferential location as

the center of the outer wall sapphire window, but $36\,\mathrm{mm}$ axially downstream of the window. The azimuthal alignment of the PMT with the UCI window caused the wave to propagate past these two instruments at approximately the same time. However, the axial separation combined with possible variations in detonation wave strength and morphology in the axial direction meant that there could be significant differences in the state being observed by the two instruments at the same time.

One high-speed Kulite pressure transducer (model EWCTV-312) was installed in the outer wall of the RDC combustion channel to record the pressure history inside of the combustion channel during a run. The Kulite was installed in a pressure port at the same axial position as the bottom of the outer wall window ($z = 0.12$ as shown in Figure 3.13) but at an azimuthal location $90°$ from the window in the circumference of the combustion channel. Because of this azimuthal separation, the instantaneous pressure measured by the sensor was not representative of the conditions at the outer wall window. The cut-off frequency characterizing the response of the sensor was $5\,\mathrm{kHz}$, which was sufficient to capture the operational frequency of the wave cycle (typically near $1.7\,\mathrm{kHz}$), but could not temporally resolve the rapid pressure rise associated with the detonation wave front which would require response times of shorter than $1\,\mu\mathrm{s}$.

Figure 3.13 provides a schematic of the relative positions of the sapphire window and other instruments within the combustion channel. The overall channel height H, as defined by the distance from the throat of the air stream of the injection system to the exhaust plane was $105\,\mathrm{mm}$ for the tests in this work.

3.4.4 System timing for RDC measurements

UCI system acquisition rate

The maximum acquisition rate for pulsed UCI measurements will be limited by either the repetition rate of the pump laser or the frame rate of the CCD camera, depending on which is smaller. The repetition rate of the laser in this system was $10\,\mathrm{Hz}$ and when the Newton camera was operated in 4×4 binning mode it could achieve frame rates of up to $11.5\,\mathrm{fps}$, making the $10\,\mathrm{Hz}$ laser rate the limiting factor for UCI acquisition. The $10\,\mathrm{Hz}$ limit was significant to applications in the RDC in two ways: it limited the throughput of data that could be achieved in a single run and it failed to capture the dynamics of the detonation wave front.

Operational limitations related to combustor heat loading and other constraints limited the fueled operation of the combustor to durations of $2\,\mathrm{s}$. Of that time about $1.5\,\mathrm{s}$ achieved stable operation. The $10\,\mathrm{Hz}$ acquisition rate resulted in approximately 15 mean-

ingful UCI measurements per run of the combustor. When the approximately 20-minute cool-down interval between runs, necessary to prevent overheating of the combustor and save the buffered high-speed data acquired during the previous run, is considered these restrictions combined to prevent efficient collection of large sets of UCI data in the RDC. This could be address in future measurements using a kHz laser system and high-speed camera. High-speed cameras are available in the RDC laboratory, however a suitable high-energy, high-repetition rate laser with acceptable pulse shape properties may need to be custom manufactured for this purpose.

The UCI system would need to achieve much higher than kHz level acquisition rates to capture the dynamics of detonation wave fronts in this facility. The passive thermal imaging measurements described in Chapter V had an effective FoV of approximately $10\,\mathrm{mm}$ in diameter. For estimation, it can be assumed that $7\,\mathrm{mm}$ of wave travel is the maximum that can be tolerated and still capture the same wave front twice within the FoV. For a wave traveling at the $1.5\,\mathrm{km/s}$ speeds typical of this facility, this would require an acquisition rate of $215\,\mathrm{kHz}$. This could be achievable with modern high-speed cameras at reduced resolutions (the Phantom v2512 is capable of $308\,000$ fps at 256×128 resolution), however the optical power output required of the pump laser at this rate would be above $1\,\mathrm{kW}$. This is unlikely to be achieved with adequate beam characteristics with current technology for long operational intervals, however this is well within the capability of pulse-burst mode laser operation. Additionally, dual-pulse systems could be used with frame-straddling or other methods to achieve microsecond scale frame intervals at lower acquisition rates.

Coordination with high-speed measurement system

To aid in the interpretation of UCI measurements in the RDC, the images that are captured must be correlated in time with other instrumentation on the RDC, such as pressure transducers and the exhaust imaging camera. Knowing the relative timing of the UCI exposures to the other instruments provided important context including the position of the wave relative to the sapphire window and evidence of the presence or absence of secondary burning processes. Because of the rapid propagation speed of the detonation wave front ($1.5\,\mathrm{km/s}$), very fast sensor responses and data acquisition are required to adequately determine relative timing. The operation of the RDC (*i.e.* opening and closing reactant flow valves, activating igniters, etc.) is controlled by a LabView program on a PC in the lab. In addition to operating the combustor, the LabView program triggers high-speed and low-speed Data AcQuisition systems (DAQs) and stores the recorded data after the run. The high-speed DAQ (NI PCI-6259) operates at a sampling rate of $500\,\mathrm{kHz}$, providing a corresponding time resolution of $2\,\mu\mathrm{s}$.

Because the exposure of the UCI image is determined by the pump laser, the laser output can be monitored to infer the timing of each UCI exposure. The laser emits radiation almost immediately after the Q-switch of the laser cavity is opened. The average time-lag between the Q-switch opening and laser radiation detected by a photodiode was measured to be approximately $1.2\,\mu s$ for operation with a $90\,\mu s$ Q-switch delay which was accounted for during data processing. To time the UCI exposures with other sensors, the "Q-switch sync" output from the laser power supply was recorded by the high-speed DAQ. The relatively short duration ($240\,ns$) of the UCI exposure means that it can be treated as an instantaneous event relative to other signals monitored by the high-speed DAQ.

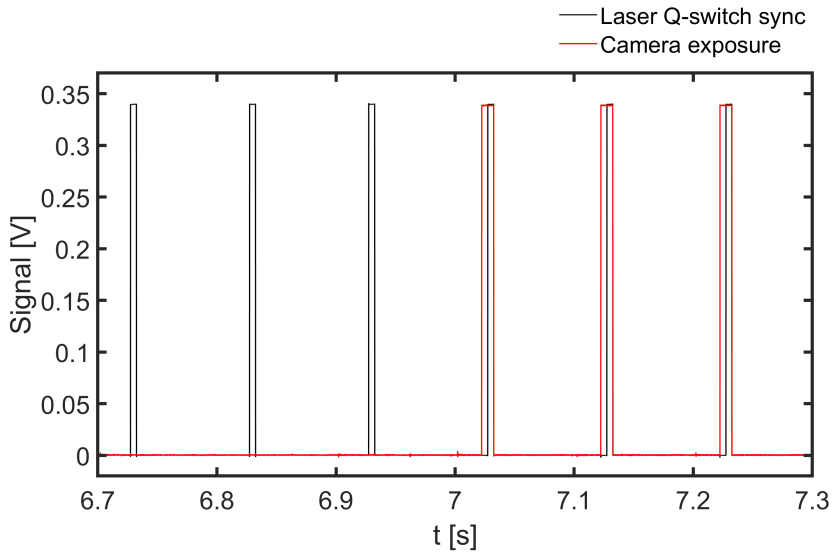

Figure 3.14: An example of the laser Q-switch sync and CCD camera fire signals measured by the high-speed DAQ during an experimental run showing the last three laser frames before activation of the camera toggle and the first three frames after activation of the camera toggle.

The same signal generator that was used to control the Q-switch delay of the $10\,Hz$ pump laser was also used to trigger the exposure of the CCD camera used to detect the UCI signal. The effective exposure time of the measurement was controlled by the duration of the laser pulse, however the exposure of the camera had to be set so that the laser pulse would be captured. This was accomplished by setting the camera's exposure time to $10\,ms$ and sending the fire signal to the camera $5\,ms$ in advance of the laser triggers.

The signal generator box continuously outputs the advanced trigger signal to the camera, and so transmission of that signal needed to be initially cut-off to have the camera activate during the run for initial frame identification. To accomplish this, a manual toggle switch was installed between the signal generator box and the external trigger input to the

camera. The camera would not receive the trigger to fire until the toggle was closed. This was done manually at approximately $0.5\,\mathrm{s}$ after the beginning of high-speed data recording so that the first frame was certain to be captured by the high-speed DAQ and occur before any combustion ignited within the RDC. Due to the manual closure of the toggle, the timing of the first frame varied between runs, but could always be identified through the high-speed data.

Each laser Q-switch signal recorded by the high-speed DAQ could potentially be a UCI exposure event, however they are only recorded if the camera was triggered to expose and read out the image data. The CCD camera had a "Fire" output signal that provided a TTL high voltage value while it was exposed. This signal was monitored by the high-speed DAQ so that it could be compared to each pulse signal from the laser to determine which laser pulses generated a UCI exposure that was recorded by the camera. The first approximately 5 laser pulses of each run occurred before the camera trigger was activated, and this was reflected in the high-speed DAQ by an absence of signal from the fire output from the camera. The first laser pulse in the data that is overlapped by a camera fire signal represents the first frame in a set of images, and so the timing of subsequent frames can be found by the timing of all subsequent laser pulses. The camera was typically run for 50 to 60 frames per set, corresponding to $5\,\mathrm{s}$ to $6\,\mathrm{s}$ of image recording per run, while the high-speed DAQ only collected data for $5\,\mathrm{s}$. This caused the final approximately 10 to 20 frames to be missed by the DAQ because they occurred after it ceased recording, but these frames were discarded anyway because they occurred after the cut-off of combustor operation. An example of the laser and camera signals monitored by the high-speed DAQ is shown in Figure 3.14. This example shows the three laser pulses (black line) before the camera activation and the first three after camera activation. The first three pulses occur without the camera triggering until the camera exposure (red line) is activated and exposures are recorded for all subsequent pulses.

A conceptual map of the data collection and system timing signals is illustrated by the diagram in Figure 3.15. This includes the three trigger signals (laser flash-lamp trigger, laser Q-switch trigger, and UCI camera trigger) that were output by the signal generator to coordinate the UCI system in time. It also shows the manual toggle that was used to activate the UCI camera trigger and the pump laser Q-switch output that was used to record the timing of UCI measurements relative to signals from other sensors that were collected by the high-speed DAQ.

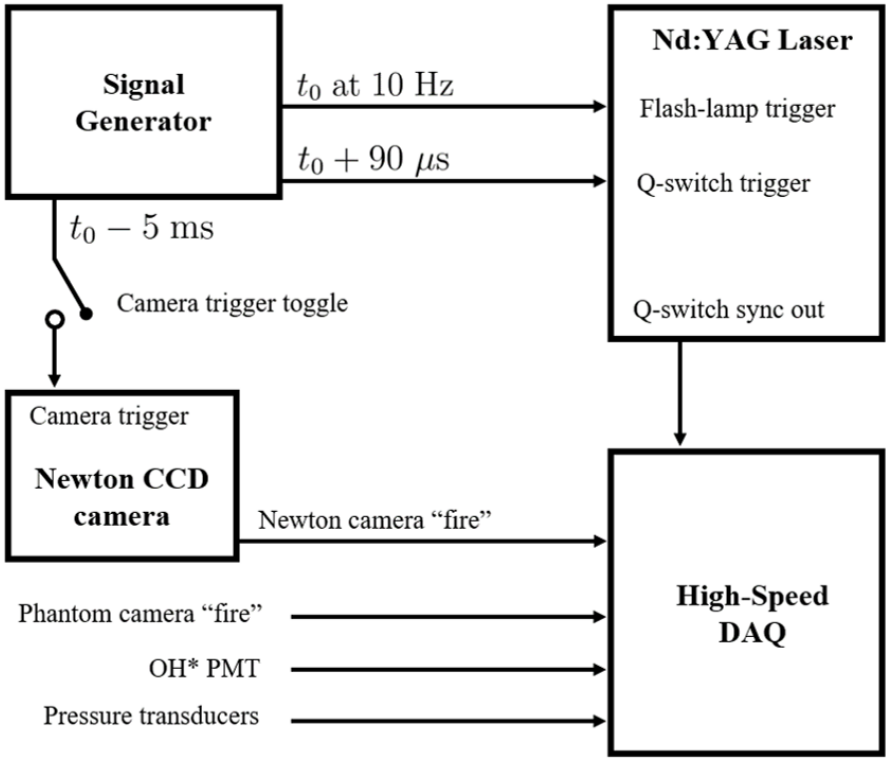

Figure 3.15: Map of signals related to UCI timing during RDC measurements.

CHAPTER IV

UCI Characterization Measurements

This chapter presents a series of benchtop measurements that were used to characterize the response of the system, validate models used to predict its response, and verify whether design parameters were representative of the physical realization of the UCI system. The response of the UCI can be considered along spatial, temporal, and spectral dimensions. All three of these types of variation were examined with comparisons between experimental observations and model predictions described in the following sections. Additionally, the spatial-spectral coupling phenomenon that has major implications for the design and interpretation of UCI measurements was characterized in detail through these measurements.

The results validate the ability of the models to accurately predict the response of this UCI system along the three primary response dimensions. Establishing the validity of these models was important because they serve as a basis for the design of experimental applications of the UCI system to study unsteady combustion phenomena. The results of the measurements also directly informed how the experiments in the RDC would be performed, specifically the choice to target thermal radiative emissions from CO_2 instead of other species. These measurements were sensitive to minor variations in the parameters of the system and were able to identify nanometer-scale discrepancies in the poling period lengths of the physical system compared to the intended design values. These differences did not compromise the operability of the system but determining them was critical for accurate modeling of the system response.

4.1 Uniform blackbody source measurements

Blackbody sources are useful targets for characterization measurements because they generate mid-IR light with well-known spatial, spectral, and temporal distributions. For the measurements in this chapter, a Graseby Instruments model IR-563/301 blackbody source was used with its maximum emission aperture of $25\,\mathrm{mm}$. The conical cavity design of the

system provided a high level of spatial uniformity across the aperture and its emission can be assumed to be constant in time.

The spectral content of a blackbody source is determined by a single parameter, its temperature, T_{B}. The relationship between a blackbody emitter's temperature and its spectral radiance is known as the *Planck curve*, which can be expressed as:

$$L_{\mathrm{q,B}}(\lambda, T_{\mathrm{B}}) = \frac{2c}{\lambda^4} \frac{10^{-6}}{\exp\left(\frac{hc}{\lambda k_{\mathrm{B}} T_{\mathrm{B}}}\right) - 1} \tag{4.1}$$

where c is the vacuum speed of light, k_{B} is the Boltzmann constant, and h is the Planck constant. This formulation takes all inputs in SI units and outputs the value of $L_{\mathrm{q,B}}(\lambda, T_{\mathrm{B}})$ in units of photons$/\mathrm{s}/\mathrm{m}^2/\mathrm{sr}/\mu\mathrm{m}$. This particular formulation was chosen to be directly compatible with the per photon QE perspective used to express many of the UCI models in Chapter II. The IR-563 source was capable of producing temperatures of up to $1050\,^{\circ}\mathrm{C}$ after a warm-up time of $30\,\mathrm{min}$ to $60\,\mathrm{min}$.

Because the blackbody source produces a spatially-uniform illumination field the model described in section 2.6 can be used to predict the response of the UCI system. For spatially-uniform sources, any variation in the signal across the image plane will be caused exclusively through the spatial-spectral coupling effects described in section 2.3.1. In the case of a blackbody spectrum, the variation in radiance is typically small over spectral intervals on the order of the mid-IR spectral bandwidths of the UCI system ($2\,\mathrm{nm}$ to $300\,\mathrm{nm}$, see Figure 2.11(b)). This makes UCI measurements of the blackbody source captured using the four shortest poling periods of the UCI system uninteresting as they will exhibit little variation in signal strength across the FoV except for the spurious spectral fringing described in section 3.2) which will extend out to until the limits either of the source's aperture or the clear aperture of the imaging optics. The longest poling period with a design length of $23.4\,\mu\mathrm{m}$ is different because of the way non-monotonic variation of Δk in the crystal manifests itself in the spatial-spectral coupling effects for that case. As shown in Figure 2.6(b), the "donut" type tuning curve suggests a limited FoV and significant variations in bandwidth across the image plane. This makes UCI of the blackbody source with the $\Lambda_{\mathrm{P}} = 23.4\,\mu\mathrm{m}$ a good example for both validation of the spatial-spectral coupling model and the assumed design parameters.

For these characterization measurements the blackbody source was operated at a temperature of $T_{\mathrm{B}} = 950\,^{\circ}\mathrm{C}$ while the UCI system was configured to use the $\Lambda_{\mathrm{P}} = 23.4\,\mu\mathrm{m}$ design length poling period at a crystal temperature of $21\,^{\circ}\mathrm{C}$. Because temporal resolution was not a concern for these measurements, the pump laser was operated in long-pulse mode

with a pulse energy of $22.5\,\mathrm{mJ}$. The image was averaged over 25 consecutive exposures to further increase the effective SNR. Figure 4.1 shows a side-by-by comparison of the experimentally measured image and a simulation computed using the same parameters as in the measurement except for a slightly longer poling period of $\Lambda_P = 23.415\,\mu\mathrm{m}$. The reason for this discrepancy will be discussed later below.

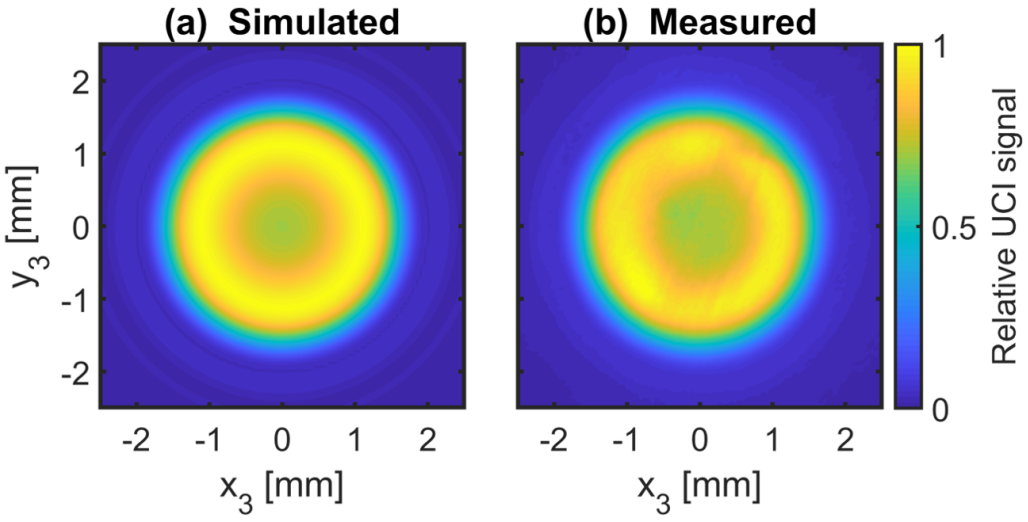

Figure 4.1: UCI of a uniform blackbody source at $950\,^{\circ}\mathrm{C}$ shown in image plane coordinates. (a) a simulated response assuming $\Lambda_P = 23.415\,\mu\mathrm{m}$ and a $21\,^{\circ}\mathrm{C}$ crystal temperature and (b) the experimentally measured image.

The simulated and measured images in Figure 4.1 show qualitative agreement in their structure. The limited FoV suggested by the design tuning curves is seen in both simulated and measured UCI responses where signal levels are negligible for distances of more than $2\,\mathrm{mm}$ from the center of the image plane. They both also show that peak response (indicative of peak spectral bandwidth) occurs away from the center of the FoV near $1.1\,\mathrm{mm}$ from the image center. One effect that is not captured by the model is that of spectral fringing due to the near-IR detection properties of back-illuminated CCD. These effects are barely visible as signal deficits in Figure 4.1(b) near ($x_3 = 0.5\,\mathrm{mm}$, $y_3 = 1\,\mathrm{mm}$) and ($x_3 = 0\,\mathrm{mm}$, $y_3 = $ -1.2 mm) caused by destructive interference fringes. The fringes are very weak compared to the example shown in Figure 3.4 because of the relatively large near-IR bandwidth generated by UCI detection of blackbody radiation with this longer poling period. Shorter poling periods show stronger fringing patterns as a result of narrowband upconverted signals and so does detection of narrowband signals near $4.2\,\mu\mathrm{m}$, as will be demonstrated by passive imaging of CO_2 thermal radiation shown later in section 4.3.

A more precise quantitative comparison of the simulated and measured UCI responses can be undertaken by plotting the pixel-by-pixel signals as a function of distance from

the center of the FoV in the image plane (the distance defined as r_3 in Chapter II). The measured UCI response as a function of image plane distance is shown by the black circles in Figure 4.2. As was previously mentioned, there was a discrepancy observed between the simulated UCI response at the design poling period of $\Lambda_P = 23.4\,\mu\text{m}$ and the measurements. The simulated response using the design poling period length is shown by the dashed-dotted red line in Figure 4.2. Comparison of the simulated response at the design condition to the observed response produced disagreements in the location of peak response ($r_3 = 1.36\,\text{mm}$ vs. $r_3 = 1.13\,\text{mm}$) and response strength at the image center (61% vs. 74%). Alternative poling period lengths tested in the simulation and are plotted in Figure 4.2 for $\Lambda_P = 23.415\,\mu\text{m}$ (solid red line) and $\Lambda_P = 23.43\,\mu\text{m}$ (dashed red line). The simulated results for $\Lambda_P = 23.415\,\mu\text{m}$ show very good agreement with the measurements with less than 5% error for the two metrics that were previously examined for the design poling period. The simulation results for $\Lambda_P = 23.43\,\mu\text{m}$ over-correct for the errors in the design poling period assumption and give relative errors of similar magnitudes with opposite signs.

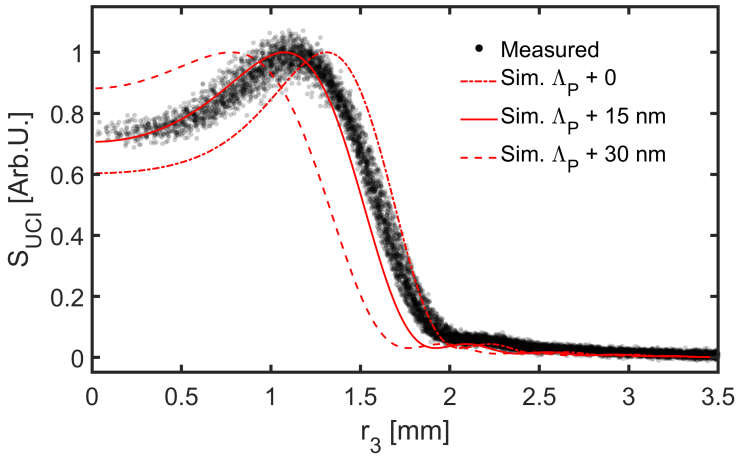

Figure 4.2: UCI signal strength in response to uniform illumination by a $950\,^{\circ}\text{C}$ blackbody source as a function of distance from the system centerline in the image plane. The measured signal at each pixel is shown by the black dots while the model prediction at different poling periods relative to the design poling period of $\Lambda_P = 23.4\,\mu\text{m}$.

These results suggest that the grating used in these tests had a systematic error in the length of the poling period of $+15\,\text{nm}$ relative to the specified design of $\Lambda_P = 23.4\,\mu\text{m}$. This amounts to a relative error in the poling period of 0.064% in aggregate over the approximately 853 domain reversals (427 periods) that are expected to occur along the length of this grating. Previous microscopy studies of periodically poled crystal domain length errors by Høgstedt *et al.* [70] and Pelc *et al.* [88] had identified root-mean-squared errors in domain length of $700\,\text{nm}$ and $410\,\text{nm}$, respectively. These would correspond to stan-

dard deviations in the average poling period length error of $24\,\mathrm{nm}$ and $14\,\mathrm{nm}$, making it reasonable to observe the amount of deviation that seems to have been measured.

The only other factors that could affect the modeled UCI response in ways that could account for the discrepancy are: the material index of refraction $n_e(\lambda, T)$, the wavelength of the pump source, the temperature of the crystal, and the focal length of the imaging lenses. The dispersive properties of LN and the emission wavelengths of Nd:YAG lasers have been extensively studied in previous literature and can be reasonably assumed to be well-known. Additionally, errors in these values would cause consistent discrepancies with other poling periods that were not observed, and so these potential causes can be rejected. The temperature of the crystal was monitored by the thermocouple installed on the copper oven and can be considered to be fixed at room temperature because of the large thermal reservoir provided by the atmosphere in the lab and copper oven that maintained the temperature near $21\,^{\circ}\mathrm{C}$ ($5\,^{\circ}\mathrm{C}$ of deviation from room temperature would be needed to account for the discrepancy assuming a poling period of $\Lambda_\mathrm{P} = 23.4\,\mu\mathrm{m}$). Finally, the imaging lenses (procured from Thorlabs) were guaranteed to have a focal length accuracy within 5% and would have produced errors in other measurements that were not observed.

Based on the evidence in these measurements and more results shown in section 4.2, it can be concluded that the poling period in the tested grating was approximately $\Lambda_\mathrm{P} = 23.415\,\mu\mathrm{m}$. Despite the very small relative magnitude of the difference between the design and observed poling period, it resulted in significant differences in system performance as shown in Figure 4.2. These differences do not compromise the operability of the system but need to be measured and accounted for if high-accuracy modeling predictions of the system response are to be performed. The response of the system is particularly sensitive at these longer wavelengths because of the behavior of Δk in LN in that wavelength range. A similar poling period discrepancy related to the $\Lambda_\mathrm{P} = 19.4\,\mu\mathrm{m}$ design grating is discussed in section 4.3.

4.1.1 Pump pulse energy sweeps

Measurements of the blackbody source were also used to test UCI temporal efficiency model, specifically its variation with pump beam pulse energy. For these tests UCI was again performed of the uniform blackbody source operated at a temperature of $950\,^{\circ}\mathrm{C}$ with the $\Lambda_\mathrm{P} = 23.415\,\mu\mathrm{m}$ poling period. The first series of tests were performed with the laser operated in long-pulse mode. Long-pulse mode operation generated pulse trains of sub-pulses over an interval of approximately $120\,\mu\mathrm{s}$ that were characterized with photodiode measurements in section 3.3.1. These pulse trains exhibited low pump intensities were

expected to be reasonably modeled by the linear response model described by Eq. (2.31). In this low-intensity limit, the UCI signal is predicted to be directly proportional to pump pulse energy.

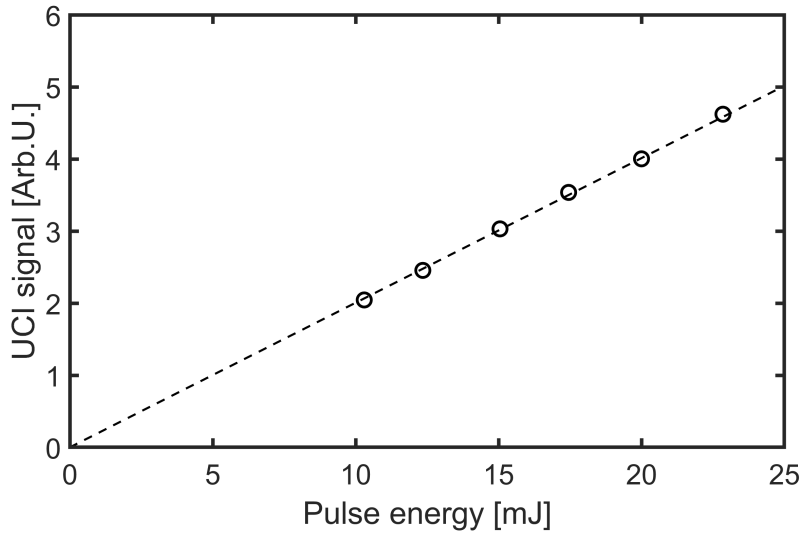

Figure 4.3: Measurements of UCI signal strength (circles) at various long-pulse pump energies compared to a linear fit (dashed line) representing the low-intensity limit model.

Figure 4.3 shows experimental measurements of the $950\,^{\circ}\mathrm{C}$ blackbody source at various pulse energies. The signal strengths were determined by summing all of the pixel values in the FoV shown in Figure 4.1. Because the spatial-spectral coupling effect that limited the FoV and produced the observed structure in the images is independent of pump intensity, this spatial integration produced signal values that are determined solely by the effects of temporal efficiency. The measured signal strengths at long-pulse pump energies between $10\,\mathrm{mJ}$ to $22.5\,\mathrm{mJ}$ are shown by the circle symbols in Figure 4.3 and the dashed line shows a linear fit to the data points anchored that is anchored at the origin. The linear fit agreed closely with the observed signal strengths, $R^2 = 0.9996$, and this is consistent with the linear response predicted by the low-intensity pulse model in Eq. (2.31). This confirms the validity of applying the low-intensity temporal efficiency model to the system when the pump laser is operated in long-pulse mode.

When the pump source was operated in Q-switched mode with optimal Q-switched delays, the output became a single pulse of an approximately Gaussian temporal shape with a $10\,\mathrm{ns}$ FWHM as determined by photodiode measurements of the emitted pulse shape. These shorter pulse durations caused much higher pump intensities within the ppLN crystal so that nonlinear η_t responses could be observed for pulse energies below $1\,\mathrm{mJ}$. The nonlinear response of the system means that the temporal and spatial variation of the pump

intensity must be considered and the integration expressed in Eq. (2.30) must be computed to model signal strength dependence on pump pulse energy. While the temporal pulse shape was well-characterized by the photodiode measurements, an accurate estimate of the spatial pump beam intensity distribution is also required to evaluate the model.

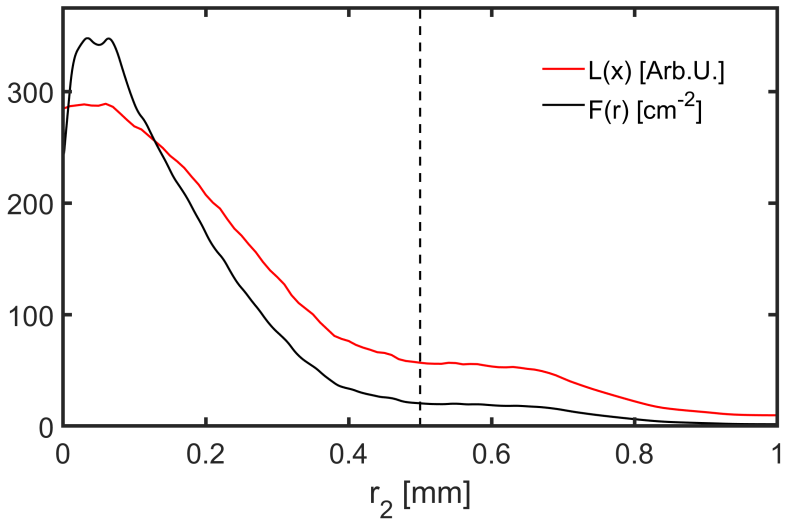

Figure 4.4: Measurements of the pump beam's line response function (red line) and the beam's normalized intensity distribution (black line) computed using the inverse Abel transform method described by O'Connell and Vogel [3].

The spatial beam profile for these tests was experimentally estimated using a scanning knife-edge technique. To do this, the crystal was removed from the Fourier plane of the 4f UCI system and replaced with a razor blade mounted vertically and installed on a micrometer-driven translation stage. The position of the blade was incrementally moved across the Fourier plane while the transmitted pump beam energy was monitored by a power meter until all of the energy was blocked. The first derivative of the measured pump energy with respect to blade position was computed using a third-order, 25-point window Savitsky-Golay differentiation [89, 90] to find the "line response function", $L(x) = -\frac{\mathrm{d}E_P}{\mathrm{d}x}$, as shown by the red line in Figure 4.4. The inverse Abel transform technique for axisymmetric beams described by O'Connell and Vogel [3] was then used to compute the corresponding radial intensity distribution, shown by the solid black line in Figure 4.4. The resulting estimate was found to be approximately a radial sinc^2 function with an FWHM of $400\,\mu\mathrm{m}$.

This resemblance to a sinc^2 function might have been due to a circular aperture that was placed upstream of the UCI system in the pump beam optical arrangement to control the size of the pump beam cross-section. This aperture was not used for future measurements

to avoid these narrow pump cross-sections and achieve spatial intensity distributions closer to Gaussian functions. The vertical dashed line shows the location of the closest edge of the poling period aperture when the crystal was aligned with the beam (the corners of the poling period would be at $r_2 = 0.707\,\mathrm{mm}$). This estimated beam shape resulted in 74% of the pulse energy falling within the aperture of the poling period. This estimate beam intensity distribution was used for the UCI temporal efficiency modeling described below.

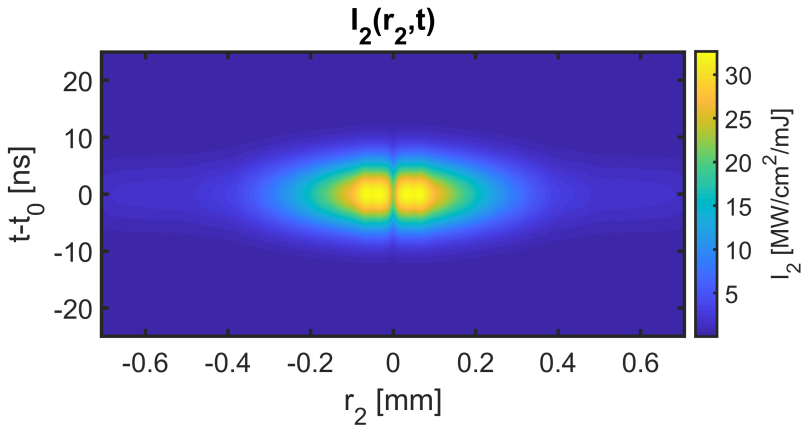

Figure 4.5: Contour plot of the spatiotemporal variation of pump beam intensity within the nonlinear crystal for unit pulse energy.

The fundamental quantity that determines SFG efficiency at a particular location and instant within the nonlinear crystal is pump beam intensity. Figure 4.5 shows a contour plot that visualizes the spatiotemporal variation in pump beam intensity with relative time on the vertical axis and position in the Fourier plane on the horizontal axis for a $10\,\mathrm{ns}$ wide Gaussian temporal pulse and the measured beam cross-section shown in Figure 4.4. This was computed for a pump beam pulse with $1\,\mathrm{mJ}$ of integrated pulse energy, and so the intensity distribution for any other pulse energy with these parameters can be found by linearly scaling the plotted distribution by the integrated pulse energy in mJ. The spatiotemporal variation of temporal efficiency within the crystal can be determined by evaluating the nonlinear efficiency relationship shown in Eq. (2.16) for the intensity at each (r_2, t) point.

Figure 4.6 shows the spatiotemporal variation of temporal efficiency within the crystal computed for the intensity distribution shown in Figure 4.5 at two different pulse energies ((a) $0.5\,\mathrm{mJ}$ and (b) $1.5\,\mathrm{mJ}$). These calculations used a nonlinear coupling coefficient value of $d_{\mathrm{eff}} = 11.2\,\mathrm{pm/V}$ (the reason for this value is discussed more below). These two pulse energies were chosen to demonstrate the effects of nonlinear temporal efficiency trends with pump intensity. The lower intensity case in Figure 4.6(a) shows peaks in η_t that coincide with the peaks in pump beam intensity while the case in Figure 4.6(b) has local minima at the peak intensity points because the optimal pump intensity has been exceeded.

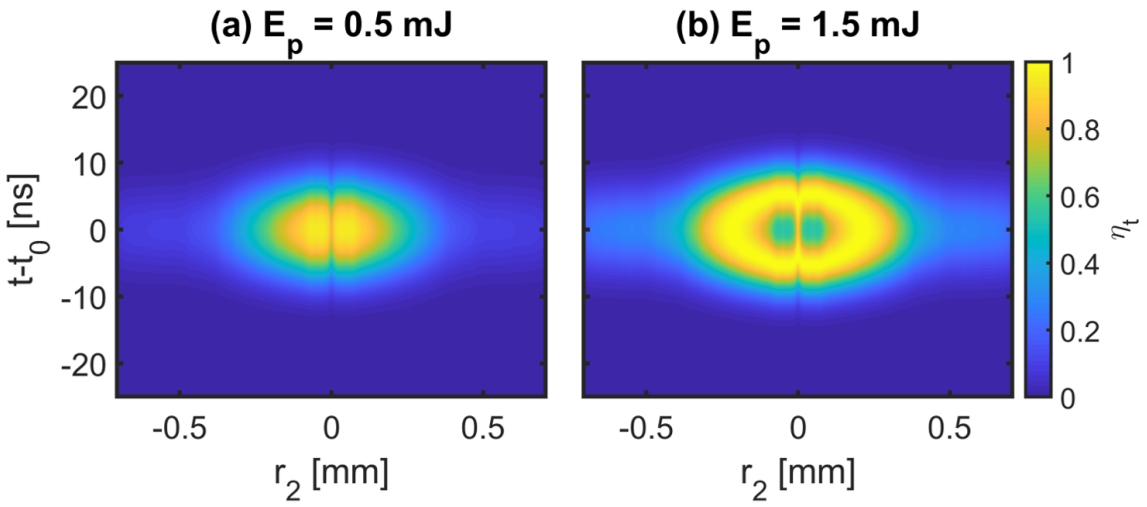

Figure 4.6: Contour plots of the spatiotemporal variation of η_t within the nonlinear crystal assuming the measured pump beam spatial profile and $d_{\text{eff}} = 11.2\,\text{pm/V}$ for pump energies of (a) $0.5\,\text{mJ}$ and (b) $1.5\,\text{mJ}$.

Signals related to these spatiotemporal efficiency variations could theoretically be experimentally measured. For example, a coherent mid-IR signal could be detected without imaging optics using a streak camera to achieve temporal resolution. However, this was not done in this work and in general, the spatiotemporal efficiency variation is not experimentally accessible. Instead, the integrated UCI signal strength can be more readily measured and compared to pulse energy, as is done in Figure 4.3. These are both spatiotemporally integrated quantities and so they are directly comparable. As long as the temporal pulse shape and beam cross-section remain the same, the UCI signal strength will be a function of changing pulse energy. In this way, the pulse energy sweep measurements can be used to characterize the nonlinear pump intensity response of the UCI signal level.

The measured UCI signal strength variation with pump pulse energy for $10\,\text{ns}$ pulses are shown by the black circles in Figure 4.7. The first four points exhibit a highly linear response, $R^2 > 0.9999$, with nonlinear effects becoming significant for pulse energies above $0.4\,\text{mJ}$. The model was evaluated by numerically computing the integral in Eq. (2.26) for each pulse energy level. The results are sensitive to the value of d_{eff} used in the analysis, and several values are reported by Shoji et al. [91] based on second harmonic generation at three different near-IR wavelengths. These can be related to the relevant nonlinear coefficient for this SFG process ($4.2\,\mu\text{m} + 1.064\,\mu\text{m} \rightarrow 0.85\,\mu\text{m}$) by the Miller scaling law [92] that has been shown to be a reasonable model for dispersive effects in LN [93]. After applying the scaling law and accounting for the $2/\pi$ scaling of nonlinear efficiency for first-order QPM, the estimates for effective nonlinear coupling coefficient fall between

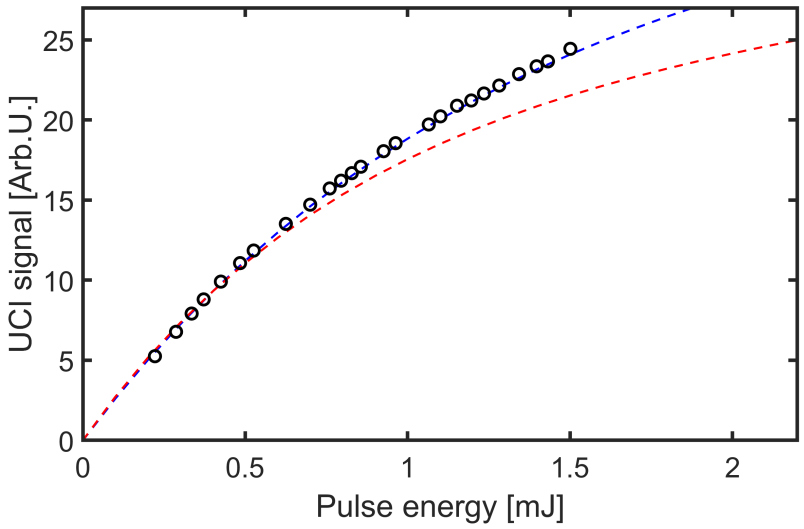

Figure 4.7: Measurements of UCI signal strength (circles) at various $10\,\mathrm{ns}$-pulse pump energies compared to two modeled trends. The lower (red dashed) line was computed using $d_{\mathrm{eff}} = 13.3\,\mathrm{pm/V}$ and the upper (blue dashed) line was computed using $d_{\mathrm{eff}} = 11.2\,\mathrm{pm/V}$.

$11.2\,\mathrm{pm/V}$ and $13.3\,\mathrm{pm/V}$. The modeled results are shown in Fig. 4.7 by the dashed blue (upper) line for the minimum estimate of $d_{\mathrm{eff}} = 11.2\,\mathrm{pm/V}$ and the dashed red (lower) line for the maximum estimate of $d_{\mathrm{eff}} = 13.3\,\mathrm{pm/V}$. The experimental measurements show close agreement with the modeled trends for the lower d_{eff} value, demonstrating the ability of the model to explain trends with pump pulse energy variation in the nonlinear response regime.

4.2 Near-IR spectroscopy measurements

The previous section examined the detection properties of the UCI system by using it to measure a known IR source. This section takes a different approach of examining the properties of the upconverted light generated by the UCI system in response to a known IR source. Just as IR tuning curves like the ones shown in Figure 2.6 can be computed for mid-IR wavelengths and locations in the object plane, equivalent curves can be computed for the resulting upconverted wavelengths and their locations in the image plane. The near-IR spectra corresponding to the upconverted light signal in the image plane can be directly detected and compared to model predictions.

To measure upconverted spectra at spatially-resolved locations in the image plane of the UCI the CCD sensor was removed from its location in the UCI configuration shown in Figure 3.1 and replaced with a fiber-optic bundle connected to a spectrometer. The fiber

bundle was mounted on a translation stage that could be used to traverse radial locations in the image plane to vary r_3. The fiber bundle (Thorlabs BFL105HS02) included seven fiber cores with diameters of $105\,\mu\mathrm{m}$ that are formed into a circular pattern on the collection end with an effective diameter of $355\,\mu\mathrm{m}$. The output end of the fiber bundle has a linear format that can be aligned with the entrance slit of a spectrometer.

Spectroscopic measurements of the near-IR upconverted signals were performed by installing the Newton CCD camera in the $0.5\,\mathrm{m}$ spectrometer that was described in section 3.2 and used to measure spectral-fringing behavior of the camera as shown in the example in Figure 3.3. As was mentioned, this spectrometer was retrofit from a monochromator configuration using a similar procedure to the one described by Airey [85] and its response was previously characterized for UV spectroscopy experiments [86]. However, this characterization of spectral detection properties does not apply to the measurements here for two reasons. First, the UV spectroscopy measurements were performed with a $2400\,\mathrm{lines/mm}$ to achieve high spectral resolutions while the near-IR measurements in this work were performed with $1200\,\mathrm{lines/mm}$ to access longer near-IR wavelengths with reduced coma aberrations. Second, the UV spectroscopy measurements were performed with a very narrow inlet slit width to achieve maximum spectral resolution (approximately $8\,\mathrm{cm}^{-1}$ resolution near $280\,\mathrm{nm}$), while in this work the low signal strengths required a maximum throughput configuration that included fully opening the entrance slit. All of the measured spectra were divided by spectra captured with direct illumination of the fiber bundle by the blackbody source to correct for the effects of spectral fringing shown in the spectrometer image in Figure 3.3.

To characterize the response of the spectrometer, including its spectral resolution and wavelength registration, calibration spectra were measured with a neon discharge lamp. The lamp populated the first ionized state of neon, Ne I, resulting in strong emission lines at well-known wavelengths cataloged in the NIST atomic spectra database [94]. The spectrometer was operated in two spectral intervals, one centered near $810\,\mathrm{nm}$ and another centered near $847\,\mathrm{nm}$, and the calibration spectra are shown in Figures 4.8 and 4.9. These show the strong Ne I lines that were used for wavelength registration and the width of the line-shapes superimposed by the spectral response of the spectrometer. The line-shape is a composite of seven peaks that are the result of a misalignment of the linear output port of the fiber bundle relative to the axis of the entrance slit of the spectrometer (one peak for each core in the bundle) with spectral widths of $1.386\,\mathrm{nm}$ at wavelengths near $808\,\mathrm{nm}$ and $1.369\,\mathrm{nm}$ at wavelengths near $850\,\mathrm{nm}$.

Upconversion signal was generated by placing the blackbody source in the object plane at roughly the center of the FoV at an operating temperature of $900\,^{\circ}\mathrm{C}$. The spectrometer

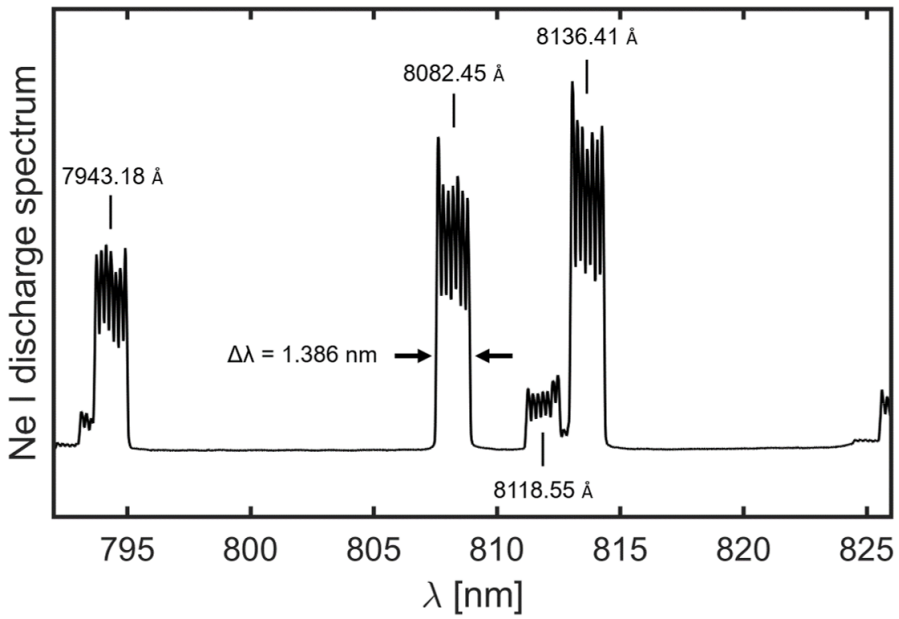

Figure 4.8: Calibration spectrum captured of strong Ne I discharge lines near $810\,\mathrm{nm}$.

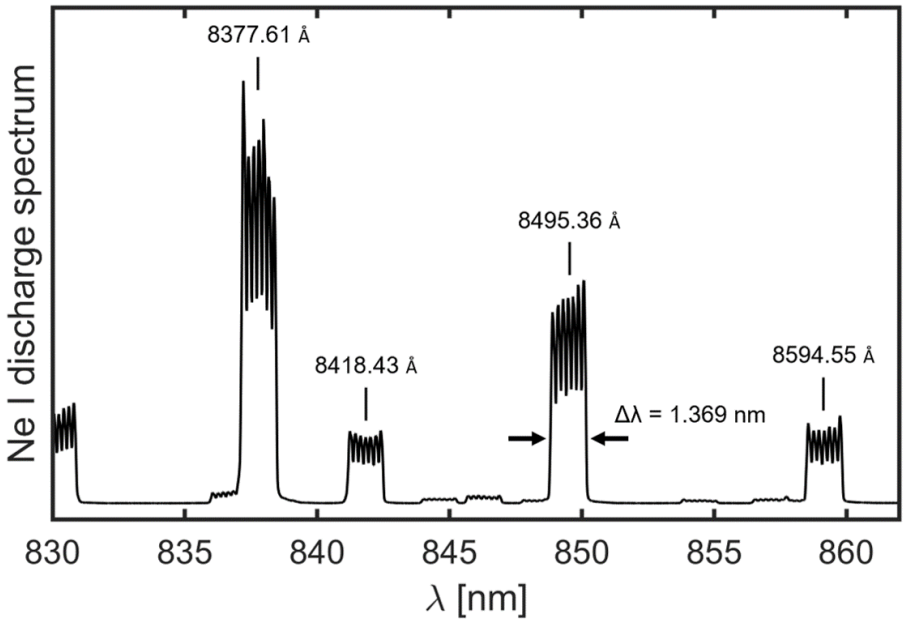

Figure 4.9: Calibration spectrum captured of strong Ne I discharge lines near $845\,\mathrm{nm}$.

was used to measure the upconverted spectra of the two longest poling periods in the crystal, $\Lambda_P = 22.45\,\mu\mathrm{m}$ and $\Lambda_P = 23.415\,\mu\mathrm{m}$. These two poling periods produced the strongest responses to the blackbody source which is why they were chosen for near-IR spectroscopy measurements. To the center of the imaging plane, the fiber bundle was moved in the vertical and horizontal directions until the shortest wavelength response was observed. From

there, spectra were captured at each location and incrementally moved away from the center of the FoV in steps of $200\,\mu\mathrm{m}$, which was 56% of the effective bundle collection diameter. The spectra at each location were averaged over 300 consecutive exposures to increase SNR. The camera was operated in "full vertical binning" mode to integrate the signal along the vertical direction on the sensor while individually reading out the 2048 pixel horizontal resolution. Because the instrument line-shape was highly oversampled by the camera (83 pixels per instrument line-shape width) a 50 pixel rolling average was applied to the measured spectral to further decrease noise.

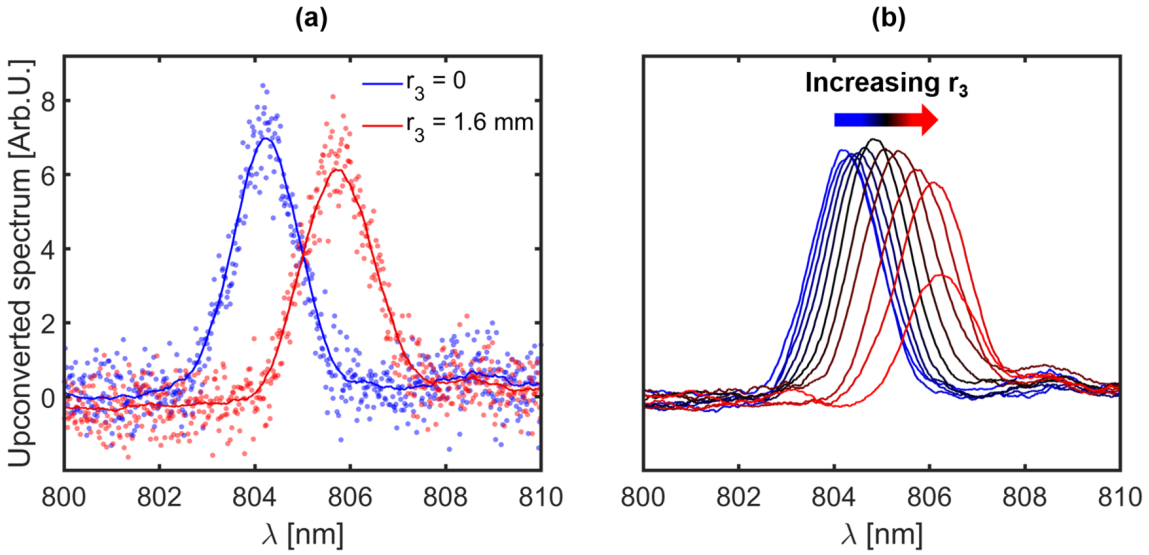

Figure 4.10: (a) Two examples of upconverted spectra captured at different locations within the image plane for $\Lambda_P = 22.45\,\mu\mathrm{m}$ showing raw data points and a 50 point moving average. (b) All measured spectra between the center of the FoV and $r_3 = 2\,\mathrm{mm}$.

Measurements with the $\Lambda_P = 22.45\,\mu\mathrm{m}$ poling period were performed with the pump laser operating in long-pulse mode with $32\,\mathrm{mJ}$ of energy per pulse and a crystal temperature of $22\,^{\circ}\mathrm{C}$. Examples of the measured spectra at two different locations in the image plane are shown in Figure 4.10(a) with the dots representing the recorded signal at each horizontal location on the CCD and the solid lines showing the 50 point rolling average. These two spectra show a nearly $2\,\mathrm{nm}$ increase in peak response wavelength at $r_3 = 1.6\,\mathrm{mm}$ compared to the center of the FoV. This is consistent with the "smile" tuning curve contour shown in Figure 2.6, which though its plotted in terms of mid-IR wavelengths mirrors the trend in upconverted wavelengths showing longer response wavelengths at greater distances from the center of the FoV. This trend can be seen in Figure 4.10(b) which shows the spectra measured at each location in the image plane with blue lines indicating proximity to the FoV center and red lines indicating locations toward the periphery of the FoV. The

spectra measured at the three largest distances from the center of the image plane ($r_3 = 1.6\,\mathrm{mm}$, $1.8\,\mathrm{mm}$, and $2\,\mathrm{mm}$) showed diminished signal strengths because the image of the blackbody source did not overlap that edge of the image plane.

The measured spectra and their radial locations can be combined to construct an upconverted tuning curve. Figure 4.11 shows a comparison of the upconverted tuning curve generated by the UCI model described in section 2.3.1 on the left half and measured with the spectrometer on the right half. The comparisons show good agreement between the model and measurements in terms of the peak response wavelength at each radial location. The measured near-IR bandwidths appear to be larger than the simulated bandwidth at the corresponding locations, but the modeled near-IR bandwidth ($1.05\,\mathrm{nm}$ FWHM) is narrower than the resolution of the spectrometer and so could not be resolved in these measurements.

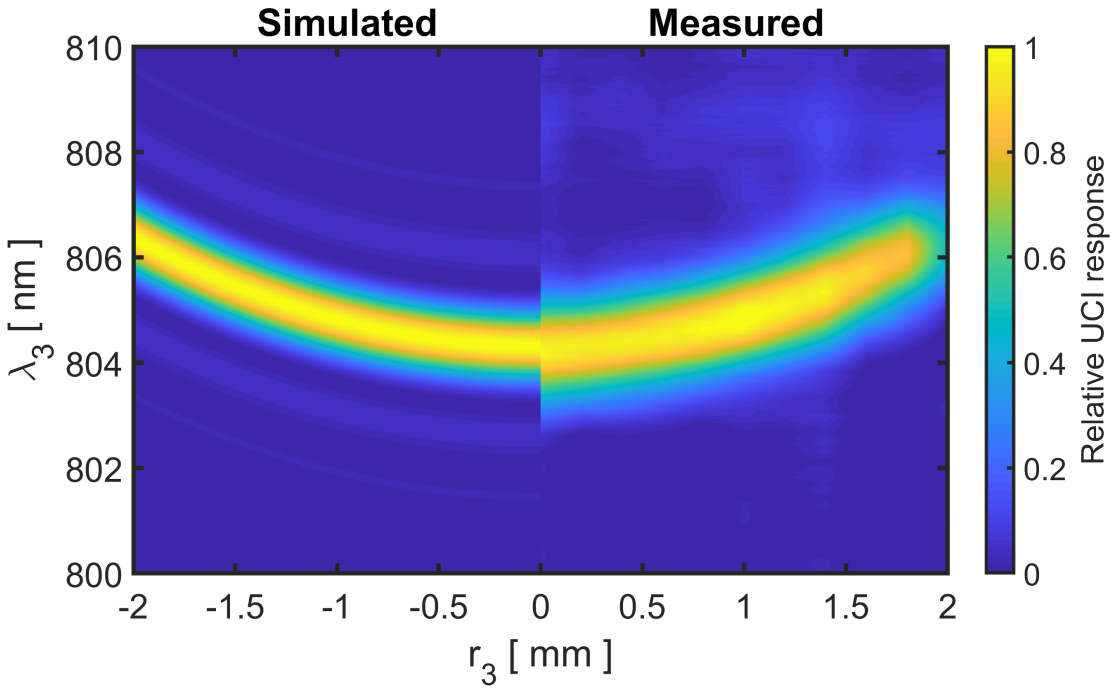

Figure 4.11: A comparison of simulated and measured near-IR response of the UCI system for upconversion of wavelengths near $3.3\,\mu\mathrm{m}$. The simulation assumes a poling period of $\Lambda_P = 22.45\,\mu\mathrm{m}$ and a crystal temperature of $22\,^{\circ}\mathrm{C}$.

The same type of measurements were performed using the $\Lambda_P = 23.415\,\mu\mathrm{m}$ poling period. Figure 4.12(a) shows two examples of the measured upconverted spectra. The spectrum at the center of the FoV shows the bimodal response that is characteristic of the "donut" shape shown in mid-IR wavelengths in the tuning curve previously shown in Figure 2.6(b). The response then moves toward a more flat-top unimodal distribution at greater displacements from the FoV center as shown by the spectrum at $r_3 = 1.0\,\mathrm{mm}$. Fig-

ure 4.12(b) shows the measured spectrum at every location color-coded by image plane location. These measurements show a few effects that were not observed in the previous spectroscopy measurements near 810 nm. The black arrow in Figure 4.12(b) indicates a deficit feature in the response that matches the mid-IR absorption signature of CO_2 when transformed into upconverted wavelengths. It is important to note that this absorption does not occur at near-IR wavelengths, but instead at mid-IR wavelengths in the path-length between the blackbody source and ppLN crystal and the spectral shape of that absorption is then transferred to the near-IR spectrum based on the relationship $\lambda_3^{-1} = \lambda_1^{-1} + \lambda_2^{-1}$. Additionally, there is an linear decrease in the strength of the measured spectra with increasing wavelength as indicated by the dashed gray line in Figure 4.12(b). This is primarily due to spectral variation in both the QE of the CCD camera and blackbody emission at these near-IR wavelengths that can become non-negligible for the bandwidth exhibited by detection with the $\Lambda_P = 23.415\,\mu m$ poling period.

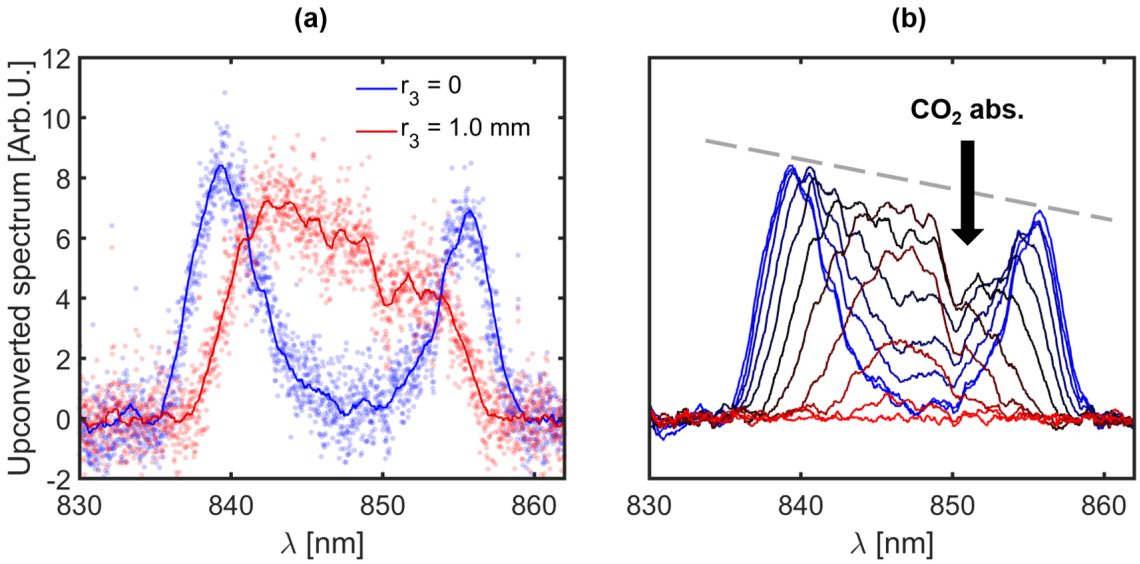

Figure 4.12: (a) Two examples of upconverted spectra captured at different locations within the image plane for $\Lambda_P = 23.415\,\mu m$ showing raw data points and a 50 point moving average. (b) All measured spectra between the center of the FoV and $r_3 = 2\,mm$. The gray line indicated a reduced response at higher wavelengths thought to be primarily due to the spectrally-dependent CCD QE and the black arrow indicates the effects of atmospheric CO_2 absorption that occurred at mid-IR wavelengths.

A correction factor was constructed to account for both effects in the simulations. Figure 4.13 shows a plot of the with predictions of the spectral influence of both effects and the corresponding correction factor. The red line shows the transmission spectra of CO_2 computed assuming atmospheric conditions, a 417 ppm concentration of CO_2, 18 cm absorption path length, and convolved with a 1 nm FWHM Gaussian shape to roughly approximate the

effect of instrument broadening by the spectrometer. The blue line shows the near-IR spectral QE curve for the Newton CCD camera with a "BU2" sensor designation as reported by Andor Technologies LTD. The dashed red line shows the blackbody spectral emission transformed to upconverted wavelengths and normalized by its strength at $839.5\,\mathrm{nm}$. To construct the correction factor, the of the product of the three effect curves was taken and then normalized to unity at $839.5\,\mathrm{nm}$ to match the peak response observed by the measured spectra in Figure 4.12. The resulting correction factor is shown by the black line in Figure 4.13 and was multiplied with the simulated upconverted spectra at every radial location to correct the simulated tuning curve.

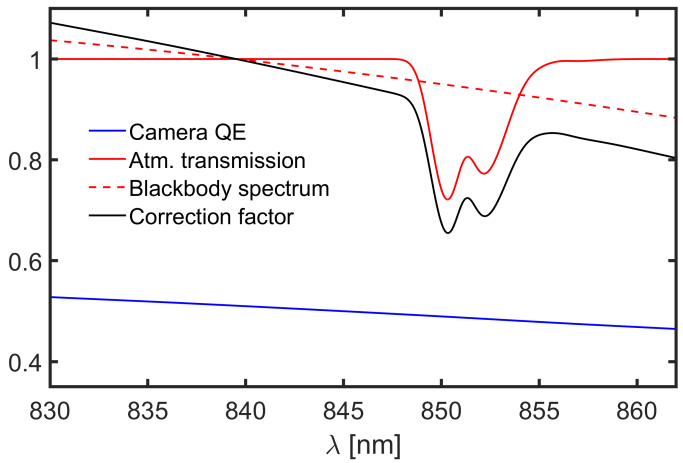

Figure 4.13: A plot of spectral effects due to atmospheric absorption (solid red line), spectral variation in blackbody emission strength (dashed red line), and spectrally-dependent CCD QE (blue line) shown relative to upconverted wavelength. These were used to generate a correction factor that was applied to the simulated UCI response (black line).

A comparison of the simulated and measured upconverted tuning curves for the $\Lambda_P = 23.415\,\mu\mathrm{m}$ poling period is shown in Figure 4.14, again with the simulated response on the left and the measured response on the right. The curves show excellent agreement in the wavelengths of peak response at each image plane location, the predicted FoV, and the effects of attenuation sources including reduced blackbody strength at longer wavelengths and CO_2 absorption near upconverted wavelengths of $850\,\mathrm{nm}$. The agreement of the two curves serves to validate the spatial-spectral model and the measurement of the deviation of the poling period from the design length that was examined in section 4.1.

The capability of the non-collinear phase-matching model of section 2.3.1 to predict spatial-spectral coupling effects is demonstrated through the experimental comparisons in Figures 4.11 and 4.14. The ability to make these high-accuracy predictions is critical to the application of UCI in many combustion diagnostics because of the unique properties of this

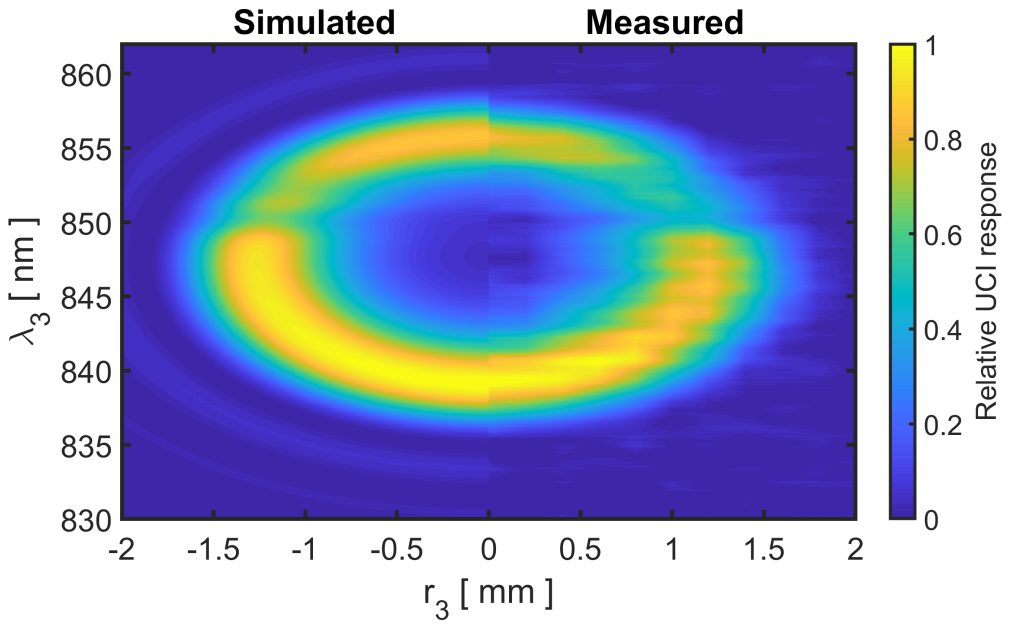

Figure 4.14: A comparison of simulated and measured near-IR response of the UCI system for upconversion of wavelengths near $4.2\,\mu\mathrm{m}$. The simulation assumes a poling period of $\Lambda_P = 23.415\,\mu\mathrm{m}$ and a crystal temperature of $22\,^{\circ}\mathrm{C}$. The simulation also accounts for the effects of atmospheric absorption and spectral QE variation of the CCD camera.

detection method. In addition to verifying the poling period discrepancy detected by blackbody imaging in section 4.1, these results show that the $\Lambda_P = 22.45\,\mu\mathrm{m}$ is manufactured close to its design length, something that could not have been detected with blackbody imaging because of its relatively uniform response to blackbody illumination.

4.3 Flat flame measurements

The UCI system was used to perform species-specific passive thermal imaging measurements in the RDC that are described in Chapter V. Before deploying the UCI system to make those measurements it was important to test how the system responds to those types of signals and identify the appropriate way to perform the measurements. This section presents UCI measurements that were taken in an approximately one-dimensional "flat flame" stabilized on a McKenna burner (a porous-plug type design with a $6\,\mathrm{cm}$ diameter) to characterize its response to passive thermal radiation from combustion environments. Before discussing the measurements, it is important to examine the physical laws that describe the thermal radiation process in hot gases.

The spectral intensity of passive thermal radiative emissions in gases is governed by Kirchoff's law of thermal radiation. This law is derived by considering a spectrally absorb-

ing gas and enforcing thermal equilibrium between it and a nearby blackbody with respect to radiative energy transfer. According to Kirchoff's law, the spectral photon flux emitted from a gas, $L_{q,\lambda}$ which will be treated with units of photons/$\mathrm{s}/\mathrm{m}^2/\mathrm{sr}/\mu\mathrm{m}$, evolves along the optical path length within a gas as [66]:

$$\frac{\mathrm{d}L_{q,\lambda}}{\mathrm{d}z} = \alpha_\lambda(z)\left[L_{\mathrm{q,B}}(\lambda, T(z)) - L_{q,\lambda}(z)\right] \tag{4.2}$$

where α_λ is the spectral absorption coefficient for the local gas conditions, $L_{\mathrm{q,B}}$ is the Planck curve at the local gas temperature, and z is the distance along the path length through the emitting gas volume. The spectral absorption coefficient is the sum of the corresponding absorption coefficients for each species present in the gas such that $\alpha_\lambda = \sum_j \alpha_{\lambda,j}$ where $\alpha_{\lambda,j}$ is the absorption coefficient associated with the j^{th} gas species. The value of $\alpha_{\lambda,j}$ at a particular set of local gas conditions can be expressed as:

$$\alpha_{\lambda,j} = X_j \frac{P}{k_{\mathrm{B}} T} \sigma_j(\lambda, P, T, \{X_i\}) \tag{4.3}$$

where X_j is the mole fraction of the gas, σ_j is the spectral absorption cross-section of the j^{th} species which has a dependence due to line-broadening effects on the local gas conditions including the composition of collisional partners as specified by $\{X_i\}$. Here the absorption coefficient for a particular species is seen to be directly proportional to the concentration of that species and the total gas pressure and inversely proportional to the gas temperature. These trends are important and will be seen in predictions of spectral radiance shown below.

To find the thermal spectral radiance at the output end of the optical path length, the expression for $\frac{\mathrm{d}L_{q,\lambda}}{\mathrm{d}z}$ must be integrated along the optical path if the gas conditions are spatially inhomogeneous. If the gas conditions, including temperature, pressure, and species composition, are constant along the optical path length, l, then the result becomes:

$$L_{q,\lambda}(l) = L_{\mathrm{q,B}}(\lambda, T)\left[1 - e^{-\alpha_\lambda l}\right] \tag{4.4}$$

The Planck curve for a particular temperature in terms of spectral photon flux takes the form was expressed previously in Eq. (4.1). The expressions in Eq. (4.4) and (4.1) explain how emitted thermal radiation will vary with the thermodynamic state of the gas. The Planck curve acts as an upper bound for emission intensity that is reached only for optically thick conditions. This shows that increasing either the emitter concentration or the total gas pressure while holding other properties constant can be expected to increase the strength of thermal emissions as it increases optical depth of the gas, which is proportional to α_λ. Variations in temperature alone will exhibit the influence of competing effects.

To examine predicted trends in thermal radiation strength as would be measured by the UCI system, the model described in section 2.6 was used to simulate the response of the UCI system to thermal radiation from H_2O and CO_2 at various gas conditions. Because the flat flame measurements were performed at atmospheric pressure conditions, the two gas properties that dictate emission signal strength were temperature and emitting species concentration. The model was used to simulate ranges of these two variables that were expected to be observed in the flat flame based on previous measurements [86] and Cantera simulations [95]. Figure 4.15(a) shows a contour plot map of the predicted UCI response variation with temperature and H_2O concentration for detection near $2.55\,\mu\mathrm{m}$ achieved using the $\Lambda_P = 19.36\,\mu\mathrm{m}$ poling period at a crystal temperature of $21\,^{\circ}\mathrm{C}$. Note the discrepancy between the poling period used for these simulations and the design value of $\Lambda_P = 19.4\,\mu\mathrm{m}$. This was another (relatively small at 0.2%) apparent manufacturing error in the mean poling period that is discussed below in section 4.3.1. Figure 4.15(b) shows a similar contour plot map of predicted UCI response to CO_2 emissions near $4.2\,\mu\mathrm{m}$ measured using the $\Lambda_P = 23.415\,\mu\mathrm{m}$ poling period at a crystal temperature of $21\,^{\circ}\mathrm{C}$.

The overall trends in both UCI response maps shown in Figure 4.15 are similar. For low temperatures, below approximately $500\,\mathrm{K}$ to $700\,\mathrm{K}$, the gas generates low radiative signal strength, which is too weak to be detected. As temperature increases past that threshold, the signal becomes significant enough to be detected and the signal strength rises with increasing temperature at all emitter concentrations until it peaks for temperatures near $2000\,\mathrm{K}$ to $2500\,\mathrm{K}$. In that temperature range the signal levels are relatively constant with temperature, demonstrating the nonlinear trend that results from the competing influences of the Planck curve and the optical depth of the gas. For all temperatures, increasing emitter concentration increases the detected signal level because this always increases the optical density of the gas.

To test the capability of the UCI system to perform single-shot measurements of thermally excited mid-IR radiation in combustion environments images were captured within a methane/air flat flame stabilized on a McKenna burner. The burner was operated with an equivalence ratio of 1.07 and a reactant velocity at the burner surface of $38\,\mathrm{cm/s}$. The temperature profile for this flame has been characterized by a previous study using OH absorption spectroscopy [86] and has been found to exhibit a maximum gas temperature of approximately $2150\,\mathrm{K}$. Cantera simulations were found to be in good agreement with the temperatures measured by absorption spectroscopy and also predicted H_2O and CO_2 concentration at each Height Above the Burner (HAB). Plots of the predicted temperature emitter concentrations as a function of HAB are shown in Figure 4.16(a). These data can be used to predict UCI response as a function of HAB by interpolating from the response

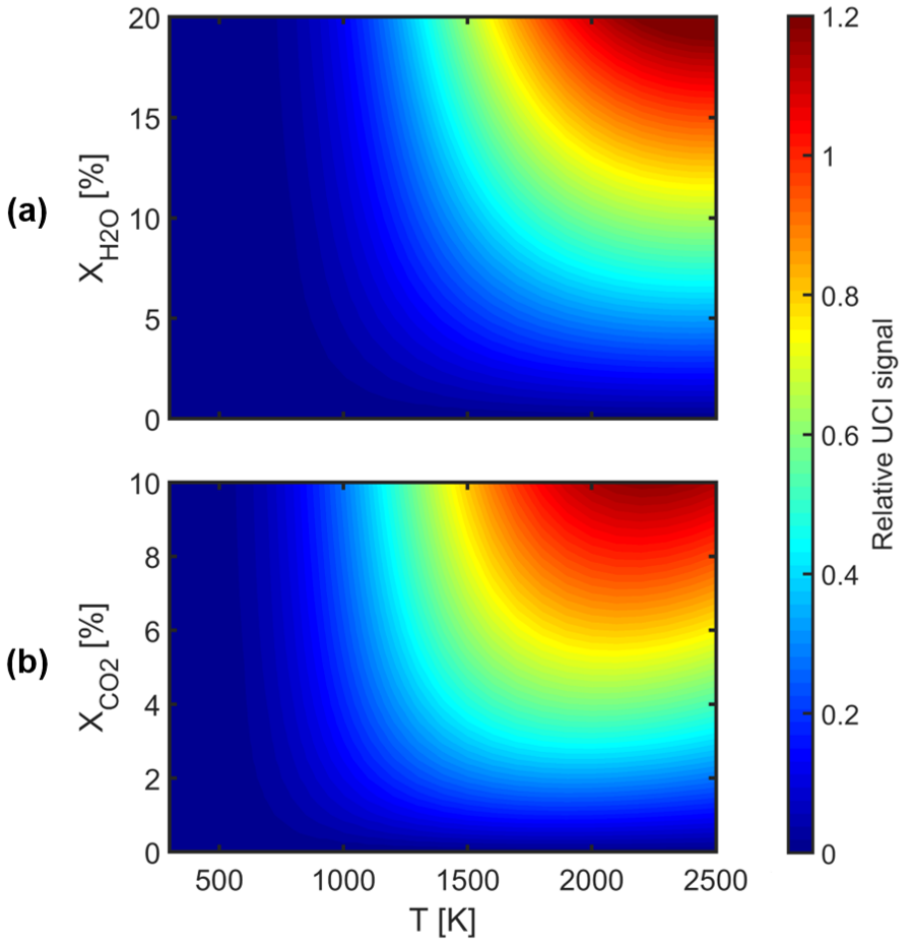

Figure 4.15: Contour plots showing the predicted variation in predicted UCI signal strength at the center of the FoV with changes in emitter concentration and temperature. (a) H_2O thermal radiation emission detected with a $19.36\,\mu\mathrm{m}$ poling period normalized by the signal at $T = 2000\,\mathrm{K}$ and $X_{H2O} = 18\%$. (b) CO_2 thermal radiation emission detected with a $22.415\,\mu\mathrm{m}$ poling period normalized by the signal at $T = 2000\,\mathrm{K}$ and $X_{CO2} = 8\%$.

maps shown in Figure 4.15. The resulting predictions of UCI response in Figure 4.16(b) as a function of HAB and scaled for clarity. The response maps in Figure 4.15 were shown only for detection at the center of the FoV for the sake of clarity, but the predicted signals in Figure 4.16(b) are shown for both the center of the FoV (solid lines) and $r_3 = 1\,\mathrm{mm}$ (dashed lines) for comparison.

The Cantera simulations show that the properties in the flame and the predicted UCI response are relatively constant for HABs of greater than $1\,\mathrm{mm}$. This indicates that the mid-IR illumination can be expected to be relatively uniform outside of $1\,\mathrm{mm}$ from the burner surface. The UCI system could resolve these sub-millimeter scale variations within the object plane of the system, however the fact that these measurements are integrated

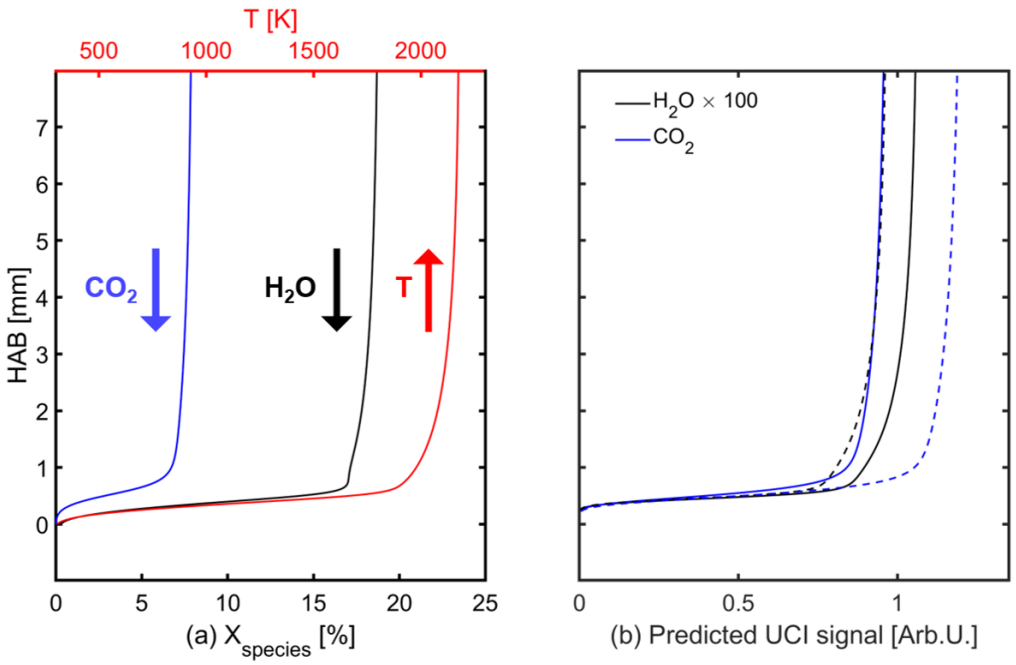

Figure 4.16: (a) A Cantera simulation of the mole fractions of CO_2 and H_2O (bottom axis) and temperature (top axis) as a function of height above the burner surface. (b) Predictions of the observed UCI signal for both CO_2 (blue lines) and H_2O (black lines, multiplied by 100) at the center of the FoV (solid lines) and $r_3 = 1\,\mathrm{mm}$ (dashed lines).

along the entire $5.4\,\mathrm{cm}$ path length through the cylindrical flame prevented full realization of the system's spatial resolution. For this reason, only the relatively homogeneous regions at HABs of greater than $1\,\mathrm{mm}$ will be examined in the UCI measurements. Comparison of the UCI response predictions at the center of the FoV and at $r_3 = 1\,\mathrm{mm}$ show differences in signal strength, but little difference in the ratio of the signal at the two r_3 locations with changing HAB. For this reason, differences in the signal strength across the FoV will be primarily due to UCI spatial-spectral coupling effects rather than variation in the local fluid properties.

For experimental measurement of the flat flame the UCI system was operated with poling periods of $\Lambda_P = 19.36\,\mu\mathrm{m}$ and $\Lambda_P = 23.415\,\mu\mathrm{m}$ to target thermal radiation from H_2O and CO_2. The crystal was maintained at room temperature ($21\,^\circ\mathrm{C}$) to simplify operation of the system and avoid cross-talk from CO_2 in the case of the $\Lambda_P = 19.36\,\mu\mathrm{m}$ measurements, which can occur when tuning to H_2O emissions near $2.7\,\mu\mathrm{m}$ at elevated crystal temperatures. The measurements were made with the laser operated in long-pulse mode at approximately $40\,\mathrm{mJ}$ per pulse since the flow field was steady and temporal resolution was not a concern. Examples of single-shot pulsed UCI measurements of radiative emissions from the McKenna burner flame are shown in Fig. 4.17(a) for the H_2O bands and (b) for

the CO_2 bands. The location of the surface of the burner is shown by the green line at HAB $= 0$ as was determined by back-illuminating the scene with a uniform blackbody source. Some signal is observed below the surface of the burner. This is due to mid-IR reflections off of the polished stainless-steel angled surface around and below the edge of the burner.

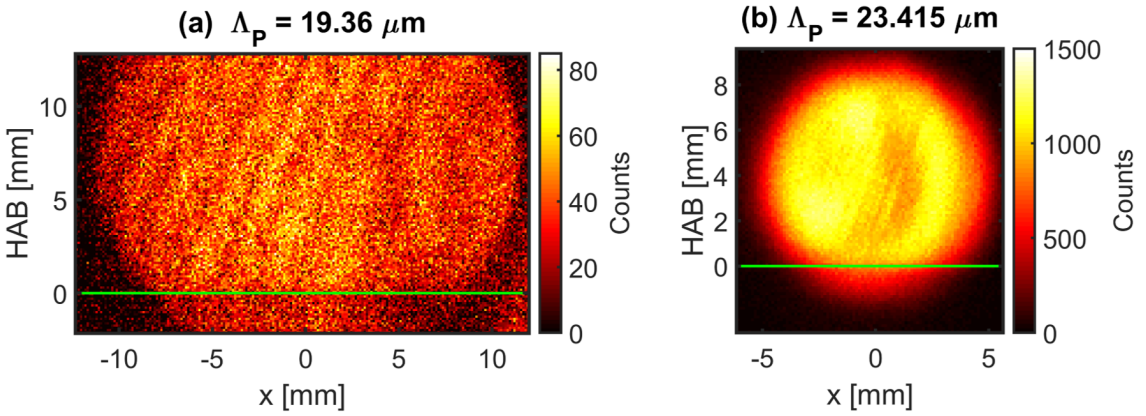

Figure 4.17: Examples of single-shot passive thermal imaging above a CH_4-air McKenna burner flame using (a) a poling period of $\Lambda_P = 19.36\,\mu m$ to detect emissions from H_2O and (b) a poling period of $\Lambda_P = 23.415\,\mu m$ to detect emissions from CO_2. A comparison of simulated and measured near-IR response of the UCI system for upconversion of wavelengths near $4.2\,\mu m$. Green lines indicate the surface of the burner.

The primary reason for the disparity between the signal strengths of the CO_2 and H_2O emissions measurements is the difference in spectral bandwidths at the two QPM wavelengths. The UCI spectral bandwidth, see Fig. 2.11, is larger by a factor of 45 at $4.2\,\mu m$ compared to the value at $2.55\,\mu m$. This difference in spectral response combined with the stronger CO_2 radiative emissions generate approximately 25 times the signal for passive imaging of CO_2 compared to H_2O. The SNRs of these single-shot images were approximately 35 for CO_2 imaging and 3.5 for H_2O imaging. The large path through the flame, approximately $5.4\,cm$, creates an optically-dense environment at both of the target wavelength bands in these measurements. The dependence on path length, l, shown in Eq. (4.4) indicates that this long path example can be considered a kind of best-case scenario for signal strength compared to the shorter paths seen in situations like the RDC combustion channel ($l = 7.6\,mm$). Additionally, the long-pulse mode operation of the pump laser at $40\,mJ$ per pulse provided stronger signals than could be achieved with the temporally resolved scheme described in section 3.3.2. Because of these reasons, **measurements in the RDC that are described in Chapter V were performed only for CO_2 radiative emissions as H_2O signals would be too weak for single-shot measurements**.

These measurements also clearly exhibit the spectral fringing phenomenon previously

described in section III. The fringe pattern is more pronounced in the measurements near $2.55\,\mu\mathrm{m}$ than those near $4.2\,\mu\mathrm{m}$ primarily because of the differences in spectral bandwidth of the two measurements. The longer wavelength detection exhibits a larger bandwidth that washes out the fringing that occurs with the greatest strength for nearly monochromatic light. This underscores why it is difficult to correct for this fringing pattern with flat-fielding because the flat-field light must exhibit the same spectral content as the ultimate target or the generated fringe pattern will be different.

4.3.1 Spectral structure in H_2O thermal emissions

In addition to examining the performance of the UCI system for single-shot thermal imaging measurements, multiple exposures can be averaged together to reduce noise and examine variations in response due to spatial-spectral coupling effects. Because of its broadband spectral acceptance and the particular spectral signature of CO_2, UCI of the flat flame radiation using the $\Lambda_P = 23.415\,\mu\mathrm{m}$ poling period does not differ much from similar measurements of the uniform blackbody source. Measurements using the $\Lambda_P = 19.36\,\mu\mathrm{m}$ poling period to detect H_2O emissions exhibit a more feature-rich spatial-spectral response field because of the distributions of strong H_2O bands and the more narrowband response of the UCI system at those wavelengths.

To examine spatial spectrum coupling in the H_2O thermal imaging measurements 25 consecutive single-shot exposures were averaged together to decrease the effects of noise in the images. This ensemble average is shown in Figure 4.18(a). The spectral fringing pattern must also be corrected out of the image because its amplitude is significantly larger than the variations caused by spatial-spectral coupling. Figure 4.18(b) shows an image of the FoV with the flame extinguished and back-illumination provided by a uniform blackbody source place behind the combustor. These images were how the surface of the burner was located in Figure 4.17. Because the upconverted signals produced by the $\Lambda_P = 19.36\,\mu\mathrm{m}$ poling period are narrowband ($0.57\,\mathrm{nm}$ bandwidth) the spectral fringing produces approximately the same pattern for images of thermal gas emissions that it does for imaging of a uniform blackbody source. The ratio of the flame emission image in Figure 4.18(a) to the blackbody image in Figure 4.18(b) to produce the ratio image in Figure 4.18(c) that eliminates most of the spurious variation due to spectral fringing. This was done with a 700 count minimum threshold applied to the blackbody image to avoid dividing by small values in non-illuminated pixels.

The ratio image in Figure 4.18(c) shows the concentric rings in the image that are characteristic of spatial-spectral coupling in the response of the UCI system to uniform

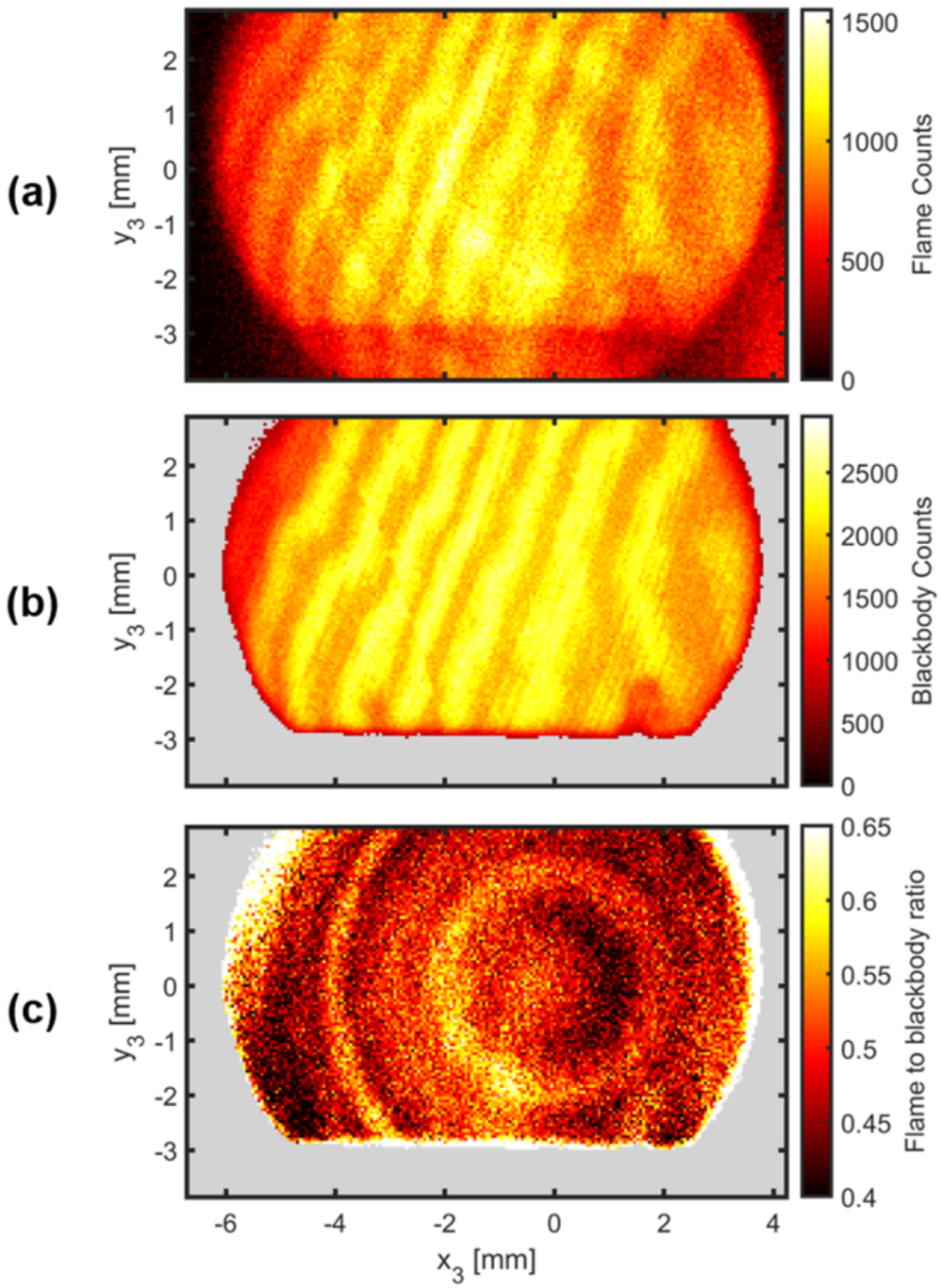

Figure 4.18: A 25 frame average of passive thermal imaging in the flat flame using the $\Lambda_P = 19.36\,\mu m$ poling period shown as (a) the signal from the flame, (b) the signal from a uniform blackbody source at $800\,^{\circ}C$ behind the burner with a 700 count threshold, and (c) a ratio of the two previous signals.

mid-IR fields with peaks in their emission spectra. The coordinates in Figure 4.18 are shown in terms of image plane distance from the central axis of the UCI imaging system

rather than position relative to the burner surface. The ratio image shows that the center of the FoV was approximately centered vertically between the burner surface and the upper limit of the sensor array and slightly to the right of the middle of the clear aperture of the imaging system. The location of the FoV center was determined by fitting circles to the rings at approximately $r_3 = 2\,\mathrm{mm}$ and $r_3 = 4\,\mathrm{mm}$. The ratio image could then be plotted as a function of r_3 of each pixel and compared to simulations of a uniform emitter, as was done above in Figure 4.2.

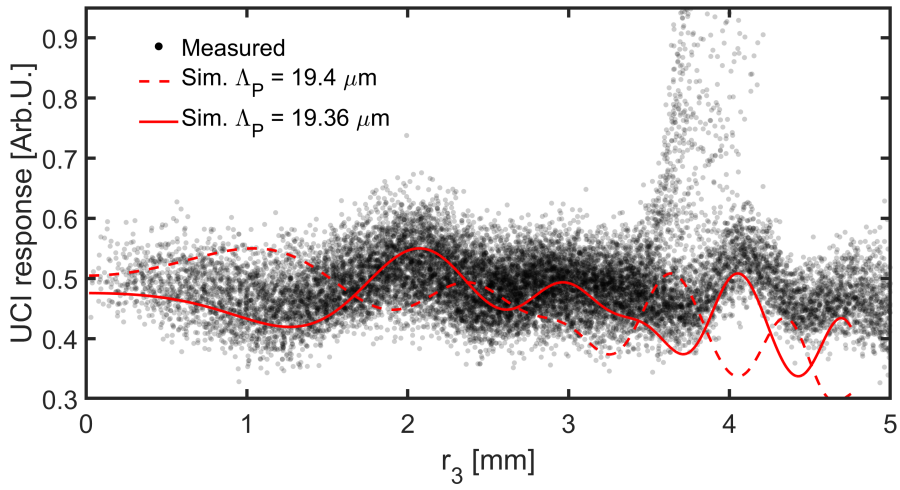

Figure 4.19: A comparison of the radial variation in the measured (black dots) H_2O thermal radiation signal in the flat flame to simulations assuming poling periods of $\Lambda_P = 19.4\,\mu\mathrm{m}$ (dashed red line) and $\Lambda_P = 19.36\,\mu\mathrm{m}$ (solid red line).

Figure 4.19 shows a plot of the measured response at each pixel (black circles) in ratio image as a function of the magnitude of the pixel's r_3 in the image plane. The plot omits points within 8 pixels of the burner surface because of aberrated occlusion of the out-of-focus blackbody illumination by the burner that caused unreliable blackbody radiation response. The very large values (above 0.6) seen between $r_3 = 3.5\,\mathrm{mm}$ to $4.2\,\mathrm{mm}$ in the data plot are due to the degraded blackbody image quality at the left and right edges of Figure 4.18(b) and should be ignored.

The uniform field UCI response model described in section 2.6 was used to simulate UCI measurements of thermal emission from H_2O at a gas temperature of $2080\,\mathrm{K}$ and an H_2O mole fraction of 18%, which are representative of the environment in the flat flame. Quantitative predictions from the model of the ratio between the flame emission signal strengths and blackbody response signal strengths were not relevant because the flat flame burner in Figure 4.18(a) and the blackbody source in Figure 4.18(b) were at significantly different distances from the imaging system's object plane and therefore could not be com-

pared due to diffraction effects. Instead, the magnitudes of the model results were arbitrarily scaled for clarity of the comparison of simulated and measured spectral response shapes.

Simulated results computed assuming the design poling period length of $\Lambda_P = 19.4\,\mu m$ and crystal temperature of $21\,^{\circ}C$ are shown by the dashed red line in Figure 4.19. There was significant disagreement between the modeled response with the design poling period and the observed response from the flat flame measurements. The model predicted a peak near $r_3 = 1\,mm$ where a trough is observed and predicted a trough near $r_3 = 4\,mm$ where a peak was observed. This evidence suggested that actual poling period in the crystal was different from the design poling period length in a similar way to the discrepancy identified in section 4.1.

Another simulation was computed assuming an alternative poling period of $\Lambda_P = 19.36\,\mu m$ at the same crystal temperature as shown by the solid red line in Figure 4.19. The model predictions using this poling period showed good agreement with the experimental observations. This included accurate prediction of the relative response near the center of the FoV, as well as the locations of peaks (near $r_3 = 2.1\,mm$, $3.0\,mm$, $4.1\,mm$, and $4.7\,mm$) and troughs (near $r_3 = 1.3\,mm$, $2.7\,mm$, $3.8\,mm$, and $4.5\,mm$). The accuracy of these predictions led to the conclusion that the true poling period in the crystal used for these measurements was $\Lambda_P = 19.36\,\mu m$, a 0.2% average error along the length of crystal that is within the range that might be expected from the manufacturing process based on previous literature. Like the previous discrepancy identified in the poling period for CO_2 detection, this difference did not compromise the performance of the system, but as Figure 4.19 shows it is critical to account for these small differences in Λ_P to accurately predict UCI response.

4.4 Nichrome coil measurements

The spatial response of the UCI can be tested by imaging a mid-IR source with a known spatial illumination field. This is often generated by back-illuminating a target with a known spatial transmission pattern, such as the Air Force 1951 resolution target standard, with mid-IR light and imaging the transmitted field. This approach was taken by Kehlet *et al.* to characterize their UCI system [33] at wavelengths near $3.3\,\mu m$. However, most commercially available resolution targets are manufactured with either soda-lime glass, N-BK7 glass, or UV quartz substrates that have poor or negligible transmission at longer wavelengths detected by the UCI system in this work, particularly at wavelengths above $4\,\mu m$. The alternative approach taken in this work is to use a blackbody emitter with a known

pattern of spatial illumination and imaging it with multiple poling periods in the system to assess spatial resolution and registration.

Specifically, a $150\,\mathrm{mm}$ length of nichrome wire (60% nickel, 80% chromium AWG 16 gauge wire) was wound into a coil shape and energized to create a spatially varying thermal glow at mid-IR wavelengths. The uncoiled ends of the wire were connected to electrodes that held the coil in the UCI system's FoV and provided a potential difference of approximately $3.5\,\mathrm{V}$ that produced temperatures estimated to be between $700\,^{\circ}\mathrm{C}$ to $900\,^{\circ}\mathrm{C}$ with emissivities between 0.65 to 0.95 depending on oxidation level [96]. The coil was formed of six loops that provided spatial variation in the mid-IR field and the AWG 16 gauge wire had a diameter of $1.29\,\mathrm{mm}$ that allowed the capability of the system to resolve millimeter-scale structures to be assessed.

Images of the heated nichrome coil were captured using both the $\Lambda_{\mathrm{P}} = 22.45\,\mu\mathrm{m}$ and $\Lambda_{\mathrm{P}} = 23.415\,\mu\mathrm{m}$ poling periods in the UCI system. These were captured using long-pulse mode operation of the pump laser with pulse energies of approximately $40\,\mathrm{mJ}$ and with a crystal temperature of $21\,^{\circ}\mathrm{C}$. These were ensemble-averaged over 250 consecutive exposures to reduce the effects of noise in the measurements. Examples of the coil images with each of the poling periods are shown in Figure 4.20 with spatial positions shown in image plane coordinates.

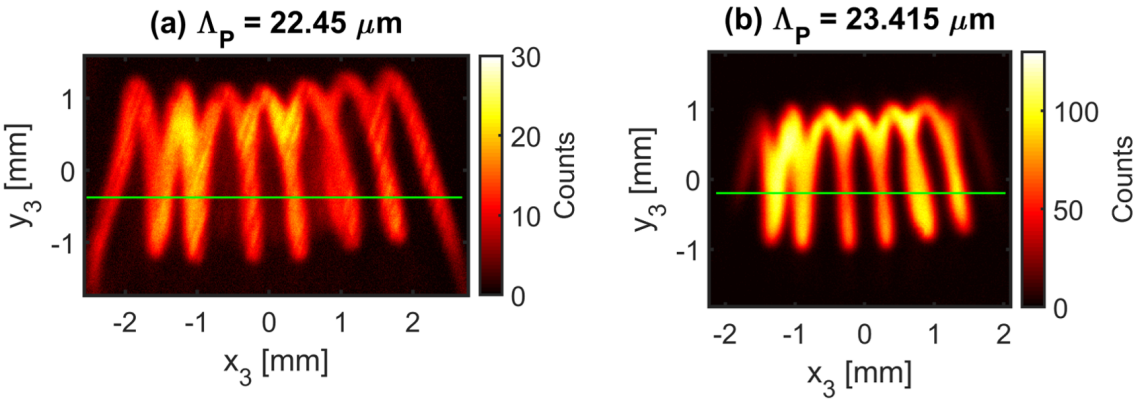

Figure 4.20: Images of a hot nichrome wire capture using (a) a $\Lambda_{\mathrm{P}} = 22.45\,\mu\mathrm{m}$ poling period and (b) a $\Lambda_{\mathrm{P}} = 23.415\,\mu\mathrm{m}$ poling period. Greens lines indicate the lines sampled for the plot shown in Figure 4.21.

Because its FoV is only limited by the clear aperture of the imaging system, the $\Lambda_{\mathrm{P}} = 22.45\,\mu\mathrm{m}$ detection can capture all six loops of the coil and the straight lengths of wire that are heading to the electrodes at the left and right edges of the frame. In contrast, the $\Lambda_{\mathrm{P}} = 23.415\,\mu\mathrm{m}$ poling period FoV is only able to capture the six loops and fades in response at the periphery were the straight wire sections are due to spatial-spectral coupling effects

that limit its FoV. Additionally, the UCI de-magnification effect described in section 2.3.1 and predicted by Eq. (2.24) cause the image of the coil to be smaller in size in the image plane when detected with the $\Lambda_P = 23.415\,\mu m$ poling period compared to detection with the $\Lambda_P = 22.45\,\mu m$ poling period despite both using the same imaging optics. Careful examination of coil images reveals that the vertical height of the coil in Figure 4.21(a) is slightly greater than $2\,mm$ while the height of the coil in Figure 4.21(b) is no more than $2\,mm$. This demonstrates the predicted de-magnification effect that grows with increasing mid-IR detection wavelength as a consequence of noncollinear phase-matching requirements.

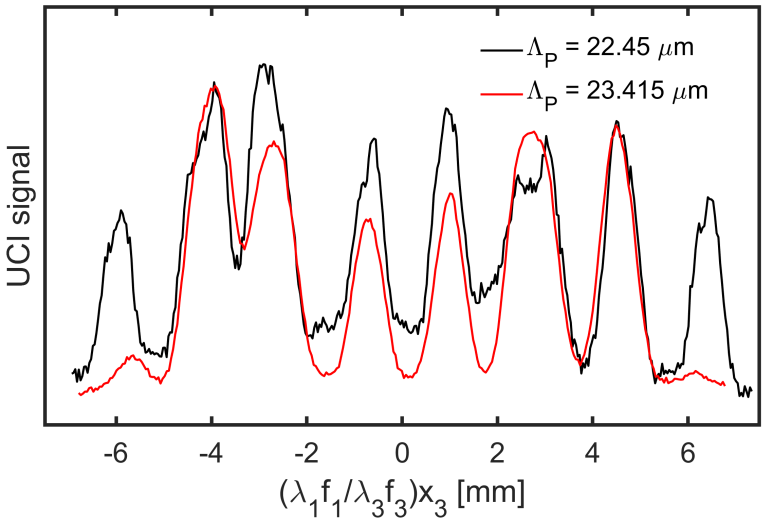

Figure 4.21: A sample of horizontal positions from the images in Figure 4.20 as indicated by the green lines. The image plane distances have been transformed into object plane coordinates using the UCI de-magnification relationship given in Eq. (2.24).

The de-magnification relationship in Eq. (2.24) can be used to directly compare the images at the two poling periods, assess the spatial resolution of the system, and project the images into object plane coordinates. For this purpose, a horizontal sampling line was defined across each of the coil images that was just below the center of the FoV as indicated by the green lines in Figure 4.21. This sampling line was selected because it overlaps all six loops and specifically samples the middle two loops where they overlap themselves to be approximately the width of the wire ($1.29\,mm$). The signal strength along each of these lines was sampled and the image plane coordinates were transformed by multiplying them by $(\lambda_1 f_1/\lambda_3 f_3)$. The focal lengths of the objective and detector lens were the same as described in the system design in section 2.5 ($f_1 = 100\,mm$ and $f_3 = 150\,mm$) and representative values were used for the mid-IR and detection wavelengths of the $\Lambda_P = 22.45\,\mu m$ poling period ($\lambda_1 = 3.295\,\mu m$ and $\lambda_3 = 804\,\mu m$) and the $\Lambda_P = 23.415\,\mu m$ poling period

($\lambda_1 = 4.15\,\mu\mathrm{m}$ and $\lambda_3 = 848\,\mu\mathrm{m}$). Note that non-negligible bandwidth of the upconversion process, particularly for the $\Lambda_P = 23.415\,\mu\mathrm{m}$ poling period, can cause additional chromatic aberrations that could potentially degrade image quality, though they were not significant in this system.

The resulting signal variation along the sampled lines are shown in Figure 4.21. The black line shows the signal sampled from the $\Lambda_P = 22.45\,\mu\mathrm{m}$ poling period image in Figure 4.21(a) and the red line shows the sampling from the $\Lambda_P = 23.415\,\mu\mathrm{m}$ poling period image in Figure 4.21(b), both in transformed coordinates. These transformed coordinates are equivalent to object plane coordinates according to Eq. (2.24) and so the observed variation can be seen as representative of the physical size of the coil features. The fact that the two samples align well in the transformed coordinates (less than $110\,\mu\mathrm{m}$ difference in the locations of features) validates the UCI de-magnification relationship for transforming upconverted image plane coordinates to common object plane coordinates. The middle two peaks in Figure 4.21 demonstrate the capability of the system to spatially resolve millimeter-scale objects. The interval between 10% of the peak value for both of the peaks in the sample shown by the red line ($\Lambda_P = 23.415\,\mu\mathrm{m}$ poling period) were $1.3\,\mathrm{mm}$, right in line with the actual diameter of the nichrome wire.

It should be noted that the interference observed between the central peaks in the sample shown by the black line ($\Lambda_P = 22.45\,\mu\mathrm{m}$ poling period) is likely due to cross-talk from the $\Lambda_P = 23.415\,\mu\mathrm{m}$ poling period being energized by the wings of the pump beam that is aligned with the adjacent poling period (the poling periods are arranged side-by-side in the crystal as shown in Figure 2.10 in order of increasing poling period with $200\,\mu\mathrm{m}$ of unpoled material separating them). A similar interference was observed while performing absorption measurements described in Chapter VI and was eliminated by placing a knife-edge in front of the crystal to occlude the pump beam from entering the unintended poling period. This motivates future designs to either incorporate a movable aperture into the design of the crystal mount or space the poling periods farther apart on the crystal chip.

4.5 Summary of measured poling period deviations

As discussed in the sections above, several of the characterization experiments were highly sensitive to the precise average poling period along the length of the crystal. The effects on measured signals and comparisons with model predictions could be used to infer the average poling period that was realized in the physical crystal. A comparison of the measured and design poling periods for the ppLN crystal in this work are shown in Table 4.1. The measurements were capable of inferring poling period deviations of greater than $5\,\mathrm{nm}$. The

Table 4.1: Measured poling periods based on the results of characterization measurements.

Design Λ_P	Measured Λ_P ($\pm 5\,\mathrm{nm}$)	$\Delta\Lambda_P$ ($\pm 5\,\mathrm{nm}$)
$14.5\,\mu\mathrm{m}$	Not measured	Not measured
$17.85\,\mu\mathrm{m}$	Not measured	Not measured
$19.4\,\mu\mathrm{m}$	$19.36\,\mu\mathrm{m}$	$-40\,\mathrm{nm}$
$22.45\,\mu\mathrm{m}$	$22.45\,\mu\mathrm{m}$	$0\,\mathrm{nm}$
$23.4\,\mu\mathrm{m}$	$23.415\,\mu\mathrm{m}$	$15\,\mathrm{nm}$

two shortest poling periods, Λ_P = $14.5\,\mu\mathrm{m}$ and Λ_P = $17.85\,\mu\mathrm{m}$, were not tested because of the low signal strengths that they would have produced in the measurement techniques that were used.

CHAPTER V

Pulsed Mid-IR UCI of CO_2 Thermal Radiation in an RDC

This chapter presents the results of pulsed mid-IR UCI measurements of time-resolved CO_2 thermal radiation emissions within the flow field of an operating RDC. Before examining the results of the measurements, section 5.1 provides a discussion of how the recorded UCI signals depended on conditions within the RDC flow field. These details are critical to understanding and interpreting the results of UCI measurements, both in terms of what they indicate about the RDC flow field and the limitations of the techniques that were used.

Results are first presented from what is referred to as the *cycle phase* perspective in section 5.5. This representation trades most of the spatial resolution of the UCI system for the ability to examine large-scale structures in the measured signals. This may seem counter-productive since the capability to achieve high spatial resolution in the highly transient environments of the RDC was a primary motivation for implementing the pulsed UCI measurements. However, this representation is important because it both demonstrates the ability of this UCI approach to study large-scale structures despite its limited FoV and gives valuable context to the individual UCI frames that are examined later. The individual UCI frames shown in section 5.6 that capture small structures and sharp gradients near the detonation wave front demonstrate the capability of pulse mid-IR UCI to achieve high spatiotemporal resolution within unsteady combustion environments.

5.1 Passive thermal imaging in the RDC

The high temperatures and pressures associated with the detonation cycle in RDCs are conducive to passive imaging of thermal radiation from gases at mid-IR wavelengths. By selecting precise wavelength ranges to detect, these measurements target the emission bands of particular gas species to observe their distribution or the local gas properties. Rankin *et*

al. [59] have previously demonstrated passive mid-IR imaging as a diagnostic tool in RDCs using a direct detection mid-IR camera with a bandpass filter to isolate spectral emissions from H_2O. Those measurements were made with a large FoV in an optically-accessible RDC such that the large-scale structures of RDC flows could be identified and studied. The major limitation of those measurements was the $5\,\mu s$ integration time that prevented resolution of events and spatial structures near the supersonic detonation wave front. The measurements presented in this chapter are intended to complement those previous mid-IR imaging studies. The limited optical access of the RDC used in this work and the limited FoV of the UCI system prevented the same type of large-scale investigations from being made. Instead, the high spatial and temporal resolution of the UCI system was leveraged to investigate small structures and rapid events near the detonation wave front in RDCs.

5.1.1 CO_2 doping

The flat flame measurements described in Chapter IV and shown in Figure 4.17 compared the capability of the UCI system to perform passive thermal imaging of emissions from H_2O and CO_2 in a combustion environment. The conclusion was that emissions from H_2O would not produce sufficient signal strength for single-shot measurements due to the UCI system's limited spectral bandwidth, but that CO_2 was a promising candidate as a target species.

The mid-IR imaging study by Rankin *et al.* [59] observed emissions from nascent H_2O that naturally evolved as a product of hydrogen-air combustion. Mid-IR imaging of CO_2 emissions could be performed in a similar way for hydrocarbon-fueled operation of an RDC where CO_2 will be produced in significant quantities as a combustion product to generate measurable signals. However, surveys of operational conditions in the RDC used in this work showed that with the system configuration available for UCI measurements stable operation could not be achieved with significant hydrocarbon fueling. Modifications to the facility are currently being performed to enable a wider range of stable operation in the RDC, including hydrocarbon-fueled operations, however they were not available for passive thermal imaging tests. This limited the cases that could be explored in this work to hydrogen-air operation of the combustor.

Because CO_2 was not produced during hydrogen-air combustion in the RDC, it needed to be doped into the reactant streams to achieve the concentrations required for effective passive thermal imaging. Tracer-based optical diagnostic methods, such as acetone PLIF [52], typically dope one of the two reactant streams in a non-premixed combustion system to observe the mixing process. In this case of passive thermal imaging, only the regions of

hot products that have already mixed and burned will be detectable, and so this approach cannot be used to monitor mixing processes. Instead, doping of one or the other reactant streams will have the effect of introducing ambiguity into the measurement in the form of uncertainty in the local emitter (CO_2) concentration due to the unobserved mixing process.

The approach taken in this work is to dope both the fuel and oxidizer reactant streams with the same concentration of CO_2 by volume. This creates an approximately constant concentration of CO_2 throughout the flow field to minimize uncertainty in emitter concentration. Figure 4.15 shows how signal strength is strongly affected by emitter concentration at a particular pressure, and so by fixing this concentration at a known value the UCI signal can be made a function of local temperature and pressure alone. Chemical reactions during the combustion process that do not conserve particle numbers will cause small variations in the mole fraction of CO_2 within the flow field, but Cantera-based simulations of detonations suggest that this will cause a relative variation of less than 10% of the doped CO_2 concentration.

Figure 5.1 shows a cross-section view in a radial plane of the RDC injection system. This shows the axial air inlet configuration with a one-sided constriction from the inner body forming a throat in the air stream (typically not choked) [48]. Fuel is injected at an angle from 120 individual injection ports inclined at an angle relative to the air stream. Both reactant streams are doped with the same concentration of CO_2 in the gas delivery upstream of the injectors. The height of the combustion channel ($H = 105\,\mathrm{mm}$) is measured from the axial midpoint of the air stream constriction (shown by the $z = 0$ dashed line).

The addition of significant amounts of CO_2 had significant impacts on the combustion process within the RDC. The CO_2 doped test cases could not be directly compared to other hydrogen-air RDC experiments or CFD simulations at equivalent conditions. This was evidenced by changes in the operational behavior of the RDC used in this campaign. The RDC achieved stable detonating operation over a smaller range of operational parameters, as the CO_2 appeared to have an inhibitory effect on the detonation process that might be intuitively expected. The CO_2 addition also appeared to either excite or suppress phenomenon including secondary combustion events [50] that may or may not have been observed for equivalent conditions without CO_2 addition. Experiments are currently ongoing to explore the effects of CO_2 that could not be reliably predicted at the time of writing this dissertation.

If the concentration of a target species is fixed, then the spectral attenuation coefficient, α_λ as defined in Eq. (4.3), will become depend only on local temperature and pressure (neglecting collisional line-broadening effects). Kirchoff's law of thermal radiation, discussed in section 4.3, therefore shows that in such a case the spectral radiance of uniform gas volume (the effects of inhomogeneous conditions is discussed below in section 5.1.2)

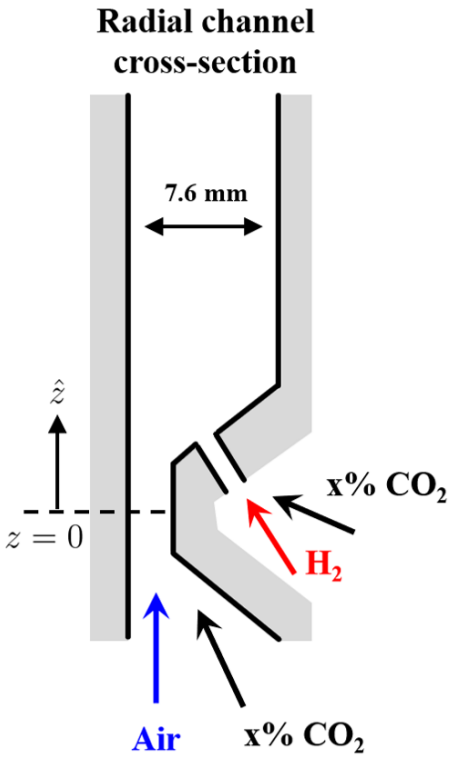

Figure 5.1: A cross-section in a radial plane of the RDC injection system with CO_2 addition in fuel and oxidizer streams.

will depend on the gas temperature, pressure, and the optical path length, l, through the gas volume. Here the emission conditions can be distinguished into two optical regimes that will determine the type of response that thermal radiation will exhibit with respect to variation in gas conditions. These are the *optically-thin* regime, defined as conditions where $\alpha_\lambda l \ll 1$ for relevant wavelengths, and the *optically-thick* regime, defined in this work as any conditions that do not fall into the optically-thick regime. If a volume of gas exists with conditions that place it in the optically-thick regime, then the nonlinear relationship shown in Eq. (4.4) will dictate its thermally-excited spectral radiance. If a gas volume can be reasonably considered to fall in the optically-thin regime, then the spectral radiance can be well-approximated by a linearized form of Eq. (4.4):

$$L_{q,\lambda}(l) \approx \tau_\lambda L_{\mathrm{q,B}}(\lambda, T) = X_j \frac{P\, l}{k_\mathrm{B} T} L_{\mathrm{q,B}}(\lambda, T) \sigma_j(\lambda, P, T, \{X_i\}) \tag{5.1}$$

where to consolidate notation the *optical depth* of the gas volume is defined as $\tau_\lambda = \alpha_\lambda l$. This shows that in the optically-thin regime, the spectral radiance is directly proportional to gas pressure while having a nonlinear temperature dependence.

The conditions in the RDC combustion channel that are most likely to fall into the

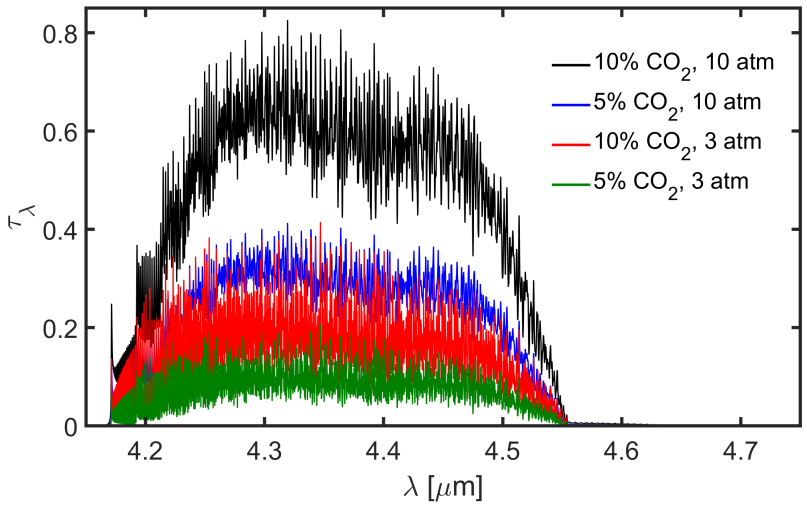

Figure 5.2: Comparison of optical depth curves calculated for gas at a temperature of $2500\,\mathrm{K}$ and a path length of $7.6\,\mathrm{mm}$ with different combinations of pressures and CO_2 concentrations.

optically-thick regime are found in the high-pressure regions immediately after the passage of the detonation wave front. Pressure transducer measurements in the RDC facility used in this work [97] and similar systems [98, 99] have recorded peak gas pressures of between $3\,\mathrm{atm}$ to $6\,\mathrm{atm}$, and simulations of laboratory-scale RDCs have predicted pressures of over $12\,\mathrm{atm}$ [63]. Depending on the level of CO_2 doping (either 5% or 10% by volume in this work), those pressures could generate optically-thick conditions in along the $7.6\,\mathrm{mm}$ channel width of the combustor at post-combustion temperatures. Figure 5.2 shows examples of τ_λ computed for the hot CO_2 vibrational bands near $4.2\,\mu\mathrm{m}$ that were targeted with the UCI system. These examples consider conditions associated with high ($10\,\mathrm{atm}$) and low ($3\,\mathrm{atm}$) estimates of the peak detonation wave pressure for both CO_2 doping levels at a representative post-combustion temperature of $2500\,\mathrm{K}$. The threshold for the optically-thick regime is typically taken to be near $\tau_\lambda \gtrapprox 0.1$, which is seen to be exceeded in all four cases shown in Figure 5.2. It should therefore be expected that regions near and immediately after the detonation wave front will exhibit nonlinear dependence of the UCI signal on local pressure. By contrast, regions of lingering hot combustion products in the post-expansion region of the flow field of RDC and the products of lower-pressure deflagration events will exhibit gas pressures of approximately $1\,\mathrm{atm}$. These regions will be representative of the optically-thin regime, and so both types of conditions will be present within the RDC.

Just as the variation in predicted UCI signal with gas conditions was visualized with contour plots in Figure 4.15 for measurements on the flat flame burner, the same can be done for UCI in the RDC combustion channel. Whereas the flat flame measurements had a

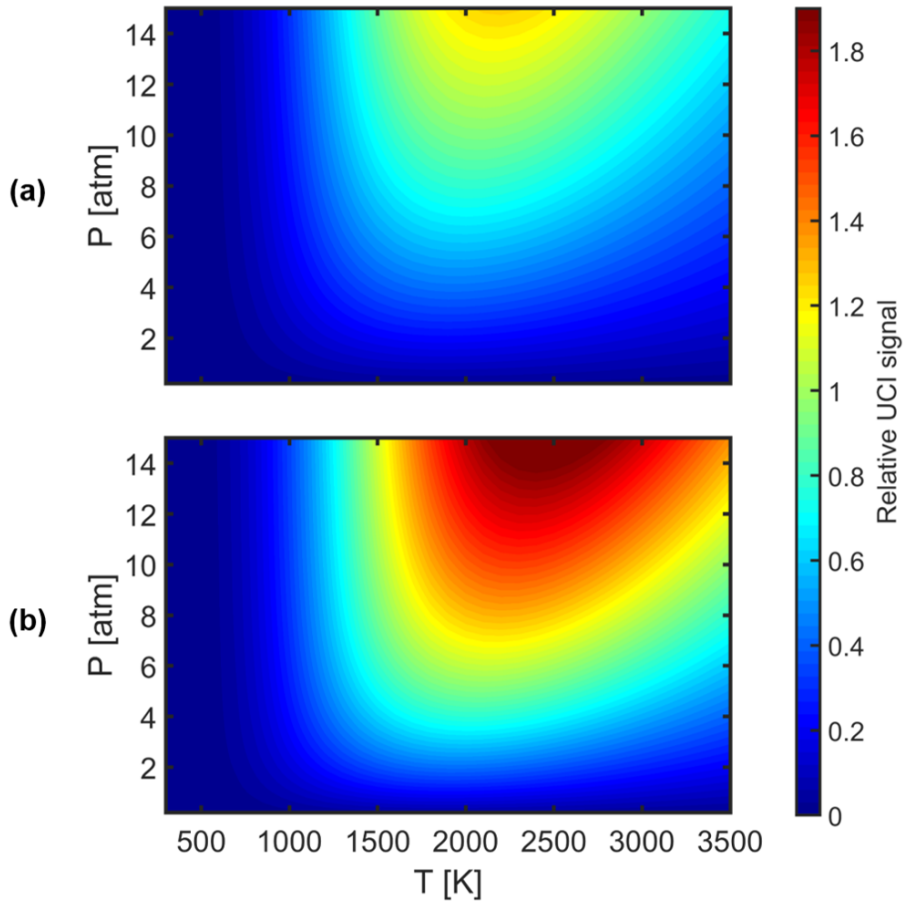

Figure 5.3: Contour plots showing the predicted variation in predicted passive thermal UCI signal strength at the center of the FoV with changes in pressure and temperature in the CO_2-doped RDC (optical path length of $l = 7.6\,\mathrm{mm}$). The plots show predictions for (a) 5% CO_2 doping and (b) 10% CO_2 doping, both normalized by the signal strength for 10% CO_2 doping at $T = 2500\,\mathrm{K}$ and $P = 6\,\mathrm{atm}$.

fixed pressure with a variable emitter concentration, the conditions in the RDC will have a fixed emitter concentration with variable pressure. Figure 5.3 shows these plots of modeled relative UCI signal strength as a function of local pressure and temperature for both CO_2 doping levels used in this work (either 5% or 10% by volume). The spectral radiance was again modeled using the nonlinear relationship given in Eq. (4.4) because it is valid in both the optically-thin and optically-thick regimes. In this instance the UCI signal levels are normalized by the same condition (10% CO_2 by volume, $T = 2500\,\mathrm{K}$, and $P = 6\,\mathrm{atm}$) to allow comparison of the relative signal strengths produced by each of the CO_2 doping levels. Here pressure plays an analogous role to the one that emitter concentration did in Figure 4.15 with monotonic variation in UCI signal along this dimension while a nonlinear relationship is again observed between UCI signal and temperature.

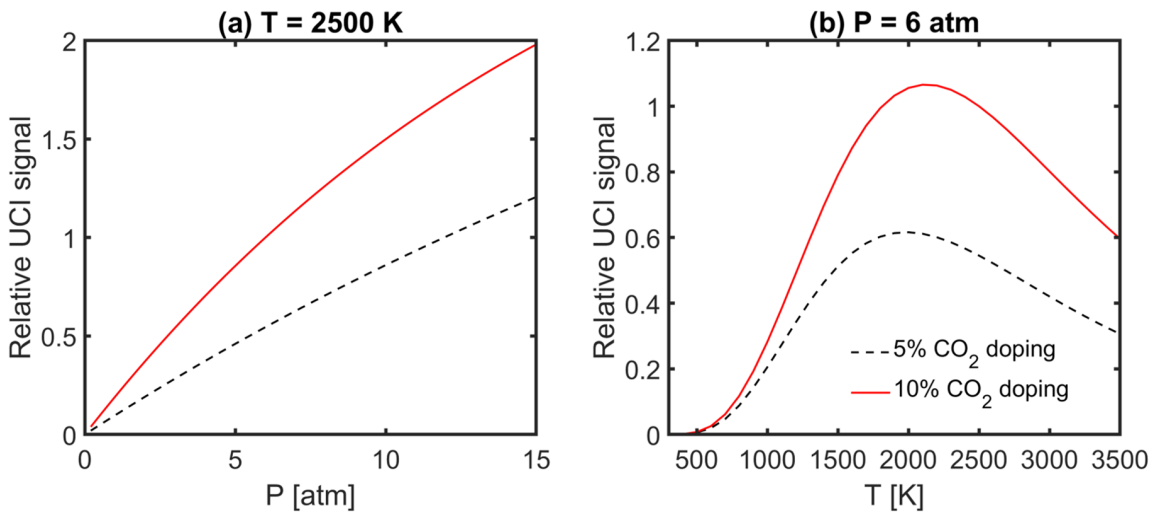

Figure 5.4: Samples of the relative UCI signal variation shown in Figure 5.3 taken along lines of (a) constant temperature at $T = 2500\,\mathrm{K}$ and (b) constant pressure at $P = 6\,\mathrm{atm}$.

To examine the trends in UCI signal in more detail Figure 5.4 shows samples taken from the UCI signal plots along lines of constant temperature (plot (a) for $T = 2500\,\mathrm{K}$) and constant pressure (plot (a) for $P = 6\,\mathrm{atm}$). The constant temperature signal trends in Figure 5.4(a) show that for low pressures the UCI signal varies linearly with gas pressure, consistent with the optically-thin model. However, as the gas pressure increases nonlinear trends associated with the optically-thick regime become important at both CO_2 doping levels. The higher emitter concentrations of the 10% doping case cause the nonlinear effects to appear sooner with increasing pressure as they become significant for pressures of $3\,\mathrm{atm}$ and above. Figure 5.4(b) demonstrates the nonlinear relationship between temperature and UCI signal. The UCI signal strength peaks near $2000\,\mathrm{K}$ for 5% CO_2 doping at $6\,\mathrm{atm}$ while the higher 10% CO_2 doping level causes a shift in the peak signal temperature to $2100\,\mathrm{K}$.

It is important to note that at post-combustion temperatures, assumed to be $1500\,\mathrm{K}$ to $2700\,\mathrm{K}$, the UCI signal varies in relative terms by less than $\pm 15\%$ for the 10% CO_2 doping case (0.791 to 1.066 in normalized UCI signal) and less than $\pm 11\%$ for the 10% CO_2 doping case (0.616 to 0.513 in normalized UCI signal). This means that for this approach to passive thermal imaging, the temperature variation in regions of new combustion products will have relatively little influence compared to variations in pressure that are expected during RDC operation. In this way, these measurements can be used to distinguish between combustion products generated by detonation mode combustion, which is characterized by elevated pressures, and deflagration mode combustion, which in RDCs is associated with lower pressures. For example, heat released near the detonation wave front may cause temperatures near $2500\,\mathrm{K}$ at pressures of $3\,\mathrm{atm}$ compared to similar temperatures generated

by deflagration in the refill regions immediately ahead of the detonation wave at pressures near 1 atm, a process defined in Chapter I as *parasitic combustion*. By the trends shown in Figure 5.4, the detonation products will produce a UCI signal that is approximately three times as strong as that associated with parasitic combustion. This makes the passive thermal imaging measurements with UCI and uniform CO_2 doping capable of detecting and visualizing the distribution of parasitic burning with relatively little context. Similarly, it is capable of monitoring the expansion processes within the post-detonation gases as the falling temperature and pressure will be reflected in falling UCI signals.

5.1.2 Effects of radial stratification

The discussion of passive thermal imaging signal dependencies in the preceding sections assumes a uniform volume of emitting gas. Specifically, this uniformity is required along the optical path length, which in this case spans the width of the combustion channel in the RDC. It has been shown that there can be significant non-uniformities in gas properties across the width of the combustion channel during RDC operation, a phenomenon that will be referred to in this work as radial stratification. Various manifestations of radial stratification have been observed in both experimental [52] and computational [64, 65] studies of RDCs. Because passive thermal imaging is a path-integrated measurement, as shown by Eq. (4.2), radial stratification will result in increased ambiguity if the measurements are interpreted from the perspective of the uniform volume analysis presented above. Without independent measurements of the radial property distributions across the width of the combustion channel, it is generally not possible to account for these effects when interpreting passive thermal imaging results.

The effects of radial stratification on measured UCI signals can be modeled by integrating the non-uniform form of Kirchoff's law in Eq. (4.2) for the distribution of gas properties across the channel width and then applying the UCI response model of section 2.6 to the computed spectral radiance. It is not practical to simulate the entire range of possible radial temperature and pressure profiles that could occur and very difficult to predict what the most likely profiles will be during operation. To obtain accurate estimates would require high-fidelity CFD simulations or radially resolved experimental measurements, neither of which have been performed yet for RDCs operating with CO_2 addition. In the absence of those data, simple example configurations can be considered that represent extreme cases of radial stratification to examine the type of effects on UCI measurements that could result. To do this, a simple two-state configuration shown in Figure 5.5 was considered. As shown in the schematic, the properties were assumed to exist in one of two states, either

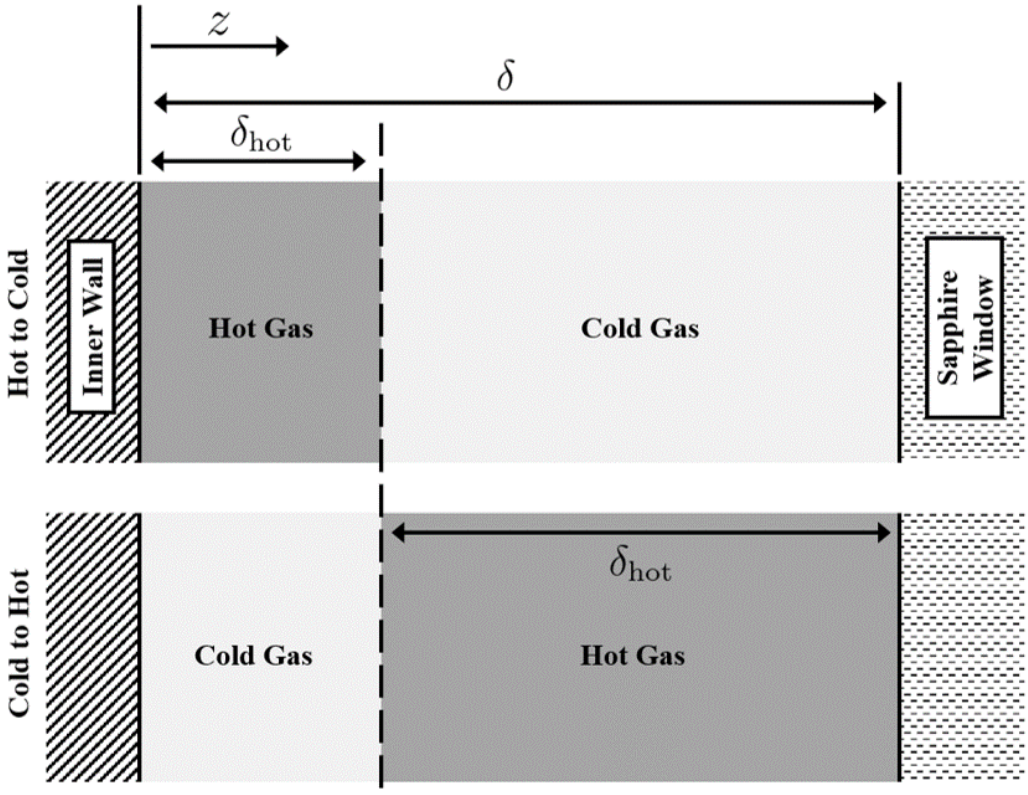

Figure 5.5: Configuration considered to examine the effects on UCI signals of radial stratification of gas properties in the combustion channel of the RDC.

a "hot" gas condition at an elevated temperature or a "cold" gas condition at the injection temperature, with a sharp division between the volumes of the gases in these two states located at some radial position within the channel. Both the case where the hot gas was located adjacent to the steel inner wall ("Hot to Cold") and the case where the hot gas was adjacent to the sapphire window in the outer wall ("Cold to Hot") were considered. Different cases of this configuration can be identified by the order of the gas states within the channel and the length of the hot gas section, defined as δ_{hot}, relative to the total channel width, $\delta = 7.6\,\text{mm}$.

For simulations of radial stratification effects, the "hot" gas temperature was taken to be $2500\,\text{K}$ as representative of combustion products and the "cold" gas temperature was taken to be $300\,\text{K}$, both at equal pressures. Two pressure and CO_2 doping combinations were considered: (a) 5% CO_2 at $3\,\text{atm}$ and (b) 10% CO_2 at $10\,\text{atm}$. These two points were chosen because they represent conditions that could be observed during RDC operation and because they represent different optical regimes with (b) exhibiting optically-thick behavior while (a) could be reasonably considered to be in the optically-thin regime. Both cases were simulated for each of the two state orderings within the channel with the proportion of "hot"

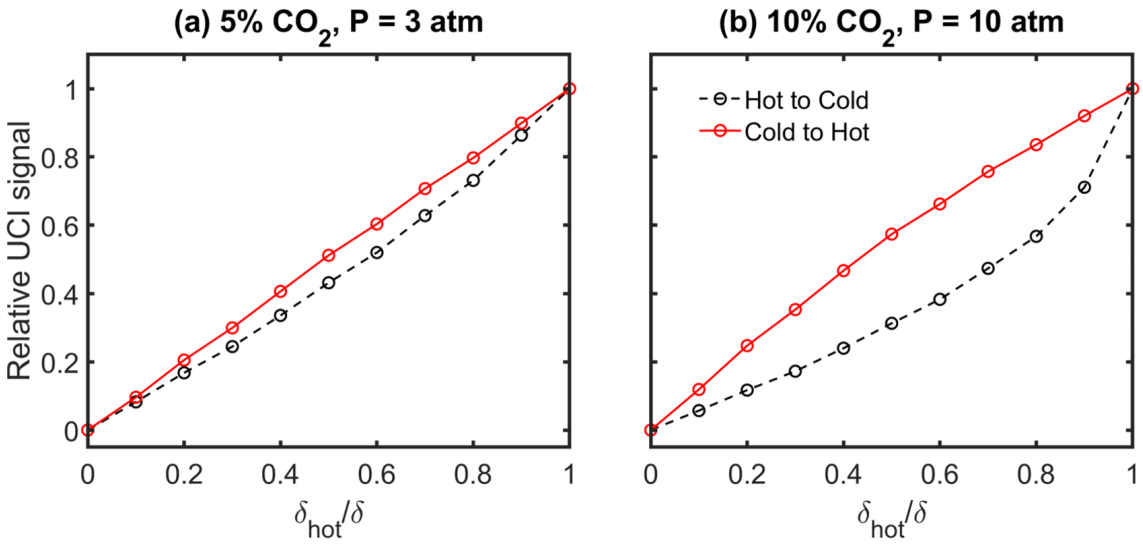

Figure 5.6: Simulations of the effects of radial stratification in the case of a division into uniform "hot" (2500 K) and "cold" (300 K) slabs. The relative variation in predicted UCI signal strength at the center of the FoV as a function of percentage of channel width occupied by hot gas for (a) 5% CO_2, $P = 3$ atm (optically-thin case) and (b) 10% CO_2, $P = 10$ atm (optically-thick case).

gas in the channel incremented from zero to $\delta_{\text{hot}}/\delta = 1$ in steps of 0.1. For each unique condition that was simulated the differential equation in Eq. (4.2) was integrated in steps of 0.1 mm along the 7.6 mm optical path. Tests of uniform conditions showed that this approach converged to the uniform model of Eq. (4.4) to within 1%, validating the choice of spatial step. The resulting spectral radiance outputs were then evaluated using the UCI response model.

The results of the simulations are shown in Figure 5.6. As could be intuitively expected, the signal was negligible for all cold gas and increased monotonically in all cases with increasing $\delta_{\text{hot}}/\delta$ until both state orderings converged at the all hot gas signal level. This shows the effect of radial stratification as a kind of spatial averaging of the gas conditions along the optical path in terms of the resulting UCI signal. In this way, a thin slab of high-pressure, high-temperature post-detonation products surrounded by cold gas would produce an intermediate UCI signal level that could be mistaken for signal generated by deflagration products by the uniform gas perspective described in the previous section. In this way, the extent of radial stratification negates some of the diagnostic capability of the CO_2 doped passive thermal emission UCI technique as more context could be required to distinguish combustion modes than just the relative signal strength in a region of the flow field. This context could include the location of the flow field region relative to the propagating detonation wave front, information that was provided in this study by other

instruments including the high-speed exhaust luminescence imaging.

Additionally, the optical regime has a significant influence on radial stratification effects. In Figure 5.6(a) shows that UCI signal strength for the "Cold to Hot" case is linear in δ_{hot} because this is effectively the signal from an optically-thin hot gas volume that is governed by Eq. (5.1) with an increasing path length. Switching to the "Hot to Cold" case causes the cold gas to spectrally attenuate the emission from the hot gas volume with the cold gas absorption bands. The relative discrepancy between the two state orderings is maximum at $\delta_{\text{hot}}/\delta = 0.3$ where the UCI from the "Cold to Hot" ordering is 22% higher than from the alternative. The discrepancy becomes much larger for the optically-thick case, where the "Cold to Hot" ordering exhibits a 111% increase in UCI signal strength compared to the alternative at $\delta_{\text{hot}}/\delta = 0.2$. This shows that the optical regime is critical for determining how important state ordering is in the effects of radial stratification. Instances of both state orderings have been observed in CFD simulations of RDC operation (without CO_2 addition), however the "Hot to Cold" case is typically more prevalent.

5.1.3 Test conditions

Previous studies of RDC operation using the same facility as in this work included surveys of large operational spaces by incremental changes in several operating parameters including reactant flow rate, global equivalence ratio, and injector geometry. These types of studies were not practical for the UCI campaign for two primary reasons.

First, the information provided by correlating UCI exposures with the relative phase in the detonation cycle as determined by high-speed imaging of luminescence from the exhaust plane of the RDC was found to greatly enhance the ability to analyze and interpret the UCI data. These cycle phase values could only be properly defined for stable operation of the RDC. The addition of CO_2 for the UCI measurements reduced the range of conditions that supported stable operation and additional limitations due to the gas delivery capability used to incorporate CO_2 into the reactants further reduced the range of flow rates that could be tested. This led to a reduced operational space that could be explored with these measurements compared to typical hydrogen-air studies.

Second, the correction procedure described below in section 5.3 as well as the cycle phase perspective presented in section 5.5 require a large number of observations, over one hundred for each case, to perform properly. As discussed in section 3.4.4, the 10 Hz acquisition rate of the UCI system combined with the limited the data throughput for each run to approximately 15 exposures. This meant that data sets for each test case typically had to be acquired over several days of testing. This precluded surveys of many different

Table 5.1: A summary of the RDC conditions for each of the operational cases used for passive thermal UCI in the RDC.

Case ID	Eq. Ratio, ϕ	CO_2 doping	Total $\dot{m}_{\text{air}}$ [g/s]	Detonation wave speed [m/s]	# of UCI observations
A	0.8	10%	200	1100	175
B	1.0	5%	200	1300	154
C	1.2	5%	200	1400	225
D	0.6	5%	400	1300	310

test cases with the UCI system, instead four test cases were chosen as the focus for UCI data collection.

Table 5.1 provides a summary of the operational conditions used for the four test cases that were examined in the UCI campaign. These cases were chosen to attempt to cover some differences in each of the primary dimensions of the operational space (equivalence ratio, CO_2 doping level, and reactant flow rate) while still satisfying the requirement that the primary detonation wave stably propagate. Other conditions were observed for a few test runs with the UCI system that did not exhibit steady operation. The UCI measurements were still capable of achieving sufficient signal strengths and spatiotemporal resolution of features near the detonation wave fronts in those cases, however because of the limitations in data analysis due to a lack of a reliable estimate of cycle phase those data are not presented here. For the remainder of this chapter some of the parameters of each case may be referenced in discussions, but each case will primarily be referred to by its case ID shown in the first column of Table 5.1.

5.2 Results of UCI measurements

All of the UCI frames captured in the RDC shown in this chapter are displayed with their spatial coordinates oriented relative to the direction that the primary detonation wave was propagating in the combustion channel at the time that the measurement was captured. The convention used in this work shows images such that detonation waves would be propagating from left to right in the frame, regardless of if a detonation wave front is present in the frame or not, where the instantaneous direction of wave travel was determined by high-speed imaging of the exhaust plane. The axial coordinates of all frames are oriented

so that the inlet of the combustion channel is below the bottom of the frame and the exhaust plane is well above the top of the frame. The origin of the coordinates in each of the frames was estimated by hand for each data set based on the approximate center of the UCI response. This point could not be precisely located relative to the center of the sapphire window, though the limited clear aperture of the window ($19\,\mathrm{mm}$) ensures that the coordinate origin is no more than $4\,\mathrm{mm}$ from the center of the window. For this reason, all of the coordinates should be viewed in a relative sense as they precisely show relative locations *within a frame*, but may have millimeter level uncertainties relative to the geometry of the combustion channel.

For the presentation of measurements in the cycle phase perspective described in section 5.5, the azimuthal coordinates (those in the circumference direction of the combustion channel that are used to track the propagation of the detonation wave, *i.e.* left and right) are transformed into an approximate phase locations in the detonation wave cycle. These cycle phase coordinates are measured by θ that takes values of $-\pi < \theta \leq \pi$. It is best to consider these θ values in a relative sense as well because it is difficult to precisely define an absolute cycle phase mapping for all of the instruments in the RDC that are located at different azimuthal and axial locations within the combustion channel and exhibit different temporal response characteristics. Also, the fact that the propagating detonation wave exhibits significant cycle-to-cycle variation in its properties makes the detonation cycle far from an ideal periodic process. This makes it difficult, if not impossible to consistently define a precise and unique cycle phase mapping within the RDC flow field even with omniscient knowledge of the entire flow that is not available in experimental studies. Despite this, approximate estimates of the corresponding cycle phase for each measurement can provide meaningful insights into important large-scale processes and trends in RDC operation. For UCI measurements in the cycle phase perspective, the azimuthal coordinates are mapped to cycle phase locations using the $467\,\mathrm{mm}$ mid-channel circumference of the combustion channel to estimate a conversion factor of $0.0135\,\mathrm{rad\,mm^{-1}}$. The mapping process and coordination of different measurements in cycle phase coordinates are further discussed in later sections in this chapter.

Each UCI frame in the RDC was captured as a raw image. These raw images include the effects of spectral fringing as discussed in Chapter III and spatial-spectral coupling as experimentally examined in Chapter IV. To avoid confusing these effects with meaningful spatial illumination patterns or allowing them to obscure subtle signals it is important to correct for them. The measurements in Chapter IV demonstrated that the spatial-spectral coupling effects can be accurately predicted and accounted for a priori with detailed knowledge of the UCI system. However, this is not possible in the case of spectral fringing effects.

Instead, a correction procedure informed by each UCI data set was used. The following section describes that correction procedure.

5.3 Correcting raw UCI measurements

Examples of UCI measurements of detonation wave fronts are shown in Figure 5.7. Examples of images of the propagating detonation wave front from cases A and C were chosen to demonstrate the image correction procedure. Both images are the raw UCI measurements with the effects of both the spatial-spectral response coupling and spectral fringing superimposed upon the thermal radiation intensity fields.

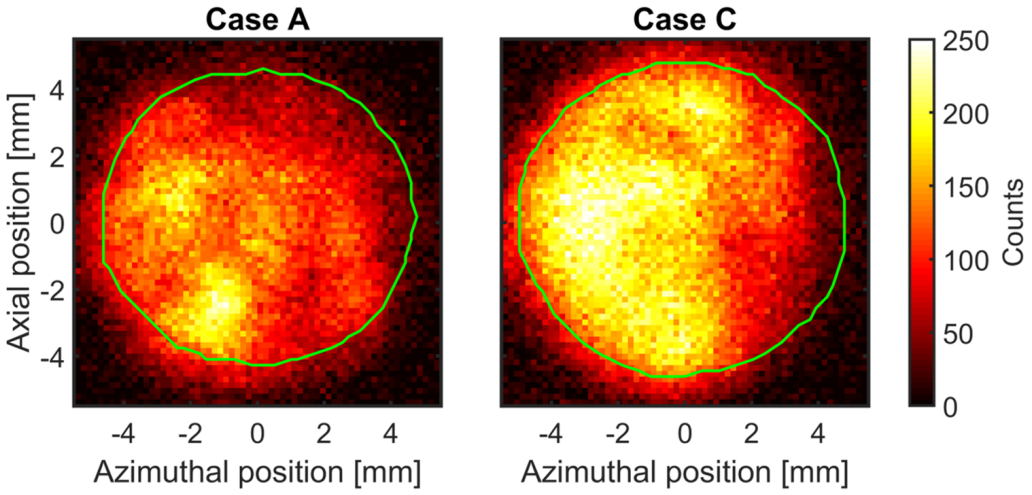

Figure 5.7: Examples of raw UCI measurements of detonation wave propagation for cases A and C. The green outlines indicate the regions where aggregate frames showed responses of at least 50% of the maximum signal response.

One aspect of the spatial-spectral coupling effect is the limited field of view for UCI measurements at this wavelength that was observed in the characterization measurements in Figure 4.2. In this case, the system will only respond to mid-IR signals within an approximately $1\,\mathrm{cm}$ diameter circular region in the object plane. An estimate of this region is shown by the green outline in the frames. This estimate was generated by a process based on an aggregate frame of many exposures that will be described below. Pixels exhibiting low or zero signal outside of this region are dim because the system does not respond to signal at those locations. In contrast, dim pixels within the region of significant response indicate lower thermal radiation signal within the field of view. In these examples, the dim regions near the right side boundaries of the frames are regions of low temperature, unburnt gas that the detonation wave front is propagating into, and the bright regions on the left side

of the frame indicate high-temperature, high-pressure combustion products.

As discussed in previous sections, it is difficult to predict the CCD spectral fringing pattern a priori to correct for those effects. One way to correct for both spectral fringing and spatial-spectral coupling effects simultaneously is to measure an appropriate flat-field response and use that to correct measurements from the combustion experiments. The flat field response must be generated by measuring a spatially-uniform source with the UCI system that exhibits the same spectral content as the target signal. A blackbody source would produce different flat field signals than would result from uniform illumination by thermally radiating CO_2 because the detected near-IR spectrum produced by blackbody illumination is broader and produces less pronounced spectral fringing pattern (compare Figures 4.1(b) and 4.17(b)). This means that flat fielding of UCI measurements in the RDC cannot be performed with blackbody illumination.

The approach to flat fielding the passive CO_2 emission images presented here is based on an *aggregate frame* that is the sum of all RDC images captured for a particular combustor operating conditions and optical alignment. If the optical alignment of the UCI system and the temperatures of the ppLN crystal and CCD sensor are maintained nearly identically between test runs, then the superimposed effects would be the same for all captured frames. If the target CO_2 thermal radiation field that is being imaged exhibits spatial distributions of signals that are random and uncorrelated between frames, then the sum of all frames can act as an approximate flat field for the measurements. Previous experimental measurements of OH distributions in the RDC flow field using chemiluminescence [100] and PLIF [**?**], as well as CFD simulations of a similar combustor [64], suggest that it is reasonable to assume there is no consistent preferential spatial illumination over a field of view of this size for randomly timed measurements. If these assumptions hold, then there is still the requirement that a sufficiently large number of exposures is averaged together to smooth out random variations in the spatial structure of exposures and approach an effective flat field exposure.

The optical alignment of the system was different for cases A and C shown in Figure 5.7, but the alignment and detector temperatures were maintained for the duration of data collection for each case. Aggregate frames were generated for each condition by summing the signals from all the exposures during the operation of the combustor for each condition (175 frames for case A and 225 frames for case B). These aggregate frames scaled to unity maximum signal level are shown in Figure 5.8 for each of the two cases. The approximately 1 cm field of view represented by the green outlines in Figure 5.7 is apparent here, as are the effects of spectral fringing. The dimming below of the frame center and the brightening above the frame center in both cases are a result of the spectral fringing

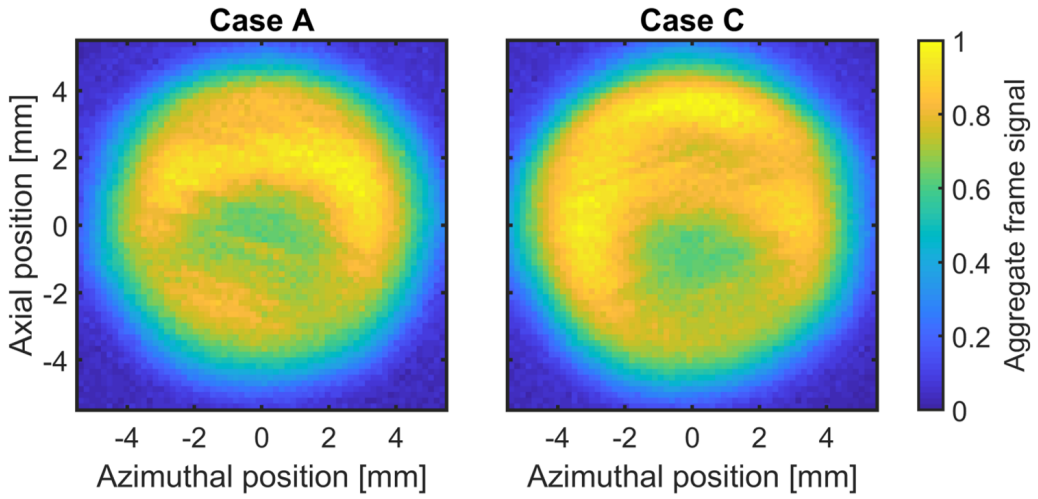

Figure 5.8: The aggregate UCI frames for cases A and C.

pattern superimposed onto the system response.

The artifacts in the raw UCI images of Figure 5.7 due to variations in the spatial response of the system can be corrected with the effective flat flame fields in Figure 5.8. Dividing the raw images by the normalized aggregate frames on a per pixel basis for each condition compensates for the variation in system response across the field of view. This would result in amplification of pure noise for regions of the frame outside of the region of non-negligible UCI response indicated by the green outline in Figure 5.7, and so a response cut-off threshold must be set below which pixels are not corrected and considered. A high threshold value will result in better minimum SNRs across the image, but a smaller FoV. Lower threshold values result in the opposite, a larger FoV with lower minimum SNR values. This work uses a threshold value of 50% of the maximum response for all UCI measurements presented in this chapter. The 50% threshold was used to identify the green boundaries shown in Figure 5.7 and any pixels outside of that boundary are discarded in the corrected frames.

The images in Figure 5.9 show the corrected versions of the raw images in Figure 5.7, as processed by the previously described flat fielding procedure. The correction eliminated artifacts that may have interfered with interpretations of the spatial structures captured in the images. For example, the bright region in the bottom half of the case C example is more spatially uniform in the corrected image than in Figure 5.7 where the effect of spectral fringing had introduced a spurious signal deficit. Similarly, the bright spot in the bottom left quadrant of case A example is shown to extend to the edge of the FoV in the corrected frame in Figure 5.9. This correction procedure has been applied to all of the UCI results shown in this chapter, including those in the cycle phase representation in section 5.5.

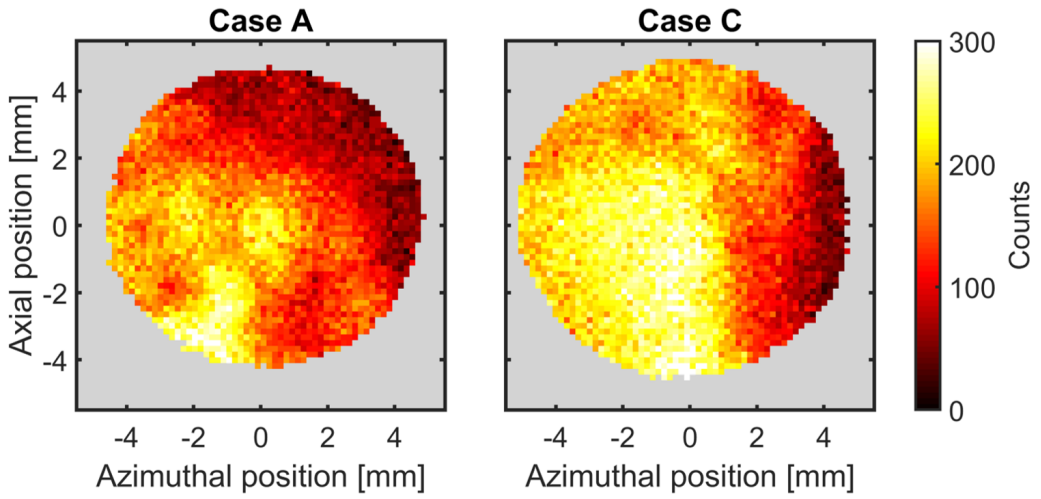

Figure 5.9: The flat field corrected UCI frames for (a) globally rich and (b) globally lean fueling conditions.

5.4 UCI composite images

Figure 5.10 shows composite images formed from all of the UCI exposures captured during the steady operation of each case. These were constructed by placing the center of each image frame at the cycle phase determined from the high-speed exhaust plane video analysis and scaling the azimuthal coordinates of the frames to have the appropriate extent along the cycle phase direction. For clarity, the frames were separated from each other in the vertical (axial coordinates) direction. It should be noted that the vertical location of the center of each frame conveys no information and was chosen for ease of viewing, however the axial coordinates within each frame continue to show the relative axial location of structures within the same frame. Note that the signal levels for case D have been scaled up by a factor of 1.5. Caution should be exercised when comparing signal levels between the different test cases. Cases B and C had the same CO_2 doping levels and pump beam properties, but case A had a higher CO_2 doping level and case D used a different pump source Q-switch delay (91 µs instead of 90 µs because ambient conditions compromised laser stability, likely resulting in a shorter effective exposure time, see section 3.3.2). For these reasons, direct comparisons of UCI signal strength between cases may not be representative of differences in mid-IR luminosity, but those comparisons are valid within the same test case. The composite images for all four cases were combined into Figure 5.10 to save space, but full-page versions of the composite images for each test case are provided in Appendix B for improved detail.

The composite UCI images are useful because they provide a comprehensive view of the recorded data in the sense that all UCI exposures are shown and they combine the cycle

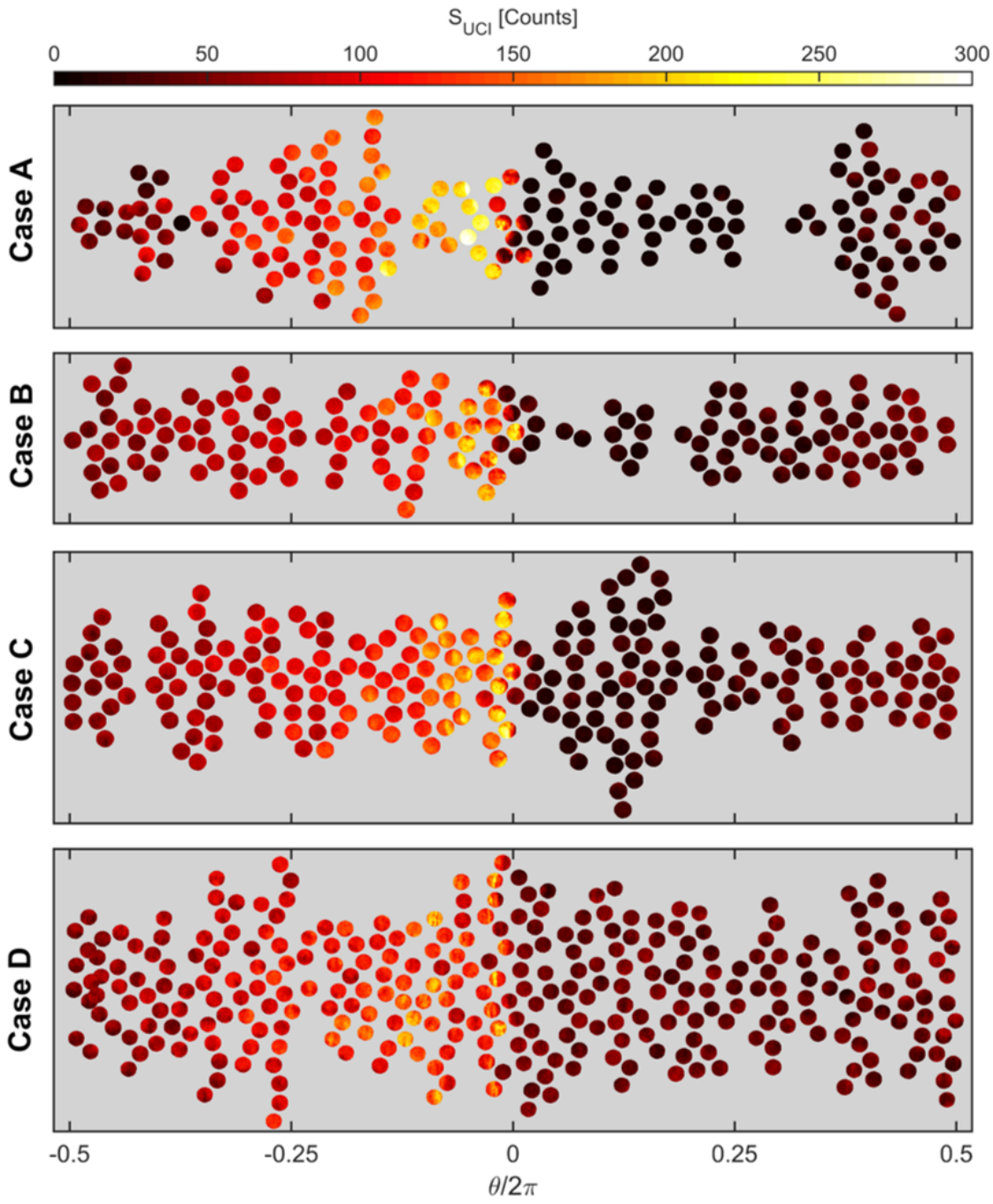

Figure 5.10: Composite images of UCI exposures for each test case run in the RDC. The signal in case D has been scaled up by a factor of 1.5 for clarity.

phase information described in section 5.5 with the spatial resolution of the individual UCI frames. As has been discussed above, the absolute values of cycle phase are difficult to consistently identify and the data collection and image analysis methods used to generate the cycle phase location estimates initially led to different apparent detonation wave front

locations in the composite images for each test case. The "raw" cycle phase location estimates generated from the high-speed exhaust plane video analysis have been shifted in the presentation of Figure 5.10 so that the apparent detonation wave front occurs at approximately $\theta = 0$. The quantitative implementation of this is described in the following section, but it should be noted that these absolute cycle phase definitions will always be essentially arbitrary. The $500\,\mathrm{kHz}$ sampling rate of the high-speed DAQ that was used to coordinate either multiple instances of UCI measurements with each other in time or UCI measurements with simultaneous measurements by different measurements resulted in a stack-up of temporal tolerances of up to $4\,\mu\mathrm{s}$. This temporal uncertainty corresponds in a spatial uncertainty of up to $6\,\mathrm{mm}$, which is on the order of the entire FoV of UCI measurements and far worse than the spatial resolution achieved in individual UCI frames. The additional uncertainty due to cycle-to-cycle variation in detonation wave structure leads to the conclusion that values of θ are not precise for spatial scales on the order of the UCI system FoV, *i.e.* length scales less than $1\,\mathrm{cm}$.

To summarize this point, the projection of transient two-dimensional detonation wave properties in the RDC onto the single cycle phase dimension defined by θ is incapable of reliably describing spatial scales that are resolved within individual UCI frames. However, results show that this projection is adequate for describing large-scale ($>1\,\mathrm{cm}$ along the azimuthal direction) spatial structures within the RDC flow field and it can be used to perform meaningful examinations of these features. Therefore, precise registration of multiple UCI instances or signals from instruments located at different positions in the combustion channel in this dimension is not relevant, but comparisons of large-scale structures between these signals are valid.

5.5 UCI cycle phase representation

The composite UCI images shown in the previous section preserved the relative axial displacements of the signals measured at each pixel within the FoV. To make direct comparisons with other pointwise measurements in the cycle phase representation, these data must be collapsed along the axial direction and plotted as a function of θ alone. This is shown in Figure 5.11 for each of the test cases. The data points in the figure represent the measured signal strength at each pixel from each UCI exposure for the corresponding test case projected onto its estimated cycle phase location. The superimposed red line shows a 3000 point rolling average applied along the θ direction to produce a unique value of the UCI signal for each cycle phase location. Note that while some of the spread in the measurements at each θ value is due to detection noise, it is primarily a result of actual

variation in the gas properties along the axial direction within the FoV. The rolling average has the effect of eliminating the axial resolution of the UCI measurements that is unique compared to the single-point nature of the pressure transducer and OH^* PMT measurement (see section 3.4.3). Some of this axial resolution will be recovered in this cycle phase perspective in section 5.5.1 to examine axial variation in mid-IR luminosity and it will be fully represented in the individual UCI frames presented in section 5.6.

Care has been taken to refer to this treatment of UCI data as a *cycle phase* representation rather than a *phase-averaged* representation. Phase-averaging implies that the periodic cycle is divided into intervals, or "bins", into which each data point is classified and then the mean value of each interval is taken to represent the signal for that phase interval. This can be done in a straightforward manner for the high acquisition rate data in these RDC tests, including the signals from the pressure transducer and PMT measurements. However, because of the limited data throughput of the UCI measurements, some cycle phase intervals contain few or no UCI measurements for some of the test cases. This would result in undefined or noisy phase-averaged values which would be undesirable for analysis purposes. Instead, the rolling average applied to the cycle phase representation achieves the same functions of unique signal generation and de-noising that phase-averaging does without the related signal definition issues. This rolling average signal will be used for all cycle phase comparisons in the rest of the chapter. It was also used for the phase dimension registration that was previously discussed; all cycle phase representations of UCI measurements were shifted so that the point where the signal reached 20% of the peak value relative to the minimum signal value on its rising edge occurred at $\theta = 0$.

A comparison of the UCI cycle phase traces for each of the four test cases is shown in Figure 5.12. As mentioned in the previous section, it is difficult to make meaningful comparisons of the signal strength between the test cases in this data set for several reasons, but the relative shapes of the signal waveforms can be compared between cases. All of the cases show a steep rise in mid-IR luminosity near $\theta = 0$ that is associated with the passage of the detonation wave front which generates hot combustion products at high temperatures. This rapid increase in luminosity in the cycle phase representation still fails to actual steepness of the compression and heat release process as measured by the individual UCI exposures shown in section 5.6, but still clearly indicates that the process occurs rapidly near the wave front. The waveforms then exhibit different trends in the expansion and refill regions behind the detonation wave front.

Case A shows a rapid decrease in mid-IR luminosity almost immediately after the detonation wave front (near $\theta/2\pi = 0.05$) that may be related to post-detonation expansion processes causing rapid decreases in temperature and pressure. Cases B and C show very

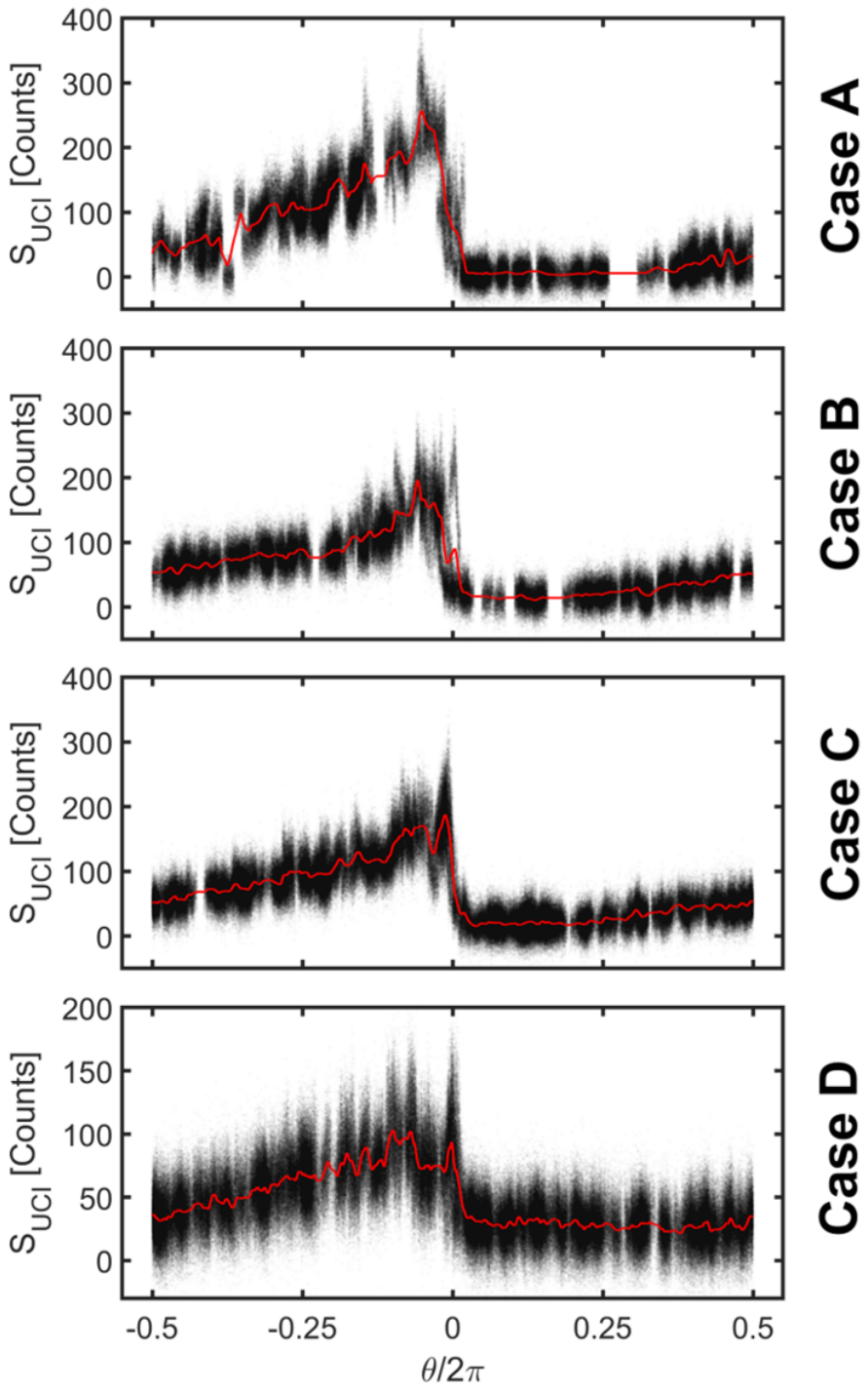

Figure 5.11: Cycle phase representations of the UCI data from each RDC test case. The dots represent the signal value from each pixel in all of UCI exposures for a particular test condition at its corresponding cycle phase value as measured from high-speed exhaust video. The red line shows a 3000 point rolling average in the θ direction.

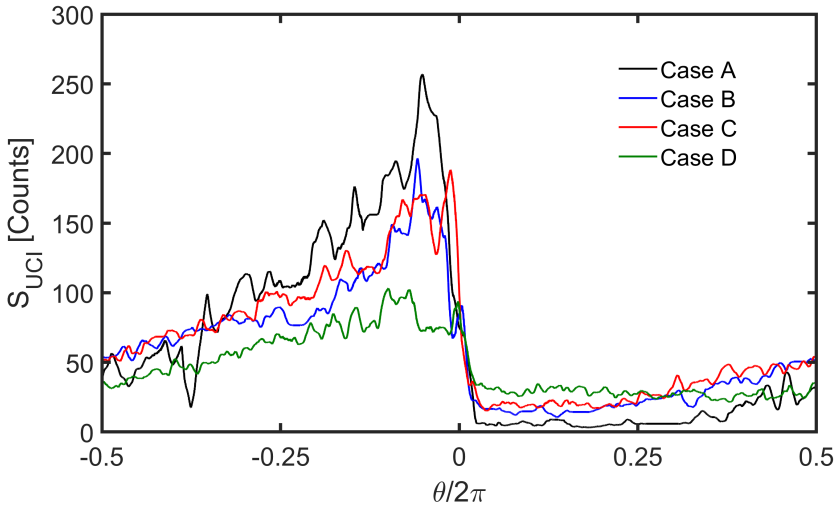

Figure 5.12: A comparison of the 3000 point rolling averages in the θ direction of UCI signal for each of the RDC test cases.

similar waveforms to each other, and both also show sudden luminosity drops after the wave front, but further behind the wave front near $\theta/2\pi = 0.1$. Case D does not show any sudden luminosity reductions in the cycle phase representation, but sudden drops are seen in some examples of individual UCI exposures from case D shown in section 5.6.2. All cases show steady reductions in luminosity for phase locations of $-0.5 < \theta/2\pi \leq -0.15$, which could correspond to gradual expansion and cooling of the post-detonation gases.

A major difference between the test cases can be seen in the phase region between $0.05 < \theta/2\pi \leq 0.4$ which corresponds to the refill process where fresh reactants are injected and mix ahead of the propagating detonation wave front. Case A shows minimal UCI signal in this region while the other three cases record non-negligible mid-IR luminosity there. This is evidence of significant parasitic combustion occurring in the fresh fill regions of cases B, C, and D, while case A shows little evidence of elevated temperatures associated with burning in the fresh reactants. These observations are corroborated by OH^* for each of the cases that are discussed and compared to UCI data in section 5.5.3. The capability of the UCI system to detect parasitic combustion and its distribution within the combustion channel is valuable for studies of the effects of secondary combustion processes on RDC operation.

The cycle phase results can be used to estimate the SNR of thermal imaging measurements in the RDC. There is no universal definition for quantitative SNR that can be applied to describe imaging measurements. For this work, the peak SNR value will be considered, defined as the representative peak signal value compared to the RMS noise value associated with dark signal and background light. This can be used to estimate the likelihood that a

Table 5.2: Estimated peak SNR values achieved by thermal imaging for each case based on an RMS noise value of 13.9 counts.

Case ID	Peak signal [Counts]	SNR
A	257	18.5
B	197	14.2
C	188	13.5
D	103	7.4

"false alarm" detection will be generated at the peak signal value by an un-illumination portion of the FoV. The noise level was estimated by computing the Root Mean Square (RMS) signal of all pixels within the FoV (after applying the corrections described in section 5.3) for the first ten frames of each data run that were captured before ignition. This produced an estimated RMS noise value of 13.9 ± 0.2 counts across all of the data runs. The peak signal value was estimated by the maximum of the 3000 point rolling phase averages shown in Figure 5.12 for each case. The FoV in the RDC measurements contains approximately 2500 pixels, and so the Rose criterion [101] indicates that a peak signal value of at least five times the RMS noise level (SNR $= 5$) is sufficient to reduce the likelihood of detecting random noise at the peak level to less than 1×10^{-3}. The computed SNR values in Table 5.2 show that this is satisfied for each case by the thermal imaging measurements.

5.5.1 Axial variation in UCI signal

The cycle phase representation shown in Figure 5.12 fully omitted any information about the relative axial locations of all of the UCI data points. The axial distribution of mid-IR luminosity measured by UCI could potentially carry information related to both typical detonation wave front morphology and refill processes, and so this section modifies the cycle phase representation to restore some of the axial resolution offered by UCI measurements. To do this, each UCI frame is divided into three zones depending on axial location: an "upstream" zone, a "middle" zone, and a "downstream" zone. The upstream zone was defined as all points below -1.5 mm relative to the frame center, the downstream zone was defined as all points above 1.5 mm from the frame center, and the middle zone contains all points in between the previous two. This division is shown in the example UCI frame in Figure 5.13.

The three axially distinct subsets of data for each test case were then treated with the

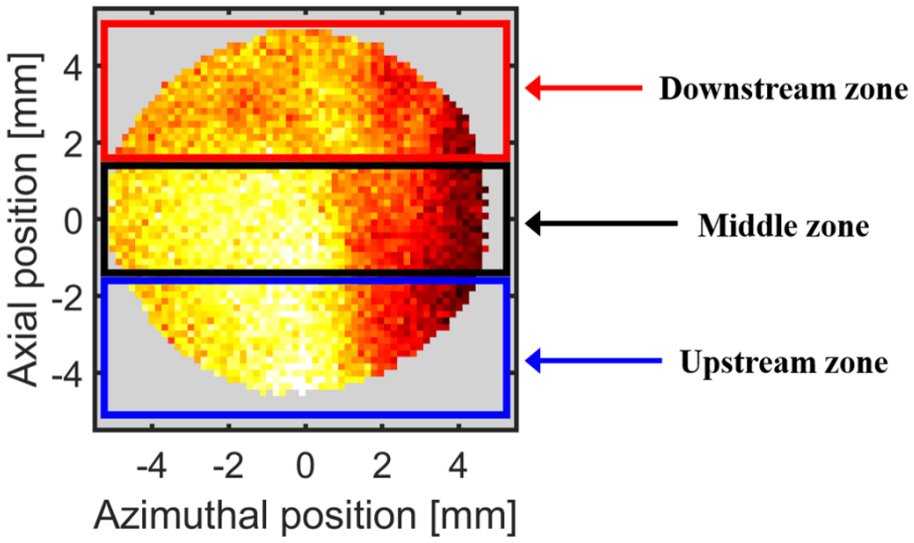

Figure 5.13: An example of a UCI frame (case C) showing the three zones that were used to examine axial variation in the UCI signal in the cycle phase perspective.

same 3000 point rolling average that was applied to the full data sets. The resulting axially-resolved UCI waveforms for each of the test cases are shown in the plots in Figure 5.14. In those plots the blue line indicates the signal in the upstream zone, the black line indicates that of the middle zone, and the red line indicates that of the downstream zone. The waveforms for each of the axial locations are generally similar to each other with the greatest nominal differences occurring near the detonation wave front. Even near the detonation wave front, the greatest differences in UCI signals between axial zones never exceeded 70 counts (this difference was observed for case B near $\theta/2\pi = 0.05$). The middle zone signal was found to almost always take an intermediate value between that of the upstream and downstream zones when there was a significant difference between them. To examine the subtle differences that occurred between the upstream and downstream zones, the difference between those two signals was computed for each case and those are plotted in Figure 5.15.

The axially-resolved UCI signal difference plot in Figure 5.15 shows the upstream zone nominal UCI value subtracted from the downstream zone signal for each cycle phase location. Cases A, B, and C show large discrepancies near the detonation wave front where the upstream zone signal is larger than that of the downstream zone at the same θ values with nominal differences between 40 to 70 counts. Examination of the plots in Figure 5.15 show that all three zones peak in signal strength at the same θ values, and so this is not evidence of a "tilt" of the wave front where one axial section could lead in front of the others. Instead, it may indicate a relative difference in the strength of the detonation wave

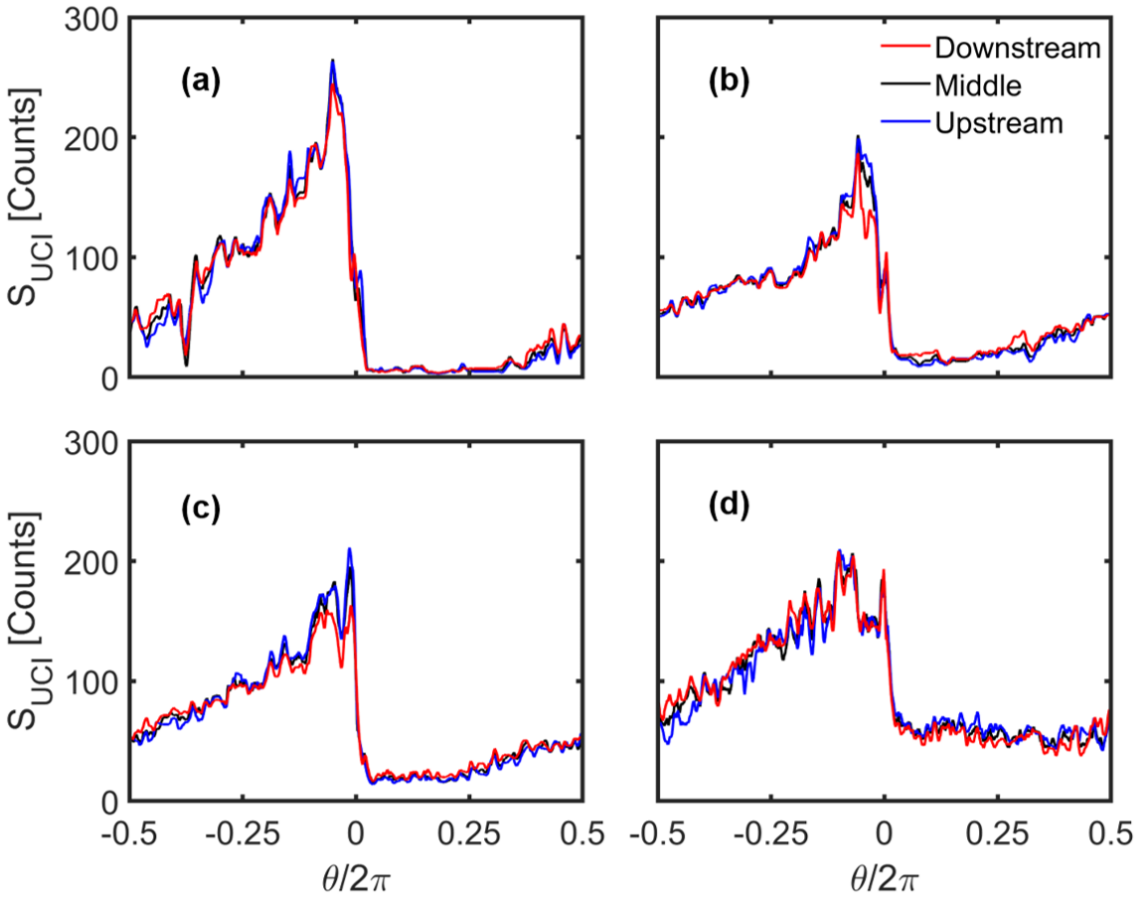

Figure 5.14: Plots of 3000 point rolling averages in the θ direction of UCI signal in each of the three relative axial location zones. The subplot labeling coincides with the case IDs: (a) case A, (b) case B, (c) case C, and (d) case D. The signal in case D has been scaled up by a factor of 2 for clarity.

at the different axial sections. The displacement of the upstream and downstream zones as measured by their axial centroid coordinates is $5.4\,\mathrm{mm}$, which is small relative to the $105\,\mathrm{mm}$ height of the combustion channel, but may span non-negligible axial structure in these detonation waves. Axial discrepancies of similar magnitudes are not observed near the wave front in case D.

Another region showing notable discrepancies in the axially-resolved UCI signals is the interval that wraps around the periodic boundaries of the θ domain as displayed and includes $-0.5 < \theta/2\pi \leq -0.25$ and $0.25 < \theta/2\pi \leq 0.5$. This interval of the detonation wave cycle typically represents a transition from the post-detonation product gas conditions to fresh reactant mixtures. All test cases exhibit preferential mid-IR illumination of the downstream zones for most of this interval. This could indicate the reactant refill process as warm product gases advect axially downstream toward the exhaust and cool reactant

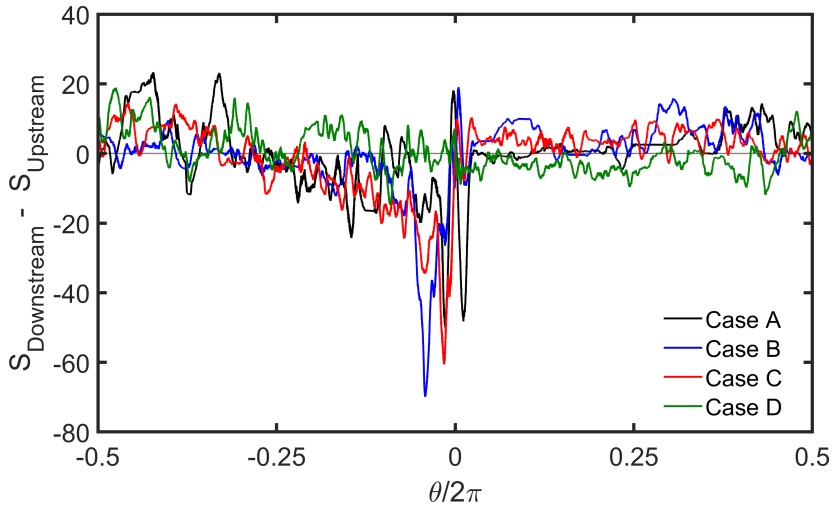

Figure 5.15: The difference in UCI signal averages between the downstream and upstream zones as a function of θ for each of the RDC test cases.

gases are forced in from the bottom of the frame to replace them. These patterns of higher mid-IR luminosity near the top of the frame are seen in individual UCI images, but they are less pronounced than the structures near detonation wave fronts because of the reduced signal strength in the exhaust/refill regions, making them harder to visualize because of reduced SNRs. This axial binning approach to the cycle phase perspective could be a tool for studying these relatively dim processes, particularly if large amounts of UCI data could be generated by enhanced acquisition rates.

5.5.2 Comparison with pressure transducer measurements

As shown above in section 5.1.1, the passive thermal UCI signal is sensitive to local gas pressure, and under some conditions exhibits a nearly linear response to pressure. The measurements cannot be used to directly quantify pressure without detailed knowledge of the temperature distribution within the flow field, but can still be used to identify trends in the pressure variation during the detonation cycle and make comparisons of the pressure within regions of hot products. The UCI measurements can be compared to pressure transducer measurements within the combustion channel to give context to the pressure response of the UCI signal and identify differences in the response characteristics of the UCI and the transducer.

Figure 5.16 shows the cycle phase UCI signal (black line) for each test condition compared to the phase-averaged pressure measured by a pressure transducer (red line) that was installed at a different location in the combustion channel (see section 3.4.3). The phase-

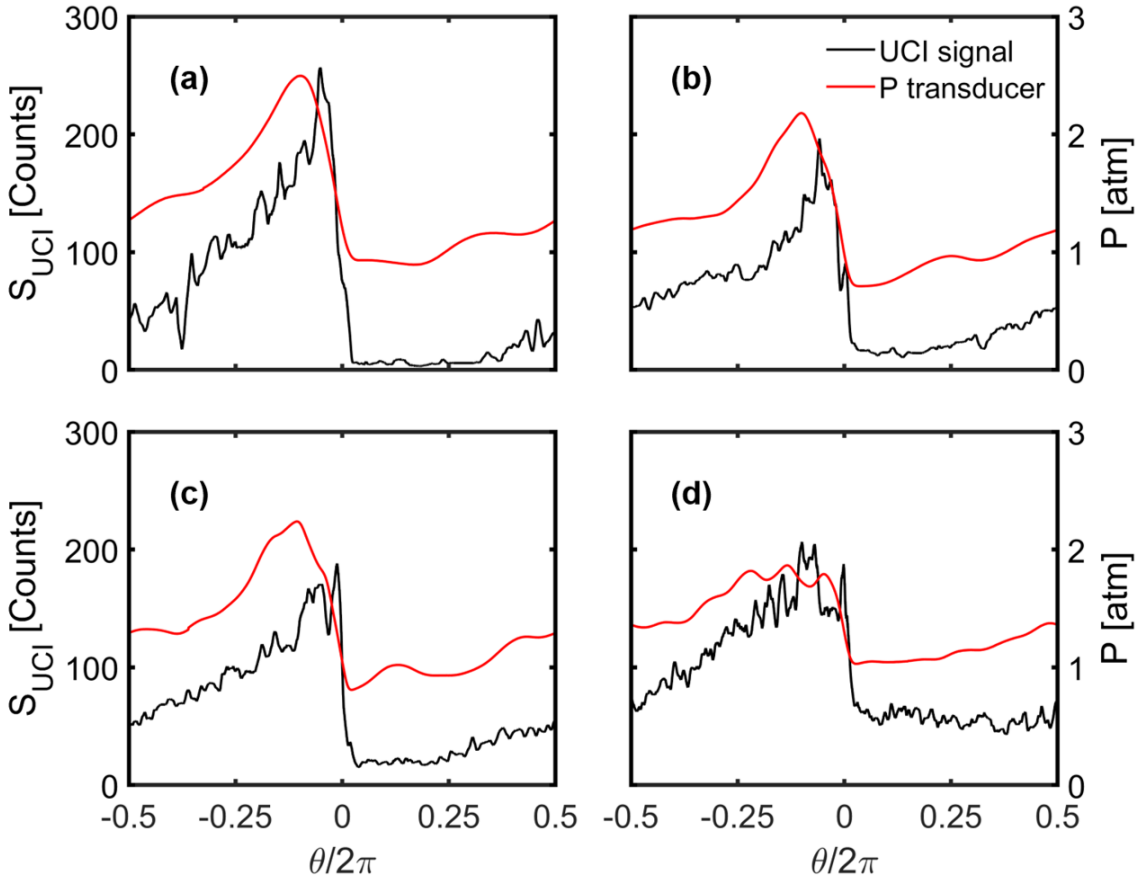

Figure 5.16: A comparison of the cycle phase UCI signal with phase-averaged pressure transducer measurements at a similar axial position. The subplot labeling coincides with the case IDs: (a) case A, (b) case B, (c) case C, and (d) case D. The signal in case D has been scaled up by a factor of 2 for clarity.

average of the pressure computed from data captured during the same experimental runs as the UCI measurements. The difference in azimuthal locations between the center of the sapphire window and the pressure transducer ($\Delta\theta = \pi/2$) meant that the registration of the two signals in the cycle phase domain was not aligned. For clarity of comparison, the phase-averaged pressure traces were shifted so that the steep rise in pressure due to the passage of the detonation wave approximately coincided with the rise in mid-IR luminosity near $\theta = 0$.

The frequency response of the pressure transducer ($5\,\mathrm{kHz}$) was sufficient for measuring the cycle frequency, which was its primary purpose but was insufficient to resolve the rapid pressure rise across the detonation wave front. This lack of response speed caused pressure transducer measurements to "smear" the steep pressure gradient over longer intervals in time, and therefore cycle phase. This was understood to cause an apparent delay in the

measured cycle phase of peak pressure and possibly also the magnitude of the measured peak pressure. The comparisons between phase-averaged pressure measurements and cycle phase UCI signals in Figure 5.16 demonstrate the limitations of the pressure transducer's response bandwidth. The detonation associated pressure rises in the phase-averaged pressure signals for cases A, B, and C occur over a phase interval of approximately $\Delta\theta/2\pi \approx 0.12$ compared to phase interval of $\Delta\theta/2\pi < 0.08$ for the rise seen in the UCI signal. The response seen in the UCI measurements is limited in these cases by the phase cycle representation and imaging process as has been previously discussed (similar responses are seen in phase-averages of the fast-responding PMT measurements in the following section), and individual UCI images of the detonation wave front show that the increases in mid-IR luminosity occur over millimeter length scales (equivalent to $\Delta\theta/2\pi$ on the order of 0.01). The fact that the phase-averaged pressure measurements do not reach these resolution limits demonstrates the limitations resulting from the sensor's bandwidth being insufficient to resolve processes near the detonation wave front.

Otherwise, the major trends in the phase-averaged pressure measurements mirror those seen in the UCI signal, as expected based on the pressure sensitivity of the UCI measurements. Case A shows a sharp peak in the pressure followed by an immediate and steep drop in pressure, similar to the waveform seen in UCI signal for that case. The phase-averaged pressure traces for cases B and C both show a narrow phase interval ($\Delta\theta/2\pi \approx 0.09$) after the pressure peak where the pressure decline is relatively slow before more rapid expansion. This same feature is represented in the corresponding UCI signals by similarly sized phase intervals where the mid-IR luminosity remains elevated before steep decay. The waveform of both pressure and UCI signal seen for case D exhibit a wider interval of constant magnitude after the peak values ($\Delta\theta/2\pi \approx 0.18$), followed by gradual, steady reductions in signal rather than steep declines seen in the other cases. The agreement in these aspects of phase-averaged pressure and UCI signal waveforms provides support for the validity of interpreting UCI signal variation as representative of pressure variations when observing regions of hot gases in the RDC.

5.5.3 Comparison with OH^* chemiluminescence measurements

Just as the UCI signal was compared to phase-averaged pressure transducer measurements in the previous section, the cycle phase UCI signal can also be compared to phase-averaged measurements of OH^* chemiluminescence by the UV PMT that was fiber-coupled to the inner wall window. The PMT measurements differ from the pressure transducer measurements in several ways. First, the PMT exhibited a fast response to changing gas conditions.

The cycle phase resolution of the phase-averaged PMT measurements will therefore be bounded by the limitations of the cycle phase perspective in the same way that the UCI measurements were. Second, the inner wall window that was used to collect the OH^* chemiluminescence signal was located at the same azimuthal position in the channel as the center of the outer wall window that was used for UCI measurements, but one-third of the channel height axially downstream from the UCI window (see section 3.4.3). This axial displacement and axial gradients that are known to exist in the RDC flow field create a different relationship between the gas conditions observed by the PMT and the UCI system than the one between the pressure transducer and the UCI system, which were nearly aligned axially but azimuthally separated. Finally, the PMT measurements are not exclusively dependent on pressure like those of the transducer but are instead interpreted as related to the local combustion reaction rate [102]. In this way, the PMT is expected to produce strong signals when observing reaction zones within the flow field, and lower (but not necessarily negligible) signals in regions of hot or cool gases that are not reacting.

Figure 5.17 shows comparisons of the phase-averaged OH^* chemiluminescence signals (red line) with the cycle phase UCI signals (black line) for each test case. The phase-averaged PMT signals were shifted like the phase-averaged pressure measurements to approximately align the deep rise in signal with $\theta = 0$. The circumstances of the PMT collection and signal processing differed slightly between each case, and so the signal magnitudes could not be directly compared to each other. Instead, each phase-averaged PMT waveform has been scaled for clarity. All cases show agreement between the PMT and UCI signals in terms of the phase interval over which the luminosity increase associated with the passage of the detonation wave occurs. As previously mentioned, both optical measurement techniques could resolve the millimeter-scale gradients near this region of the flow and are similarly limited by the cycle phase representation.

The sharp peak in the PMT signals is understood to represent the combustion reactions associated with heat release by detonative burning near the wave front. This heat release and high post-wave pressures create the high mid-IR luminosity regions that generate corresponding peaks in the UCI signal. OH^* chemiluminescence decline following the peak signal value as the distance behind the wave increases. Cases A, B, and C exhibit non-negligible OH^* chemiluminescence signals in the post-wave region that has been associated with commensal combustion of remaining reactants that were not consumed by the wave front [102]. Heat addition due to commensal combustion is expected to raise the temperature of the combustion product regions but have a limited effect on the local pressure. As shown above in section 5.1.1, the UCI signal level is relatively insensitive to changes in temperature in gases that are already at post-combustion temperatures, and

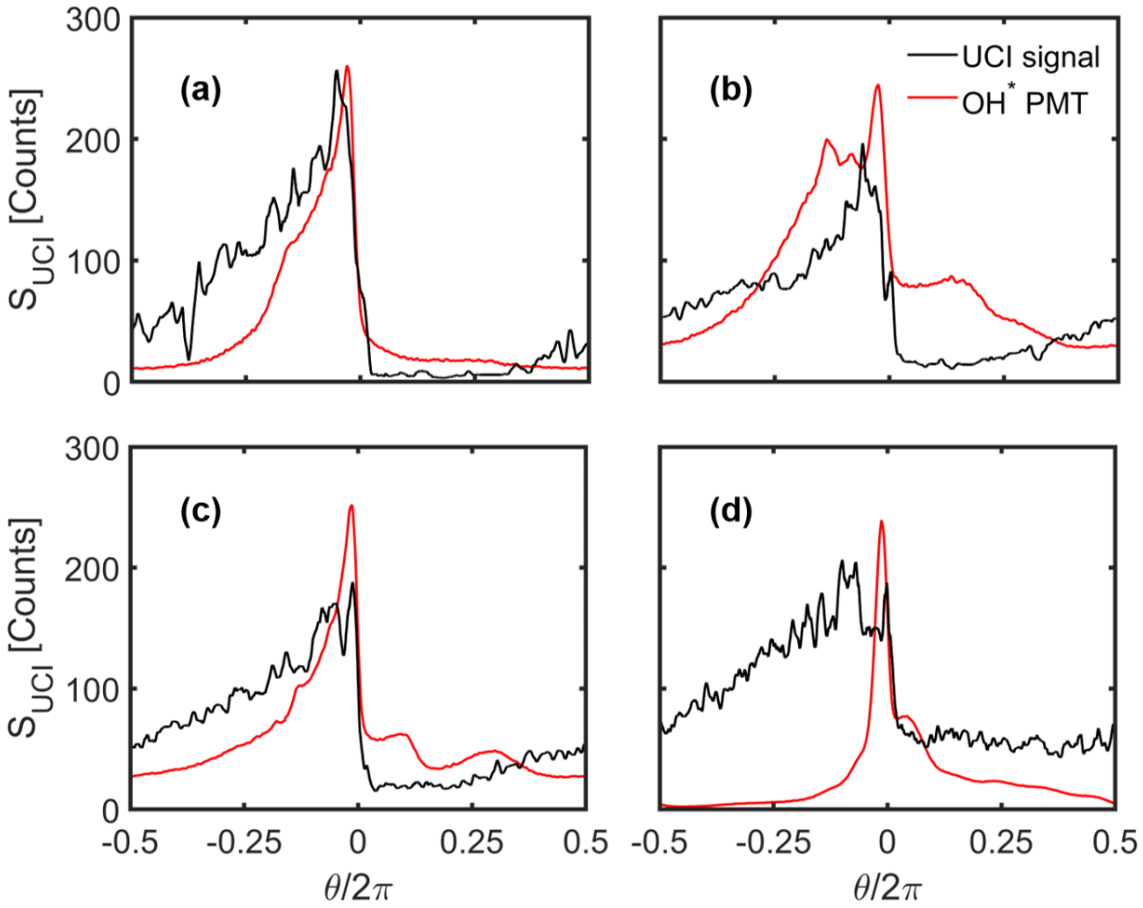

Figure 5.17: A comparison of the cycle phase UCI signal with phase-averaged OH^* chemiluminescence PMT measurements at a downstream axial position. The subplot labeling coincides with the case IDs: (a) case A, (b) case B, (c) case C, and (d) case D. The signal in case D has been scaled up by a factor of 2 for clarity.

so these commensal combustion processes were expected to have little impact on the UCI signal. This is consistent with the observations in Figure 5.17 where differences in the distributions of commensal combustion between the test cases do not produce noticeable signatures in the UCI signal. The lack of post-wave OH^* chemiluminescence signal intensity in case D indicates an almost complete absence of commensal combustion in that case. Still, there was significant UCI signal measured in the post-wave regions of the flow because the elevated temperatures behind the wave produce thermal mid-IR luminosity regardless of whether reactions are taking place or not. In this way, CO_2 UCI measurements can detect hot gas regions due to combustion products or shock-based compression that do not generate significant OH^* chemiluminescence. These two tools therefore complement each other to develop an understanding of the hot regions of the RDC flow field.

In addition to detecting commensal combustion reactions, the OH^* chemiluminescence

measurements indicate the presence of parasitic combustion in cases B, C, and D by the elevated PMT signals immediately ahead of the detonation wave front. The effects of parasitic combustion are seen in the non-negligible UCI signals in the pre-wave regions of those cases, indicating post-combustion temperatures at the refill region pressures. Case A shows negligible levels of both OH^* chemiluminescence and UCI signals immediately ahead of the wave, indicating that the reactant mixture region remained relatively cool and did not host significant reactions.

Observations of parasitic combustion events and their effects in both signals also appear to display some axial variation within the flow field. The OH^* chemiluminescence signal in case D shows a peak in reactivity ahead of the wave for only a relatively short phase interval ($\Delta\theta/2\pi \approx 0.09$). In contrast, the UCI signal shows that there is non-negligible mid-IR luminosity indicating elevated temperatures throughout the entire pre-wave fill region. This may indicate that most of the parasitic combustion occurs relatively far upstream, and reactions associated with parasitic combustion only occur at the axial location of the inner wall window in these tests (58% of the channel height downstream of the injection plane) shortly before the arrival of the detonation wave front. Similar trends with slightly longer pre-wave intervals of significant OH^* chemiluminescence are seen in cases B and C that also exhibited evidence of parasitic combustion. Future surveys that vary the axial position of the UCI measurements by leveraging the modularity of the RDC design could be used to investigate this potential axial structure of parasitic combustion effects.

5.6 Spatiotemporally resolved UCI near wave fronts

In addition to using the cycle phase representation of the UCI data to examine large-scale structures in the RDC flow field, the individual UCI frames captured during the tests can be used to examine the small structures in the RDC flow field. The UCI system is uniquely capable of producing high spatial resolution images of structures near the detonation wave front because of its short effective integration time ($240\,\mathrm{ns}$) compared to the longer integration times used in previous passive mid-IR imaging measurements in RDCs using direct detection [59]. All of the individual UCI frames captured during this campaign can be seen in with low detail in the composite images shown above in Figure 5.10 (also in Appendix B). This section displays a sampling of UCI frames in more detail that are rich in small-scale features and gradients that demonstrate the spatiotemporal resolution achieved by the system.

Regions of the RDC flow field far from the detonation wave front, such as the reactant refill region, show some spatial structure in the UCI measurements, but they are typically

gradual changes in luminosity that are low in amplitude and spread across most of the FoV. Regions close to the detonation wave front display sharp gradients and millimeter-scale structures with variation in both the azimuthal and axial directions. Additionally, these near-wave regions are where temporal resolution is essential because of the supersonic propagation speed of the wave front. For these reasons, the example images in this section focus on regions of the flow field captured near the detonation wave front. Specifically, examples were chosen that feature two distinct processes in the detonation wave: rapid compression and heat release at the detonation wave front (see section 5.6.1) and rapid expansion processes in the region immediately behind the detonation wave front (see section 5.6.2).

5.6.1 Detonation wave front images

Figure 5.18 shows a collection of two examples of UCI frames from each test case that capture mid-IR luminosity fields near the leading edge of detonation wave fronts in the RDC. Neglecting potential pre-heating effects due to parasitic combustion, the idealized one-dimensional structure of a detonation wave comprises an initially cool gas that is compressed by a propagating shock wave followed by rapid heat release at elevated pressures [103]. The pressure and temperature rise due to compression by the leading shock wave occurs on micrometer length scales below the spatial resolution of the UCI system, and so is expected to appear as a sharp edge separating the low signal strengths associated with cool reactant gases from the intermediate signal strengths associated with compressed reactants at elevated post-shock temperatures. The spatial interval between the shock wave and the reaction zones that produce significant heat release within the detonation wave is known as the *induction length* and typically takes values on the order of a millimeter in RDC systems. The heat release following the induction length will produce maximum combustion product temperatures at pressures near the post-shock values before subsequent expansion processes occur. This is expected to result in the highest mid-IR luminosity in the regions immediately following the induction length.

This general structure is represented in the UCI frames capturing detonation wave front propagation. Specifically, Figures 5.18(b), (c), and (g) show low-luminosity regions indicative of cold reactant gases toward the right side of the frames with a distinct sharp edge of intermediate mid-IR luminosity (between 100 to 150 counts) near the middle of the frames. This intermediate luminosity appears to correspond to post-shock gas conditions of elevated pressures and temperatures that are higher than reactant temperatures, but below post-combustion temperatures. Frames (b) and (d) show intervals of $\geq 5\,\mathrm{mm}$ behind

the apparent shock front without significant increases in luminosity, which is longer than expected induction lengths. This could indicate that the reactant mixture in these regions of the flow was not conducive to immediate ignition, perhaps because of insufficient mixing. Frame (g) shows an increase in luminosity to maximum luminosity levels for case C after an interval of $3\,\mathrm{mm}$ with limited variation in the axial direction, consistent with the one-dimensional idealization of the detonation wave process.

Other frames including (a), (c), (e), (f), and (h) do not clearly show regions of low-luminosity cool gas associated with fresh reactants but do show rapid increases in luminosity up to the highest observed signal levels (near 300 counts for cases A, B, and C and 200 counts for case D). This appears to show the rapid heat release process associated with detonative burning occurring over millimeter length scales.

In addition to the structure along the direction of wave propagation, the example UCI frames show significant axial variation in properties near the wave front. Studies have shown that detonation waves propagating in two and three-dimensional environments will exhibit variation orthogonal to the direction of their propagation even when propagating into homogeneous mixtures [60, 61]. The non-premixed RDC creates inhomogeneous reactant mixtures that introduce mechanisms for generating additional detonation wave structure in the axial direction [104]. Frames (c) and (e) show significant variation in luminosity along the axial direction, despite exhibiting wave structures that appear to be oriented to propagate azimuthally. Frames (a), (b), and (d) appear to show noticeable tilts in the orientation of the strong luminosity gradients, suggesting that the wave is not traveling exclusively in the azimuthal direction in these areas. Frames (a) and (f) show small "hot spots" of isolated high luminosity that are approximately $2\,\mathrm{mm}$ in diameter. These could represent either local ignition kernels or pressure spikes due to multi-dimensional effects in the detonation system. These types of observations can be used to enhance the understanding of detonation wave front morphology and the underlying processes.

These measurements demonstrate the high spatiotemporal resolution that can be achieved with the pulsed UCI system and the importance of this resolution capability in studies of detonation processes. The millimeter-scale structures and sharp, sub-millimeter scale gradients resolved in Figure 5.18 are advecting through the FoV at near the detonation wave front propagation speeds on the order of $1\,\mathrm{km/s}$. Measurement integration times on the order of microseconds would cause smearing of these small-scale features as they traveled across the field of view and potentially evolved in time. In this way, the $240\,\mathrm{ns}$ time resolution of the pulsed UCI system was necessary for spatially-resolved imaging measurements in these environments.

5.6.2 Expansion region images

Figure 5.19 shows a set of frames that was sampled that capture regions of decreasing mid-IR luminosity behind the detonation wave front that are characteristic of expansion processes within combustion products. The expansion process behind the detonation wave front is important to understanding RDC physics and designing practical systems because it is influential in determining the exhaust conditions at the exit of the combustion chamber. Excessive pressure loss or non-ideal entropy generation in the expansion process could compromise the pressure gain nature of RDCs that is the source of potential efficiency benefits associated with this technology. Because decreases in both pressure and temperature associated with gas expansion in combustion product zones cause decreases in thermal mid-IR luminosity, the mid-IR UCI measurements are capable of observing the effects of these processes. Although the gas propagation speeds are slower than those near the detonation wave front, sufficient temporal resolution is still required to avoid smearing small structures and sharp gradients in these regions of the flow field.

The frames in Figure 5.19 show regions of high luminosity on the right side of the FoV with a transition to lower luminosity on the left side of the FoV. These transitions appear to be very abrupt, with significant changes in luminosity level of up to a factor of two occurring over spatial intervals of less than $1\,\mathrm{mm}$. Several computational studies, such as one by Zhdan *et al.* [105], predicted rapid expansion processes shortly after the passage of the detonation wave that appear to be consistent with UCI observations.

Davidenko *et al.* [62] predicted that part of the expansion in the combustion products would occur by expansion fans anchored at the top and bottom axial ends of the detonation wave front that emanate back into the post-wave regions. These expansion fans would cause rapid expansion at an angle relative to the azimuthal propagation of the detonation wave. For regions closer to the bottom detonation wave near the injection plane this would appear to be a sharp gradient in density that extends from the lower right side of the combustion products toward the top left. The location of the sapphire window is closer to the injection plane (the window frame extends from 12% to 36% of the height of the channel above the injection plane, see section 3.4.3), and so a gradient in mid-IR luminosity at this angle would be expected in the UCI measurements as a result of the effects of these expansion fans. Frames (a), (b), (c), and (f) in Figure 5.19 appear to show this angled expansion process in the lower halves of the FoV. This evidence supports the existence of a significant expansion fan anchored near the injection plane in those test cases.

Frame (g) shows another interesting example of post-wave structure observed with the UCI measurements. This frame shows both a rapid increase in mid-IR luminosity near the center of the FoV, likely associated with heat release from combustion reactions, followed

almost immediately by a rapid decrease in luminosity. The high luminosity zone shows little variation in the axial direction along the entire height of the FoV and is only $2\,\mathrm{mm}$ thick in the axial direction. This orderly structure stands in contrast to the amorphous distribution of high luminosity seen in the other example from case D in frame (h). This instance exhibits significant variations in both the azimuthal and axial directions. This large qualitative difference between the observed in the same region of the flow field for the same case demonstrates the significance of cycle-to-cycle variations in the RDC that can be lost in the cycle phase perspective presented in section 5.5. The examples in Figure 5.19 show how mid-IR UCI measurements of passive thermal radiation can be used to study phenomena beyond compression and heat release, such as post-wave expansion.

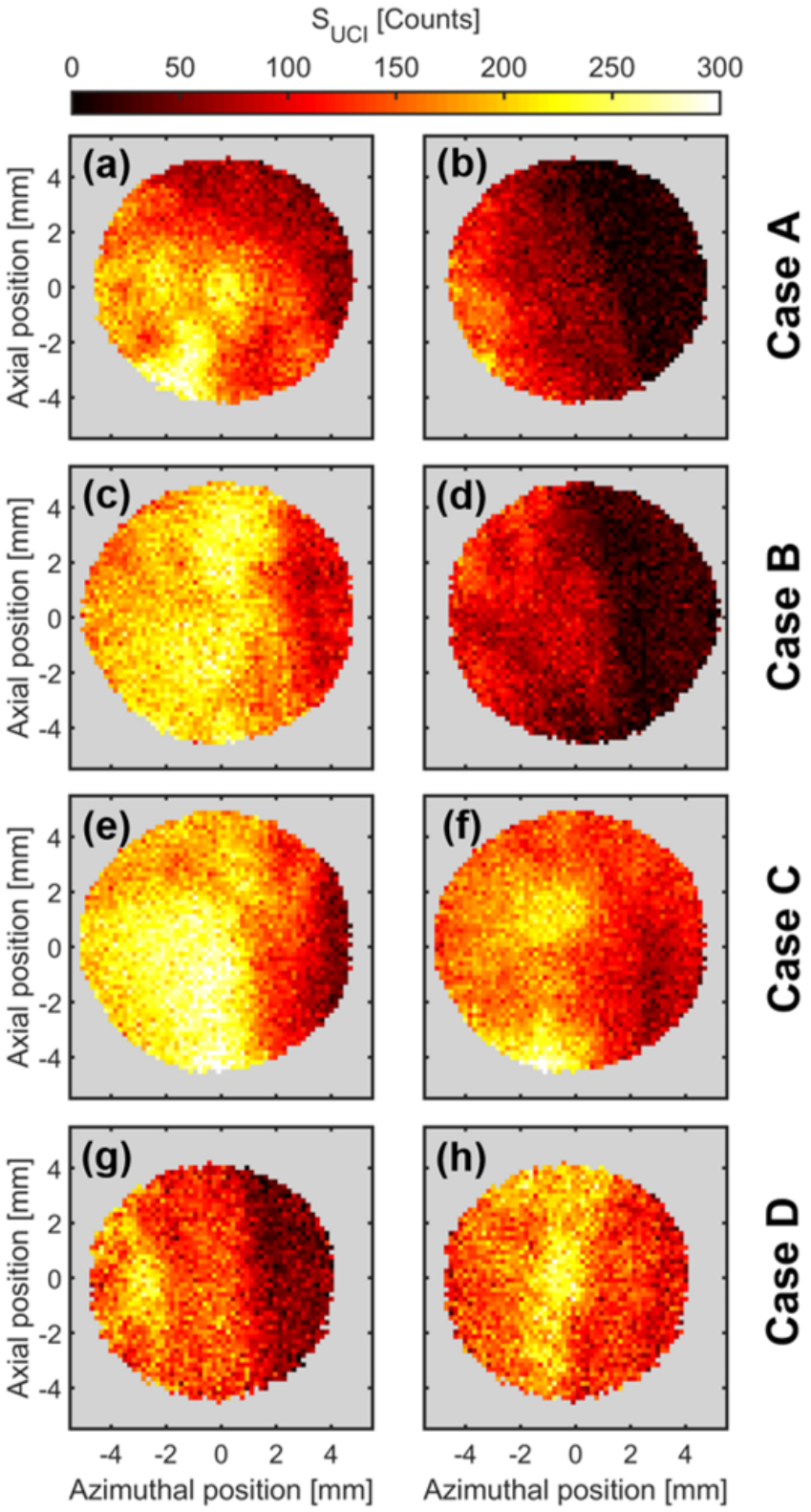

Figure 5.18: Two examples of UCI frames capturing detonation wave fronts from each RDC test case. The signal in case D has been scaled up by a factor of 1.5 for clarity.

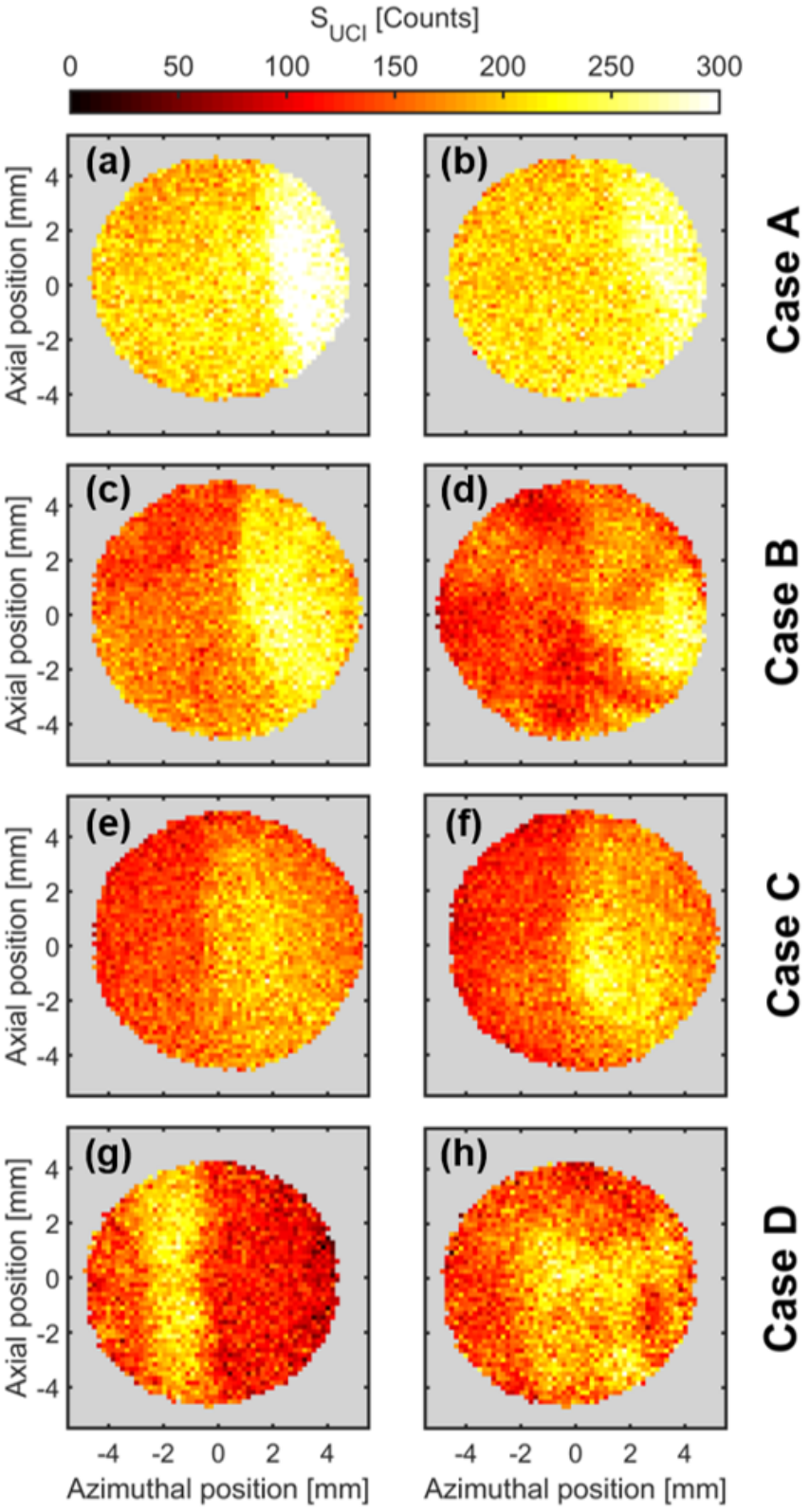

Figure 5.19: Two examples of UCI frames capturing expansion regions immediately behind detonation wave fronts from each RDC test case. The signal in case D has been scaled up by a factor of 1.5 for clarity.

CHAPTER VI

Mid-IR Absorption Imaging of Hydrocarbon Fuels

This chapter examines the use of mid-IR UCI for observing the distribution of hydrocarbon fuels within the flow field of the RDC through the detection of mid-IR absorption across the combustion channel. This type of measurement could be implemented in the RDC by installing a small, high-temperature blackbody emitter in the center-body of the RDC to back-illuminate the combustion channel for the UCI system installed on the outer wall window (see 3.10). Hydrocarbon fuel species exhibit strong, isolated mid-IR absorption lines near $3.3\,\mu\mathrm{m}$ due to C–H stretch vibrational bands, making them good targets for detection by absorption. These measurements could be applied to study fuel injection and mixing processes that are critical to the operation of non-premixed RDCs. Additionally, this technique could be used to observe and study the buffer regions of high or low fuel concentrations in the refill regions that have been hypothesized to exist (see section 1.4.3).

Due to the operational characteristics of the RDC facility at the time of this work, stable detonations could not be sustained in the combustor with hydrocarbon fuels. This prevented the absorption imaging diagnostic from being performed in the RDC as a part of this effort. However, on-going modifications to the facility will soon enable operation with full hydrocarbon fueling. To prepare for this opportunity, hydrocarbon mid-IR absorption measurements were performed in reference cells with a benchtop UCI configuration to characterize the response of the UCI system in these types of measurements. The results of those measurements are presented in this chapter and are used to predict the response of the system to conditions relevant to the RDC environment. This informs recommendations about which fuel species will be the most effective for achieving measurement goals in the RDC.

6.1 Absorption cell measurements

Measurements of absorption in known gaseous environments help characterize the UCI system developed and prepare it for application in hydrocarbon absorption imaging experiments in the RDC. The effects of spatial-spectral coupling will cause a non-uniform response to spectral absorption across the FoV, and so measurements in controlled absorption cells allow for models of these effects to be tested. Additionally, the observed absorption signal will depend on the precise spectral response of the system and be highly sensitive to deviations in the realized spectral bandwidth from that predicted by models. The absorption cell measurements will allow for the evaluation of which hydrocarbon fuel species are appropriate for absorption imaging measurements in the RDC. Ethane, one candidate fuel species, has incomplete IR spectrum data in the HITRAN [4] and NIST databases [5]. These measurements will be useful to calibrate empirical absorption models that can predict and interpret ethane absorption measurements in the RDC.

6.1.1 Absorption cell setup

Two evacuable reference cells were used to perform absorption characterization measurements, one with a long absorption path ($109\,\mathrm{cm}$) and one with a short absorption path ($7.6\,\mathrm{cm}$). Two absorption path lengths were necessary because strong absorption by ethane at the gas concentrations used for testing produced insufficient signal strengths of the transmitted signal in the long path cell. The long path reference cell was stainless steel with a $109\,\mathrm{cm}$ absorption path length. The input and output ends of the cell have sapphire windows installed with AR coatings for wavelengths between $2\,\mu\mathrm{m}$ to $5\,\mu\mathrm{m}$. The cell has a gas inlet and outlet ports welded into its sidewalls. The short path reference cell is a rectangular volume with independent anodized aluminum walls that are sealed with silicone gaskets. Three $50\,\mathrm{mm}\times 50\,\mathrm{mm}$ quartz windows provide optical access to the cell and have sufficient transparency near $3.4\,\mu\mathrm{m}$ for absorption measurements. Photographs of both of these cells are shown in Figure 6.1.

Both cells used the same two-port gas delivery and pressure monitoring configuration shown by the diagram in Figure 6.2. The output port was connected to a vacuum pump with a tee to a pressure gauge used to monitor the evacuation and fill processes. The inlet port of the cell is connected through a tee to lines for a chosen target gas and a non-absorbing buffer gas, in this case, nitrogen gas. The test gas and buffer gas lines have needle valves installed to meter the inlet flow and give precise control over the gas concentrations within the cell.

To operate the gas cell for absorption measurements the cell was evacuated using the

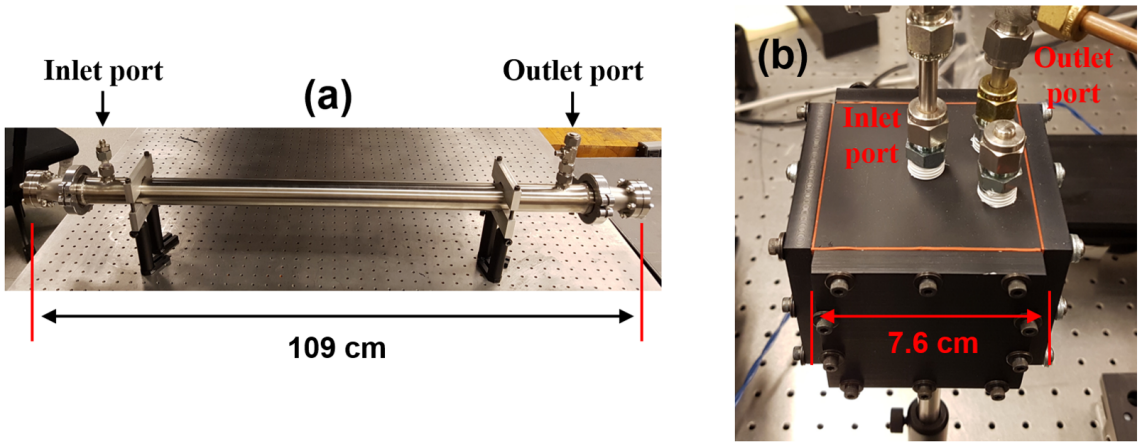

Figure 6.1: Photographs of the (a) long path length and (b) short path length absorption cells used for hydrocarbon absorption tests.

connected vacuum pump. The valve to the pump line was then closed and the needle valve in the test gas line was opened and modulated to allow slow, controlled in-flow of the absorbing species. The cell was filled until the desired absorber partial pressure was reached on the monitoring gauge and then the needle valve was fully closed. The gauge used to monitor the pressure in the reference cells read pressures in units of psi with 0.05 psi divisions. All absorber partial pressures were converted and are reported in kPa for the remainder of this section. The buffer gas valve was then opened to bring the pressure within the cell up to $1\,\mathrm{atm}$ with nitrogen buffer gas. With the gas composition prepared, a $25\,\mathrm{mm}$ aperture blackbody source (Infrared Industries model 463) operated at $900\,^{\circ}\mathrm{C}$ was placed behind the cell's inlet window and aligned with the cell's axis.

The UCI system configuration used in the absorption cell measurements was the bench-top arrangement used for characterization measurements presented in Chapter IV. For absorption cell measurements the pump laser was operated in long-pulse mode because temporal resolution was unnecessary. For most absorption measurements the crystal oven was operated without heating, except for ethane absorption measurements that required elevated crystal temperatures ($55\,^{\circ}\mathrm{C}$) to access ethane's strongest absorption band.

An important alteration to the UCI system for absorption measurements is the installation of a knife-edge attached to the oven that occludes stray pump beam light from entering unintended periodically poled gratings. The crystal is constructed with each grating placed side-by-side on the chip with $0.2\,\mathrm{mm}$ separating them. Initial absorption measurements showed non-negligible UCI signals even when the cell was flooded with a high ($>70\,\mathrm{kPa}$) ethylene partial pressure that should have eliminated all signal. These residual signals were found to closely match predictions of uniform blackbody UCI imaging using the $23.415\,\mu\mathrm{m}$

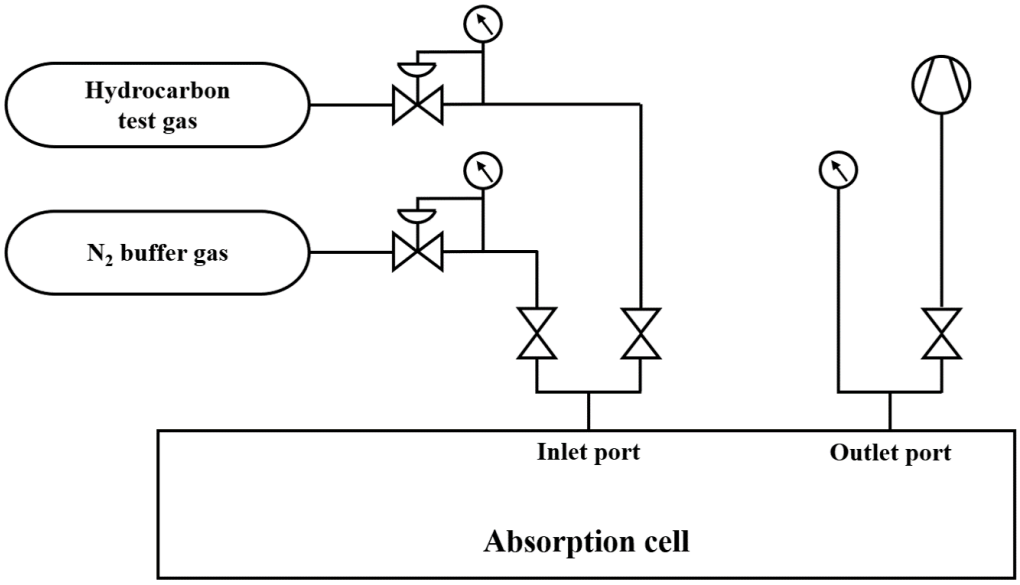

Figure 6.2: A schematic showing the gas delivery configuration used for hydrocarbon absorption measurements in the absorption cells.

poling period grating that neighbors the $22.45\,\mu\mathrm{m}$ grating in the crystal that is used to access hydrocarbon spectral bands. This evidence suggested that energy from within the wings of the laser pump beam was exciting upconversion of the blackbody radiation above $4\,\mu\mathrm{m}$ in wavelength within the $23.415\,\mu\mathrm{m}$ grating that contaminated measurements of hydrocarbon spectral absorption. A knife-edge was subsequently installed to block pump beam energy from entering the $23.415\,\mu\mathrm{m}$ grating while carefully avoiding occlusion of the pump beam from the $22.45\,\mu\mathrm{m}$ grating to the greatest extent possible.

6.1.2 Hydrocarbon test gases

This experimental setup was used to measure the response of the UCI to absorption by three gaseous hydrocarbon fuel species: methane, ethylene, and ethane. The $22.45\,\mu\mathrm{m}$ poling period grating was used to detect absorption of mid-IR light between $3.28\,\mu\mathrm{m}$ to $3.4\,\mu\mathrm{m}$. Strong absorption bands of methane and ethylene near $3.34\,\mu\mathrm{m}$ could be observed with the crystal operated at room temperature ($21\,^{\circ}\mathrm{C}$) while strong absorption by ethane near $3.4\,\mu\mathrm{m}$ was targeted by heating the crystal to leverage the temperature tunability of the UCI system. Table 6.1 summarizes the test conditions for each gas.

These experimental observations were compared to predicted UCI responses to validate and calibrate models that can be used to design the implementation of absorption imaging in the RDC. Simulations of the UCI absorption measurements used the same framework that was employed to predict the response of the system to uniform blackbody sources in

Table 6.1: Hydrocarbon test gases used for reference cell absorption experiments.

Species	Path length [cm]	P_{abs} [kPa]	$T_{crystal}$ [°C]
Methane (CH_4)	109	1.4, 2.8, 4.1, 5.5, 6.9	21
Ethylene (C_2H_4)	109	1.4, 2.8, 4.1, 5.5, 6.9	21
Ethane (C_2H_6)	7.6	6.9, 13.8, 20.7, 27.6	55

section 2.6. For gas cell absorption measurements, the cold gas absorption mechanism incorporated the effects of hydrocarbon absorption of light form the blackbody source. First, the response of the UCI system to uniform illumination by the blackbody source was computed without any absorption due to the target hydrocarbon species. Then a second simulation was performed to compute the response of the UCI system to a blackbody spectrum that experienced spectral absorption by the test gas at prescribed concentration and path length. The ratio of these two predicted images was used for comparison with the experimentally measured absorption response that varied across the image plane due to spatial-spectral coupling effects.

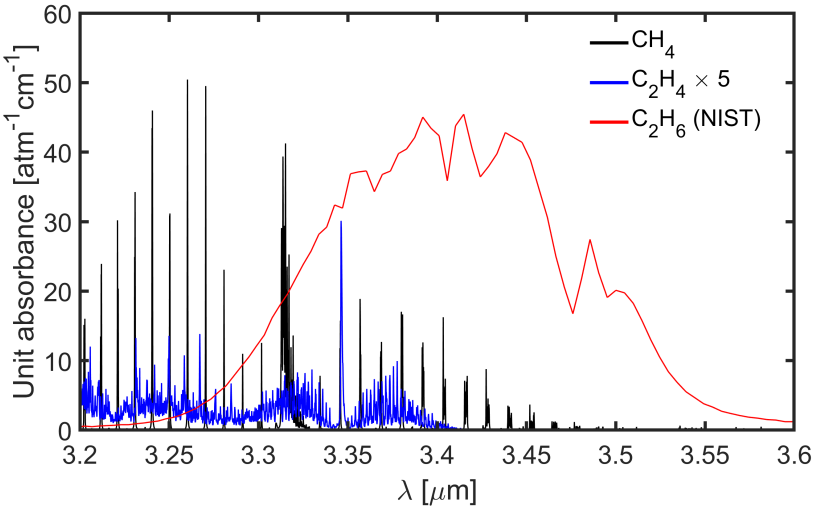

Figure 6.3: Calculated mid-IR absorption spectra for the three hydrocarbon fuel species listed in Table 6.1 provided displayed in terms of optical depth per unit pressure in atm of the absorbing species per unit path length in cm. The methane and ethylene absorption spectra were computed using parameters from the HITRAN database [4] with ethylene scaled up by a factor of 5 for clarity. The ethane absorption spectrum was generated from data provided in the NIST WebBook [5] and is arbitrarily scaled for clarity because absolute values were not available.

Accurate spectral data for each of the hydrocarbon fuel species is required to simulate the spectral absorption that they will cause. Data describing the line-by-line spectral absorption of methane and ethylene were taken from the HITRAN database [4]. The mid-IR spectral data for ethane in HITRAN were incomplete and did not contain the strong C–H stretch vibrational bands that are examined in this work. NIST WebBook [5] provides measured mid-IR spectra data for ethane and several other hydrocarbon species, however these are low resolution and give only relative spectral shapes, not quantitative absolute absorption values required for modeling. For this reason, the system response model for ethane will need to be developed empirically from the absorption cell test results rather than simulated a priori.

Figure 6.3 shows the modeled unit spectral absorbance in terms of optical depth per unit absorber partial pressure (in atm) per unit path length as a function of wavelength for the three hydrocarbon species that were tested. The absorption spectra of methane (black line) and ethylene (blue line) were generated based on the HITRAN absorption data. The ethylene spectrum has been scaled up by a factor of 5 for clarity of comparison with the stronger methane absorption lines. The low-resolution, relative spectral shape provided by NIST for ethane is shown by the red line in Figure 6.3. Because the ethane data did not provide estimates of the absolute absorption strength, the ethane spectrum has been arbitrarily scaled for comparison with the other fuel species. Unlike the other species, the ethane spectrum shown in the plot was not used for any modeling, instead replaced with an empirical approach, and is only shown in the plot for context.

Differences in the spectral profiles between methane and ethylene shown in Figure 6.3 can be used to predict differences that will appear in the response of the UCI system to their spectral absorption. The methane spectrum in this wavelength range is characterized by sharp peaks of strong spectral lines with intervals of low absorption separating them except for one broader feature near $3.31\,\mu\mathrm{m}$ associate with the Q branch. The isolated peaks are much narrower than the spectral bandwidth of the UCI system used to detect this signature ($19.8\,\mu\mathrm{m}$). This means that even as they saturate near 100% attenuation at their peaks, the UCI system will detect light from the spectral intervals between the peaks and report significant transmitted signal at locations on the sensor. In this way, the strong, isolated methane lines will cause the absorption signal to respond to relatively low concentrations of methane but show diminishing changes in signal as the methane concentration is raised. In contrast, the ethylene spectrum is characterized by more evenly distributed weak absorption lines. These will require greater concentrations of ethylene to produce significant absorption responses but will also cause more total attenuation in the UCI measurements at high concentrations compared to methane. These trends are apparent

in the absorption cell measurement results and RDC simulations described below.

6.1.3 Absorption measurements and data reduction

The experimental measurements were collected by first evacuating the gas cell and taking a reference UCI exposure. The test gas fill procedure was then used to fill the test cell with a known quantity of the target gas and a nitrogen buffer. Then an absorption signal UCI exposure was captured that could be compared through pixel-by-pixel ratios to the reference image to find the spectral transmission. Each measurement was performed with the blackbody source operated at a temperature of $900\,^{\circ}\mathrm{C}$ and between $30\,\mathrm{mJ}$ to $32\,\mathrm{mJ}$ of pump beam energy. The reference and signal images were averaged over 300 exposures to increase the SNR.

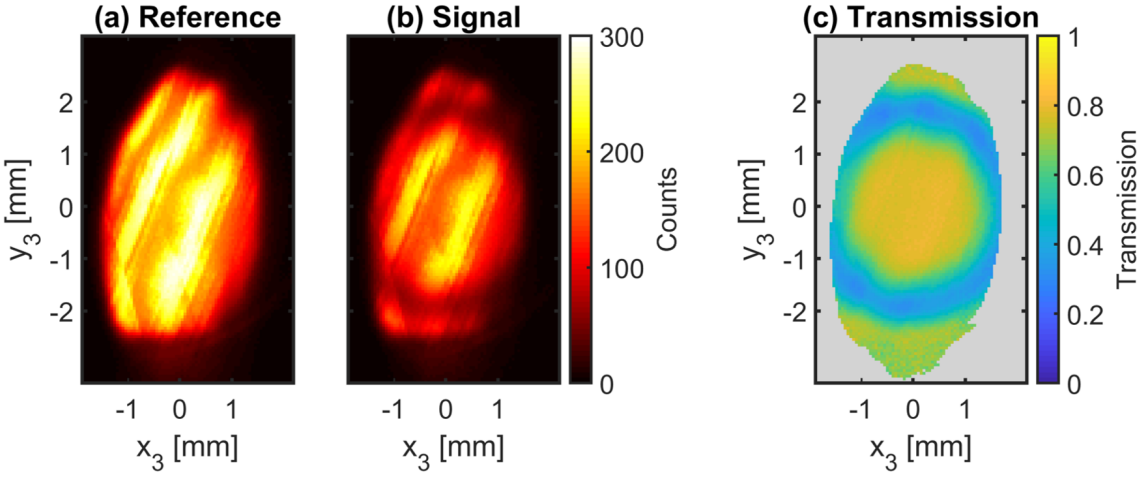

Figure 6.4: An example of absorption hydrocarbon absorption measurements for $5.5\,\mathrm{kPa}$ of methane in the $109\,\mathrm{cm}$ path length absorption cell. The images show (a) the reference image of the blackbody illumination, (b) the signal image from the transmitted mid-IR light, and (c) the resulting transmission field for a reference image threshold value of 25 counts.

Examples of the reference, signal, and resulting transmission images are shown in Figure 6.4. These were measured for methane as a test gas at a partial pressure of $5.5\,\mathrm{kPa}$. The strange shape of the illumination field is a result of the fact that the detected image is a caustic formed by the mid-IR light glancing off the cylindrical inner walls of the long path absorption cell. This was achieved through a small change in the alignment of the cell relative to the blackbody emitter and the UCI system and was found to concentrate the freely propagating light to the UCI system better, producing greater signal strengths.

An important feature to note about the measurements is the presence of spectral fringing in not only the reference and signal images, but also (faintly) in the transmission images.

The spectral fringing pattern in each exposure is dependent on the precise spectral content of the light being measured. The absorption by the test gas changes the spectral content being detected across the image plane which causes the spectral fringing to change its pattern, not just its intensity, between the reference and signal images. The differences in the fringing patterns of the reference and signal images result in an effective fringing pattern in the transmission image. The contrast in the resulting transmission fringing pattern has a lower amplitude than those in the reference and signal images, but still causes artifacts in the absorption data as will be shown further below.

The concentric symmetry of the UCI system response due to spatial-spectral coupling is demonstrated by the ring-shaped feature shown in Figure 6.4 due to narrowly spaced Q branch lines in the methane absorption spectrum. As was done for the H_2O thermal emission measurements shown in Figure 4.19, the absorption measurements can be displayed in terms of radial distance in the image plane. Increasing distances from the center of the FoV correspond to increasing mid-IR wavelengths, however because the system was not designed to operate as a spectrometer the spectral bandwidth at each radial location is relatively broad ($19.8\,\mathrm{nm}$) producing poor spectral resolution. And so while a mapping from r_3 to λ_1 could be done in terms of a peak response wavelength, it has been avoided here because the relatively broad spectral response does not produce clear representations of the narrow spectral features being measured.

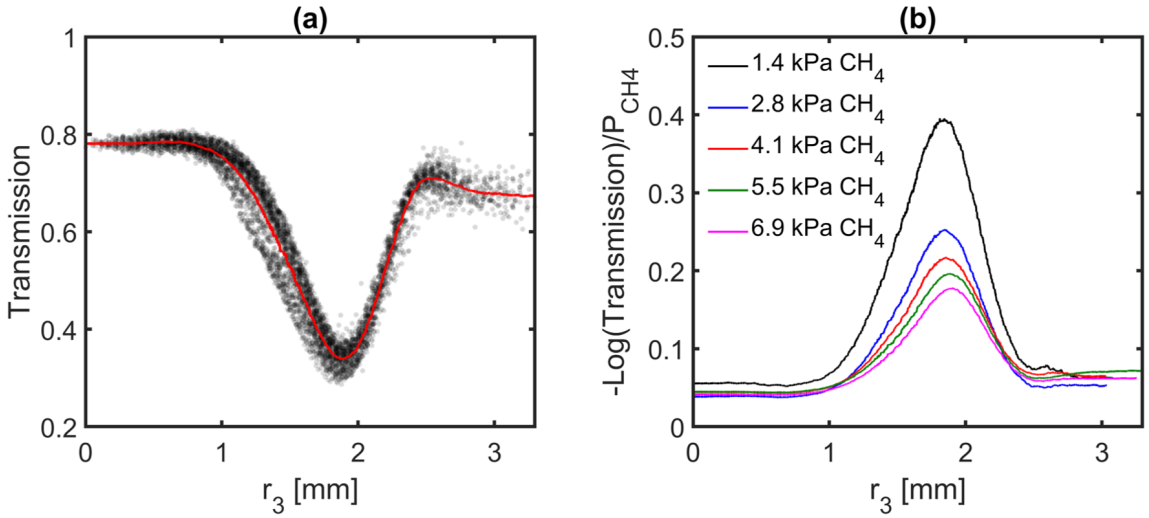

Figure 6.5: (a) The transmission signal for $5.5\,\mathrm{kPa}$ of methane in the $109\,\mathrm{cm}$ path length absorption cell shown in radial coordinates in the image plane. (b) The negative natural logarithm of transmission in radial coordinates scaled down by the partial pressure of methane for each case.

Figure 6.5 shows the methane absorption results plotted in radial image plane coordi-

nates. Figure 6.5(a) shows the individual pixel values from Figure 6.4(c) (black dots) and a 100 point rolling average (red line) that was used to mitigate the effects of noise and spectral fringing in all of the measurements. The large dip near $r_3 = 1.9\,\mathrm{mm}$ represents the effects of closely spaced Q branch lines while the lower magnitude attenuation below $r_3 = 1.0\,\mathrm{mm}$ and above $r_3 = 2.5\,\mathrm{mm}$ are the result of R and P branch lines, respectively, though they are not resolved through this spatial-spectral coupling effect. Figure 6.5(b) shows the negative natural logarithm of the transmission data (with the 100 point rolling average applied), which is equivalent to an effective optical depth, for each methane concentration with the spectral curves scaled down by the methane partial pressure.

In a spectrally resolved measurement, the measured optical depth should be proportional to the spectral absorption cross-section of the target species at those gas conditions. The fact that when changes in methane concentration are accounted for by dividing the optical depth by the measured partial pressure the data in Figure 6.5(b) do not collapse to a single spectral shape reflects the lack of effective spectral resolution in these measurements. Rather than the UCI response at each point being a direct measurement of methane absorption at a particular wavelength, it is modified by the broad spectral response of the UCI in what becomes akin to a spectral instrument response function. As has been mentioned previously, this prevents resolution of isolated absorption lines in the methane spectrum and direct comparison of UCI absorption observations with the modeled spectra shown in Figure 6.3. Instead, the observations must be compared to simulation results from the UCI response model that account for the effects of UCI spectral bandwidth on measurements.

6.1.4 Absorption cell measurement results

Figure 6.6 shows the UCI measurements of methane absorption at five different concentrations. The solid lines show the 100 point rolling average of the measured data while the dashed lines show the a priori UCI model simulations of the measurements computed for the target methane concentrations. These measurements were all captured with a crystal temperature of $21\,^{\circ}\mathrm{C}$ and individual pump pulse energies of $31.5\,\mathrm{mJ}$ in long-pulse mode. The modeled and observed responses both exhibit the expected shape in the image plane coordinates with a strong dip above $r_3 = 1\,\mathrm{mm}$ associated with Q branch absorption and higher, approximately constant transmission values at other locations due to underresolved absorption by strong isolated lines. However, there are discrepancies between the modeled and observed responses in two aspects: the location of the peak of the transmission dip in the image plane and the magnitude of attenuation at all radial locations.

The UCI response models predict that the minimum transmission point in the methane

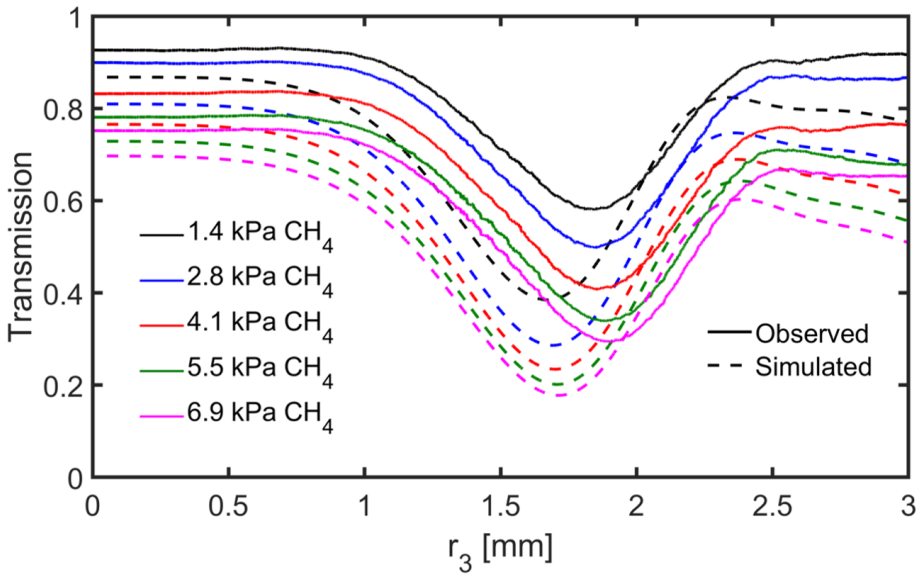

Figure 6.6: A comparison between the measured and simulated transmission responses of the UCI system in radial coordinates for each partial pressure of methane tested in the absorption cell.

absorption measurements will occur approximately $180\,\mu\mathrm{m}$ closer to the center of FoV than is observed. Through the spatial-spectral coupling effect, this implies that the measurements were detecting shorter wavelengths at each radial location in the image plane than would be expected. The location of this peak attenuation feature is highly sensitive to environmental conditions, through the temperature of the nonlinear crystal, and manufacturing tolerances, through the poling period of the nonlinear crystal. The discrepancy would be eliminated by performing the simulations with either $2.5\,^{\circ}\mathrm{C}$ reduction in crystal temperature or a $10\,\mathrm{nm}$ reduction in assumed poling period ($22.44\,\mu\mathrm{m}$ instead of $22.45\,\mu\mathrm{m}$). The temperature of the air in the room and the crystal oven were monitored during the experiments and were seen to be stable near $21\,^{\circ}\mathrm{C}$. Additionally, the measurements were repeated on three different days at similar conditions and were found to exhibit the same minimum transmission location. This seems to suggest that the temperature estimate for these measurements of $21\,^{\circ}\mathrm{C}$ was not the issue. The poling period was established by near-IR measurements in Chapter IV to be within $5\,\mathrm{nm}$ of the design poling period of $22.45\,\mu\mathrm{m}$. A crystal temperature excursion during those near-IR spectroscopy measurements from the measured $22\,^{\circ}\mathrm{C}$ to $25\,^{\circ}\mathrm{C}$ could account for the discrepancy, but there is no evidence that this occurred. At this time the exact cause of this difference cannot be determined. This difference does not compromise the application of this diagnostic because the crystal temperature would be adjusted for those measurements to shift the maximum attenuation response toward the center of the FoV by heating the crystal and checking its spectral re-

sponse.

The discrepancy between the observed and modeled attenuation levels is important because it could affect the optimal fuel species choice when designing the absorption imaging measurements and interpretation of the results of those measurements. The exact cause of this discrepancy is also not known at this time. It could be related to differences in the predicted and realized spectral bandwidths due to causes such as errors in the estimate of the crystal length and random variations in the domain lengths of the periodically poled grating. A significantly broader spectral response will result in less measured attenuation in the UCI signal for these species. For the RDC response prediction shown in section 6.2, both the a priori simulation results and a version of those results scaled to match the observations shown in Figures 6.6 and 6.7 (the same discrepancy is seen in the ethylene results) for the sake of context and comparison.

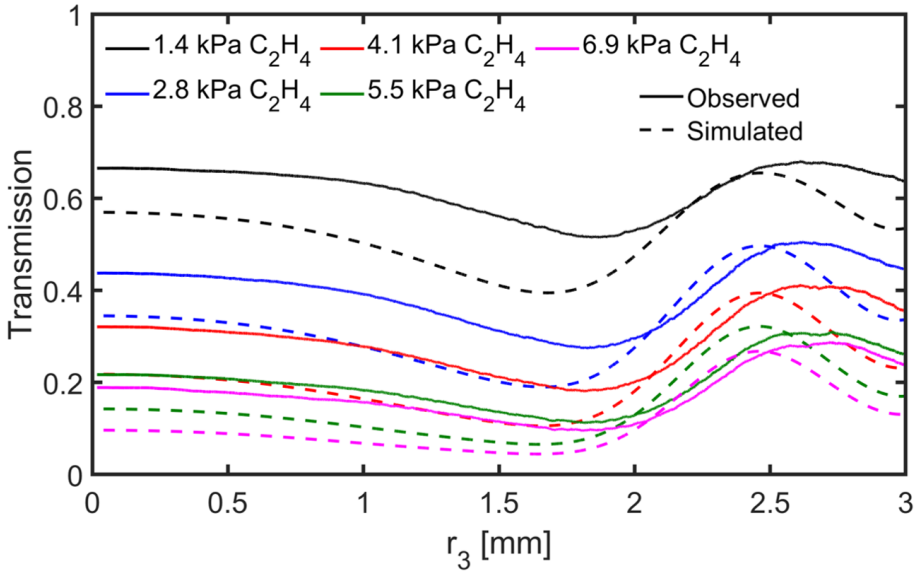

Figure 6.7: A comparison between the measured and simulated transmission responses of the UCI system in radial coordinates for each partial pressure of ethylene tested in the absorption cell.

Figure 6.7 shows the same type of absorption measurements for ethylene as the test gas at the same concentration levels. These measurements were also performed with a crystal temperature of $21\,^{\circ}\mathrm{C}$ and individual pump pulse energies of $31.5\,\mathrm{mJ}$ in long-pulse mode. The simulations and observations both show the same general radial response shape associated with ethylene detection, including a trough of increased attenuation located away from the center of the FoV. These results show similar discrepancies in the location of the attenuation peak and attenuation magnitude between the modeled and observed responses that were seen in the methane measurements. These are likely due to the same causes and

will be treated in the same way in the following section.

Comparing the results of ethylene absorption in Figure 6.7 to those for methane in Figure 6.6 shows some of the trends predicted above based on examination of the absorption spectra in Figure 6.3. The long path length of reference cell used in these measurements caused optically-thick conditions even for the lowest target species partial pressures, and so the greater low-concentration attenuation of methane is not apparent here, though it will be seen in the simulations in section 6.2. But the predicted increased attenuation by ethylene at optically-thick conditions due to its more closely spaced spectral lines is apparent in this comparison. This shows that ethylene may be a better absorption target than methane at higher concentrations because of its stronger attenuation and more even UCI response across the FoV.

Ethane measurements differed from those of methane and ethylene because its strongest absorption features occur at longer wavelengths near $3.4\,\mu\mathrm{m}$. This required the crystal temperature to be heated to $55\,^{\circ}\mathrm{C}$ to leverage the temperature tuning capability of the UCI system to detect those longer wavelengths. This had the effect of shifting the predicted peak response wavelength at the center of the FoV from $3.295\,\mu\mathrm{m}$ to $3.345\,\mu\mathrm{m}$. In addition to the different operating temperature of the ppLN crystal, the short path ($7.6\,\mathrm{cm}$) had to be used to avoid over-attenuation of the mid-IR illumination that would lead to poor detection SNRs.

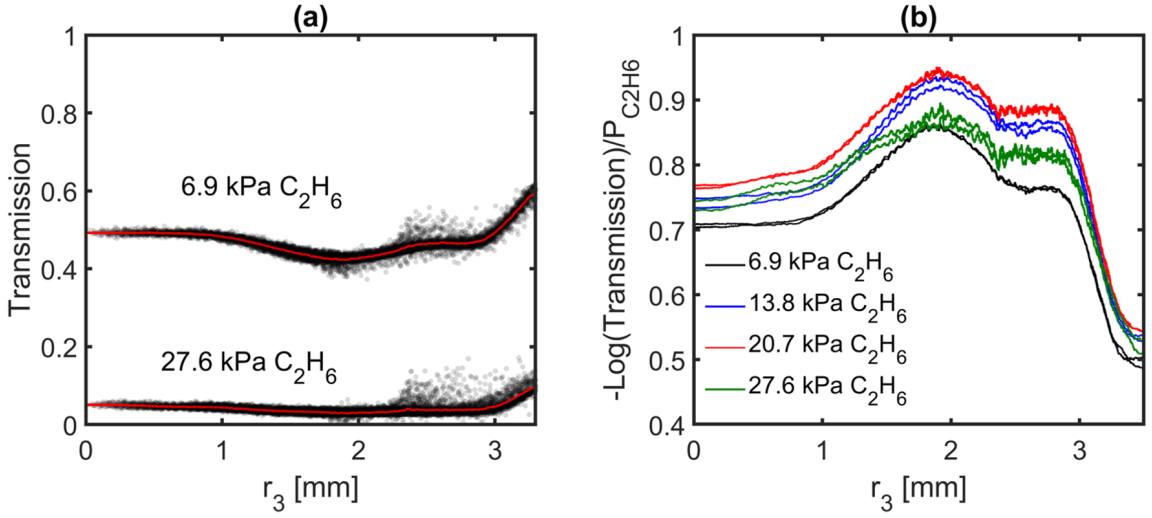

Figure 6.8: (a) The transmission signal for $6.9\,\mathrm{kPa}$ and $27.6\,\mathrm{kPa}$ of ethane in the $7.6\,\mathrm{cm}$ path length absorption cell shown in radial coordinates in the image plane. (b) The negative natural logarithm of transmission in radial coordinates scaled down by the partial pressure of ethane for each case.

The experimental observations of ethane absorption captured with the UCI system are

shown in Figure 6.8. Figure 6.8(a) shows examples of the transmission data points recorded for ethane absorption in the reference cell at two partial pressures, $6.9\,\mathrm{kPa}$ and $27.6\,\mathrm{kPa}$. The solid red lines show 100 point rolling averages that were used to de-noise the measured signals for subsequent analysis. The transmission measurements were performed twice at each ethane partial pressure to ensure repeatability of the measurements. Figure 6.8(b) shows the same effective optical depth scaling for ethane that was plotted for methane in Figure 6.5(b). Unlike the results for methane, the ethane curves show a much better collapse with all of the curves falling within $\pm 8\%$ of the mean value of all of the curves across the FoV out to $r_3 = 3\,\mathrm{mm}$. This is due to the more densely populated, relatively broad absorption spectrum exhibited by ethane at these wavelengths compared to the methane spectrum that was comprised of sharp, isolated peaks. This improved optical depth scaling for ethane allows for direct extrapolation of the system response to different concentrations and path lengths with improved accuracy.

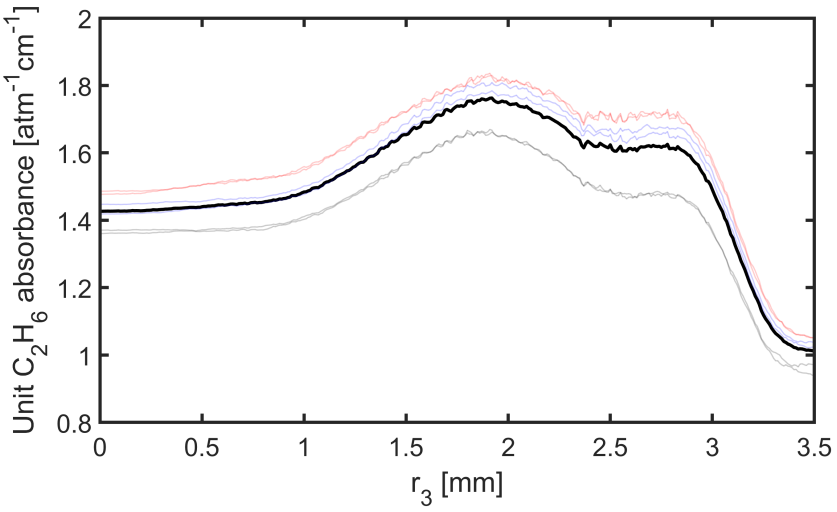

Figure 6.9: Empirically determined unit absorbance of ethane as determined by UCI absorption cell measurements superimposed over the corresponding measurements used to compute it.

This scaling is important because of the lack of quantitative ethane absorption data in available databases prevented a priori prediction of ethane absorption. Instead, an empirical approach based on the results of the absorption cell experiments was needed for modeling purposes. To allow for convenient extrapolation of the measured attenuation, the results shown in Figure 6.5(b) were rescaled to account for the optical path length ($7.6\,\mathrm{cm}$) and expression of pressure units in terms of atm. The response curves for ethane partial pressures of $6.9\,\mathrm{kPa}$, $13.8\,\mathrm{kPa}$, and $20.7\,\mathrm{kPa}$ were then averaged together to produce a single representative unit absorbance curve shown by the thick black line in Figure 6.9. The re-

sponse for $27.6\,\mathrm{kPa}$ was excluded because it produced strong attenuation that significantly reduced its SNR and ability to resolve the response near $r_3 = 1.8\,\mathrm{mm}$.

Ethane absorption responses shown in the following section were computed by multiplying the unit absorbance curve shown in Figure 6.9 by the appropriate path length ($0.76\,\mathrm{cm}$ in the RDC) and ethane partial pressure and then taking the negative exponential of that curve. The differences in the measured curves in Figure 6.8(b) suggests an uncertainty of $\pm 8\%$ in terms of optical depth using this approach. This will translate an approximately similar uncertainty in relative absorption (one minus the transmission) at lower attenuation levels and be transformed in a nonlinear way for optically-thick conditions.

6.2 Simulation of RDC absorption imaging

The absorption cell experiments validated models of UCI measurements of methane and ethylene absorption and calibrated the model of ethane spectral absorption. These models can now be used to predict measurement performance in new environments and choose appropriate fuel species for absorption imaging. In the case of the RDC combustion channel, absorption imaging will be intended primarily to identify the *buffer regions* that have been hypothesized to exist in the RDC flow field as discussed in section 1.4.3. These buffer regions will be at gas conditions close to those of the injected gases and be either almost entirely fuel or nearly devoid of fuel. Detecting fuel-rich buffer regions will be best achieved by an absorption diagnostic that detects a strong attenuation for pure fuel or nearly pure fuel volumes within the combustion channel. Detection of fuel-lean buffer regions may still be possible if context can be provided by other measurements and the absorption imaging system can distinguish well-mixed reactant regions from buffer regions containing little or no fuel. Therefore, absorption imaging of both pure fuel and well-mixed fuel concentrations at representative design equivalence ratios will be considered.

The parameters that are expected to describe the relevant conditions for buffer regions and well-mixed reactant regions in the RDC are a $7.6\,\mathrm{mm}$ path length, $0.8\,\mathrm{atm}$ static pressure, $300\,\mathrm{K}$ temperature, and equivalence ratios (hydrocarbon-air operation) between 0.8 and 1.4 in the case of well-mixed regions. These types of measurements use a small package blackbody emitter installed in the inner body of the RDC that operates at a blackbody temperature of approximately $1100\,\mathrm{K}$. The FoV of the UCI absorption measurements in the RDC is limited by the clear aperture of the inner body window which is $9\,\mathrm{mm}$.

The UCI response model was employed with the HITRAN absorption model to predict absorption signals for methane and ethylene fueled operation of the RDC. These were used in two forms, the direct results that produced discrepancies in the absorption cell

measurements, shown by the dashed lines in Figures 6.6 and 6.7, and a version that was scaled by a factor that would create agreement with the experimentally observed absorption magnitudes for the $1.4\,\mathrm{kPa}$ cases in the absorption cell measurements. It is not assumed that the scaled versions of the simulations would more accurately represent signals measured in the RDC but they are presented for the sake of context and comparison. Predictions of the ethane absorption signal were made using the empirical model shown in Figure 6.9.

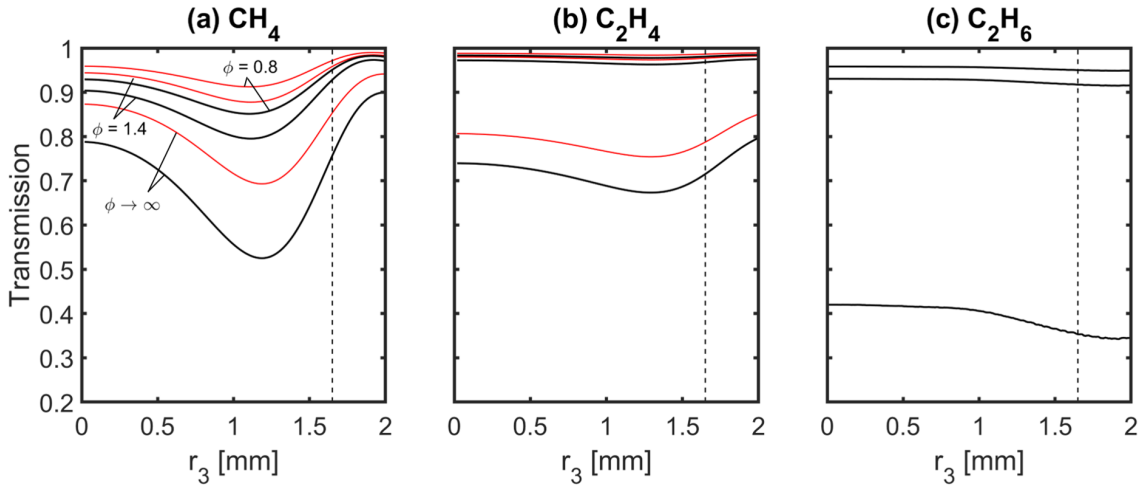

Figure 6.10: Predicted transmission signals in image plane coordinates through the RDC combustion channel for mixtures of hydrocarbon fuels at various equivalence ratios: $\phi = 0.8$, $\phi = 1.4$, $\phi \to \infty$ (pure fuel). (a) UCI response to methane absorption detected with a crystal temperature of $29\,^{\circ}\mathrm{C}$ computed using the HITRAN absorption model (black lines) and a response scaled to the roughly match absorption cell observations (red lines). (b) UCI response to ethylene absorption detected with a crystal temperature of $28\,^{\circ}\mathrm{C}$ computed using the HITRAN absorption model (black lines) and a response scaled to the roughly match absorption cell observations (red lines). (c) UCI response to ethane imaging computed using the empirically determined response model for a crystal temperature of $55\,^{\circ}\mathrm{C}$ shown in Figure 6.9. Vertical dashed lines show the clear aperture of the inner wall window ($r_1 = 4.5\,\mathrm{mm}$) transformed into image plane coordinates.

The results of the RDC absorption simulations are shown in Figure 6.10 for all three hydrocarbon fuel examined in this chapter. For methane and ethylene predictions shown in plots (a) and (b), the black lines show the direct results of simulations using the UCI response model for each of the three fueling conditions (from top to bottom: $\phi = 0.8$, $\phi = 1.4$, $\phi \to \infty$ (pure fuel)). The red lines in those plots show the model predictions for those same fueling conditions with the attenuation scaled down to match the attenuation magnitude observed in the absorption cell measurements. It is not assumed that these values accurately predict the absorption response in the RDC, but are presented to provide some representation of the smaller absorption response of UCI system that was apparent

in the absorption cell measurements. Plot (c) shows the predicted UCI response to the same three fueling conditions with ethane as predicted by the empirical response model. The vertical dashed lines in each of the plots indicate the clear aperture of the inner wall window ($r_1 = 4.5\,\mathrm{mm}$) transformed into image plane coordinates.

A primary goal for these measurements in the RDC would be to detect fuel-rich poorly-mixed regions that indicate either insufficient mixing efficacy of the injection system design or buffer regions due to differing responses of the two injection components. These types of measurements prioritize the response of the system at high fuel concentrations. In this respect, all three hydrocarbon fuel species could be viable targets for detection at 100% fuel concentrations as they all produce attenuation levels of greater than 12% across the FoV even when accounting for the reduced absorption responses for methane and ethylene that were observed in the absorption cell measurements. However, pure fuel conditions represent an example of extreme conditions that might be found in the RDC. Actual realizations of fuel-rich zones and buffer regions may exist at an intermediate concentration of fuel that is high but not necessarily entirely fuel. Additionally, it would be desirable to be able to resolve some of these differences in fuel concentration, *e.g.* distinguishing 50% fuel concentrations from 100% fuel concentrations.

With these considerations in mind, ethane appears to be the best candidate absorption target of the three fuel species considered here. Ethane's minimum predicted attenuation level within the relevant FoV is 58% which significantly exceeds even the maximum un-adjusted attenuation levels of both methane (48%) and ethylene (33%). Additionally, the broader absorption signature of ethane produces a more uniform attenuation response over the FoV that would be easier to interpret than those of methane and ethylene where accurate corrections for spatial-spectral coupling effects would be needed. The greater high-concentration attenuation and uniformity of response to changing concentrations shown in Figure 6.8(b) would also make ethane detection more capable of resolving different intermediate fuel concentrations. For these reasons, **ethane is the recommended hydrocarbon fuel species for mid-IR absorption imaging measurements in the RDC.**

An alternative goal for the absorption diagnostics might be to distinguish well-mixed reactant regions from poorly-mixed fuel-lean zones or buffer regions that are almost entirely devoid of fuel. This type of measurement would prioritize the response of the system to lower fuel concentrations corresponding to the predictions for equivalence ratios between 0.8 to 1.4 as a representative range. These results show that ethylene would be a poor target for the detection of well-mixed reactant zones because of its low attenuation at these lower concentrations. Even the un-adjusted predictions of ethylene response show less than 5% attenuation at both lean and rich mixture levels, which would be difficult to

distinguish from fuel-free zones in measurements without relatively high SNRs. Ethane performs slightly better than ethylene and produces attenuation levels of 4.5% for $\phi = 0.8$ and 7% for $\phi = 1.4$. These are improvements but it may be difficult to detect these signals in small regions of the FoV. As expected because of the nature of its absorption spectrum, as well as the increased mole fractions of methane at each equivalence ratio compared to the alternatives, methane performs the best in terms of attenuation for well-mixed conditions. This includes outperforming ethane across most of the FoV for equivalence ratios both with and without adjustments to the absorption magnitude. Peak attenuation values for methane occur near $r_3 = 1.1\,\mathrm{mm}$ and are 20.5% (12.5% adjusted) for $\phi = 1.4$ and are 15% (9% adjusted) for $\phi = 0.8$. These attenuation levels indicate that detection of well-mixed regions with methane fueling with realistic equivalence ratios and detection SNRs may be possible. Still, this would be a secondary goal of absorption imaging measurements in the RDC compared to detecting fuel-rich regions. For this reason, ethane remains a preferred absorption target candidate for situations except for those specifically aiming to distinguish well-mixed regions from fuel-devoid ones.

CHAPTER VII

Evaluation of Pulsed Mid-IR UCI for Unsteady Combustion Studies

This chapter presents a critical discussion of the key attributes of UCI that include both benefits and limitations of this approach to mid-IR imaging depending on the specific application. After that discussion, a list provides a general classification of several potential diagnostic applications as highly appropriate, somewhat appropriate, and not appropriate for the use of UCI based on its attributes and the observations of this work.

Spectral selectivity and tunability of UCI

One of the greatest strengths of UCI for combustion applications is its spectral selectivity due to the SFG phase-matching condition the underlies the upconversion process. Typical nonlinear crystal lengths between $5\,\mathrm{mm}$ to $100\,\mathrm{mm}$ can result in spectral detection bandwidths for mid-IR wavelengths on the order of $1\,\mathrm{nm}$ to $100\,\mathrm{nm}$. For detection of monochromatic or narrowband signals, the spectral selectivity of UCI systems is a major advantage. Unlike typical optical band-pass filters that exhibit maximum transmission in their pass-band of between 50% to 90%, with the low-end usually seen for very narrow pass-bands and high-extinction ratios, UCI can theoretically achieve 100% efficiency for its phase-matched wavelength. Similarly, they can be designed to reject nearby wavelengths with a high-extinction ratio, theoretically 0% response for particular wavelengths at the trough of the sinc^2 spectral response shown in Eq. (2.17). These theoretical efficiencies and extinction ratios are not achieved in practice due to unavoidable non-idealities, but they can be approached in well-designed and implemented systems. The narrow separations that can be achieved between the effective stop-bands and pass-bands in UCI spectral response can be leveraged in creative ways in combustion diagnostics, such as collecting Stokes-shifted LIF signals while suppressing elastic scattering of the excitation laser wavelength. These types of spectral filtering schemes can be implemented with flexibility and real-time tuning

because of the tunability of the UCI response achieved through temperature control of the nonlinear crystal.

While the narrow spectral responses that can be achieved with UCI can be advantageous for detecting narrowband signals, such as those often generated by laser-excited processes, they can also be a detriment for detection of broadband processes, such as thermal radiation. As an example, the mid-IR imaging in RDCs performed by Rankin *et al.* [59] targeted emissions from H_2O using a relatively broad ($66\,\mathrm{nm}$ wide) band-pass filter and direct detection. That same H_2O emission band could not be detected with sufficient signal strengths for single-shot UCI imaging partially because of the limited spectral bandwidth of the UCI system ($7\,\mathrm{nm}$) at these mid-IR wavelengths. This limitation could be addressed by decreasing the length of the nonlinear crystal, but that would increase the pump laser source power required to achieve the desired upconversion efficiencies. Ultimately, the implications of UCI spectral response are highly application dependent.

Spatial-spectral coupling in UCI

The spectral response characteristic of UCI discussed above must be considered in the context of the spatial-spectral coupling effect that results from noncollinear phase-matching in the 4f UCI configuration. The combination of spatial-spectral coupling and a narrowband spectral response results in only a limited region of the FoV that would respond to a monochromatic signal. This issue has been addressed in prior work by proposals including progressive sweeps of crystal temperature [33] and crystal angle using critical phase-matching [73] while imaging a static illumination field. While these approaches could be effective for imaging static scenes or performing phase-averaged imaging, they cannot be used for temporally resolved imaging of processes in highly transient unsteady combustion environments. For this reason, it is recommended that pulsed mid-IR UCI measurements be designed with either sufficient bandwidth of the target signal or the UCI spectral response to achieve a sufficient FoV.

In any case, spatial-spectral coupling is important in applications of UCI and must be considered both when designing measurements and when interpreting their results. In many cases, such as the detection of monochromatic signals discussed above, these effects are unwanted and are at best tolerated when using UCI. In the case of non-broadband sources, spatial-spectral coupling adds complexity to the analysis and interpretation of results. However, this effect can be leveraged to perform spectroscopic measurements at mid-IR wavelengths. By using optics to form mid-IR light carrying a spectral signal of interest into a uniform field, it can then be "imaged" by the 4f UCI system to detect features in the spectrum that are mapped from wavelength to position on the sensor. This effect was used

in Chapter IV to measure an approximate representation of the emission spectrum of hot H_2O and in Chapter VI to perform similar measurements of the absorption spectra of hydrocarbon species. However, the design of this system was not optimized for spectroscopy and so it produced very low spectral resolution in these types of measurements. Wolf *et al.* [106] designed a UCI-based spectroscopy system that achieved a spectral resolution of $2.3\,\mathrm{nm}$ near $4.3\,\mu\mathrm{m}$ and Tidemand-Lichtenberg *et al.* [107] demonstrated a similar system that achieved spectral resolutions of $3.2\,\mathrm{nm}$ to $170\,\mathrm{nm}$ over the wavelength range of $5\,\mu\mathrm{m}$ to $10\,\mu\mathrm{m}$. This is also the working principle that upconversion-based commercially available spectrometers offered by NLIR [43] rely on. This shows that spatial-spectral coupling may be considered a beneficial effect if the goal of a measurement is related to spectroscopy or hyperspectral imaging.

Polarization sensitive detection

Because the phase-matching condition is polarization-dependent, only one polarization component of the incident mid-IR light is efficiently upconverted in the UCI system. In this way, UCI exhibits polarized detection that can be beneficial or detrimental depending on the measurements being performed. In the case of laser-based techniques that produce coherent, polarized signals, the polarized nature of UCI (and more broadly UCD) is very useful. Direct detection alternatives must use either plate polarizers or polarizing beamsplitters to isolate these signals which typically have efficiencies of 90% or less and have finite extinction ratios that depend on their design. UCD can theoretically achieve 100% conversion efficiency (this is never achieved due to inefficiencies and only occurs at one instant in pulsed pump operation) and very high effective extinction ratios if properly designed to minimize any phase-matching of the cross-polarized mid-IR light component. This property has been leveraged in prior work to perform pointwise IR DFWM [12, 40], pointwise IR polarization spectroscopy [13], and IR DFWM imaging [38, 39].

For measurements of incoherent, unpolarized mid-IR light this polarization selectivity acts as a penalty that limits the maximum achievable QE to 50%. In theory, this could be avoided in such instances by splitting the mid-IR by polarization components and sending them to two parallel UCI systems with orthogonal phase-matched polarizations. This would be impractical as it would more than double the setup complexity and requirements for the pump laser, as well as compromising SNR benefits because of the independent readout noises experienced by the two halves of the detected signal. UCI will likely not be appropriate for these cases where above 50% QE is required, but as demonstrated by the incoherent mid-IR measurements in this work, this limitation does not preclude the use of UCI for applications where the lower efficiency is acceptable and offset by the benefits of

the approach.

Temporal resolution and controllable time-gating of UCI measurements

A primary advantage of pulsed UCI in unsteady combustion applications is the time-gating and associated temporal resolution that these measurements exhibit because of the relationship between pump beam intensity and upconversion efficiency. Direct detection cameras can achieve some level of time-gating, however current top-of-the-line commercial systems can only achieve a minimum exposure time of approximately $270\,\mathrm{ns}$. This may be sufficient for some applications, such as the passive thermal imaging presented in this work but might be insufficient for optimal performance in other applications. Pulsed UCI systems exhibit minimum exposure times determined by the width of the pump pulse regardless of the detection properties of the camera. Time gating as short as $100\,\mathrm{fs}$ has been demonstrated with mode-locked Ti:sapphire laser pump sources [15]. The measurements were this precise time-gating is required are typically laser-excited processes. In many of these diagnostics, the same laser pulses that are used as part of the excitation source for the diagnostic signal can be used to also pump the UCI system. For example, in a mid-IR PLIF process that is excited by an Nd:YAG-pumped tunable dye laser, the residual $1064\,\mathrm{nm}$ radiation from the Nd:YAG pulse can be used to pump the UCI system in a way that is appropriately time-gated and synchronized.

The preceding paragraph discussed time-gating from the perspective of rejecting background signals, but as has demonstrated by the passive thermal imaging measurements in Chapter V, it can also play the role of determining time-resolution in the case of passive measurement techniques. Here, the precise control of the temporal response of the UCI system can be useful but also places substantial requirements on the pump beam laser source. In this work, the pump laser was designed to output $10\,\mathrm{ns}$ pulse widths and only by operating as far as possible from the design condition of the laser could pulse widths appropriate for passive thermal imaging be achieved. If a laser with sufficient flexibility and control is not available, this could prevent the application of pulse UCI in some circumstances. This makes pulse-shaping laser systems, such as the Amplitude Agilite laser [83], ideal for passive imaging applications of UCI. Those systems can produce sharp temporal pulse profiles with tunable pulse widths that can be used to tailor the temporal response of the measurements. Alternatives to pulse-shaping of the laser output to control the temporal profile of the pump beam include external pulse-stretching techniques. Ring-cavity pulse-stretchers, like the one implemented by Kojima and Nguyen [108], were investigated for the measurements in this work. That approach was found to be expensive, difficult to align and maintain, and inefficient for the spatial intensities required by UCI, and so it concluded

to not be practical for pump pulse-shaping.

While the temporal resolution offered by pulsed UCI is important for many unsteady combustion applications, there are many other instances in combustion science where UCI can be applied that do not require precise time-gating. In those cases, cw pump sources can be employed to allow for longer integration times leading to higher signal levels. In these cases, the temporal response of the system is again determined by the temporal characteristics of the detector, like in direct detection. Because upconversion efficiencies depend on pump beam intensities, high pump powers are often needed for cw operation, typically on the order of $100\,\mathrm{W}$. This is difficult to achieve with external pump sources, and so cw UCI systems often use intra-cavity pumping schemes where the nonlinear crystal is incorporated into the resonant cavity of the pump source [32]. Developing these types of systems requires additional design work related to the pump source, but might be the best option for some combustion applications and be more easily packaged into self-contained systems (see Dam *et al.* [42]).

Sensitivity to manufacturing tolerances and environmental conditions

The characterization measurements in Chapter IV and the spectral absorption measurements in Chapter VI demonstrate that mid-IR UCI systems are highly sensitive to small relative changes in both the design parameters of the system, particularly the poling period used in QPM-based measurements, and the environmental conditions of the measurement system, primarily the temperature of the nonlinear crystal. Changes to the average poling period on the order of nanometers and/or changes to the crystal temperature on the order of $1\,^{\circ}\mathrm{C}$ were shown to have measurable effects on the spectral response of the system and spatial-spectral coupling phenomenon. For the passive thermal UCI measurements described in Chapter V this had a minimal effect on the measurements because of the image correction scheme that was employed. However, for hydrocarbon absorption imaging measurements with certain species failure to predict and control these effects could compromise the measurement.

These concerns should be considered when designing a UCI measurement, particularly for field measurement systems [35] or measurements in hostile environments where the ambient temperature can change in dramatic and uncontrollable ways, such as a coal gasification plant [109]. In some cases, it may be sufficient to monitor the temperature of the crystal to account for these effects when interpreting the captured measurements. In other cases, it may compromise operability if the ambient conditions cannot be overcome by an adequate temperature control system.

Limited aperture due to crystal size and pump beam energy constraints

As is discussed in Chapter II, the spatial cross-section of the SFG process limits the aperture size of the UCI system in the Fourier plane. This limitation can be due either to the size of the nonlinear crystal (periodically poled crystals are typically limited to between $0.5\,\mathrm{mm}$ to $2\,\mathrm{mm}$ in thickness) or the beam diameter that can be sufficiently energized by the pump source. The effects of this limited Fourier plane aperture were mostly discussed in the context of spatial resolution that can be achieved by the system. This is certainly a major concern and should be considered when designing a UCI system, ensuring that the crystal size and pump beam cross-section can accommodate the required spatial resolution. However, this effect also limits the signal strength that can be achieved by a system. In photography, in addition to the effects on image sharpness, the aperture of a camera lens is typically enlarged in low-light situations to allow greater throughput of light and increase the measured brightness. The rigid limit on aperture size prevents this from being done in UCI. In the current system, only a small fraction of the mid-IR light collected by the objective lens is upconverted because most of it falls on regions of the Fourier plane that are outside of the crystal aperture. If the thickness of the crystal could be increased by a factor of two and the power of the pump beam could be increased by a factor of four, then the passive thermal imaging measurements in the RDC could achieve approximately four times the current signal strength. This should be considered when designing a UCI system for the detection of weak, incoherent mid-IR signals. Despite the improved low-light performance of UCI compared to direct detection due to a lower noise floor, optical collection efficiency can limit the achievable UCI signal strength in these cases.

For imaging coherent signals, this is less of a concern because of the nature of coherent imaging in a 4f configuration. For coherent imaging, the light intensity in the image plane will be concentrated near the central axis of the optical system with any significant transverse distribution away from the central axis due to multiple diffraction orders related to the spatial frequencies associated with the object-plane illumination field. This is discussed in more detail by Morishita *et al.* [38, 39] concerning the coherent imaging of IR DFWM signals.

7.1 Suitability of UCI for particular diagnostic applications

Based on the results of this work and other prior work, this section provides a list of potential applications of UCI for combustion studies classified by how readily applicable

UCI might be. These classifications represent judgments based on the consideration of important attributes discussed above in the context of each application. The class of *highly suitable* diagnostics are those that leverage the unique properties of UCI to produce measurements that are far superior to direct detection alternatives or would not be possible without UCI. The class of *somewhat suitable* applications are those that leverage certain aspects of UCI to perform better than direct detection alternative in some circumstances, but UCI may not always be the superior choice. The class of *not suitable* diagnostics will be techniques where UCI either cannot be used or will rarely outperform direct detection alternatives.

Mid-IR UCI is **highly suitable** for the following types of optical diagnostics:

- Detection of mid-IR DFWM and polarization spectroscopy signals in both imaging and pointwise modes
- Detection of mid-IR LIF signals
- Ultrafast (sub-nanosecond scale) IR imaging

Mid-IR UCI is **somewhat suitable** for the following types of optical diagnostics:

- Species-specific passive thermal imaging and absorption imaging
- Time-resolved mid-IR spectroscopy

Mid-IR UCI is **not suitable** for the following types of optical diagnostics:

- Wide FoV imaging of narrowband signals
- Applications to unpolarized light detection requiring an effective QE in excess of 50%

CHAPTER VIII

Conclusions and Future Work

8.1 Summary of work, objectives, and contributions

This work is a design and experimental study of the application of pulsed mid-IR UCI to study unsteady combustion processes within an RDC. This work was carried out to meet the objectives described in section 1.2. The first objective, to develop, implement, and characterize a pulsed mid-IR UCI system suitable for unsteady combustion experiments, is addressed by Chapters II, III, and IV. The theory governing the underlying nonlinear optical processes of UCI was used to construct models for the performance of a UCI system design. These models were used to generate a system design that targeted spectral absorption/emission bands of H_2O, CO, CO_2, and hydrocarbon fuel species. Chapter II presents these modeling techniques and the resulting system design that was implemented in this work.

Chapter III describes the practical details of the implementation of the UCI system design. This includes descriptions of the key components in the UCI system, including the silicon CCD camera, pump beam laser source, and the optical arrangement, and how they impact system performance. The Q-switch tuning of the pump laser described in section 3.3.2 was particularly important to the implementation of pulsed UCI for passive thermal imaging in unsteady combustion environments. The $240\,\mathrm{ns}$ effective exposure time achieved a compromise between the competing demands of signal strength and temporal resolution in the RDC. The sub-microsecond temporal resolution was necessary to resolve small scale structures that were advecting at supersonic speeds near the detonation wave front. This shows the importance of the tunable temporal response of pulsed UCI systems in unsteady combustion. This is especially beneficial in that it separates the temporal resolution of the measurements from the performance of the detector. In this case, the effective integration time including possible exposure during read-out of the CCD camera was approximately $70\,\mathrm{ms}$, which would be unusable for measurements in the RDC without the

time-gating effects of pulsed UCI.

The results of a suite of measurements that were used to characterize the response of the pulsed mid-IR UCI system are presented in Chapter IV. These measurements characterized the system response along spatial, temporal, and spectral dimensions, as well as examining the effects of the spatial-spectral coupling phenomenon that is important to interpreting UCI measurements. These measurements verified models of UCI system performance and demonstrated the high sensitivity of the UCI measurements to the parameters of the nonlinear crystal. Discrepancies in the average manufactured poling periods in the nonlinear crystal on the order of $10\,\mathrm{nm}$ and/or changes in crystal temperature on the order of $1\,^{\circ}\mathrm{C}$ were detected through measurements of the systems spectral response and manifestations of the spatial-spectral coupling effect. While this did not compromise the operability of the UCI system, it becomes important when predicting the precise response of the system to illumination sources that exhibit feature-rich spectra.

The second objective of this work, to design and implement diagnostics that use pulse mid-IR UCI to study unsteady combustion in an RDC, is treated by the measurement results presented in Chapters V and VI. The pulsed UCI system developed in this work was used for passive mid-IR imaging of thermal radiative emissions from CO_2-doped hydrogen-air operation of an RDC and the results are presented in Chapter V. Those passive thermal imaging measurements represent the first examples of fully spatiotemporally resolved (defined as sub-millimeter spatial resolution, sub-microsecond temporal resolution) mid-IR imaging in an operating RDC. Previous mid-IR imaging in RDCs by Rankin *et al.* provided insight into the large-scale structures of RDC flow fields, but exhibit compromised resolution of near-wave structures due to the $5\,\mu\mathrm{s}$ integration time that was used. The pulsed UCI measurements in this work leveraged a shorter effective exposure time ($240\,\mathrm{ns}$) to resolve sharp gradients at detonation wave fronts that were traveling at speeds above $1\,\mathrm{km/s}$, as well as millimeter-scale flow structures immediately behind the detonation wave front. These capabilities of the pulsed UCI system combined with the nature of thermal radiation from gases allowed these measurements to observe relative distributions of pressure within the hot combustion regions of the RDC flow field. Measurements in the RDC identified apparent rapid expansion processes in post-combustion regions behind the detonation wave front that occurred over spatial intervals of $1\,\mathrm{mm}$ or less. Observations of expansion gradients at an angle relative to the propagation direction of the detonation wave provide evidence for the effects of expansion fans anchored at the bottom of the detonation wave front, as have been predicted by models of RDC flows [62]. Pulsed UCI will be a useful tool for further experimental studies of these expansion processes.

Based on the results of the RDC experiments, as well as previous design analysis and

Table 8.1: Estimated and measured performance parameters for the pulse UCI system in this work.

Parameter	Minimum	Maximum
Mid-IR center wavelength	1.84 µm	4.38 µm
Mid-IR detection bandwidth	2.4 nm	353 nm
Spatial resolution (Δ_{PSF})	170 µm	400 µm
Temporal resolution	19 ns	240 ns
SNR in RDC measurements	7.4	18.5

characterization measurements, some parameters related to performance can be identified and summarized. Table 8.1 provides a summary of the key performance parameters of the system. Each of these parameters is given in terms of the minimum and maximum values that were achieved or estimated for the system. These values may correspond to different poling periods (mid-IR spectral bands) of the system. Some of the definitions of these values may involve subtleties or differ from conventional definitions, and so it is important to consider the context for each provided in the preceding chapters.

A hydrocarbon absorption imaging diagnostic using the pulsed UCI system was developed to detect the distributions of fuel-rich concentrations within the RDC flow field. Previous work on non-premixed RDCs hypothesized the existence of *buffer regions* that were almost entirely fuel or devoid of fuel depending on the dynamics of the injection scheme, as described in section 1.4.3. This diagnostic technique was designed to detect the presence and distribution of these buffer regions with the RDC by showing significantly different absorption responses to regions of entirely fuel or regions lacking fuel. Limitations on the ability of the RDC to operate with pure hydrocarbon fuels at the time of this work prevent the implementation of the diagnostic in the RDC, but benchtop absorption experiments were performed to test the response of the UCI to hydrocarbon absorption. The results of those proof-of-concept experiments are presented in Chapter VI. They showed that all three hydrocarbon fuel species that were examined could be used for absorption imaging measurements in the RDC to identify fuel-rich regions, but that ethane would provide the best performance for these types of measurements.

The third objective of this work, to evaluate pulse mid-IR UCI as a tool for combustion science, is addressed by the discussion Chapter VII. That discussion outlines how important characteristics of UCI may be beneficial or limiting for diagnostic applications depending on the specifics of the approach being considered.

8.2 Conclusions

1. The mid-IR UCI system designed in this work produced a narrowband spectral response that enabled species-specific imaging measurements.

   (a) The system exhibited spectral bandwidths between $2\,\mathrm{nm}$ to $300\,\mathrm{nm}$ for detection over the range of $1.9\,\mu\mathrm{m}$ to $5\,\mu\mathrm{m}$ ($7\,\mathrm{cm}^{-1}$ to $160\,\mathrm{cm}^{-1}$ over the range of $2400\,\mathrm{cm}^{-1}$ to $5400\,\mathrm{cm}^{-1}$ when expressed in terms of wavenumber).

   (b) When performing thermal emission imaging, the narrowband spectral bandwidth can limit what species can be targeted for single-shot measurements. In this work, it prevented H_2O emission imaging in the RDC and instead limited the target species to CO_2. A design analysis showed that the spectral bandwidth of the UCI system could be increased by decreasing the length of the nonlinear crystal, however this would place an additional burden on the pump laser system to produce sufficient pump pulse energy to achieve adequate signal strength. This would be beyond the capabilities of the laser used in this work but might be achievable with a more powerful laser.

2. The spectral response and the spatial-spectral coupling effects of a QPM-based system are sensitive to nano-scale scale deviations of a crystal's poling period.

   (a) Characterization measurements were used to infer deviations in the realized poling period of the crystal in the system of -$40\,\mathrm{nm}$ (relative to the design value of $\Lambda_P = 19.4\,\mu\mathrm{m}$) and +$15\,\mathrm{nm}$ (relative to the design value of $\Lambda_P = 23.4\,\mu\mathrm{m}$).

   (b) These deviations did not compromise the application of the UCI system for the measurements in this work, but they must be considered and measured when applying 4f UCI to precision spectral measurements.

3. The results in this work demonstrated high spatiotemporal resolution in mid-IR images captured in the highly transient environment of the RDC.

   (a) Temporal resolution of the pulsed UCI system was controlled by the pulse width of the pump laser. This produced an effective $240\,\mathrm{ns}$ exposure time, satisfying the sub-microsecond resolution requirements of the RDC.

   (b) The temporal resolution of the system allowed the realization of sub-millimeter spatial resolution near the supersonically propagating detonation wave front. The spatial resolution was primarily limited by the spatial point-spread induced by the limited aperture of the pump beam in the Fourier plane of the 4f arrangement. This was

estimated to be a Gaussian FWHM of $400\,\mu\mathrm{m}$ in object plane coordinates, satisfying the resolution requirements for these measurements.

(c) Pulsed UCI measurements of thermal emissions from CO_2 within the RDC produced peak SNR values between 7.4 to 18.5 that satisfied the Rose criterion of 5 [101] to enable single-shot measurements.

4. CO_2 doped H_2-air operation of the RDC produced thermal imaging measurements that were sensitive to local temperature and pressure and revealed small-scale structures and sharp gradients near detonation wave fronts.

(a) Simulations of both thermal emission from CO_2 and the UCI response to that radiation showed that signals from this diagnostic were relatively insensitive to temperature changes at post-combustion temperatures but roughly proportional to local pressure at all conditions. This allows the diagnostic to identify high-pressure regions near the detonation wave front. By combining these measurements with others that are sensitive to heat release rate, such as OH^* chemiluminescence, the amount of combustion that occurs in the high pressure regions can be determined, an important consideration in RDC combustion physics.

(b) Pulsed UCI frames captured near detonation wave fronts show as much as a factor of two change in mid-IR luminosity over intervals of one millimeter or less. These indicate sharp gradients in the flow properties near the detonation wave front that have not been resolved in previous mid-IR imaging measurements. The frames also show small high-luminosity spots of less than $2\,\mathrm{mm}$ in width that require high spatiotemporal resolution to observe.

(c) Examples of UCI frames captured from $20\,\mathrm{mm}$ to $50\,\mathrm{mm}$ behind the detonation wave front show sharp ($<1\,\mathrm{mm}$ in extent) reductions in mid-IR luminosity. These are indicative of rapid expansion processes behind the peak pressure location in detonation waves, demonstrating the capability of these measurements to characterize and observe such processes.

5. Benchtop hydrocarbon absorption measurements demonstrated the ability of back-illuminated UCI to identify fuel-rich regions within an environment like the RDC combustion channel.

(a) Results indicated that all three hydrocarbon fuel species that were considered (methane, ethylene, and ethane) could be detected within the channel in volumes of pure fuel.

(b) Ethane was identified as the best fuel species for identifying fuel-rich zones over a broad range of rich mixing ratios as it produced 58% absorption in pure fuel regions compared to maximum values of 48% for methane and 33% for ethylene.

8.3 Future work

Pulsed mid-IR UCI presents a wide range of opportunities for applications to study unsteady combustion. The pulsed UCI system developed in this work provides the capability to perform several types of mid-IR diagnostics in the RDC laboratory and other combustion experiments. This section provides a set of recommendations for ways that the current system can be improved and further applied, as well as types of diagnostics that were not examined in this work that could be performed with either this system or a new UCI system design.

8.3.1 Modifications to and applications of the UCI system

High-rate pump laser system and camera for improved data output from UCI measurements in the RDC

A major limitation of the pulsed mid-IR UCI measurements of thermal radiation in the RDC that are presented in Chapter V was the 10 Hz acquisition rate of the UCI system that is described section 3.4.4. The low acquisition rate combined with the short test durations achievable in the RDC made it impractical to study a wide range of conditions in a couple of ways. First, many time-consuming runs needed to be performed to build up a sufficient UCI data set to analyze and characterize a particular condition. Second, multiple runs under the same precise optical configuration of the system were needed to perform corrections to the raw UCI measurements so that they could be analyzed. Data from several experimental runs was not usable for the analyses presented in this work because the system configuration was changed before a sufficient number of exposures could be captured to properly apply the image correction techniques described in section 5.3.

Significantly increasing the acquisition rate of the UCI system would solve both problems. If an acquisition rate of just 1 kHz could be achieved, something well within the limits of modern camera and laser systems, then *more UCI observations could be taken during a single RDC test run than in the dozens of tests performed to generate the data set shown in Chapter V*. At that rate, only one or a few runs would be needed for each operating case to sufficiently sample the flow field with UCI, and the data from each run could be image corrected with just the exposures from that same run. This would allow for UCI

studies to be performed that sufficiently sample a wide operating range of the combustor within a day or two. The time saved with this new testing procedure could be used to vary the axial position of the outer wall sapphire window so that different axial locations within the RDC channel can be studied with UCI for the same operating conditions. In this way, a more complete view of the RDC flow field could be developed with the UCI measurements despite the limited axial FoV of any one exposure.

This acquisition rate enhancement will require both the repetition rate of the pulse pump laser system and the frame rate of the camera to be increased. Visible/near-IR camera systems that are commercially available commonly achieve frame rates above $10\,000$ fps, and several high-speed cameras are currently available in the RDC laboratory that are readily capable of kHz operation in the UCI system. There are not currently any pulsed laser systems available within the laboratory that would be suitable for temporally resolved UCI collection above $10\,\mathrm{Hz}$, however several potential systems are currently being considered that could fill this need.

The general requirements for a high-rate pump laser system for UCI are that it outputs pulses at a sufficiently high rate (target: $\geq 1\,\mathrm{kHz}$), it achieves sufficient energy per pulse (target: $\geq 5\,\mathrm{mJ}$ based on the results in Chapter V that were produced with approximately $6\,\mathrm{mJ}$ per pulse), and that it has an appropriate temporal pulse shape. The first two requirements are satisfied by a large variety of commercially available Diode-Pumped Solid-State (DPSS) Nd:YAG lasers, but the last requirement on the temporal pulse characteristics is harder to satisfy for most of those systems and is critically important to applications for passive thermal imaging. If the pulse duration is too short then insufficient signal strength is generated, but if it too long then temporal resolution is compromised. Based on modeling and the results of passive thermal UCI measurements performed in this work, a Gaussian temporal pulse profile with an FWHM between $100\,\mathrm{ns}$ to $500\,\mathrm{ns}$ is expected to produce adequate performance in passive thermal UCI measurements in the RDC. One possible solution is the Amplitude Mesa HP DPSS Nd:YAG laser system [83]. The specifications for this system show that it would produce $7.5\,\mathrm{mJ}$ of light with the proper polarization at a $10\,\mathrm{kHz}$ repetition rate with a Gaussian pulse width of approximately $120\,\mathrm{ns}$. This provides the desired repetition rate and pulse energy, but the pulse width is on the low end of the acceptable range and will result in reduced signal strengths.

Another option is the Amplitude Terra laser system. This is a DPSS laser system based on Nd:YLF as a gain medium, which produces an output wavelength of $1053\,\mathrm{nm}$ instead of the $1064\,\mathrm{nm}$ pump wavelength used in this work. Typically a change in pump wavelength would require a redesign of the crystal used in the UCI system, however for the crystal described in section 2.5 this new pump wavelength can be used to target the strong CO_2

emission bands near $4.2\,\mu\mathrm{m}$ with the $22.45\,\mu\mathrm{m}$ poling period by heating the crystal to near $200\,^{\circ}\mathrm{C}$. In this way, the Terra system would be compatible with passive thermal UCI measurements in the RDC using the same system configuration. The Terra laser configured for IR output is expected to generate $310\,\mathrm{ns}$ pulse widths with $6.4\,\mathrm{mJ}$ per pulse at $5\,\mathrm{kHz}$. This would provide near optimum pulsed UCI performance and a factor of 500 increase in data output compared to the current UCI system.

Implementation of the hydrocarbon absorption imaging diagnostic in the RDC

Implementation of the mid-IR absorption imaging diagnostic in the RDC was prevented by the inability when this work was performed to achieve stable operation of the combustor with the high concentrations of hydrocarbon species within the injected fuel that would be required to perform these types of measurements. Modifications to the RDC facility are underway at the time of writing this that will enable operation with fully hydrocarbon fueling of the combustor over a range of conditions. Once these modifications are complete, the pulsed mid-IR UCI system can be used to identify fuel-rich regions within the combustion channel during operation with ethane as the sole fuel component. These measurements would be performed with the same integration onto the RDC facility as described in Chapter III except that they would use the $22.45\,\mu\mathrm{m}$ poling period instead of the $23.415\,\mu\mathrm{m}$ poling period to access hydrocarbon absorption bands and the inner and outer wall windows would be co-aligned to provide mid-IR back-illumination from inside of the combustor's center-body.

These absorption measurements would best be performed as part of a campaign complemented by using the previously mentioned high-acquisition rate version of the pulsed UCI system to perform passive thermal imaging of the flow field. The use of hydrocarbon fuels would generate nascent CO_2 within the hot product regions and so CO_2 doping would not be necessary for these thermal imaging measurements. Complete studies of various operating cases using passive thermal CO_2 UCI measurements at different axial positions could be used to map flow fields for those regions to identify potential buffer regions defined in section 1.4.3. It has been hypothesized that these buffer regions consist almost entirely of unmixed fuel or air. The hydrocarbon absorption imaging technique could be used to study cases where these possible buffer regions exist to determine if they have this type of unmixed composition. This would provide a direct test of an RDC combustion physics hypothesis using pulsed mid-IR UCI.

8.3.2 Potential applications of UCI in unsteady combustion

Mid-IR PLIF

As Chacon and Gamba demonstrated through OH detection with UV PLIF [2], PLIF with mid-IR detection can be employed to image the distributions of other species within the RT-RDC. The quartz windows currently installed in the RT-RDC prohibit imaging measurements at wavelengths above $4\,\mu\mathrm{m}$. They will also exhibit poor transmission for H_2O transitions near $2.7\,\mu\mathrm{m}$. However, the current quartz windows are highly transparent in the range of CO transitions near $2.3\,\mu\mathrm{m}$ and hydrocarbon C-H stretch vibrational bands near $3.4\,\mu\mathrm{m}$, and future changes to the window material will make the wavelength ranges accessible.

Kirby and Hanson [110] have demonstrated schemes for single-photon IR PLIF of CO and CO_2. These single-photon excitation techniques can be desirable because of the increased linearity of the diagnostic response to absorber concentration and laser fluence compared to more common multi-photon IR PLIF techniques [111]. UCI is readily applicable for these applications because of its low-light sensitivity and improved noise characteristics compared to direct detection. Additionally, the narrowband spectral response can be leveraged to reject much of the scattered laser light and still detect slightly Stokes-shifted fluorescence signals. This technique could be used to detect the distributions of several reactant (hydrocarbons), intermediate (CO and NOx), and product (H_2O and CO_2) species within the RT-RDC flow field.

Mid-IR DFWM imaging

While PLIF measurements must be performed in the RT-RDC design variant, it is possible to perform similar species-specific imaging measurements in the conventional RDC design using planar DFWM imaging. Planar DFWM imaging is similar to the pointwise DFWM measurements used by Høgstedt *et al.* [12] and Hot *et al.* [40], except that two of the required three laser beams are formed into sheets to allow for planar interrogation, as was demonstrated by the measurements of Morishita *et al.* [38, 39]. A major challenge of this approach will be the need to maintain precise alignment of all three laser beams in the presence vibrations caused by oscillating reaction forces in the combustor as the detonation wave propagates. This can potentially be addressed using optical phase-conjugate mirrors to ensure proper pump beam overlap, as was demonstrated by Winter *et al.* [112] for UV DFWM imaging of OH. It should be noted that both PLIF and DFWM imaging applications of UCI detection require adequate mid-IR laser excitation sources.

Mid-IR spectroscopy

This work, and many other recent UCI examples such as the system reported by Pedersen *et al.* [32], utilized a 4f optical imaging arrangement with the nonlinear medium placed at its Fourier plane. Chapter II shows how this leads to noncollinear phase-matching within the nonlinear medium that generates the spatial-spectral coupling effect. In this way, a UCI system can be designed to operate as a spectrometer by mapping different locations within an image to different bands of mid-IR wavelengths. This has been leveraged in several of the prior UCI examples [42, 33, 41] to perform IR spectroscopy measurements and is the operating principle underlying the upconversion-based spectrometers sold by NLIR [43]. This effect was used in measurements described in Chapters IV and VI to perform benchtop characterization measurements of UCI response to spectral emission and absorption signals, respectively. However, this system was not designed specifically for spectroscopy measurements, and so it exhibits poor spectral resolution when operated in this mode. Chapter II describes how a system could be designed for spectroscopy of either IR emission or absorption in RDCs (a key change is making the crystal length longer than the one used in this work to improve spectral resolution). Whether applied to absorption or emission spectroscopy, UCD-based approaches would be effective for mid-IR bands, especially for time-resolved measurements.

APPENDIX A

Sellmeier Coefficients and Models for Common Nonlinear Materials

For LN, the index of refraction can be conveniently computed as a function of both wavelength and temperature immediately from the temperature dependent Sellmeier equation. Gayer *et al.* [7] give the form of that equation:

$$n^2_{\text{LN}}(\lambda, T) = a_1 + b_1\, f(T) + \frac{a_2 + b_2\, f(T)}{\lambda^2 - (a_3 + b_3\, f(T))^2} + \frac{a_4 + b_4\, f(T)}{\lambda^2 - a_5^2} - a_6\lambda^2 \qquad \text{(A.1)}$$

where:

$$f(T) = (T - 24.5^{\text{o}}\text{C})(T + 570.82^{\text{o}}\text{C}) \qquad \text{(A.2)}$$

The parameters for this Sellmeier equation are provided [7] for both 5% and 1% MgO-doped LN crystals and are shown in table A.1 (5% MgO-doped LN is usually preferred for its superior photorefractive damage resistance).

Data related to the index of refraction of KTP and KTA are not in the same format. First, an index of refraction at 25°C for a given λ must be computed as $n_0(\lambda) = n(\lambda, 25^{\text{o}}\text{C})$ before the adjustment for temperature variation is made. Fradkin *et al.* [113, 114] give Sellmeier equations and parameters for $n_0(\lambda)$ for both KTP and KTA in slightly different forms such that Eq. (A.3) must be used for KTP while Eq. (A.4) should be used for KTA:

$$n^2_{0,\text{KTP}}(\lambda) = A + \frac{B}{1 - \frac{C}{\lambda^2}} + \frac{D}{1 - \frac{E}{\lambda^2}} - F\,\lambda^2 \qquad \text{(A.3)}$$

$$n^2_{0,\text{KTA}}(\lambda) = A + \frac{B}{1 - \left(\frac{C}{\lambda}\right)^2} + \frac{D}{1 - \left(\frac{E}{\lambda}\right)^2} - F\,\lambda^2 \qquad \text{(A.4)}$$

where the values for the parameters are given in table A.2.

Once the values for the constant temperature index of refraction are determined for a given set of wavelengths, the temperature dependent index of refraction offset $\Delta n(\lambda, T)$

Table A.1: Temperature dependent Sellmeier equation parameters for MgO-doped LN [7]

Parameter	5% MgO-doped Congruent LN	5% MgO-doped Stoichiometric LN
a_1	5.756	5.078
a_2	0.0983	0.0964
a_3	0.2020	0.2065
a_4	189.32	61.16
a_5	12.52	10.55
a_6	1.32×10^{-2}	1.59×10^{-2}
b_1	2.860×10^{-6}	4.677×10^{-7}
b_2	4.700×10^{-8}	7.822×10^{-8}
b_3	6.113×10^{-8}	-2.653×10^{-8}
b_4	1.516×10^{-4}	1.096×10^{-4}

must be computed and added to $n_0(\lambda)$. The form of the expression for $\Delta n(\lambda, T)$ is given by Emanueli [8], which is the same for both KTP and KTA:

$$\Delta n(\lambda, T) = n_1(\lambda)\,(T - 25^{\circ}\mathrm{C}) + n_2(\lambda)\,(T - 25^{\circ}\mathrm{C})^2 \tag{A.5}$$

where the linear and quadratic coefficients are found from:

$$n_{1,2}(\lambda) = \sum_{m=0}^{3} \frac{a_m}{\lambda^m} \tag{A.6}$$

The a_m coefficients for each instance of this equations are given in a table in Emanueli [8] which is recreated in table A.3.

Finally, the index of refraction for either KTP and KTA at a given wavelength and temperature can be found by adding the $\Delta n(\lambda, T)$ value to the value of $n_0(\lambda)$:

$$n_{\mathrm{KTx}}(\lambda, T) = n_{0,\mathrm{KTx}}(\lambda) + \Delta n_{\mathrm{KTx}}(\lambda, T) \tag{A.7}$$

Table A.2: Sellmeier equation parameters for KTP and KTA crystals

Parameter	KTP [113]	KTA [114]
A	2.12725	1.214331
B	1.18431	2.225328
C	5.14852×10^{-2}	0.178542
D	0.6603	0.310017
E	100.00507	8.989998
F	9.68956×10^{-3}	0.009381

Table A.3: Coefficients for KTP and KTA $\Delta n(\lambda, T)$ equation [8].

	KTP		KTA	
Parameters	$n_1 \times 10^6$	$n_2 \times 10^8$	$n_1 \times 10^6$	$n_2 \times 10^8$
a_1	9.9587	-1.1882	-6.1537	-0.96751
a_2	9.9228	10.459	64.505	13.192
a_3	-8.9603	-9.8136	-56.447	-11.78
a_4	4.1010	3.1481	17.169	3.6292

APPENDIX B

Large RDC Composite Images

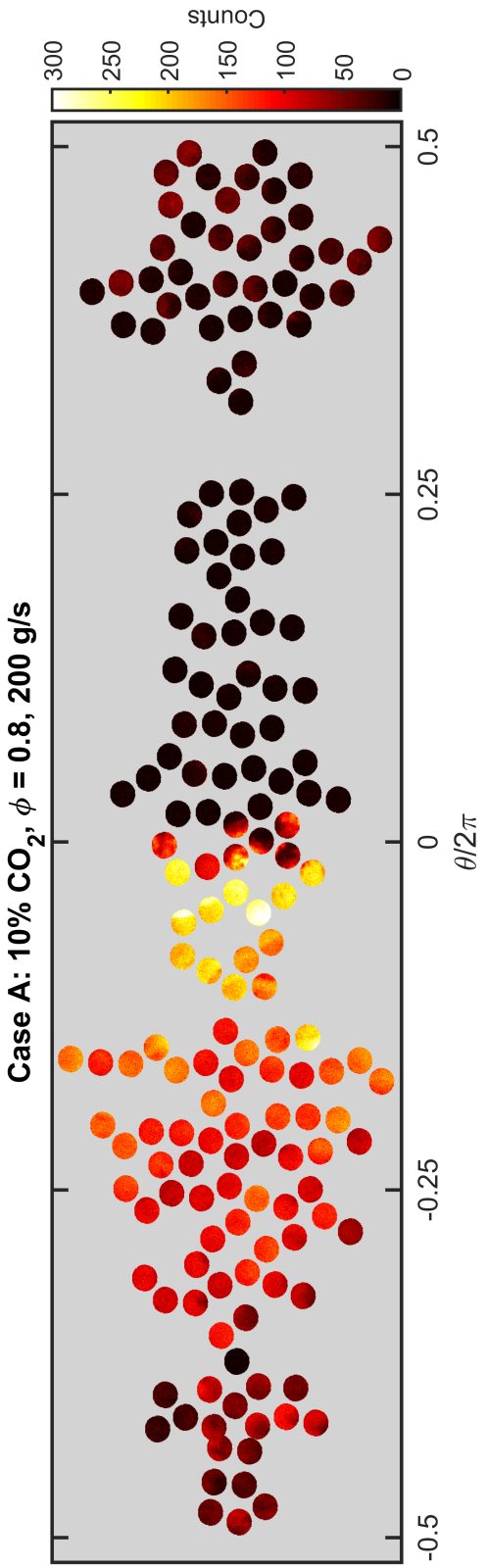
Case A: 10% CO_2, ϕ = 0.8, 200 g/s
Counts
300
250
200
150
100
50
0
0.5
0.25
0
-0.25
-0.5
$\theta/2\pi$

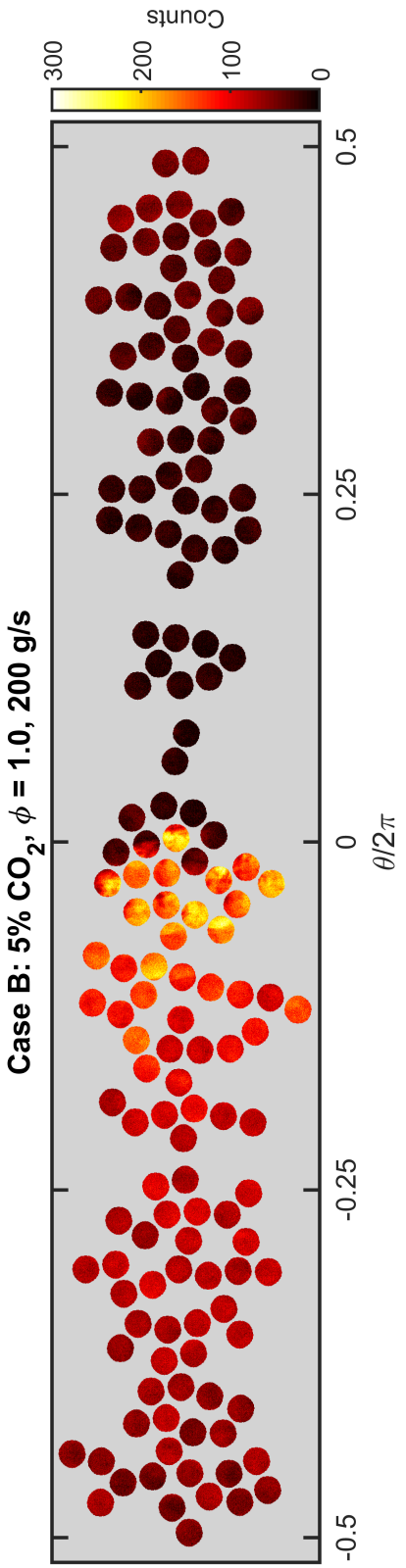
Case B: 5% CO_2, ϕ = 1.0, 200 g/s
Counts
300
200
100
0
0.5
0.25
0
-0.25
-0.5
$\theta/2\pi$

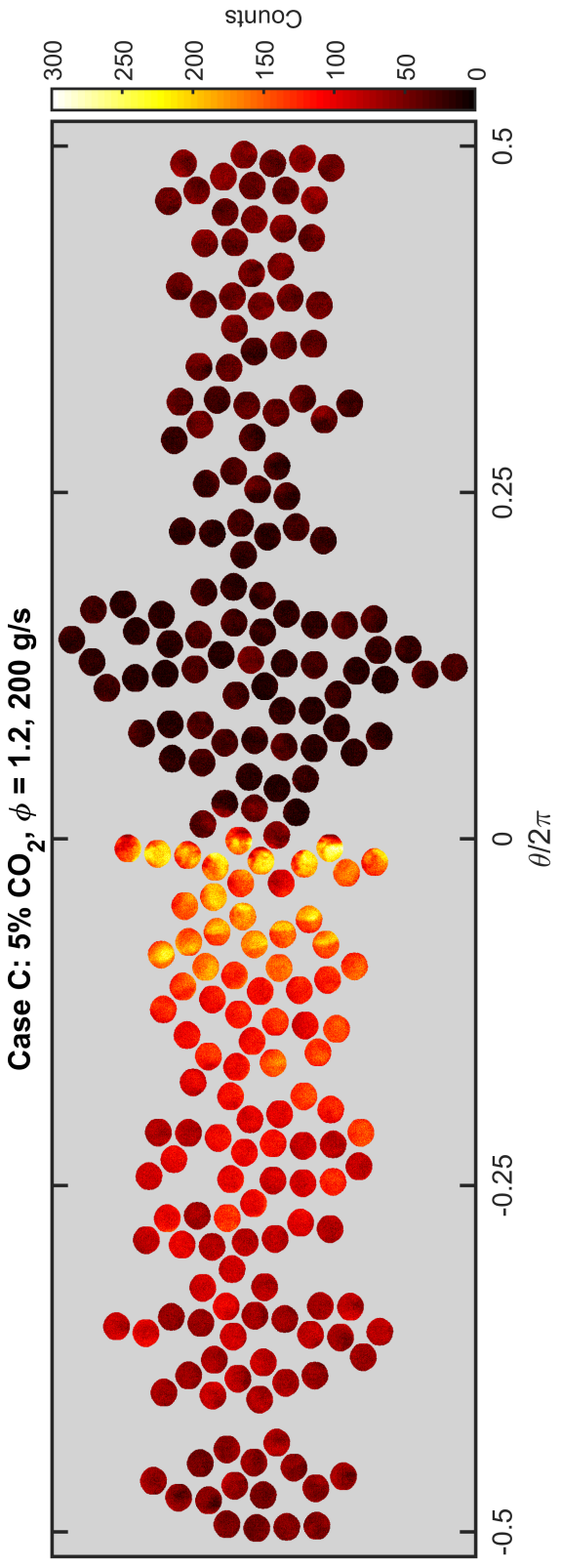
Case C: 5% CO_2, ϕ = 1.2, 200 g/s
Counts
300
250
200
150
100
50
0
0.5
0.25
0
-0.25
-0.5
$\theta/2\pi$

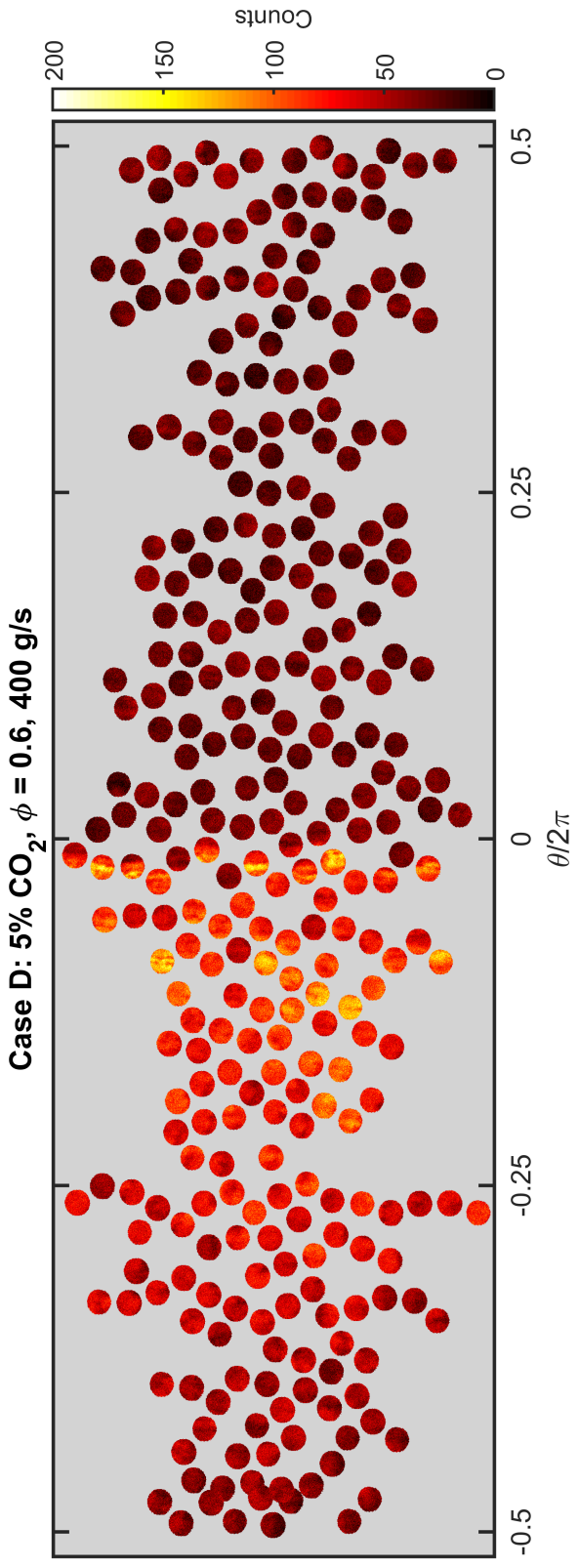
Case D: 5% CO_2, ϕ = 0.6, 400 g/s
Counts
200
150
100
50
0
0.5
0.25
0
-0.25
-0.5
$\theta/2\pi$

BIBLIOGRAPHY

[1] Hishida, M., Fujiwara, T., and Wolanski, P., "Fundamentals of rotating detonations," *Shock Waves*, Vol. 19, No. 1, Feb. 2009, pp. 1–10.

[2] Chacon, F. and Gamba, M., "OH PLIF Visualization of an Optically Accessible Rotating Detonation Combustor," *AIAA Propulsion and Energy 2019 Forum*, American Institute of Aeronautics and Astronautics, Aug. 2019.

[3] O'Connell, R. M. and Vogel, R. A., "Abel inversion of knife-edge data from radially symmetric pulsed laser beams," *Applied Optics*, Vol. 26, No. 13, July 1987, pp. 2528.

[4] Gordon, I., Rothman, L., Hill, C., Kochanov, R., Tan, Y., Bernath, P., Birk, M., Boudon, V., Campargue, A., Chance, K., Drouin, B., Flaud, J.-M., Gamache, R., Hodges, J., Jacquemart, D., Perevalov, V., Perrin, A., Shine, K., Smith, M.-A., Tennyson, J., Toon, G., Tran, H., Tyuterev, V., Barbe, A., Császár, A., Devi, V., Furtenbacher, T., Harrison, J., Hartmann, J.-M., Jolly, A., Johnson, T., Karman, T., Kleiner, I., Kyuberis, A., Loos, J., Lyulin, O., Massie, S., Mikhailenko, S., Moazzen-Ahmadi, N., Müller, H., Naumenko, O., Nikitin, A., Polyansky, O., Rey, M., Rotger, M., Sharpe, S., Sung, K., Starikova, E., Tashkun, S., Auwera, J. V., Wagner, G., Wilzewski, J., Wcisło, P., Yu, S., and Zak, E., "The HITRAN2016 molecular spectroscopic database," *Journal of Quantitative Spectroscopy and Radiative Transfer*, Vol. 203, Dec. 2017, pp. 3–69.

[5] Linstrom, P., "NIST Chemistry WebBook, NIST Standard Reference Database 69," 1997.

[6] Barh, A., Rodrigo, P. J., Meng, L., Pedersen, C., and Tidemand-Lichtenberg, P., "Parametric upconversion imaging and its applications," *Advances in Optics and Photonics*, Vol. 11, No. 4, Dec. 2019, pp. 952.

[7] Gayer, O., Sacks, Z., Galun, E., and Arie, A., "Temperature and wavelength dependent refractive index equations for MgO-doped congruent and stoichiometric LiNbO3," *Applied Physics B*, Vol. 91, No. 2, April 2008, pp. 343–348.

[8] Emanueli, S. and Arie, A., "Temperature-Dependent Dispersion Equations for $KTiOPO_4$ and $KTiOAsO_4$," *Applied Optics*, Vol. 42, No. 33, 2003, pp. 6661.

[9] Moffatt, J. E., Tsiminis, G., Klantsataya, E., de Prinse, T. J., Ottaway, D., and Spooner, N. A., "A practical review of shorter than excitation wavelength light emission processes," *Applied Spectroscopy Reviews*, Vol. 55, No. 4, 2020, pp. 327–349.

[10] Kinch, M. A., "Fundamental physics of infrared detector materials," *Journal of Electronic Materials*, Vol. 29, No. 6, June 2000, pp. 809–817.

[11] Djuric, Z., Livada, B., Jovic, V., Smiljanic, M., Matic, M., and Lazic, Z., "Quantum efficiency and responsivity of InSb photodiodes utilizing the Moss-Burstein effect," *Infrared Physics*, Vol. 29, No. 1, Jan. 1989, pp. 1–7.

[12] Høgstedt, L., Dam, J. S., Sahlberg, A.-L., Li, Z., Aldén, M., Pedersen, C., and Tidemand-Lichtenberg, P., "Low-noise mid-IR upconversion detector for improved IR-degenerate four-wave mixing gas sensing," *Optics Letters*, Vol. 39, No. 18, Sept. 2014, pp. 5321.

[13] Pedersen, R. L., Hot, D., and Li, Z., "Comparison of an InSb Detector and Upconversion Detector for Infrared Polarization Spectroscopy," *Applied Spectroscopy*, Vol. 72, No. 5, Dec. 2017, pp. 793–797.

[14] "FLIR," https://www.flir.com/.

[15] S., A. A., O'Donnell, C. F., Kumar, S. C., Ebrahim-Zadeh, M., Tidemand-Lichtenberg, P., and Pedersen, C., "Mid-infrared upconversion imaging using femtosecond pulses," *Photonics Research*, Vol. 7, No. 7, June 2019, pp. 783.

[16] Kiefer, J. and Ewart, P., "Laser diagnostics and minor species detection in combustion using resonant four-wave mixing," *Progress in Energy and Combustion Science*, Vol. 37, No. 5, Sept. 2011, pp. 525–564.

[17] Maiman, T. H., "Stimulated Optical Radiation in Ruby," *Nature*, Vol. 187, No. 4736, Aug. 1960, pp. 493–494.

[18] Franken, P. A., Hill, A. E., Peters, C. W., and Weinreich, G., "Generation of Optical Harmonics," *Physical Review Letters*, Vol. 7, No. 4, Aug. 1961, pp. 118–119.

[19] Armstrong, J. A., Bloembergen, N., Ducuing, J., and Pershan, P. S., "Interactions between Light Waves in a Nonlinear Dielectric," *Physical Review*, Vol. 127, No. 6, Sept. 1962, pp. 1918–1939.

[20] Midwinter, J. E., "Image conversion from 1.6 micrometers to the visible in lithium niobate," *Applied Physics Letters*, Vol. 12, No. 3, Feb. 1968, pp. 68–70.

[21] Warner, J., "Spatial resolution measurements in up-conversion from 10.6 micrometers to the visible," *Applied Physics Letters*, Vol. 13, No. 10, Nov. 1968, pp. 360–362.

[22] Boyd, G. D., Gandrud, W. B., and Buehler, E., "Phase-matched up conversion of 10.6-micrometer radiation in $ZnGeP_2$," *Applied Physics Letters*, Vol. 18, No. 10, May 1971, pp. 446–448.

[23] Janesick, J. R., Elliott, T., Collins, S., Blouke, M. M., and Freeman, J., "Scientific Charge-Coupled Devices," *Optical Engineering*, Vol. 26, No. 8, Aug. 1987.

[24] Chiou, W., "Geometric Optics Theory of Parametric Image Upconversion," *Journal of Applied Physics*, Vol. 42, No. 5, April 1971, pp. 1985–1993.

[25] Firester, A. H., "Parametric Image Conversion: Part I," *Journal of Applied Physics*, Vol. 40, No. 12, Nov. 1969, pp. 4842–4849.

[26] Firester, A. H., "Holography and Parametric Image Conversion: Part II," *Journal of Applied Physics*, Vol. 40, No. 12, Nov. 1969, pp. 4849–4853.

[27] Firester, A. H., "Image Upconversion: Part III," *Journal of Applied Physics*, Vol. 41, No. 2, Feb. 1970, pp. 703–709.

[28] Milton, A. F., "Upconversion – a Systems View," *Applied Optics*, Vol. 11, No. 10, Oct. 1972, pp. 2311.

[29] Falk, J. and See, Y. C., "Internal cw parametric upconversion," *Applied Physics Letters*, Vol. 32, No. 2, Jan. 1978, pp. 100–101.

[30] Bryan, D. A., Gerson, R., and Tomaschke, H. E., "Increased optical damage resistance in lithium niobate," *Applied Physics Letters*, Vol. 44, No. 9, May 1984, pp. 847–849.

[31] Houe, M. and Townsend, P., "An introduction to methods of periodic poling for second-harmonic generation," *Journal of Physics D: Applied Physics*, Vol. 28, No. 9, 1995, pp. 1747.

[32] Pedersen, C., Karamehmedović, E., Dam, J. S., and Tidemand-Lichtenberg, P., "Enhanced 2D-image upconversion using solid-state lasers," *Optics Express*, Vol. 17, No. 23, Oct. 2009, pp. 20885.

[33] Kehlet, L. M., Tidemand-Lichtenberg, P., Dam, J. S., and Pedersen, C., "Infrared upconversion hyperspectral imaging," *Optics Letters*, Vol. 40, No. 6, March 2015, pp. 938.

[34] Israelsen, N. M., Petersen, C. R., Barh, A., Jain, D., Jensen, M., Hannesschläger, G., Tidemand-Lichtenberg, P., Pedersen, C., Podoleanu, A., and Bang, O., "Real-time high-resolution mid-infrared optical coherence tomography," *Light: Science & Applications*, Vol. 8, No. 1, Jan. 2019.

[35] Høgstedt, L., Fix, A., Wirth, M., Pedersen, C., and Tidemand-Lichtenberg, P., "Upconversion-based lidar measurements of atmospheric CO_2," *Optics Express*, Vol. 24, No. 5, March 2016, pp. 5152.

[36] Wolf, S., Trendle, T., Kiessling, J., Herbst, J., Buse, K., and Kühnemann, F., "Self-gated mid-infrared short pulse upconversion detection for gas sensing," *Optics Express*, Vol. 25, No. 20, Sept. 2017, pp. 24459.

[37] Imaki, M. and Kobayashi, T., "Infrared frequency upconverter for high-sensitivity imaging of gas plumes," *Optics Letters*, Vol. 32, No. 13, Jul 2007, pp. 1923–1925.

[38] Morishita, K., Higuchi, Y., and Okada, T., "Infrared laser spectroscopic imaging based on degenerate four-wave-mixing spectroscopy combined with frequency-upconversion detection," *Optics Letters*, Vol. 24, No. 10, May 1999, pp. 688.

[39] Morishita, K., Kawaguchi, N., and Okada, T., "Quality in upconversion imaging of infrared degenerate four-wave mixing spectroscopy," *Optics Communications*, Vol. 184, No. 5-6, Oct. 2000, pp. 443–450.

[40] Hot, D., Pedersen, R. L., Weng, W., Zhang, Y., Aldén, M., and Li, Z., "Spatially and temporally resolved IR-DFWM measurement of HCN released from gasification of biomass pellets," *Proceedings of the Combustion Institute*, Vol. 37, No. 2, 2019, pp. 1337–1344.

[41] Barh, A., Pedersen, C., and Tidemand-Lichtenberg, P., "Ultra-broadband mid-wave-IR upconversion detection," *Optics Letters*, Vol. 42, No. 8, April 2017, pp. 1504.

[42] Dam, J. S., Tidemand-Lichtenberg, P., and Pedersen, C., "Room-temperature mid-infrared single-photon spectral imaging," *Nature Photonics*, Vol. 6, No. 11, Sept. 2012, pp. 788–793.

[43] "NLIR Mid-Infrared Sensors," https://www.nlir.com/.

[44] Eidelman, S., Grossmann, W., and Lottati, I., "Review of propulsion applications and numerical simulations of the pulsed detonation engine concept," *Journal of Propulsion and Power*, Vol. 7, No. 6, Nov. 1991, pp. 857–865.

[45] Jones, S. M. and Paxson, D. E., "Potential Benefits to Commercial Propulsion Systems from Pressure Gain Combustion," *49th AIAA/ASME/SAE/ASEE Joint Propulsion Conference*, American Institute of Aeronautics and Astronautics, July 2013.

[46] Bykovskii, F. A., Zhdan, S. A., and Vedernikov, E. F., "Continuous Spin Detonations," *Journal of Propulsion and Power*, Vol. 22, No. 6, Nov. 2006, pp. 1204–1216.

[47] Anand, V. and Gutmark, E., "Rotating detonation combustors and their similarities to rocket instabilities," *Progress in Energy and Combustion Science*, Vol. 73, July 2019, pp. 182–234.

[48] Duvall, J., Chacon, F., Harvey, C., and Gamba, M., "Study of the Effects of Various Injection Geometries on the Operation of a Rotating Detonation Engine," *2018 AIAA Aerospace Sciences Meeting*, American Institute of Aeronautics and Astronautics, Jan. 2018.

[49] Chacon, F., Feleo, A., and Gamba, M., "Secondary Waves Dynamics and Their Impact on Detonation Structure in Rotating Detonation Combustors," *Shock Waves*, 2020 – under review.

[50] Chacon, F. and Gamba, M., "Study of Parasitic Combustion in an Optically Accessible Continuous Wave Rotating Detonation Engine," *AIAA Scitech 2019 Forum*, American Institute of Aeronautics and Astronautics, Jan. 2019.

[51] Naples, A., Hoke, J., Karnesky, J., and Schauer, F., "Flowfield Characterization of a Rotating Detonation Engine," *51st AIAA Aerospace Sciences Meeting including the New Horizons Forum and Aerospace Exposition*, American Institute of Aeronautics and Astronautics, Jan. 2013.

[52] Rankin, B. A., Fugger, C. A., Richardson, D. R., Cho, K. Y., Hoke, J., Caswell, A. W., Gord, J. R., and Schauer, F., "Evaluation of Mixing Processes in a Non-Premixed Rotating Detonation Engine Using Acetone PLIF," *54th AIAA Aerospace Sciences Meeting*, American Institute of Aeronautics and Astronautics, Jan. 2016.

[53] Rankin, B. A., Richardson, D. R., Caswell, A. W., Naples, A. G., Hoke, J. L., and Schauer, F. R., "Chemiluminescence imaging of an optically accessible non-premixed rotating detonation engine," *Combustion and Flame*, Vol. 176, Feb. 2017, pp. 12–22.

[54] Cho, K. Y., Codoni, J. R., Rankin, B. A., Hoke, J., and Schauer, F., "High-Repetition-Rate Chemiluminescence Imaging of a Rotating Detonation Engine," *54th AIAA Aerospace Sciences Meeting*, American Institute of Aeronautics and Astronautics, Jan. 2016.

[55] Athmanathan, V., Fisher, J. M., Ayers, Z., Cuadrado, D. G., Andreoli, V., Braun, J., Meyer, T., Paniagua, G., Fugger, C. A., and Roy, S., "Turbine-integrated High-pressure Optical RDE (THOR) for injection and detonation dynamics assessment," *AIAA Propulsion and Energy 2019 Forum*, American Institute of Aeronautics and Astronautics, Aug. 2019.

[56] Athmanathan, V., Braun, J., Ayers, Z., Fisher, J., Fugger, C. A., Roy, S., Paniagua, G., and Meyer, T. R., "High speed imaging of injection backflow and recovery in a Turbine-integrated High-pressure Optical RDE (THOR)," *AIAA Scitech 2020 Forum*, American Institute of Aeronautics and Astronautics, Jan. 2020.

[57] Fugger, C. A., Cho, K. Y., Hoke, J., Gomez, M. G., Meyer, T. R., Schumaker, S. A., and Caswell, A. W., "Detonation Dynamics Visualization From Megahertz Imaging," *AIAA Scitech 2020 Forum*, American Institute of Aeronautics and Astronautics, Jan. 2020.

[58] Chacon, F. and Gamba, M., "Development of an optically accessible continuous wave Rotating Detonation Engine," *2018 Joint Propulsion Conference*, American Institute of Aeronautics and Astronautics, July 2018.

[59] Rankin, B. A., Codoni, J. R., Cho, K. Y., Hoke, J. L., and Schauer, F. R., "Investigation of the structure of detonation waves in a non-premixed hydrogen–air rotating detonation engine using mid-infrared imaging," *Proceedings of the Combustion Institute*, Vol. 37, No. 3, 2019, pp. 3479–3486.

[60] Pintgen, F., Eckett, C., Austin, J., and Shepherd, J., "Direct observations of reaction zone structure in propagating detonations," *Combustion and Flame*, Vol. 133, No. 3, May 2003, pp. 211–229.

[61] Mével, R., Davidenko, D., Austin, J., Pintgen, F., and Shepherd, J., "Application of a laser induced fluorescence model to the numerical simulation of detonation waves in hydrogen–oxygen–diluent mixtures," *International Journal of Hydrogen Energy*, Vol. 39, No. 11, April 2014, pp. 6044–6060.

[62] Davidenko, D., Gökalp, I., and Kudryavtsev, A., "Numerical modeling of the rotating detonation in an annular combustion chamber fed with hydrogen-oxygen mixture," *Third European combustion meeting*, 2007.

[63] Cocks, P. A., Holley, A. T., and Rankin, B. A., "High Fidelity Simulations of a Non-Premixed Rotating Detonation Engine," *54th AIAA Aerospace Sciences Meeting*, American Institute of Aeronautics and Astronautics, Jan. 2016.

[64] Sato, T. and Raman, V., "Hydrocarbon Fuel Effects on Non-premixed Rotating Detonation Engine Performance," *AIAA Scitech 2019 Forum*, American Institute of Aeronautics and Astronautics, Jan. 2019.

[65] Sato, T. and Raman, V., "Detonation Structure in Ethylene/Air-Based Non-Premixed Rotating Detonation Engine," *Journal of Propulsion and Power*, May 2020, pp. 1–11.

[66] Linne, M. A., "Chapter 3 - The Equation of Radiative Transfer," *Spectroscopic Measurement*, edited by M. A. Linne, Academic Press, London, 2002, pp. 35 – 73.

[67] Cho, K. Y., Sell, B., Hoke, J. L., and Schauer, F. R., "Hydrocarbon Fuel Absorption Measurement in Rotating Detonation Engine," *2018 AIAA Aerospace Sciences Meeting*, American Institute of Aeronautics and Astronautics, Jan. 2018.

[68] Goldenstein, C. S., Almodóvar, C. A., Jeffries, J. B., Hanson, R. K., and Brophy, C. M., "High-bandwidth scanned-wavelength-modulation spectroscopy sensors for temperature and H2O in a rotating detonation engine," *Measurement Science and Technology*, Vol. 25, No. 10, Sept. 2014, pp. 105104.

[69] Peng, W. Y., Cassady, S. J., Strand, C. L., Goldenstein, C. S., Spearrin, R. M., Brophy, C. M., Jeffries, J. B., and Hanson, R. K., "Single-ended mid-infrared laser-absorption sensor for time-resolved measurements of water concentration and temperature within the annulus of a rotating detonation engine," *Proceedings of the Combustion Institute*, Vol. 37, No. 2, 2019, pp. 1435–1443.

[70] Høgstedt, L., *Parametric Processes for Generation and Low Noise Detection of Infrared Light: Experimental and Numerical Investigation of Fundamental Parameters for the Design of PPLN-based Light Sources and Detector Systems*, Ph.D. thesis, Technical University of Denmark (DTU), 2016.

[71] Sutherland, R. L., *Handbook of Nonlinear Optics*, CRC Press, April 2003.

[72] Boyd, R., "Nonlinear optics," 1992.

[73] Junaid, S., Tomko, J., Semtsiv, M. P., Kischkat, J., Masselink, W. T., Pedersen, C., and Tidemand-Lichtenberg, P., "Mid-infrared upconversion based hyperspectral imaging," *Optics Express*, Vol. 26, No. 3, Jan. 2018, pp. 2203.

[74] Andrews, R., "Wide angular aperture image up-conversion," *IEEE Journal of Quantum Electronics*, Vol. 5, No. 11, 1969, pp. 548–550.

[75] Fejer, M. M., Magel, G. A., and Lim, E. J., "Quasi-Phase-Matched Interactions In Lithium Niobate," *Nonlinear Optical Properties of Materials*, edited by H. R. Schlossberg and R. V. Wick, SPIE, Jan. 1990.

[76] Maestre, H., Torregrosa, A. J., Fernández-Pousa, C. R., and Capmany, J., "IR-to-visible image upconverter under nonlinear crystal thermal gradient operation," *Optics Express*, Vol. 26, No. 2, Jan. 2018, pp. 1133.

[77] Rustagi, K., Mehendale, S., and Meenakshi, S., "Optical frequency conversion in quasi-phase-matched stacks of nonlinear crystals," *IEEE Journal of Quantum Electronics*, Vol. 18, No. 6, 1982, pp. 1029–1041.

[78] Fejer, M. M., Magel, G., Jundt, D. H., and Byer, R. L., "Quasi-phase-matched second harmonic generation: tuning and tolerances," *IEEE Journal of Quantum Electronics*, Vol. 28, No. 11, 1992, pp. 2631–2654.

[79] Thompson, D. E., McMullen, J. D., and Anderson, D. B., "Second-harmonic generation in GaAs "stack of plates" using high-power CO2laser radiation," *Applied Physics Letters*, Vol. 29, No. 2, July 1976, pp. 113–115.

[80] Pedersen, C., Hu, Q., Høgstedt, L., Tidemand-Lichtenberg, P., and Dam, J. S., "Non-collinear upconversion of infrared light," *Optics Express*, Vol. 22, No. 23, Nov. 2014, pp. 28027.

[81] Dam, J. S., Pedersen, C., and Tidemand-Lichtenberg, P., "Theory for upconversion of incoherent images," *Optics Express*, Vol. 20, No. 2, Jan. 2012, pp. 1475.

[82] Kim, Y. S. and Smith, R. T., "Thermal Expansion of Lithium Tantalate and Lithium Niobate Single Crystals," *Journal of Applied Physics*, Vol. 40, No. 11, Oct. 1969, pp. 4637–4641.

[83] "Amplitude Laser," https://amplitude-laser.com/.

[84] Howell, S. B., *Handbook of CCD Astronomy*, Cambridge University Press, April 2006.

[85] Airey, D., "Performance of a fibre-optic coupled, high-resolution spectrograph with CCD camera recording of solar Hα and Hβ absorption spectra," *Journal of the British Astronomical Association*, Vol. 116, No. 6, 2006, pp. 309–319.

[86] White, L. and Gamba, M., "Underresolved absorption spectroscopy of OH radicals in flames using broadband UV LEDs," *Journal of Quantitative Spectroscopy and Radiative Transfer*, Vol. 209, April 2018, pp. 73–90.

[87] Chacon, F. and Gamba, M., "OH PLIF Visualization of an Optically Accessible Rotating Detonation Combustor," *AIAA Propulsion and Energy 2019 Forum*, American Institute of Aeronautics and Astronautics, Aug. 2019.

[88] Pelc, J. S., Phillips, C. R., Chang, D., Langrock, C., and Fejer, M. M., "Efficiency pedestal in quasi-phase-matching devices with random duty-cycle errors," *Optics Letters*, Vol. 36, No. 6, March 2011, pp. 864.

[89] Savitzky, A. and Golay, M. J. E., "Smoothing and Differentiation of Data by Simplified Least Squares Procedures." *Analytical Chemistry*, Vol. 36, No. 8, jul 1964, pp. 1627–1639.

[90] Steinier, J., Termonia, Y., and Deltour, J., "Smoothing and differentiation of data by simplified least square procedure," *Analytical Chemistry*, Vol. 44, No. 11, sep 1972, pp. 1906–1909.

[91] Shoji, I., Kondo, T., Kitamoto, A., Shirane, M., and Ito, R., "Absolute scale of second-order nonlinear-optical coefficients," *Journal of the Optical Society of America B*, Vol. 14, No. 9, Sept. 1997, pp. 2268.

[92] Miller, R. C., "Optical second harmonic generation in piezoelectric crystals," *Applied Physics Letters*, Vol. 5, No. 1, July 1964, pp. 17–19.

[93] Alford, W. J. and Smith, A. V., "Wavelength variation of the second-order nonlinear coefficients of $KNbO_3$, $KTiOPO_4$, $KTiOAsO_4$, $LiNbO_3$, $LiIO_3$, β- BaB_2O_4, KH_2PO_4, and LiB_3O_5 crystals: a test of Miller wavelength scaling," *Journal of the Optical Society of America B*, Vol. 18, No. 4, April 2001, pp. 524.

[94] Kramida, A. and Ralchenko, Y., "NIST Atomic Spectra Database, NIST Standard Reference Database 78," 1999.

[95] Goodwin, D. G., Moffat, H. K., and Speth, R. L., "Cantera: An Object-oriented Software Toolkit for Chemical Kinetics, Thermodynamics, and Transport Processes," \url{http://www.cantera.org}, 2017.

[96] Baumeister, T., *Marks' standard handbook for mechanical engineers*, McGraw-Hill, New York, New York London, England, 2007.

[97] Chacon, F. and Gamba, M., "Development of an optically accessible continuous wave Rotating Detonation Engine," *2018 AIAA Aerospace Sciences Meeting*, American Institute of Aeronautics and Astronautics, Jan. 2018.

[98] Wolanski, P., "Detonation engines," *J. KONES Powertrain Transp.*, Vol. 3, No. 11, 2011.

[99] Bohon, M., Bluemner, R., Paschereit, C., and Gutmark, E., "High-speed imaging of wave modes in an RDC," *Experimental Thermal and Fluid Science*, Vol. 102, April 2019, pp. 28–37.

[100] Chacon, F. and Gamba, M., "Study of Parasitic Combustion in an Optically Accessible Continuous Wave Rotating Detonation Engine," *AIAA Scitech 2019 Forum*, American Institute of Aeronautics and Astronautics, Jan. 2019.

[101] Rose, A., *Vision: human and electronic*, Springer US, 1974.

[102] Feleo, A., Chacon, F., White, L. W., and Gamba, M., "Evaluation of OH Emission for Determining Operation of a Rotating Detonation Engine," *AIAA Scitech 2019 Forum*, American Institute of Aeronautics and Astronautics, Jan. 2019.

[103] Zeldovich, Y. B., "On the theory of the propagation of detonation in gaseous systems," 1950.

[104] Paxson, D. E., "Examination of wave speed in rotating detonation engines using simplified computational fluid dynamics," *2018 AIAA Aerospace Sciences Meeting*, 2018, p. 1883.

[105] Zhdan, S. A., Bykovskii, F. A., and Vedernikov, E. F., "Mathematical modeling of a rotating detonation wave in a hydrogen-oxygen mixture," *Combustion, Explosion, and Shock Waves*, Vol. 43, No. 4, July 2007, pp. 449–459.

[106] Wolf, S., Kiessling, J., Kunz, M., Popko, G., Buse, K., and Kühnemann, F., "Upconversion-enabled array spectrometer for the mid-infrared, featuring kilohertz spectra acquisition rates," *Optics Express*, Vol. 25, No. 13, June 2017, pp. 14504.

[107] Tidemand-Lichtenberg, P., Dam, J. S., Andersen, H. V., Høgstedt, L., and Pedersen, C., "Mid-infrared upconversion spectroscopy," *Journal of the Optical Society of America B*, Vol. 33, No. 11, Oct. 2016, pp. D28.

[108] Kojima, J. and Nguyen, Q.-V., "Laser pulse-stretching with multiple optical ring cavities," *Applied Optics*, Vol. 41, No. 30, Oct. 2002, pp. 6360.

[109] Sur, R., Sun, K., Jeffries, J. B., Hanson, R. K., Pummill, R. J., Waind, T., Wagner, D. R., and Whitty, K. J., "TDLAS-based sensors for in situ measurement of syngas composition in a pressurized, oxygen-blown, entrained flow coal gasifier," *Applied Physics B*, Vol. 116, No. 1, Sept. 2013, pp. 33–42.

[110] Kirby, B. J. and Hanson, B. K., "Imaging of CO and CO2 using infrared planar laser-induced fluorescence," *Proceedings of the Combustion Institute*, Vol. 28, No. 1, Jan. 2000, pp. 253–259.

[111] Loge, G. W., Tiee, J. J., and Wampler, F. B., "Multiphoton induced fluorescence and ionization of carbon monoxide (B $1\Sigma^+$)," *The Journal of Chemical Physics*, Vol. 79, No. 1, July 1983, pp. 196–202.

[112] Winter, M., Radi, P. P., and Stampanoni, A., "Double phase-conjugate four-wave mixing of OH in flames," *Symposium (International) on Combustion*, Vol. 24, No. 1, Jan. 1992, pp. 1645–1652.

[113] Fradkin, K., Arie, A., Skliar, A., and Rosenman, G., "Tunable midinfrared source by difference frequency generation in bulk periodically poled KTiOPO4," *Applied Physics Letters*, Vol. 74, No. 7, Feb 1999, pp. 914–916.

[114] Fradkin-Kashi, K., Arie, A., Urenski, P., and Rosenman, G., "Mid-infrared difference–frequency generation in periodically poled KTiOAsO_4 and application to gas sensing," *Optics Letters*, Vol. 25, No. 10, May 2000, pp. 743.